



# Università degli Studi di Ferrara

DOTTORATO DI RICERCA IN  
"SCIENZE DELLA TERRA"

CICLO XXIX

COORDINATORE Prof. Coltorti Massimo

ENVIRONMENTAL IMPACT ON UNESCO  
HERITAGE SITES IN PANAMA

Settore Scientifico Disciplinare GEO/09

**Dottorando**

Dott.ssa Ciantelli Chiara

(firma)

**Tutore**

Prof.ssa Bonazza Alessandra

(firma)

**Tutore**

Prof.ssa Vaccaro Carmela

(firma)

Anni 2014/2016



*Dedicated to  
my beloved parents, Patrizia and Cesare,  
to my grandfather, Giovanni  
and to Giacomo*



## *Table of contents*

<b>Abstract</b>	i
<b>Introduction</b>	1
<b>1. Chapter 1 - State of the Art</b>	3
<b>1.1. Historic Background</b>	3
<i>1.1.1. Panamá Viejo</i>	4
<i>1.1.2. Portobelo and San Lorenzo</i>	5
<i>1.1.3. The sites nowadays</i>	7
<b>1.2. Environmental Context</b>	8
<i>1.2.1. Geographical Position and Current Climate</i>	8
<i>1.2.2. Geological and Geomorphological Setting</i>	15
<i>1.2.3. Pollution and Anthropogenic Agents</i>	20
<b>1.3. Climate Change</b>	23
<i>1.3.1. Impact of the Environment on Cultural Heritage</i>	25
<i>1.3.1.1 Deterioration Phenomena</i>	25
<i>1.3.1.2 Evaluation of Damage</i>	27
<b>1.4. Previous Investigations and Interventions</b>	30
<i>1.4.1. Panamá Viejo</i>	30
<i>1.4.2. Portobelo and San Lorenzo</i>	34
<b>2. Chapter 2 – Materials and Methods</b>	35
<b>2.1 Survey, Sampling campaign and in situ observations</b>	35
<i>2.1.1 Panamá Viejo</i>	36
<i>2.1.2 Portobelo</i>	55
<i>2.1.3 San Lorenzo</i>	67
<b>2.2 Analyses Performed</b>	71
<b>2.3 Selection of Monitoring Stations and Climate Models</b>	73
<b>3. Chapter 3 - Materials Characterization and Damage Evaluation</b>	77
<b>3.1 Observation of thin sections by Polarized Light Microscopy (PLM)</b>	77
<i>3.1.1 Panama Viejo</i>	77

3.1.2	<i>Portobelo and San Lorenzo</i>	88
3.2	<b>X-Ray Powder Diffraction Analysis (XRPD)</b>	102
3.3	<b>Environmental Scanning Electron Microscopy Analysis (ESEM-EDS)</b>	108
3.3.1	<i>Materials Characterization</i>	108
3.3.2	<i>Evaluation of the State of Conservation</i>	128
3.4	<b>X-Ray Fluorescence Spectroscopy (XRF)</b>	137
3.5	<b>Mercury Intrusion Porosimetry Analysis (MIP)</b>	146
3.6	<b>Ion Chromatography Analysis (IC)</b>	154
4.	<b>Chapter 4 - Extraction of Climate Parameters</b>	159
4.1	<b>Comparison between climate simulations and monitoring stations</b>	159
4.1.1	<i>Panama Viejo area</i>	159
4.1.2	<i>Area near Panama Viejo</i>	164
4.1.3	<i>Area near San Lorenzo</i>	168
4.1.4	<i>San Lorenzo area</i>	177
4.1.5	<i>Portobelo area</i>	179
4.2	<b>Bias Correction</b>	181
4.2.1	<i>Panama Viejo area</i>	182
4.2.2	<i>Area near Panama Viejo</i>	189
4.2.3	<i>Area near San Lorenzo</i>	196
4.2.4	<i>San Lorenzo area</i>	203
4.2.5	<i>Portobelo area</i>	206
5.	<b>Chapter 5 - Damage evaluation using damage functions</b>	209
5.1	<b>Surface Recession</b>	209
5.1.1	<i>Panama Viejo area</i>	210
5.1.2	<i>Area near Panama Viejo</i>	212
5.1.3	<i>Area near San Lorenzo</i>	214
5.1.4	<i>San Lorenzo area</i>	216
5.1.5	<i>Portobelo area</i>	218
5.1.6	<i>Maps of Surface Recession</i>	220
5.2	<b>Salt Transitions</b>	223
5.2.1	<i>Panama Viejo area</i>	223

5.2.2	<i>Area near Panama Viejo</i>	225
5.2.3	<i>Area near San Lorenzo</i>	226
5.2.4	<i>San Lorenzo area</i>	227
5.2.5	<i>Portobelo area</i>	228
<b>5.3</b>	<b>Biomass Accumulation</b>	230
5.3.1	<i>Panama Viejo area</i>	230
5.3.2	<i>Area near Panama Viejo</i>	232
5.3.3	<i>Area near San Lorenzo</i>	234
5.3.4	<i>San Lorenzo area</i>	236
5.3.5	<i>Portobelo area</i>	238
5.3.6	<i>Maps of Biomass Accumulation</i>	240
<b>6.</b>	<b>Chapter 6 – Final considerations</b>	241
<b>6.1</b>	<b>Conclusions</b>	241
6.1.1	<i>Materials Characterization and Damage Evaluation</i>	241
6.1.2	<i>Determination of the environmental context and damage evaluation using damage functions</i>	242
<b>6.2</b>	<b>Future perspectives</b>	244
6.2.1	<i>Short-term in situ effects</i>	244
6.2.2	<i>Long-term research activities</i>	244
	<b>Acknowledgements</b>	247
	<b>References</b>	249
	<b>Appendix - Figures and Tables</b>	255
	<b>ANNEX 1 - Diffractograms</b>	275
	<b>ANNEX 2 – Publications, Proceedings, Presentations</b>	303





## ***Abstract***

The Panamanian isthmus, nowadays mostly known for its famous Canal, hosts two sites inscribed on the World Heritage List: the Archaeological site of Panama Viejo (XVI cent.) and the Fortresses of Portobelo and San Lorenzo (XVII-XVIII cent.).

In order to support the conservation and valorisation of these places, in 2014 a collaboration work has been started among the Patronage of Panama Viejo, the Patronage of Portobelo and San Lorenzo, the Institute of Atmospheric Sciences and Climate of the Italian National Research Council (ISAC-CNR) and the Department of Physics and Earth Sciences of the University of Ferrara (Italy).

Firstly, the project was focused on the characterization of rocks belonging to the masonries, in conjunction with the evaluation of their state of conservation and damage estimation in relation with the environmental impact. Furthermore, potential quarries of raw material supply have been identified and sampled, in order to define the provenance of the materials employed in the buildings and to compare the differences between the preservation of the rocks utilized in the masonries with the outcropping ones. Therefore, after a survey and sampling campaign, specimens underwent mineralogical-petrographic, physical and chemical analyses (Stereomicroscope, PLM, XRPD, SEM-EDX, XRF, MIP and IC), highlighting at Panamá Viejo masonries mainly composed of polygenic breccias, tuffites, basaltic andesites, rhyolites and sporadic rhyodacites. Only breccias and andesites outcrops were identified at the site of Panamá Viejo. Considering Portobelo fortifications, coral limestones and sandstones have been identified as principal construction materials; while basaltic andesite has been observed only at *Fuerte de San Fernando*, where an outcrop of this material was present. Finally, at Fort San Lorenzo, tuffites and grainstones have been detected in the masonries. These latter ones were mainly utilized for composing corners (as ornamental parts of the portals and the base blocks), moreover, possible quarries of both have been found.

Concerning the state of conservation, the most diffused deterioration phenomena are due to biological growth, exfoliation and detachment, disintegration (sanding and pulverization), salt encrustations and chromatic alteration (in particular affecting rhyolites).

Successively, in order to determine the environmental context, a selection of monitoring stations, near the sites of interest, recording climate parameters (near-surface air temperature, relative humidity and rainfall amount), have been selected among national Panamanian networks. Besides, the same parameters were collected from two climate models: EC-Earth, with a resolution of 25 km, and Arpege, with a resolution of 50 km, and compared with the monitored records. The climate variables were extracted both from historical simulations and future scenarios, in order to utilize them for possible upcoming damage predictions. Indeed, utilizing environmental data and applying specific damage functions it was possible to assess the deterioration phenomena occurring on heritage materials, as surface recession, cycles of salts transition and biomass accumulation.

Considering the first one, it was utilized Lipfert function modified (related to the karst effect), valid for carbonate rocks having a porosity lower than 25%. It showed a higher surface recession in the Northern area, of Portobelo and San Lorenzo, especially considering the data extracted from EC-Earth experiment, both for the past and the future situation.

In consideration of the salts cycles of dissolution and crystallization, halite has been elected as a priority phase of investigation, since sodium and chloride resulted ones of the most abundant ions in the samples, detected in all sites, also taking into account their proximity to the sea. In the past (1979-2008), transition cycles of halite highlighted that the higher frequency of this phenomenon is recorded

during the dry season (end of November/December to April/beginning of May). In general, making a comparison between the past and future conditions and among the sites, Portobelo results the less interested by this phenomenon, while the area near San Lorenzo seems to be the most affected.

In order to estimate the biomass accumulation on hard acid stones, calculated considering the organic carbon accretion on the surfaces, the function developed by Gomez-Bolea et al. (2012) was applied. The highest yearly biomass values are recorded, both in the past and future, in the areas on the North shore, especially at Portobelo, reaching  $21 \text{ g cm}^{-2}$ .

In conclusion, the obtained results contribute significantly to the formulation of guidelines and development of strategies for current and future preservation of the sites, and represent a fundamental knowledge for further related analysis, in order to increase the awareness of the possible risks connected with the climate change impact on Cultural Heritage.

## Introduction

Always more frequently, the cutting-edge issue of climate change and its effects is a daily fact that we need to deal with. Several fields are increasing the awareness of the possible risks connected with it, and recently, especially in Europe, the Cultural Heritage sector is beginning to be conscious of the potential problems related with the climate change impact on the materials composing our “tangible culture”. Nevertheless, further steps are needed in order to ensure a sustainable culture, for assuring the best preservation of monumental complexes, archaeological sites, historical urban centres, artefacts, etc., for guaranteeing their fruition by the future generations.

With the aim of enhancing the knowledge in this field, in particular in an area not yet largely investigated concerning this topic as Central America, in 2014 the present PhD research work started. Subject of this study are two sites of global importance: the monumental site of Panamá Viejo, the first Spanish settlement on the Pacific Panamanian coast, and the Spanish military fortifications arising on the Northern littoral of the isthmus. Both are inscribed on the List of World Heritage; in particular, the Fortifications on the Caribbean Side of Panama have been inscribed on the List of World Heritage in Danger, since 2012.

This research involves an international partnership, formed by the Institute of Atmospheric Sciences and Climate, ISAC-CNR (Bologna, Italy), the Department of Physics and Earth Sciences of the University of Ferrara (Italy) and the two Panamanian Patronages: the *Patronato Panamá Viejo* and the *Patronato de Portobelo y San Lorenzo*, aimed at managing and preserving the sites.

From the environmental point of view, these places represent an interesting comparative study, since the different locations permit a comparison between a rural site (Portobelo and San Lorenzo Fortifications) and another one totally embedded in an urban context (Panamá Viejo site, within Panama City); nevertheless, both are exposed to the same climate conditions. In order to have a complete comprehension of the sites, an overview of the state of the art has been performed in Chapter 1, concerning the historical, environmental and geological background, as well as the interaction between environment and monuments and, finally, the previous analyses and interventions realized. Subsequently, the project was firstly focused on the material characterization of the stone masonries belonging to the different sites, choosing to analyse only rocks, since mortars will be object of successive investigations. In conjunction with the materials identification, it was also performed the evaluation of the state of conservation and damage in relation with the environmental impact. Furthermore, possible quarries of raw materials supply have been identified and sampled, in order to define the provenance of the stones employed in the buildings fabrication, and to compare the differences between the preservation of the rocks utilized in the masonries with the outcropping ones. For performing this preliminary and fundamental part of the research work, a survey and sampling campaign were realized in order to select the representative specimens of the different rock typologies utilized in the several buildings. Moreover, the samples were chosen on the base of their state of conservation, indeed selecting rocks showing high deterioration phenomena (procedures are described in Chapter 2.1).

In order to characterize precisely and investigate in detail the building constituents, mineralogical-petrographic, physical and chemical analyses have been performed, through the techniques enumerated hereinafter:

- Stereomicroscope observations;
- Polarized Light Microscopy (PLM) investigations;
- X-Ray Powder Diffraction (XRPD) analysis;

- Environmental Scanning Electron Microscopy and micro-chemical investigations (ESEM-EDX);
- X-ray fluorescence (XRF);
- Mercury Intrusion Porosimetry (MIP);
- Ion Chromatography (IC);

Procedures are described in Chapter 2.2, while results are discussed in Chapter 3.

Successively, in order to determine the environmental context, a selection of monitoring stations near the sites of interest, recording climate parameters (near-surface air temperature, relative humidity and rainfall amount), have been selected among national Panamanian networks. Besides, the same parameters were collected from two climate models: EC-Earth, with a resolution of 25 km, and Arpege, with a resolution of 50 km. The climate variables were extracted both from historical simulations and future scenarios, in order to utilize them for future damage predictions. Both the selection of monitoring stations and the description of the climate experiments utilized are illustrated in Chapter 2.3; while the extraction of parameters from models are within Chapter 4.

Finally, using environmental data and applying them in specific damage functions, as surface recession, biomass accumulation and transition of salts, it is possible to assess the deterioration phenomena occurring on these heritage materials (Chap. 5).

In conclusion, this research work has allowed us to produce projections of potential climate change impacts on the Panamanian heritage, considering the over time slow changes and not the extreme events, since the effects of the first ones are measurable through math relations of specific variables, by the comparison of the future (2009-2100) to the recent past (1979-2008) situation. Thanks to the obtained results, it will be possible to contribute at the formulation of guidelines aiming at the short term preservation of the sites and to have fundamental knowledge available for further risk assessment related to climate change impact (Chap. 6).

# 1. Chapter 1 - State of the Art

## 1.1. Historic Background

Panamá, the narrowest part of the isthmian region of the American continent, nowadays is mostly known for its famous Canal, a huge engineering work of great importance for global trade. Being a crucial and strategic crossroad for commercial routes is a feature that Panamá has since the XVI century, when it linked the "New World" and the "Old World".

Rodrigo de Bastidas discovered this strip of land for the first time, in 1501, sailing along its north-eastern coast. One year later, Christopher Columbus explored, on the Caribbean littoral, the currently named Bocas del Toro, Veragua, the Chagres River and a bay that he called "Portobelo". Afterwards, the region was conquered by the Spaniards, at first, occupying the Caribbean coasts and then, reaching the opposite shore, where they founded the first Spanish settlement on the Pacific Ocean, in the 1519, the currently named Panamá Viejo.

During the XVI-XVII centuries, this region grew in importance for the Spanish commercial traffic. Indeed, it represented a new route for the trade of spices from Asia, and for precious metals, carved in the neighbouring areas. For these reasons, it hosted an *ante litteram* "World Expo": the Portobelo Fair (1597-1731), one of the most important meeting of international commercial activity at this time, attracting a great amount of merchants, but also drawing the attention of the others powers of the time, as England. This carried several attacks by pirates and corsairs, on both coasts of the isthmus, marking radically the history of this land (Correa de Sanjur, 1976) (Mena García, 1997) (de Arango, 2006) (Patronato de Panamá Viejo y Embajada de España en Panama, 2006) (Arroyo, 2010).

Locations of the sites under study, Panamá Viejo monumental site and fortresses of Portobelo and San Lorenzo are represented in Figure 1.1.1.



Figure 1.1. 1 Map showing the locations of Panamá Viejo monumental site and fortresses of Portobelo and San Lorenzo (modified from <http://www.freeworldmaps.net/centralamerica/panama/panama-map-physical.jpg>).

### 1.1.1. Panamá Viejo

Archaeological studies revealed that the first human's settlements, in the area of the current Panamá Viejo, date back to 1000 years ago. At that time, this oceanfront land was swampy, full of mangroves and rivers, with a great abundance of water, allowing a rich fishing. When the Spaniards arrived in that part of the isthmus, they found an anglers' village, of the indigenous population *Cueva*, called Panamá, which probably meant "abundance of fish, trees and butterflies" (Correa de Sanjur, 1976).

On the 15<sup>th</sup> of August, 1519, Pedrarias Dávila, hailing from Segovia and governor of Castilla del Oro, reached this village and founded the town of Panamá La Vieja, which represented the first Spanish outpost on the Pacific littoral and a base for their expansion on this coast (Fig 1.1.1.1).

After 154 years of the town foundation, Henry Morgan, a British corsair, docked at the Atlantic coast, looting Portobelo and headings towards Panamá town. On the 28<sup>th</sup> of January 1671, in order to avoid the invasion of the town, its Governator, Juan Pérez de Guzmán, set fire to it. After this traumatic event, Panamá Viejo was abandoned and its materials used to build a new settlement closer to the Ancón Hill, the currently named "Casco Antiguo" and represented in Figure 1.1.1.2 (Patronato de Panamá Viejo y Embajada de España en Panama, 2006) (Correa de Sanjur, 1976).

The Panama Viejo Historical Monument Complex was declared in 1976 and about 20 years later the Patronato Panama Viejo was created aimed at its preservation and valorisation.



Figure 1.1.1. 1 Map of Panamá Viejo by Bautista Antonelli (XVI century) - Museo Naval de Madrid (Arroyo, 2015).



Figure 1.1.1. 2. Pictures of monuments at Panamá Viejo at the beginning of XX century - Biblioteca del Canal de Panamá.

Addressing the attention to the constructions subject of the study here presented, the complexes investigated are eight and specifically the following listed and described (Mena García, 1992; Tejeira Davis, 2007; <http://www.panamaviejo.org/>):

1. *Fortín de la Natividad* built in the XVII century (probably after 1616), with the oldest wall possibly attributable to the southern one, it was aimed at defending the town from the West side. During the 1950s and 1960s it underwent several reconstruction projects, nevertheless these changes are not documented.
2. *Convento de San Francisco*, founded by the Franciscan order, the first arrived in the Americas, was built from 1603. It was one of the largest in Panama City, including a dormitory, church, cloister with a patio, surrounded by a wall without windows, occupying approximately 5000 m<sup>2</sup> (currently 3000 m<sup>2</sup>).
3. *Hospital de San Juan de Dios*, originally named “Saint Sebastian Hospital”, was created two years after the foundation of Panama Viejo town. It was called San Juan de Dios from 1620, named after the order that took over the hospital in that period. The convent original area of 2500 m<sup>2</sup> is currently reduced to 1500 m<sup>2</sup> and it was formed by a large stonewall house, which included a church, cloisters, salons, rooms, patios and the Military Hospital.
4. *Convento de las Monjas de la Concepción* is hosted in an area of 1500 m<sup>2</sup> at the Western end of the city. The church was built after the fire of 1671, so a century later of the town foundation. After the town destruction, the facade of the church was moved to realize the current *Iglesia de la Merced* at Casco Antiguo and the remains of its walls were used to build the city walls. Moreover, during the 20<sup>th</sup> century, its ruins were damaged during the construction of the “first” *Vía Cincuentenario*, dividing the complex and the church in half.
5. *Convento de la Compañía de Jesus*, located close to the Plaza Mayor, it was founded in 1578 by the Jesuit priest Miguel de Fuentes and built out of wood. From the beginning of the 17<sup>th</sup> the convent was converted in stone masonries and pre-made structures, drawn by the architect Father Andrés Alonso de Valladolid, using clay as joint mortar. The remains visible today correspond to the church and the main cloisters, date from the period after the 1621 earthquake.
6. *Casa Terrín* is formed by several houses facing the Plaza Mayor, built around 1600 by Francisco Terrín, one of the most powerful inhabitants of the city. The wall interested by our sampling arises near this complex.
7. *Torre de la Catedral* was built, as we currently know it in stone masonry, between 1619 and 1626, after several wooden structures, by initiative of Bishop Francisco de Cámara. In particular, the tower (used as belfry and watchtower) was much more solidly built than the rest of the building.
8. *Casas Reales* were erected on bare rock foundations, next to the seaside, in several phases throughout the XVI century, protected by a palisade, and a moat separated it from the rest of the city. It hosted the offices of the royal government as The Royal Treasury, the Royal Court, the court prison, the governor’s residence and other official rooms. Seriously damaged during the 1621 earthquake, in 1647 the Casas Reales were demolished and after the abandonment of the town, the tides eroded their walls. In the middle of the XX Century a police station was built next to these structures and in the 1970s-1980s the Defense Forces built great amounts of infrastructure on top of the Royal Houses, including a heliport.

### ***1.1.2. Portobelo and San Lorenzo***

The fortresses of Portobelo and San Lorenzo arise on the North side of the Panamanian isthmus, facing the Caribbean Sea.

As aforementioned, their history is strictly connected with the management of the commercial routes between the American and the European continents, indeed thanks to their position these sites were chosen in order to protect the Spanish territories and harbours.

Specifically Portobelo, after one year of the discovery by Columbus, underwent to several phases of defence constructions. The first defence system and urban design was attributed to the Italian engineer Bautista (Battista) Antonelli (years 1596 - 1597), but it is during the second stage, realized from 1663 to 1685, that the military fortifications started to sprout up. In this period, on the southeast coast of the bay, San Jerónimo foundations redoubt were built (1664 – 1670).

However, through a military building renewal campaign, carried out in 1753 – 1760 by the engineers Ignacio Sala and Manuel Hernández, the number and the dimensions of the constructions were enlarged. During this third phase, the San Fernando redoubt, lower and upper batteries; the Santiago de la Gloria redoubt and battery (1768 -1770 modifications); the San Jerónimo fort-battery, the powder magazine and the Farnesio battery tower were realized.

Located on a promontory beside the Chagres River mouth, about 70 km east of Portobelo Bay, Fort San Lorenzo construction covered almost one century, from the 1575 to 1768. The works on the first defence buildings (1575 – 1595) had been directed by Antonelli, while successive improvements were carried out during the 17<sup>th</sup>-18<sup>th</sup> centuries, precisely during 1676 – 1680 and 1761 – 1768 (this latter one designed by Hernandez), after its taken and destruction, firstly performed by the corsair Henry Morgan (1671) and secondly by the British admiral Edward Vernon (1740). This latter one is responsible to the destruction of the main fortifications in Portobelo and the taking of the village.

Nevertheless, after few decades these sites would lose their strategic importance and, consequently, their function would be modified and/or abandoned. Indeed, as a result of the ending of Portobelo's Fair (1731) and the independence from Spain (1821), in 1869 San Lorenzo was turned into a state prison by the Columbian authorities until 1903, year of the foundation of the Panamanian Republic, when it was abandoned.

All the fortresses from the beginning of the 20<sup>th</sup> century until the 70s had been in a state of neglect. For instance, the lower section of Fort Santiago de la Gloria, underwent to erosion by waves action; while several part of Fort San Jerónimo were partially covered by vegetation, from microflora to higher plants. In addition, the east wall of lower battery collapsed in 1996. The Fort had been used as a boat port, showing temporary installations, probably baths, built in the walls perimeter. Considering Fort San Fernando, it was almost totally covered by vegetation as shown in the following picture (Fig.1.1.2.1) (World Monument Fund, 2003; Tejeira Davis, 2007; <http://whc.unesco.org/en/list/135>).





Figure 1.1.2. 1 Pictures of San Fernando at the beginning of the XX century and during the 70s (from World Monument Fund et al, 2003).

### ***1.1.3. The sites nowadays***

At the beginning of the XX century, after the creation of the Republic of Panamá, Panamá Viejo was declared first "public monument" (1912) and still now, it represents a symbol of national identity.

In the last decades, the archaeological site of Panamá Viejo (2003), Casco Antiguo (1997) and the Fortifications on the Caribbean Side of Panamá (1980), have been included in the World Heritage List of UNESCO, specifically in the last decade (<http://whc.unesco.org/en/list/790>). In particular, the Portobelo and San Lorenzo Fortresses have been inscribed on List of World Heritage in Danger since Jun 27, 2012 (<http://whc.unesco.org/en/list/135>).

## 1.2. Environmental Context

### 1.2.1. Geographical Position and Current Climate

According with the "thermal zones of the Earth", the climate classification created by Köppen-Geiger and validated for the second half of the 20th century by Kottek et al. (2006), the area of Panama has been classified as an equatorial climate, within the types listed below and showed in Figure 1.2.1.1:

- Af: "Equatorial monsoon";
- Am: "Equatorial rainforest, fully humid";
- Partially, Aw: "Equatorial savannah with dry winter";

This classification adopts a first letter to indicate the main climate typologies, in our case an A, referred to equatorial zone, showing a minimum of temperature greater than or equal to +18 °C, while the second letter indicates precipitation (P) conditions. Criteria used, and concerning Panamanian area, are respectively: f, with  $P_{\text{minimum}} \geq 60$  mm; m, with  $P_{\text{annual}} \geq 25 (100 - P_{\text{minimum}})$ ; w, with  $P_{\text{minimum}} < 60$  mm in winter.

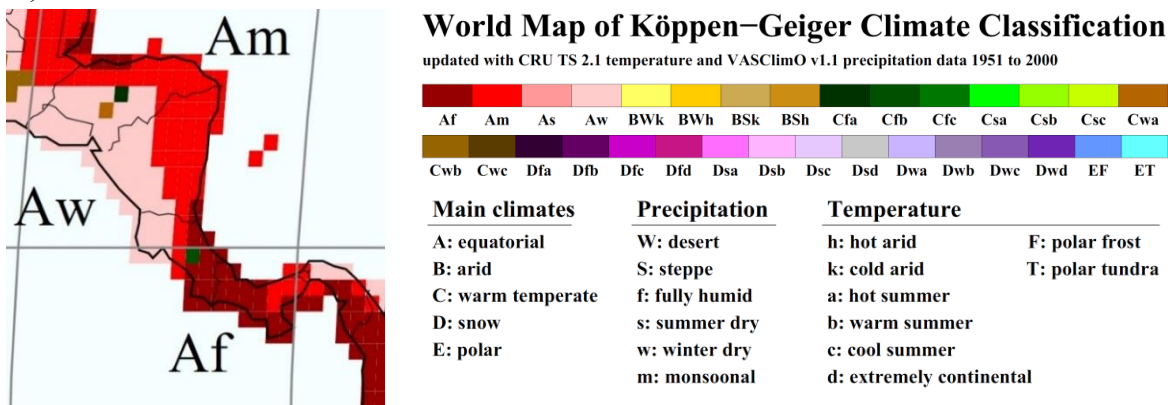
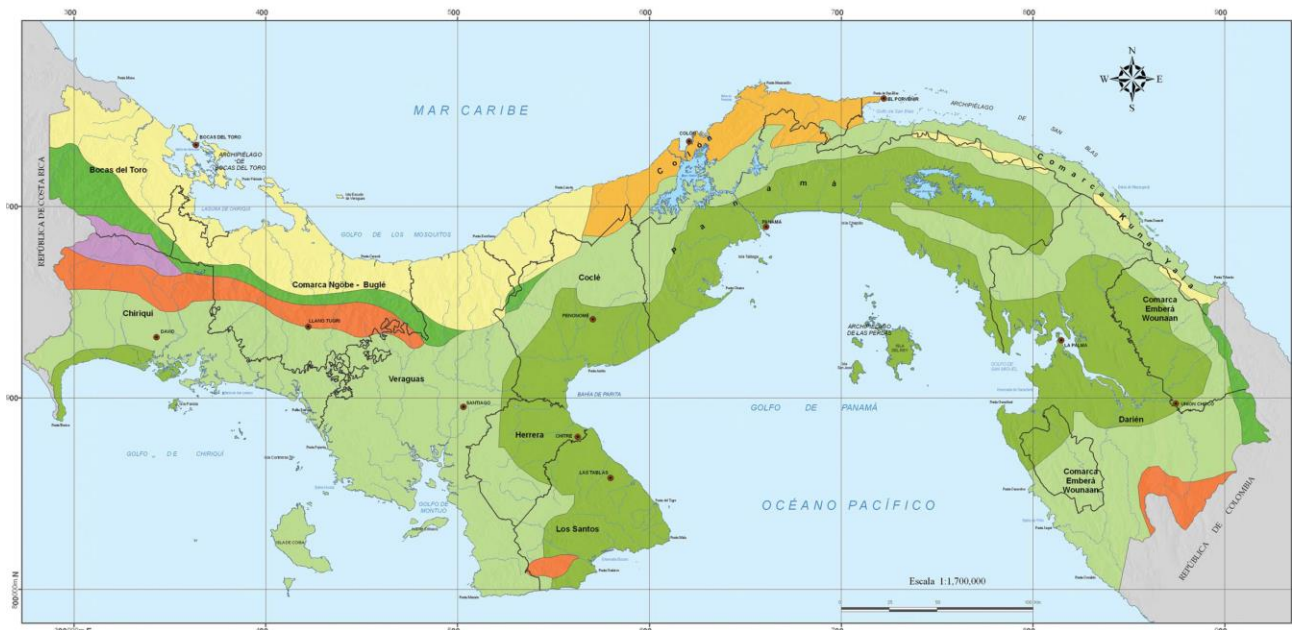


Figure 1.2.1. 1. Particular of the World Map of Köppen-Geiger Climate Classification, showing the Panamanian Isthmus (Kottek et al, 2006).

In 2000, a Panamanian geographer and historian, Dr Alberto A. McKay, developed a specific classification of the isthmian environment, taking into account the influence of the oceanic masses (Autoridad Nacional del Ambiente, 2010). Indeed, this strip of land is largely conditioned by the maritime presence, the interaction between atmosphere and ocean determines the high values of both temperature and humidity, which characterize the air circulating between the two oceans (Atlantic and Pacific). In addition, this region is located in the Intertropical Convergence Zone (ITCZ), where the northeast and southeast trade winds (Alisei) converge. This situation produces the presence of two separated seasons in the majority of this territory: the dry and rainy season. The latter one is the most durable, covering the period from April until November/December; for that reason the yearly precipitation amount records high values as 3500 mm on the Caribbean coast and 2300 mm on the Pacific littoral. Regarding temperature, no significant variations are observed during the whole year, which shows 27°C as annual mean value in both seasons.

More specifically, Dr McKay identified seven different climate typologies for Panama, displayed in Figure 1.2.1.2:



## Leyenda

### Tipos de clima según McKay:

<ul style="list-style-type: none"> <li><span style="display: inline-block; width: 20px; height: 10px; background-color: #4CAF50; margin-right: 5px;"></span> Clima Tropical de Montaña Baja</li> <li><span style="display: inline-block; width: 20px; height: 10px; background-color: #8BC34A; margin-right: 5px;"></span> Clima Subecuatorial con estación seca</li> <li><span style="display: inline-block; width: 20px; height: 10px; background-color: #FFF9C4; margin-right: 5px;"></span> Clima Tropical Oceánico</li> <li><span style="display: inline-block; width: 20px; height: 10px; background-color: #FFC107; margin-right: 5px;"></span> Clima Tropical Oceánico con estación seca corta</li> </ul>	<ul style="list-style-type: none"> <li><span style="display: inline-block; width: 20px; height: 10px; background-color: #8BC34A; margin-right: 5px;"></span> Clima Tropical con estación seca prolongada</li> <li><span style="display: inline-block; width: 20px; height: 10px; background-color: #FF9800; margin-right: 5px;"></span> Clima Oceánico de Montaña Baja</li> <li><span style="display: inline-block; width: 20px; height: 10px; background-color: #9C27B0; margin-right: 5px;"></span> Clima Tropicales de Montaña Media y Altas</li> </ul>
---	--

Figure 1.2.1. 2. Panamanian Climate typologies according with McKay classification in 2000 (Autoridad Nacional del Ambiente, 2010).

1. *Tropical Oceanic Climate*: with temperature average values around 25-27°C, and high yearly total amount of precipitations reaching 4346 mm. The dry season is absent and in all months more than 100 mm of rainfall are recorded.
2. *Tropical Oceanic Climate with short dry season*: temperature average values are around 25.5°C on the coastal area and 26.5°C in the continental part. Precipitations are abundant, reaching annual amounts of 4760 mm. Dry season has a brief duration of 4-10 weeks, with 40-90 mm of precipitations between February and March.
3. *Subequatorial Climate with dry season*: climate mostly diffused in Panama, with temperature average values of 26.5-27.5°C in the areas <20 m above sea level and 20°C at height of 1000 m above sea level (asl). Precipitations reach values around 2500-3519 mm, with a length of the dry season of 3-4 month.
4. *Tropical Climate with prolonged dry season*: it is the warmest climate, with temperature average values of 27-28°C, recording the lowest amount of precipitation, lower than 2500 mm and 1122 in few areas. During the long-lasting dry season it is characterized by strong winds, with mid-high clouds, low humidity and, consequently, high evaporation.

5. *Oceanic Climate of low mountain*: it is referred to areas upper than 900-1000 m (asl), characterized by low temperatures (18°C), abundant annual rainfall (3710 mm) and absence of dry season, a part of few weeks in February.
6. *Tropical Climate of low mountain*: areas upper than 900-1000 m (asl), featured by high precipitation.
7. *Tropical Climate of mid-high mountain*: it characterizes zone higher than 1600 m (asl). It shows low temperature, especially during night-time; average values are of 17.4°C at 1700 m (asl), 14.8°C at 2300 m (asl) and 10-11°C at 3000 m (asl) even reaching 0°C during the dawn.

As shown in Figure 1.2.1.2, our areas of interest, Portobelo, San Lorenzo and Panamá Viejo are characterized by two of these seven classification groups. In particular, the *Tropical Oceanic Climate with short dry season* characterises Portobelo and San Lorenzo, while in Panamá Viejo a *Tropical Climate with prolonged dry season* is present. As aforementioned, these two zones show different annual precipitation amount, higher on the North coast than on the Southern one, nevertheless in both cases the dry season is clearly recognizable from the rainy one observing the monthly rainfall distribution (Fig. 1.2.1.3).

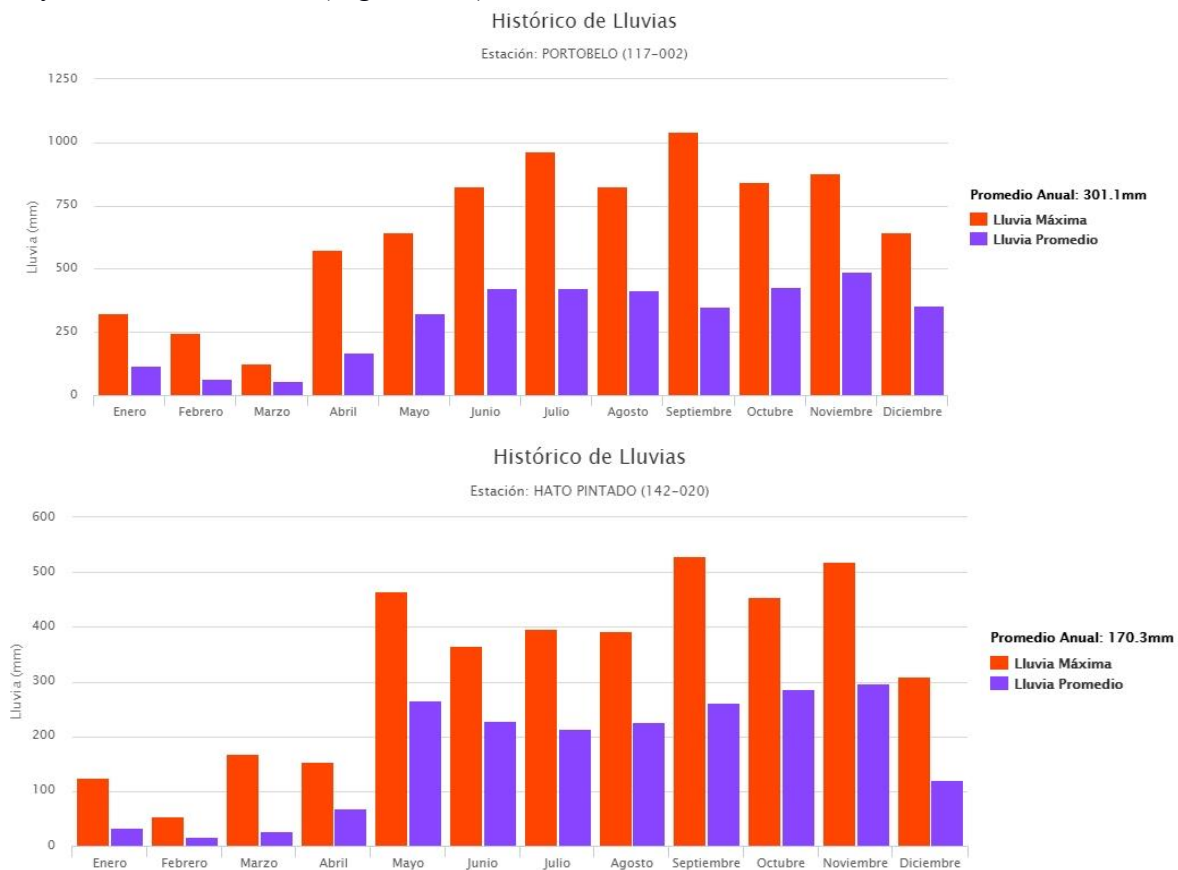


Figure 1.2.1. 3. Comparison between the monthly maximum (red) and the average (violet) of precipitation in Portobelo (up, timespan 1908-2004) and near Panamá Viejo (Hato Pintado, down, timespan 1987-now), curtesy of Hidrometeorología de la Empresa de Transmisión Eléctrica, S.A. ([http://www.hidromet.com.pa/clima\\_historicos.php?sensor=2](http://www.hidromet.com.pa/clima_historicos.php?sensor=2)).

Furthermore, it has to be underlined that generally in Panama rainfall events are very intense, with quite short duration, and prolonged during the rainy season, which covers the majority of the year (8-10 months). Recent studies demonstrated that in the last years precipitations around Panamá City has increased exceeding long-term averages, nevertheless the beginning and the duration of the rainy, and, consequently, of the dry season have been changing (Paton, 2015). The concentration of

precipitations in specific periods (as mid-August, always according to Paton, 2015), cause also the increment of the rain intensity, triggering linked effects on the monuments exposed to it, such as a higher mechanical erosion and chemical deterioration, due to the water permeation in the structures (Camuffo, 1995).

In addition, this phenomenon, in conjunction with the growth of urbanization frequently without a planning, caused the increase of surface runoff. Effectively, the fast proliferation of urban areas, especially the overbuilding and roads paving, creates waterproof surfaces; consequentially the rainfall water cannot be drained by the ground provoking, as result, extreme events that are: erosion, sediments and floods. Finally, the runoff can carry contaminants dissolved in it, thus it represents a source of danger both for the human beings and for the Cultural Heritage, which can be exposed to these salts and/or pollutants dissolved in water (Autoridad Nacional del Ambiente, 2010; Gázquez et al. 2015; Brimblecombe, 2016; Ordóñez et al. 2016).

According to Satterthwaite (2007) the Panamanian region can be affected by an increase of heat waves: "most cities in Africa, Asia and Latin America and the Caribbean will experience more heat waves. Even small increases in average temperature can result in large shifts in the frequency of extremes (Kovats and Aktar, 2008). For larger, higher-density cities, the temperatures in central "heat islands" can be several degrees higher than in surrounding areas; in tropical cities, the temperature difference can reach 10 degrees by the end of the night."

In considering the surroundings of our sites of interest, it has to be underlined the sea proximity and, consequently, the sea level and tidal variations. In 1963, a work was published on the sea level variation at Panama region (Roden, 1963), collecting records from 1909 to 1962, and highlighting the sea level increase of  $8.5 \pm 1.5$  cm at Balboa (at the South entrance of Panama Canal) and  $7.1 \pm 2.0$  cm at Cristobal (North entrance of Panama Canal), correlating this increment mainly to land subsidence.

Strictly linked with the sea level rise, tides in Panama record high variation. In the Caribbean littoral, the tidal level measures an average of the minimum amplitude of 0.015 m, reaching a maximum of 0.84 m. While, on the Pacific coast higher variations have been recorded, with a daily average amplitude of 1.5 m, reached twice a day, and showing periodical maximum values of 6.7 m (these tides are called "aguajes") (Alba Carranza, 1946; Jay, 2009).

This factor is responsible for the progressive coastal erosion in the last five centuries, which carried the ruins of Panamá Viejo to be distant only 100 m from the sea (Strong, 2009); causing also the erosion of the archaeological monuments, in particular of "Casas Reales", the complex erected in the part nearest the coast (Figs. 1.2.1.4-1.2.1.5).



Figure 1.2.1.4 Low tide view at Casco Antiguo bastion (Panama City). Picture took in the end of August 2014 at 11:00 a.m.



Figure 1.2.1.5 Walls of one of the structures belonging to the complex "Casas Reales" showing the erosion due to the sea waves action.

Considering the Caribbean littoral (Fig. 1.2.1.6), the Fortresses located in Portobelo are principally exposed to the water action, mainly due to rainfall and sea water. In the specific case, San Jeronimo undergoes to the sea intrusion, especially during storms; however also the daily tidal variations causes the erosion of the external walls and water infiltration (Figs. 1.2.1.7-1.2.1.9).

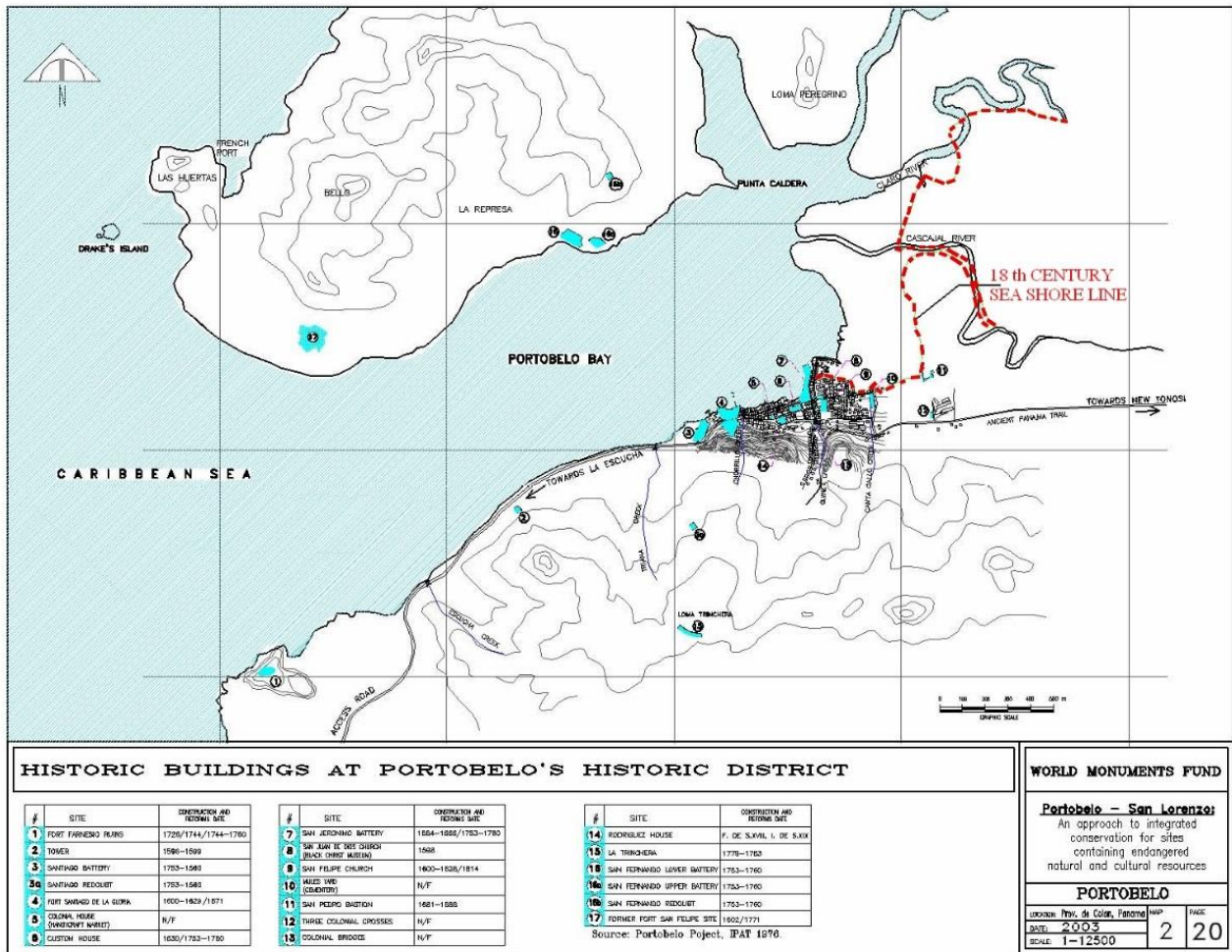


Figure 1.2.1. 6. Map of Portobelo Bay. With the red-dotted line is highlighted the 18th century seashore line (World Monument Fund et al., 2003).



Figure 1.2.1.7. External view of sea-front walls of Fort San Jeronimo. Picture took in the beginning of September 2014 at 4:00 p.m.



Figure 1.2.1.8. Inner view of sea-front walls of Fort San Jeronimo. Picture took in the beginning of September 2014 at 12:00 a.m.



Figure 1.2.1.9. Inner view of sea-front walls of Fort San Jeronimo. Picture took in the beginning of September at 2014 4:00-5:00 p.m.

This fortification shows also settling problems, due to the nature of the ground which is a sandy soil. Even San Fernando is subjected to the sea water permeation, additionally in the inner part of the Fort (Fig. 1.2.1.10). In the case of Santiago, *La Bateria*, it is built on a site with a high phreatic level, so often there is water emerging from the ground (Fig. 1.2.1.11). In addition, in 2010, a landslide occurred from the mountain above, causing the deviation of a natural spring, which gushed from a fountain located in a corner of the Fortress, leading to the water flooding from others splits or from the ground.



Figure 1.2.1.10 Entrance of the "Bateria Baja" of Fort San Fernando. The proximity of the sea is clearly visible.



Figure 1.2.1.11 Water emerging in the ground of Fort Santiago – Bateria.

Another factor, which has to be considered, is the wind erosion, especially considering Fort San Lorenzo, which stands out on a promontory at a height of about 20 meters on the sea level (Fig. 1.2.1.12), in conjunction with others extreme events, as rainfalls and wind driven rain already mentioned above.



Figure 1.2.1. 12. Aerial view of Fort San Lorenzo (<http://www.planur-e.es/>).



### 1.2.2. Geological and Geomorphologic Setting

In recent decades, several geological researches in fields of volcanology, geochemistry, hydrogeology, geophysics, conducted by the Institute of Hydrology and Electricity (IRHE), have contributed to give a better understanding of the geological evolution of Panama, especially about its volcanology (Candanedo and Fábrega, 1999).

The complex region formation is due to multifarious interactions among five plates, two continental, the North and South American ones, and three oceanic shelves called Caribbean, Cocos and Nazca (Fig. 1.2.2.1); this latter one is still subducting beneath the Panamanian portion of the Caribbean plate (Knutzen, 2010).

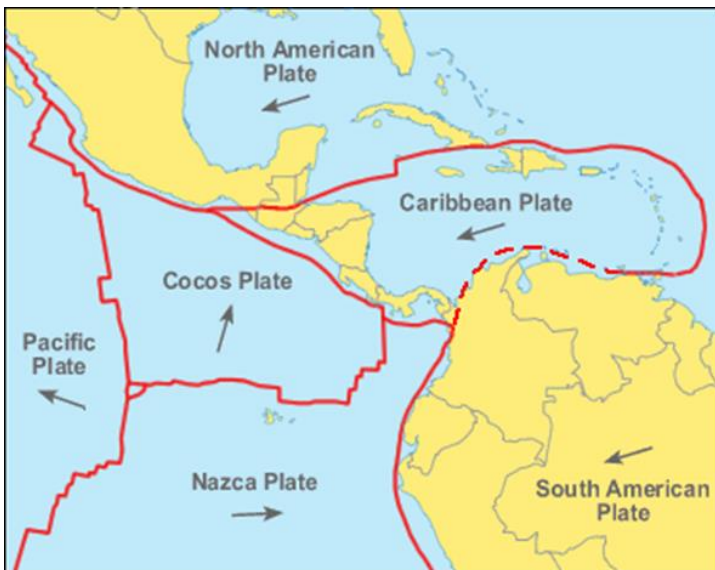


Figure 1.2.2.1. <http://plate-tectonic.narod.ru/central-america-plate-tectonics01.gif>

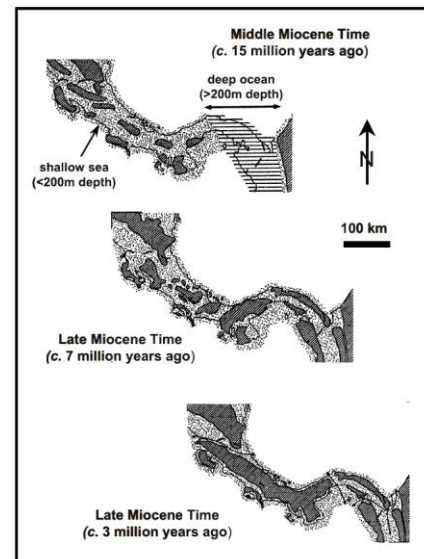


Figure 1.2.2.2. Paleogeographic reconstruction of the development of the Central American isthmus since Middle Miocene time (from Harmon, 2005).

Tectonic activity, which originated the isthmus, started during late Cretaceous, approximately 90-75 Ma ago, coinciding with the period of major growth of the Caribbean Large Igneous Province (CLIP), a flood basalt basement derived from the mafic magma emission of Galapagos hotspot/plume (Serrano, 2011; Smithsonian Tropical Research Institute, 2011). After long and complex processes, during the Oligocene and Miocene time, an arc of volcanic islands arisen, which nowadays constitutes part of the Central America Volcanic Arc (CAVA), extending from Guatemala to the northern Panama. Formation of basins of sediments followed, gradually linking the islands and finally creating the Panamanian strip of land (about 3 Ma ago) and, consequently, interrupting the marine circulation between the Pacific and Caribbean area (Harmon, 2005) (Fig. 1.2.2.2).

As it is justifiable and according with the statement of Cunningham et al. (1984), nearly 70 percent of the isthmus consists of volcanic rocks and also clearly shown in Figure 1.2.2.3.

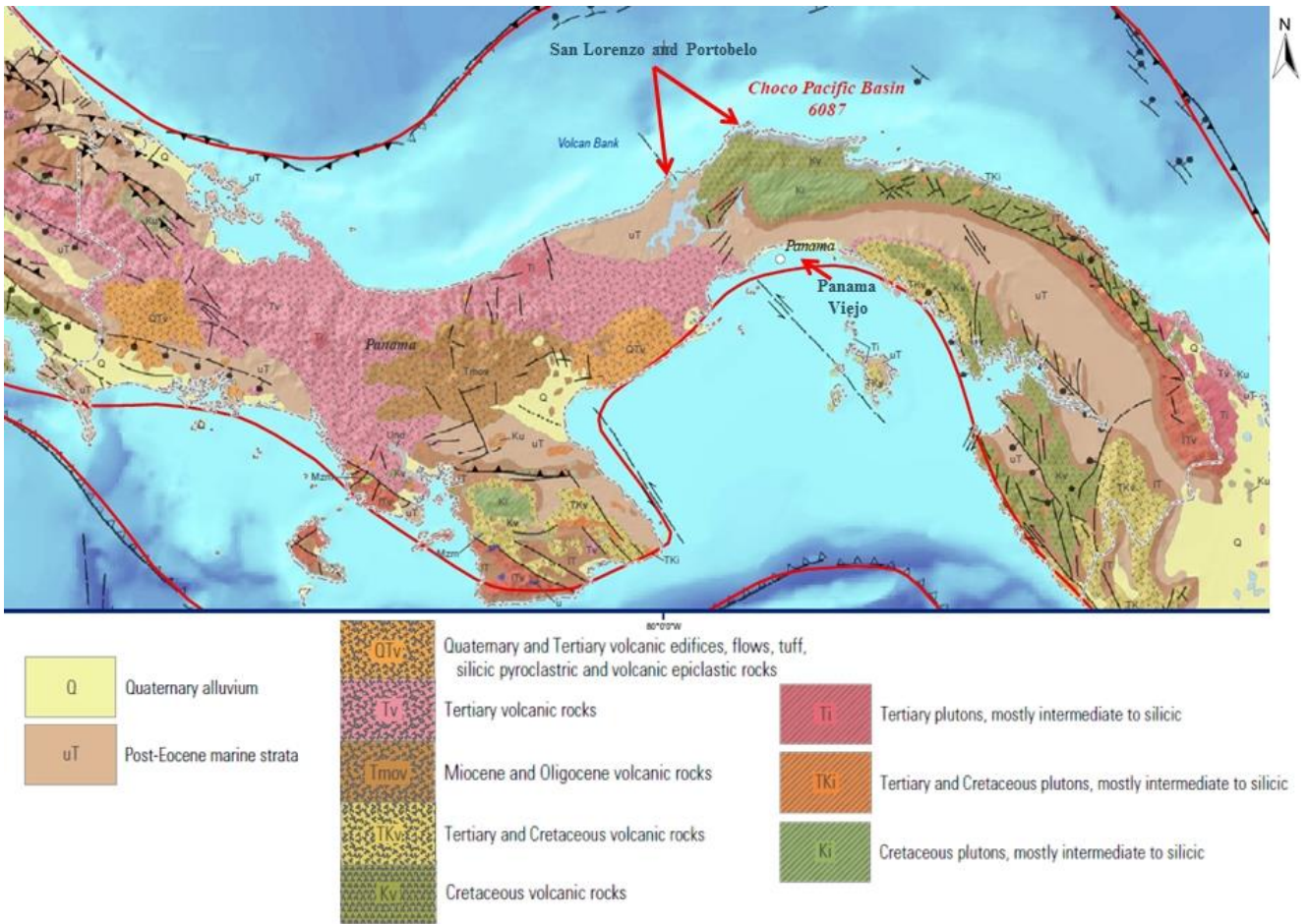


Figure 1.2.2.3. (Modified from French and Schenk, 2000).

Considering specifically San Lorenzo, it rises in the outcropping area of Chagres sandstone, Toro limestone, Gatun Formation (sandstone, siltstone, tuff and conglomerate) and alluvium or fill sediments. While in Portobelo, formations of altered basaltic and andesitic lavas and tuff are present, in addition to dioritic and dacitic rocks, alluvium or fill sediments and fringing coral reef (Fig. 1.2.2.4 and Tab. 1.2.2.1).

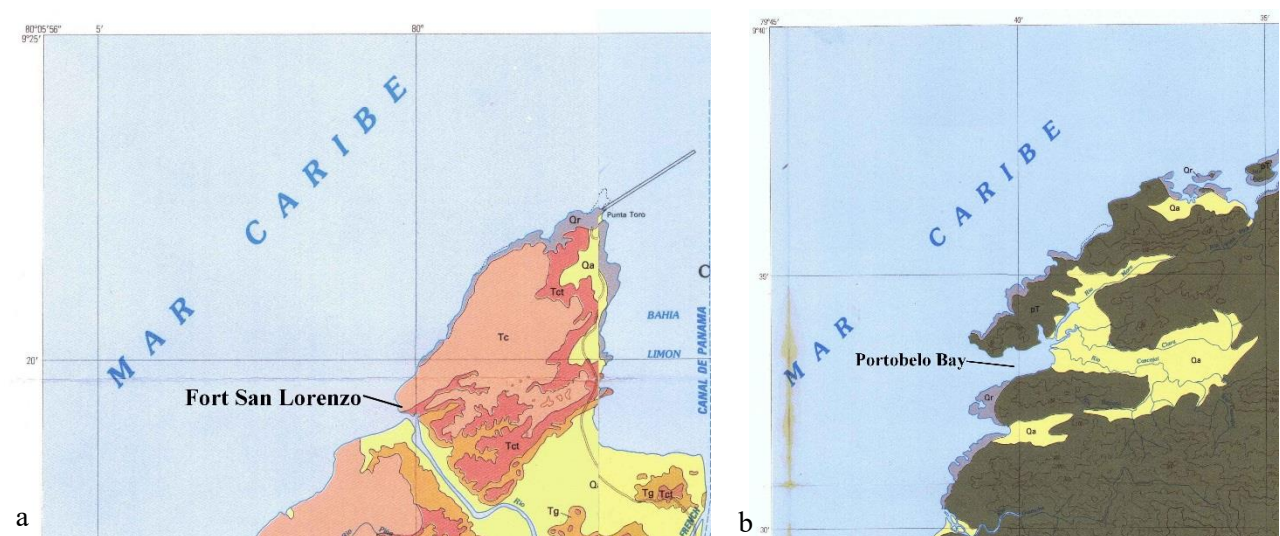


Figure 1.2.2.4. Geological Map 1:25000 of a. San Lorenzo area and b. Portobelo area (modified from Stewart and Woodring, 1980).

Observing the surroundings of Panamá Viejo the formations present are: Panamá, marine facies (tuffaceous sandstone and siltstones, algal and foraminifera limestones) and volcanic facies (agglomerates, generally andesitic in fine-grained tuffs and streamed deposited conglomerates). Moreover, there is La Boca Formation (with siltstones, sandstone, tuff and limestones); finally, alluvium or fill sediments, basalts and andesite (Fig. 1.2.2.5 and Tab. 1.2.2.1).

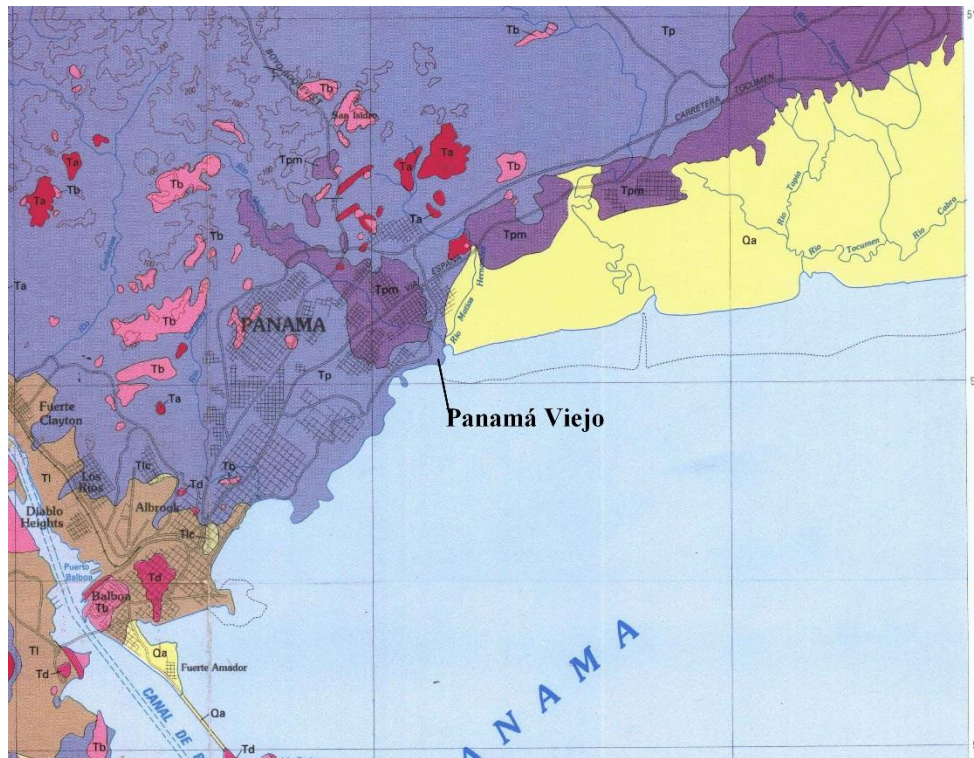


Figure 1.2.2.5. Geological Map 1:25000 of Panamá Viejo area (modified from Stewart and Woodring, 1980).

Table 1.2.2.1 Legenda of Formations, Symbols and Descriptions of rocks showed in figures 1.2.2.4-5 (modified from Stewart and Woodring, 1980).

<b>Sedimentary Rocks</b>	
Undivided Holocene sediments, principally alluvium or fill	Qa
Holocene fringing coral reefs	Qr
Chagres Sandstone, late Miocene or early Pliocene. Massive, generally fine-grained sandstone	Tc
Toro Limestone, basal member of Chagres Sandstone. Coquina	Tct
Gatun Formation, middle Miocene. Sandstone, siltstone, tuff and conglomerate	Tg
Alhajuella Formation, upper member, late early Miocene. Tuffaceous sandstone, calcareous sandstone and limestone	Tau
Alhajuella Formation, lower member, late early Miocene. Calcareous sandstone.	Tal
La Boca Formation, early Miocene. Mudstone, siltstone, sandstone, tuff and limestone	Tl
Emperador Limestone, member in lower La Boca. Coraliferous limestone	Tle
Pedro Miguel Formation, early Miocene. Fine-to coarse-grained agglomerate	Tpa
Cucaracha Formation, early Miocene. Bentonitic clay shale, carbonaceous clay shale and in lower part, a thin ash flow tuff	Tca
Las Cascadas Formation, early Miocene. Agglomerate and soft, fine-grained tuff	Tlc
Culebra Formation, early Miocene. Calcareous sandstone and siltstone	Tcb
Caraba Formation, late Oligocene. Principally a dacite porphyry agglomerate. In type area, conglomerate, fossiliferous calcareous sandstone and limestone	Tcr
Caimito Formation, late Oligocene, marine. Tuffaceous sandstone, tuffaceous siltstone, tuff and foraminiferal limestone	Tcm
Caimito Formation, volcanic facies, late Oligocene. Agglomerate and tuffaceous graywacke	Tcv
Quebrancha Limestone, member of Caimito Formation, late Oligocene. Foraminiferal limestone and calcareous siltstone	Tcqu
Bohio Formation, early to late Oligocene. Conglomerate, principally basaltic and graywacke sandstone	Tbo
Bohio Formation, marine facies, early to late Oligocene. Calcareous sandstone and small-pebble conglomerate	Tbm
Panama Formation, early to late Oligocene. Principally agglomerate, generally andesitic in fine-grained tuff. Includes stream-deposited conglomerate	Tp
Panama Formation, marine facies, early to late Oligocene. Tuffaceous sandstone, tuffaceous siltstone, algal and foraminiferal limestone. Sandy siltstone in basal part of formation in Quebrancha syncline	Tpm
Bas Obispo Formation, Oligocene(?). Agglomerate and hard tuff	Tba
Marine rocks, late Eocene. Sandstone and siltstone	Tue
Gatuncillo Formation, middle and late Eocene. Mudstone, siltstone, quartz sandstone, algal and foraminiferal limestone	Tgo
Pre-Tertiary. Altered basaltic and andesitic lavas and tuff. Includes dioritic and dacitic intrusive rocks	pT
<b>Volcanic Rocks</b>	
Intrusive and extrusive basalt, middle and late Miocene	Tb
Intrusive dacite and dacite porphyry, Miocene	Td
Andesite, equal in age to Las Cascadas Formation, early Miocene	Tlca
Intrusive and extrusive andesite, Oligocene and early Miocene	Ta
Volcanic rocks, undifferentiated, generally early Miocene or older	Tv

Regarding Panamá Viejo area, a recent thesis has performed specific analysis on the geology of the archaeological site realizing a characterization of the superficial soil in order to establish a geological pattern of the area where the colonial structures are erected (Grajales Saavedra, 2012). The study divided the area in ten survey points, showed in Figure 1.2.2.6, showing the presence of a volcanic eruption on the coast near the Casas Reales Complex. Specifically, the rocks, showing a aphanitic texture, are mainly characterized by andesite, which showed a superficial oxidation, in addition in the area n.2 agglomerates have been detected, as andesitic agglomerate. Finally, pyroclastic outcrops have been identified near the complex of the "Torre de la Catedral".

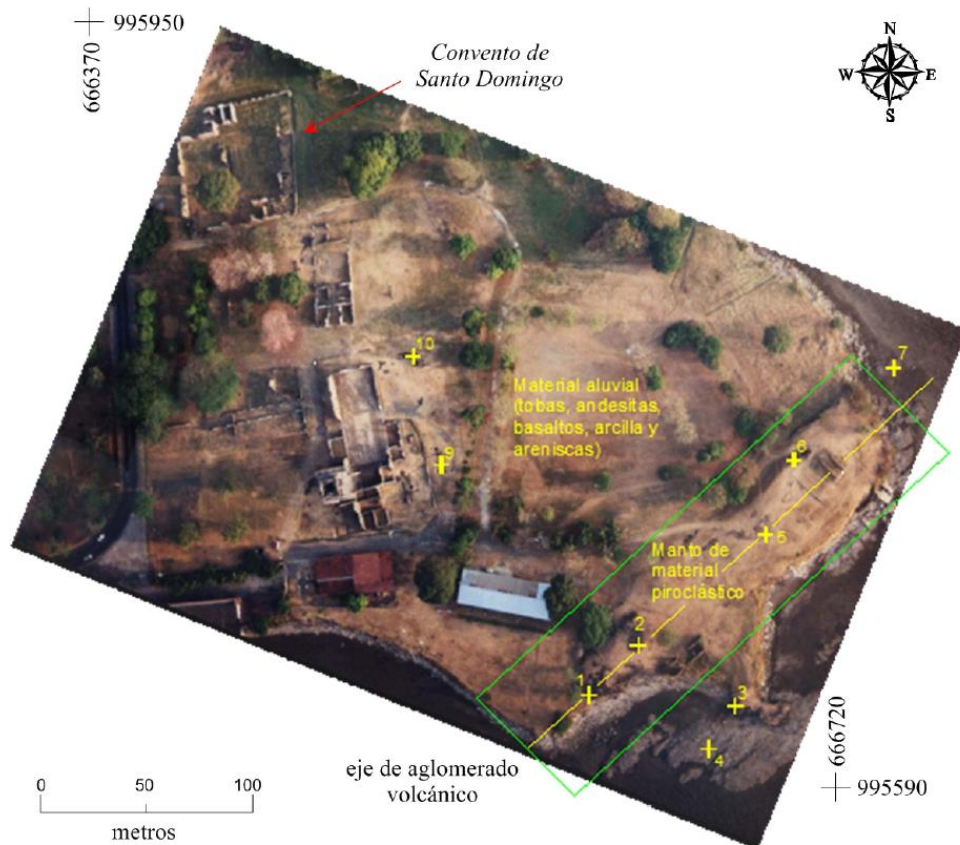


Figure 1.2.2. 6. Soil characterization of the monumental complex of Panamá Viejo (Pinzón y González, 2004).

### 1.2.3. Pollution and Anthropogenic Agents

The Isthmus of Panama can be summarized in the following numbers:

- Width: 75.517 km<sup>2</sup>
- Inhabitants: 3.661.868 (2013), almost tripling the population in 40 years (1961-2003, Fig.1.2.3.1).
- Metropolitan Area (MA) of Panama City :
  - Inhabitants: 1.3 million (40% of the total)
  - Registered vehicles: 557.000
  - Dwellings: 402.196

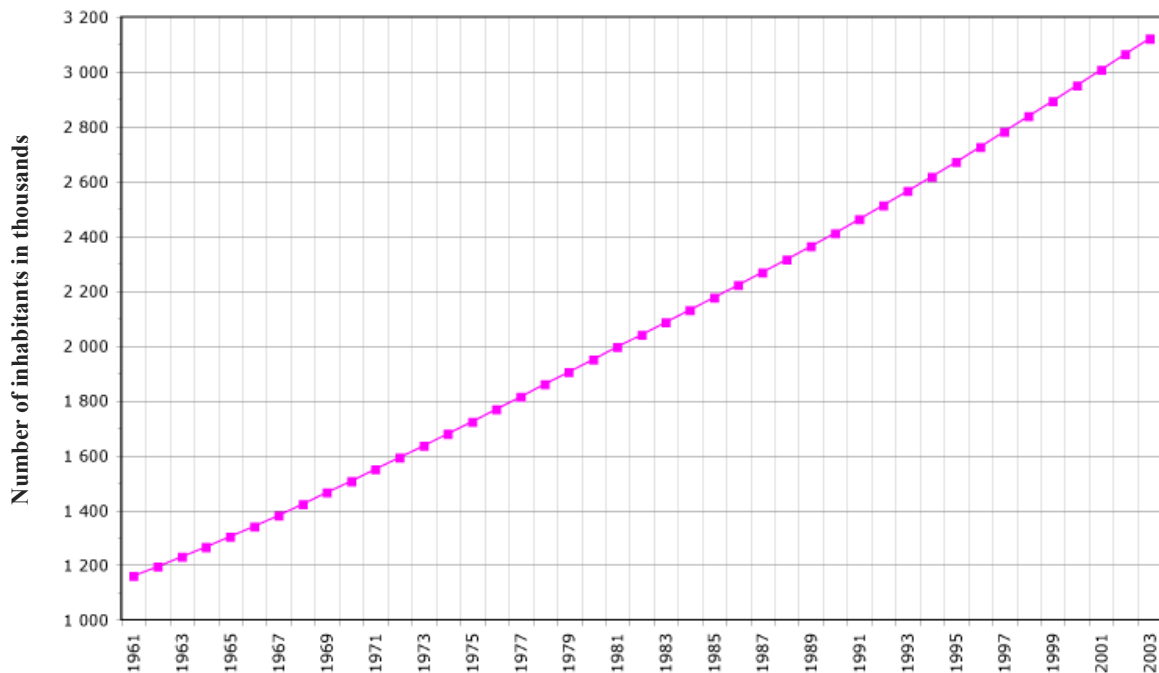


Figure 1.2.3. 1. Panama's population (1961-2003) Data FAOSTAT, year 2005 (<http://faostat.fao.org/faostat/help-copyright/copyright-e.htm>).

- Energy annual consumption: 380.680.472 gallons
- Economical activities: 21.023
  - 1.627 manufacturing industries:
    - 800 belong to the province of Panama.
    - 188 industries (16%) generate emissions.

Considering the distribution of GDP (Gross Domestic Product) the main sector is represented by services, as shown in Figure 1.2.3.2.

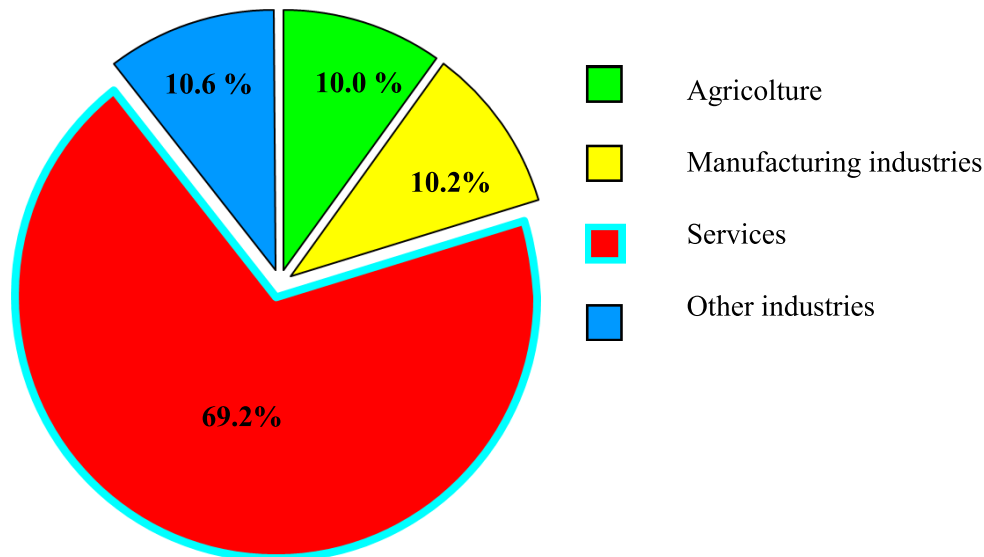


Figure 1.2.3. 2. GDP (Gross Domestic Product) (Forte, 2008).

Panama presents an advantageous situation; in terms of good dispersion conditions and since there are not heavy industries and active volcanoes. Nevertheless, it has been registered a considerable growth of the vehicles number and, consequently, an increase in pollution emissions, especially in the MA of Panama City. Moreover, the dispersion conditions are changing, depending on the rapid and unplanned urbanization.

Therefore, in this region the 90% of pollution is due to vehicular emissions, mostly (64.2%) concentrated in the Province of Panama, where traffic congestion is responsible of the major local problems. Considering the emission of sulphur dioxide there is an intensification of 13% because of the increasing of consumption of fossil fuel. Growing the numbers of vehicles, the nitrogen oxides rise 48%, while 62% the hydrocarbons, and 35% the carbon monoxide.

Finally, no epidemiological studies have been carried out in the past in correlation with the pollution effects on human health, however, respiratory diseases are among the main causes of illness expected in Panama (Forte, 2008). Only recently, researches have been addressed to the connection with human health and pollution (Urriola García et al., 2014; Zúñiga et al., 2016).

According with these observations, Panamá Viejo can be exposed to pollution effects, even considering that since 1950 until 2012, a traffic-congested street, *Vía Cincuentenario*, had crossed the archaeological site, and nowadays it runs along the northern side of the site.

On the contrary, regarding the Fortresses of Portobelo and San Lorenzo, they can be considered in a rural area, even if the Forts of San Jeronimo, San Cristobal, Santiago and partially Farnesio are closer to the little town of Portobelo, so can they can be partially affected by the interaction with pollutants mainly due to vehicular traffic origin.

Additionally, we have to take into account the proximity of the Panama Canal and consequently, the ship emissions correlated. In 2016, the expansion project of the structure should be completed in May, allowing the transit of vessels that can carry up to 13.000/14.000 TEUs<sup>1</sup>, doubling the Canal's capacity, indeed the existing locks allow the passage of vessels that can carry up to 5.000 TEUs. It

<sup>1</sup> TEU: twenty-foot equivalent unit: a standard measure for a container for transporting goods, used to calculate how many containers a ship can carry, or a port can deal with. It corresponds with 40 m<sup>3</sup> approximately.

will have a direct impact on economies of scale and international maritime trade, but it means also a changing of emissions.

In particular, pollutants related with the ship emissions are (Whall, 2010):

- Sulphur Oxide (SO<sub>2</sub>),
- Nitrogen Oxides (NO<sub>x</sub>),
- Non-Methane Volatile Organic Compounds (NMVOCs) derived as 99% of total hydrocarbons,
- Primary PM<sub>10</sub> derived as 95% of total particulate matter,
- Primary PM<sub>2.5</sub> derived ad 90% of total particulate matter,
- Carbon Dioxide (CO<sub>2</sub>)

According to Corbett et al. (2012), the expansion of the Canal will provide:

- "Substitution of larger ships can reduce the CO<sub>2</sub> footprint of cargoes carried by containership through an expanded Canal.
- Using a 10% diversion from the west coast to the east coast, the effects of the Panama Canal expansion on CO<sub>2</sub> emissions are negligible due to longer distances traveled.
- System-wide and intermodal consideration can improve freight transport from origin to destination."

The reduction of CO<sub>2</sub> emission is confirmed also by de Marucci 2012, affirming that, within its first year of operation, the third set of locks will abate more than 9.6 million tons of CO<sub>2</sub>, reaching 20.4 million tons of CO<sub>2</sub> per year in 2025.

Finally, it has to be underlined that Panama through the Law 42 (20<sup>th</sup> of April 2011), established guidelines for national policy on biofuels and electricity produced by biomass.



### 1.3. Climate Change

According to NASA, climate change can be defined as a long-term change in the typical or average weather of a region or city, up to a change in Earth's overall climate (<http://www.nasa.gov/audience/forstudents/5-8/features/nasa-knows/what-is-climate-change-58.html>).

In 2007, the Panama Government drafted an Executive Decree on the National Policy on Climate Change, N. 35 (26<sup>th</sup> of February 2007), "*Por el cual se aprueba la Política Nacional de Cambio Climático, sus principios, objetivos y líneas de Acción*", regarding the national policy in order to manage the Climate Change, recognising its potential contribution in increasing the vulnerability of natural, economic and social systems.

Almost twenty years before, in 1988 it was created an international body for assessing the science related to climate change, called Intergovernmental Panel on Climate Change (IPCC). It was set up by the World Meteorological Organization (WMO) and United Nations Environment Programme (UNEP) to provide policymakers with regular assessments of the scientific basis of climate change, its impacts and future risks, and options for adaptation and mitigation (<http://www.ipcc.ch>).

It is divided in three working groups (WG), respectively: WG I: Physical Science Basis; WG II: Impacts, Adaptation and Vulnerability; WG III: Mitigation of Climate Change – and the Task Force on National Greenhouse Gas Inventories (TFI). According to these groups, IPCC authors are producing reports on these themes.

In particular, IPCC publishes regularly Assessment Reports of the state of knowledge on climate change. The latest one provided is the Fifth Assessment Report (AR5), in November 2014 (IPCC, 2014).

This latter one includes for the first time the Cultural Heritage, specifically in the WG3, section 3.4.3 Wellbeing: "*Most policy concerned with climate change aims ultimately at making the world better for people to live in. That is to say, it aims to promote people's wellbeing. A person's wellbeing, as the term is used here, includes everything that is good or bad for the person — everything that contributes to making their life go well or badly. -...-In the context of climate change, many different metrics of value are intended to measure particular components of wellbeing: among them are the numbers of people at risk from hunger, infectious diseases, coastal flooding, or water scarcity. These metrics may be combined to create a more general measure. Schneider et al. (2000) advocates the use of a suite of five metrics: (1) monetary loss, (2) loss of life, (3) quality of life (taking account of forced migration, conflict over resources, cultural diversity, and loss of cultural heritage sites), (4) species or biodiversity loss, and (5) distribution and equity.*"

In addition, this concept has been adopted also by UNESCO, which has recently published a report on the increasing vulnerability of World Heritage sites to climate change impacts and the potential implications for and of global tourism, thus including also another fundamental factor that is the "final user" (Markham et al. 2016).

For these reasons and according to the definition of Cesare Brandi (1977) of the restoration process<sup>2</sup>, the protection of the physical consistency of an historic object, against the possible risks due to climate change it is absolutely necessary, in order to preserve the duality of its historical and aesthetic value for a sustainable culture.

---

<sup>2</sup> " *Il restauro costituisce il momento metodologico del riconoscimento dell'opera d'arte nella sua consistenza fisica e nella duplice polarità estetica e storica, in vista della sua trasmissione nel futuro.*

### **1.3.1. Impact of the Environment on Cultural Heritage**

#### **1.3.1.1. Deterioration Phenomena**

The Heritage exposed outdoor undergoes to several interaction with the surrounding environment that can produce alteration phenomena and damages with different kind of impact on the monuments, constituting diverse dangers (Brimblecombe, 2016; Amoroso, 2002).

In order to classify in a univocal way the stone decay, subject of this thesis work, in 1988 a specific board was formed aimed to define the deterioration phenomena that can affect the stony monuments, meaning both natural and artificial stone, such as ceramics, bricks, mortars and plasters. This panel was composed by the Institutes of “*Centro di Studio sulle cause di deperimento e sui metodi di conservazione delle opere d’arte*” of the National Research Council (CNR) in Milan and Rome, in collaboration with the “*Istituto Centrale per il Restauro*” (ICR) of Rome. They have drawn up a list of the definitions of the possible alteration phenomena collected in the document: *Normal Raccomandazioni NorMaL - 1/88. Alterazioni macroscopiche dei materiali lapidei: lessico* (and successively upgraded, in 2006, with the normative UNI 11182:2006).

Moreover, a taxonomic classification of the typologies of deterioration was carried out by Honeyborne (1998) and then integrated by Brimblecombe (2010). Therefore, according to the authors, the deterioration phenomena can be divided in two modes, as follows:

- 1) Decay due to “loss of material” that can be related to a physical deterioration that can occur in correlation with thermoigrometric changes and pollutant action. These factors can originate tensions within the material, causing disintegration and detachments, generated by three classes:
  - i. *Salt weathering*, related to the salt-cycles of crystallisation, divided in two subclasses efflorescence and crypto-efflorescence.

These phenomena can be responsible to deteriorations forms such as, honeycombs and tafoni (in conjunction with the erosion due to the wind action), which creates an "ideal" substrate for additional damage factors, so biological colonization, being areas of retention of humidity and which can hosts deposited particles and others salts, triggering a chain process (Smith, 2003).

In order to understand better the mechanisms of crystallisation and solubilisation of salts affecting masonries, Arnold and Zender (1989) have determined and assembled the equilibrium relative humidity (RH) and temperature (T) of the principal salts known occurring in walls. In Table 1.3.1.1.1 salts have been listed, having equilibrium RH between 75% and 96%, for temperature within 20 and 30°C, thus selecting and underlining the equilibrium range more suitable for the Panamanian environment.

According to Camuffo (2016), it has to be considered that these values can be different in salt mixtures. Moreover, he underlines that the differences of values between the deliquescence relative humidity (DRH) and the crystallisation relative humidity (CRH) for aerosol solution of salts, is negligible on material surface or inside pores. Therefore, in the masonries we can consider the two threshold (both of DRH and CRH) coincident.

Table 1.3.1.1. 1. Equilibrium RH (%) and T (°C) of some soluble salts. Selected the T (°C) range and highlighted the RH values more suitable for the Panamanian area from Arnold and Zender (1989).

Salt		Temperature (°C)			Relative humidity (%)
Name	Formula	20	25	30	
	Antarcticite	CaCl <sub>2</sub> • 6H <sub>2</sub> O	30.8	28.6	22.4
	Bischofite	MgCl <sub>2</sub> • 6H <sub>2</sub> O	33.1	32.8	32.4
	Potassium Carbonate	K <sub>2</sub> CO <sub>3</sub> • 2H <sub>2</sub> O	43.2	43.2	43.2
	Nitrocalcite	Ca(NO <sub>3</sub> ) <sub>2</sub> • 4H <sub>2</sub> O	53.6	50.5	46.8
	Nitromagnesite	Mg(NO <sub>3</sub> ) <sub>2</sub> • 6H <sub>2</sub> O	54.4	52.9	51.4
	Ammonium Nitrate	NH <sub>4</sub> NO <sub>3</sub>		61.8	
Panama range	Nitratite	NaNO <sub>3</sub>	75.4	74.3	73.1
	Halite	NaCl	75.5	75.3	75.1
	Thenardite	Na <sub>2</sub> SO <sub>4</sub>	82	82.8	84.3
	Sylvite	KCl	85.1	84.3	83.6
	Epsomite	MgSO <sub>4</sub> • 7H <sub>2</sub> O	90.1	88.3	88
	Natron	Na <sub>2</sub> CO <sub>3</sub> • 10H <sub>2</sub> O	97.9	88.2	83.2
	Mirabilite	Na <sub>2</sub> SO <sub>4</sub> • 10H <sub>2</sub> O	93.6	91.4	87.9
	Niter	KNO <sub>3</sub>	94.6	93.6	92.3
	Arcanite	K <sub>2</sub> SO <sub>4</sub>	97.6	97.3	97

Cycles of dissolution and crystallisation of these compounds are responsible of the weakening of the structures, which undergoes mechanical stress, material loss and, lastly, the aesthetical damage.

- ii. Acid gases action, so due to the pollution effect as the acid rain dissolution especially of calcium carbonate rocks.
  - iii. Freezing and, in particular for the area under study, we have to consider the thermoclastism. The first one involves the presence of water in the material; during the liquid-solid transition, the increment of volume can generate cracks, fractures and detachments. While the thermoclastism concerns a thermal stress that can occur by the impact of solar radiation and temperature fluctuations causing a granular disaggregation and material exfoliation due to the differential thermal expansion and contraction of mineral grains and surface–subsurface stone (Bonazza et al., 2009a).
- 2) "Gaining of materials", as soiling, biomass accumulation, black crusts and encrustation formations, etc. In this case, the monument act as a substrate of other material growth and the interaction between the two can cause deterioration of the original surface.

Following the Italian example, in 2008, the International Scientific Committee for Stone (ISCS) of the International Council on Monuments and Sites (ICOMOS) realized an illustrated glossary on stone deterioration patterns (ICOMOS-ISCS, 2008).

Therefore, the definitions of deterioration phenomena observed in this present work refer to this glossary.

### 1.3.1.2. *Evaluation of Damage*

In the last decades, several authors treat the issue of the weathering of building materials, as described in the last work of Dario Camuffo (2016).

Considering the stone masonry, the first step for evaluating the damages is the characterization of the material, therefore analysing its composition, so its mineralogy, petrography and physical features (e.g. porosity), that are necessary for the comprehension of its current state of conservation. Moreover, the deterioration phenomena aforementioned (Sub-chap.1.3.1.1) can be modified (accelerated/slowed, increased/decreased, etc.) by the climate changes; therefore, it is fundamental to find tools to understand these phenomena in regards to the climate impact.

According to literature, in order to reproduce the processes of changes that a material can undergo if exposed to particular conditions, several damage or dose-response functions have been developed. As Strlič et al. (2013) assume: "*Damage functions can be defined as functions of unacceptable change to heritage dependent on agents of changes*", thus mathematical expressions can be considered instruments for modelling materials modifications, allowing us to evaluate the past, current and future damages.

Regarding these latter ones, it is possible to realize a "predictive maintenance" (Strlič et al. 2013) carrying out predictions based on climate models, which are mathematical formulation "constructed from studies of the current climate system, including atmosphere, ocean, land surface, cryosphere and biosphere, and the factors that influence it such as greenhouse gas emissions and future socio-economic patterns of land use" (Cassar and Pender, 2005).

Indeed, extracting from the models the parameters that can act as stressors, such as rainfall, relative humidity and temperature, it is possible to apply them in dose-response functions, representing different kind of material damages. Moreover, in order to have a feedback of the model reliability the same parameters can be collected from monitoring stations and applying them in the same equations, the results obtained by the simulated and the real situation can be compared.

In the last decades, in the European area several works have been realized in this sector, considering dose-response functions for estimating the damages on stone materials belonging to monuments. Dividing the equation in typology of deterioration process measured, we can consider damages that cause loss of material: as thermoclastism (thermal stress) affecting marbles (Bonazza et al., 2009a), surface recession due to rainfall action on carbonate buildings (Kucera et al., 2007; Bonazza et al., 2009b; Inkpen et al. 2012), salt transitions (Grossi et al., 2011) and cryoclastism (freez-thaw effect) (Brimblecombe et al., 2006). While, referring to accumulation of material, functions have been created for soiling and blackening phenomena (Brimblecombe et al., 2009) and biodeterioration (Gomez-Bolea et al., 2012).

Moreover, in 2012, Sabbioni et al. published an atlas regarding the climate change impact on European Cultural Heritage, collecting all the results produced by the 6 FP Noah's Ark Project, (2004-2007).

Climate changes can have multiple effects on the sites under study, both considering catastrophic events, such as the extreme ones (heat waves, tornadoes, tsunami and hurricanes) and slow changes, for instance, salts cycles, biological growth, surface recession. Existing damage functions regarding climate change impact on cultural heritage are available mainly for these latter ones, thus related to effects of slow changes, since they are more predictable than the extreme events, because the consequences of them are more difficult to foresee.

Taking into account the Panamanian climate conditions, the possible composition of the materials belonging to the buildings under study (see *Geological and Geomorphological Setting*, Sub-chap. 1.2.2), their potential deterioration phenomena and the damage functions developed in the field of stone materials conservation, the following three equations have been applied (see Chap.5):

- 1) Surface recession, according to Lipfert (1989) is due to the effect of rain washout, following represented and described (Tab. 1.3.1.2.1):

$$L = 18.8 \cdot R + 0.016 [H^+] \cdot R + 0.18 (v_{dS} [SO_2] + v_{dN} [HNO_3])$$

Where:

Table 1.3.1.2. 1. Legend of the Lipfert function terms.

L = surface recession per year ( $\mu\text{m year}^{-1}$ )	
18.8 = intercept term based on the solubility of $\text{CaCO}_3$ in equilibrium with 330 ppm $\text{CO}_2$ ( $\mu\text{m m}^{-1}$ ) R = precipitation (m $\text{year}^{-1}$ )	Clean rain effect due to rain at pH~5.6 in equilibrium with atmospheric $\text{CO}_2$ (karst effect)
0.016 = constant valid for precipitation pH in the range 3–5 [ $\text{H}^+$ ] = hydrogen ion concentration ( $\mu\text{mol l}^{-1}$ ) evaluated from rain yearly pH R = precipitation (m $\text{year}^{-1}$ )	Acid rain effect, caused by rain with additional acidity due to the presence of sulfuric and nitric acid
0.18 = conversion factor from ( $\text{cm s}^{-1}$ ) ( $\mu\text{g m}^{-3}$ ) to $\mu\text{m}$ $v_{dS}$ = deposition velocity of $\text{SO}_2$ ( $\text{cm s}^{-1}$ ) [ $\text{SO}_2$ ] = $\text{SO}_2$ concentration ( $\mu\text{g m}^{-3}$ ) $v_{dN}$ = deposition velocity of $\text{HNO}_3$ ( $\text{cm s}^{-1}$ ) and [ $\text{HNO}_3$ ] = $\text{HNO}_3$ concentration ( $\mu\text{g m}^{-3}$ ).	Dry deposition of gaseous pollutants, especially $\text{SO}_2$ and $\text{NO}_x$ , occurring between precipitation events

In particular, for the present study has been chosen the Lipfert modified equation,  $L = 18.8 \cdot R$ , developed by Bonazza et al. (2009b), where only the karst effect is considered, since it has been demonstrated that the clean rain effect was the dominant term, accounting for 50–90% of stone loss. Furthermore, in the mentioned study, it has been calculated also another constant, corresponding to 21.8, that is the intercept term based on the solubility of  $\text{CaCO}_3$  in equilibrium with 750 ppm of  $\text{CO}_2$ , since the future concentration of carbon dioxide is expected to be higher than the past of 330 ppm.

Finally, it has to be underlined that this function has been demonstrated to be valid only for carbonate rocks having a porosity lower than 25%.

- 2) Salt transitions cycles have been considered for the halite compound. Indeed, considering the proximity to the sea of all the sites under study and the equilibrium RH (%) and T ( $^{\circ}\text{C}$ ) of NaCl (see Tab.1.3.1.1.1) corresponding to 75.3% at  $25^{\circ}\text{C}$  and 75.1% at  $30^{\circ}\text{C}$ , the dissolution-crystallisation transformations can occur. Specifically, assuming the T as a constant and according with Grossi et al. (2011) the frequency of cycles have been calculated counting the number of times the average daily RH crossed the DRH/CRH of 75.3% or 75.1% on consecutive days. Only the transitions that occurred when the humidity was decreasing, therefore passing from liquid to solid state, were counted. Thus it can be affirmed that the number of transitions is virtually the number of dissolution-crystallisation cycles.
- 3) Biomass accumulation, considered as organic carbon accretion on the surfaces, it has been obtained utilizing the Gomez-Bolea et al. (2012) function:

$$B = \exp^{(-0.964 + 0.003P - 0.01T)}$$

Where the quantity of biomass B (mg), on surface unity ( $\text{cm}^{-2}$ ) is obtained applying the annual amount of precipitation P (mm) and the annual mean of temperature T ( $^{\circ}\text{C}$ ).

Nevertheless, it has to be mentioned that this function has been validated for horizontal surfaces of hard acid stones in nonurban European environments.

## 1.4. Previous Investigations and Interventions

### 1.4.1. Panamá Viejo

#### Previous Analysis

In the 1996, the Instituto Nacional de Cultura decided to start a conservation plan of the construction materials belonging to the Archaeological Site of Panamá Viejo.

It is important to underline that in this period *Panama La Vieja* were still crossed and divided in half by *Vía Cincuentenario*, realized in the 1950 in order to celebrate the fiftieth anniversary of the Republic. It was one of the most important communication routes of Panama City, so one of the major traffic arteries, which led to important sites of the town as the airport. In order to draw up advices for the best preservation of the main ruins of the archaeological area a mesoscopic investigation on the materials was performed, with the support of the Universidad Nacional Autónoma of Mexico, specifically by Eng. Luis Torres Montes (1996). In particular, he carried out a research work concerning the state of conservation and the deterioration phenomena shown by the masonries and the pavements, analysing sixteen monuments, following listed:

1. Las Casas Reales
2. La cathedral
3. El cabildo
4. Casas Francisco Terrín
5. Casa Alarcón
6. La Casa de los Genoveses
7. Iglesia y Convento de Santo Domingo
8. Iglesia y Convento de la Compañía de Jesús
9. Iglesia y Convento de la Concepción
10. Hospital de San Juan de Dios
11. Iglesia y convento de San Francisco
12. Iglesia y Convento de la Merced - Fachada de la Iglesia de la Merced (now located in the new Church of Mercy, Casco Antiguo)
13. Puente del Matadero
14. Fuerte de la Natividad
15. Iglesia de San José
16. Puente del Rey

The investigation affirmed the existence of three typologies rocks employed in the masonries:

- 1) Sandstones, divided by colour: yellow, observed utilized usually for the facing (if compact) and grey, employed in specific area of the masonry as corners, jambs, arches, etc..
- 2) Evaporitic limestone utilized at Casa Terrín. It showed very high compactness and almost absent porosity. Peculiarity of this stone was the deterioration phenomena which characterized the surface with a red discoloration.
- 3) Volcanic rocks of basaltic composition: characterized by a great durability and strength, used especially in pavements.

Considering the decay processes, they were mainly attributed to hydrolysis in almost all the rock typologies analysed. Moisture was recognized as the main problem, keeping the material wet in an almost permanent way, and causing, for example, the arenisation of the sandstones, or rather the dissolution of the stone cement, provoking the decohesion of grains, which consequently lead to the



erosion of the architectural surface. Moreover, limonitization and hematitization have been observed, especially in the rock composing Casa Terrín masonry, and sporadically also in the sandstones. Finally, salts crystallisation has been also detected.

Furthermore, biological activity was noticed on the materials surface, as whitish film probably due to lichens action, which proliferated on the stones. In particular, the presence of lichens was observed with a specific distribution on the masonry, depending on water permeation. Thus, their growth on specific areas and stones, can indicate that these materials are more exposed or not to water infiltration.

Finally, the high percentage of relative humidity (often more than 85%), is also cause of the huge growth of higher plants, as trees and shrubs, sporadic bryophytes (moss) and photosynthetic bacteria. Regarding the higher plants, the most dangerous species observed was the “Panama Tree”, which develops roots that propagate at a great distance, and affects walls, foundations, joints, and causing significant damage. Considering the photosynthetic bacteria, it was diffusely observed a cyanobacteria, called “alga negra” (*Oscillatoria sp.*). Regarding this biological colonization, Macedo et al. (2009) have demonstrated that “cyanobacteria and chlorophyta colonize a wide variety of substrata and that this is related primarily to the physical characteristics of the stone surface, microclimate and environmental conditions and secondarily to the lithotype”. Moreover, according to the author, the “alga negra” was not considered dangerous for the stone, nevertheless it suggests the presence of high humidity, in addition to representing an aesthetic damage. On the contrary, the growth of lichens was considered a serious problem, because these organisms, through the production of oxalic acid and other organic acids, can cause chemical damages. In addition, they keep the stone wet, obstructing the water evaporation and, lastly, the detachment of lichens can leave cavities in the masonry, representing a source for further damages.

Considering the pollutants action, despite of the presence of the traffic congested *Via Cincuentenario*, the constructions did not shown black crusts. In addition, efflorescence, exfoliation and flaking were observed in isolated form.

Eng. Torres Montes underlined also the presence of products previously applied as repairing and restoration mortars, which were probably cement based mortars, causing degradation, since they have higher hardness and less porosity than the original materials, representing a discontinuity in the masonry, therefore a factor that may cause other future damages and contributing to the precipitation of soluble salts within the structure.

Ultimately, the research work took into account also vibrations due to traffic origin, acts of vandalism and neglect as causes of damages of significant relevance.

After this study, in 2000, a thesis work was carried out by Sanchez Nava, consisting in a preliminary characterization of materials, in terms of chemical, mineralogical and petrographic analyses, as well as physical features investigation (e.g. density, porosity, water absorption and hardness).

On the basis of the investigations performed, the presence of three typologies of stone were confirmed, in particular two kind of sedimentary stones (grey and yellow sandstones), while the previously called “Evaporitic Limestone” was defined as a volcanic rock, specifically a rhyolitic tuff which belonged to Casa Terrín.

Regarding the sandstones, they have been attributed to the same sedimentary unit. In addition, the mineralogical and petrographic investigations revealed that they are principally formed by

fragments of: volcanic rocks, tuffs and carbonaceous bioclasts (in different proportions) in a volcanoclastic matrix, while the cement is mainly formed by calcite.

Considering the state of conservation of these materials, it was observed that the sandstones showed a higher susceptibility to decay than the rhyolite. This was explained by the heterogeneity of the sandstones composition, driving them to a differential degradation. The different size of clasts, confers a high porosity to the sandstones, in conjunction with a high water absorption, which were recognized as responsible for the alteration processes.

Furthermore, the sandstones samples exhibited others degradation forms as: arenitisation, lack of cement due to calcite dissolution and re-crystallisation, presence of expansive clay minerals and hematization phenomena.

Regarding the rhyolite, it revealed an external part clearly affected by deterioration, characterized by iron minerals, in a state of alteration, conferring a reddish coloration to the stone surface. Further the aesthetic damage, this “crust” showed different physical characteristics from the original inner part, having a higher hardness, so it can lead to a differential deterioration. However the rhyolite was defined as a very resistant stone, with more homogeneous structure than the sandstones. On the other hand, it showed micro-porosity, which confers a high capillary absorption, favouring the deterioration due by water permeation.

In conclusion, the thesis work revealed that all the stone types analysed exhibit deterioration, nevertheless in a not so advanced state, which obviously depends on the different nature of the rock.

Finally, in 2014, a Master Thesis was performed on the issue: "Environmental impact on the Archaeological Site of Panamá Viejo: collection and elaboration of microclimate and air quality data"(Ma, A.Y. 2013/2014). The work selected, in a range of 120 km around the archaeological site of Panama Viejo, 11 monitoring stations providing general monthly information of three or more parameters (temperature, precipitation, relative humidity, insulation duration and evaporation) and 4 monitoring points recording daily temperature and precipitation detailed for the recent 5 years (2010-2014). Then, Lipfert and Biomass accumulation functions have been applied with this data.

Considering the quantification of different types of deterioration phenomena, utilizing the damage functions, it was recognized that the rainy season represented the period when both biomass accumulation and surface recession show higher values, therefore during this time it is presumable that monuments are more exposed to these deterioration phenomena. In order to deepen and complete this study the present thesis work was born, in order to give a more complete overview of the past and future environmental impact on the materials belonging to this archaeological site.

#### Maintenance and Restoration Works

In the last decades, the archaeological site underwent to several maintenance and restoration works. Considering the monuments subject of the here presented research, these interventions (if present they are listed in Table 1.4.1.1) have been taken into account during the selection of sampling points.

Table 1.4.1. 1. Maintenance and restoration works, updated to 2011/2012 (Arroyo, 2011), performed on monuments selected for the here presented PhD research.

Site	Interventions
Fortín de la Natividad	2004: grinded-bricks pavement 2006: consolidation S-wall
Convento de las Monjas de la Concepción	2002-2003: consolidation and intervention works 2005: consolidation of N-wall 2006: restoration of the S-wall crowing of the altar (with bricks in order to avoid the water infiltration) and consolidation of N-Chapel. 2009: cistern ( <i>aljibe</i> ) consolidation.
Casas Reales	2007: breakwaters, filling and consolidation works of the South area. 2010: consolidation of one of the walls facing North.
Hospital de San Juan de Dios	2005: relocation of stones in the masonry 2006: consolidation of shored up walls
Convento de San Francisco	2005: consolidation of W-wall 2006: consolidation of E-wall
Convento de la Compañía de Jesús	2004: inner consolidation of N and E walls. 2008: consolidation of the whole complex, except the S-E area (east of the nave) 2009: intervention
Torre de la Catedral	2006: the part upper the first floor was completely restored. Works to ensure the proper rain runoff, to prevent the water absorption by walls. In addition, the walls have been fully integrated using similar materials and techniques as those used in colonial structures.

#### ***1.4.2. Portobelo and San Lorenzo***

During the 1970-71 the Instituto Panameño De Turismo (IPAT) performed the "Portobelo Pilot Plan" in order to develop a documentation and a conservation campaign, carrying out deforestation and consolidation works at the sites (World Monuments Fund, 2003).

In the 1980 all the Caribbean Fortifications of Panama have been included in the World Heritage List of UNESCO (<http://whc.unesco.org/en/list/135>); nevertheless, in 2002, an inspection of the World Monuments Fund described the Forts in a weak state of preservation (World Monuments Fund, 2003).

Later, since 2012 until now, they belong to the List of World Heritage in Danger. Thus in 2013 the Instituto Nacional de Cultura of the Panamanian Government developed a Risk Assessment Study and published an Emergency Plan in order to safeguard the sites. Unfortunately, this plan would not be executed in the short term, but thanks to the Patronato of Portobelo and San Lorenzo on site staff, cleaning, maintenance and some consolidation works are carrying on (Osorio Ugarte, 2015).

Considering San Lorenzo complex, in the last years it has been subjected to several studies, principally aimed to realize architectural surveys, such as the recent 3D model realized by Bertocci and Parrinello (2015), important step to obtain a digital database of the masonries and to allow us achieving a virtual reconstruction of the building.

Nevertheless, citing the UNESCO, regarding the current state of conservation, the structure presents a "fragile state and accelerated degradation by environmental factors and the lack of maintenance" (<http://whc.unesco.org/en/soc/3198>). Therefore, it is fundamental to identify the chemical and physical features of the materials, part of the buildings, in order to understand what are the possible risks affecting these structure, in correlation with the environmental conditions.














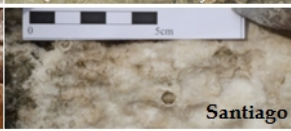
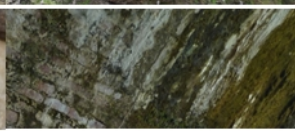

## 2. Chapter 2 – Materials and Methods

### 2.1 Survey, Sampling campaign and in situ observations

During the period of August-September 2014, the Panamanian rainy season, a sampling campaign was performed with the aim of collecting representative specimens of the different rock typologies utilized in the masonries of the several buildings belonging to the Panamá Viejo, Portobelo and San Lorenzo sites.

In addition to the diverse lithology, the samples were chosen on the base of their state of conservation, indeed rocks showing high deterioration phenomena have been selected. In particular, the major damaging morphologies are summarize and listed in the table below (Tab. 2.1.1).

Table 2.1. 1. Most diffused deterioration phenomena observed at Panamá Viejo, Portobelo and San Lorenzo sites.

	Panamá Viejo	Portobelo	San Lorenzo
<b>Biodeterioration (algae, moss, lichens colonization and presence of vascular plants)</b>	 Fortín de la Natividad	 San Fernando	
<b>Exfoliation and detachment</b>	 San Francisco	 Santiago	
<b>Disintegration</b>	 Concepción	 Santiago	
<b>Erosion</b>	 Casas Reales	 San Jeronimo	
<b>Salt encrustations</b>	 Concepción	 Santiago	
<b>Chromatic alterations</b>	 Casas Ferrin		

Moreover, other samples were collected at outcrops found near the constructions and/or in the proximity of the sites under study.

It has to be underlined that mortars and plasters also constitute the masonries, sampled at the same time, but they will be subject of successive studies.

Therefore, 54 samples of rocks belonging to the several complexes, at the different sites were collected and in the following subchapters are described, divided for site of belonging to.

### 2.1.1 Panamá Viejo

At Panamá Viejo, twenty-seven samples of natural stone have been selected and collected from eight buildings and remains, while three more specimens were sampled from different outcrops, possible quarries for the construction materials utilized.

The sampled monuments and outcrops are listed and showed on the map in Figure 2.1.1.1.



Figure 2.1.1. 1 Map of Panamá Viejo (<http://www.patronatopanamaviejo.org/ppv2014/en/>).

On the left the monuments and outcrops sampled are listed.

macroscopic description in situ, summarized in Table 2.1.1.1.

lected and a

Table 2.1.1. 1. Samples, lithotypes, state of conservation and location of sampling (for the description of the Fort elements see Spiteri, 1994; for the definition of breccia see Saccani, 2014).

Sample	Lithotype	State of conservation	Sampling location
PANAMA VIEJO - Masonries			
<i>Convento de las Monjas de la Concepción</i>			
PV CC 4	Breccia	Differential erosion/ Alveolization (coving)	N side of the chapel, h140 cm
PV CC 5	Breccia	High decay: exfoliation and biological colonisation (algae)	N wall of the nave, h 365 cm
PV CC 6	Breccia	High decay: exfoliation and biological colonisation (algae)	Outer wall of the Church, near an eaves, faced S and exposed to the old Via Cincuantenario, h 165-170 cm
<i>Casas Reales</i>			
PV CR 4	Breccia	Elevated Biological colonisation and exfoliation	S wall, h 160 cm
<i>Casa Terrin</i>			
PV CT 1	Rhyolite	Biological colonisation (lichens) and discoloration (?)	Wall on the W side of Casa Terrin. Sample collected from the N side, h 165 cm
PV CT 2	Rhyolite	Good	Wall on the W side of Casa Terrin. Sample collected near the S-E corner, ground level
<i>Convento de San Francisco</i>			
PV FC 4	Breccia	Good/ Slightly good	E wall of the navy, ground level
PV FC 5	Breccia	Exfoliation.	E wall of the navy, h 106 cm
PV FC 6	Altered volcanic rock	Good/ Slightly good	E wall of the Convent, h 170 cm
PV FC 7	Breccia	Exfoliation, differential	W wall, h 175 cm

Sample	Lithotype	State of conservation	Sampling location
PV FC 8	Breccia	erosion/alveolization Exfoliation, differential erosion/ alveolization and biological colonisation (algae)	W wall, h 100 cm
PV FC 9	Altered volcanic rock	Exfoliation, differential erosion/ alveolization and partial biological colonisation (algae)	W wall, h 200 cm
PV FC 11	Breccia	Blackening + biological colonisation (algae)	S-W side of the wall of the complex 9.70 m from the new via Cincuentenario, h 140 cm
<i>Fortín de la Natividad</i>			
PV FN 1	Breccia	Biological colonisation (algae), exfoliation and decohesion	S wall – External part, h 100 cm
PV FN 2	Breccia	Slightly good	S wall – External part, h 20 cm
PV FN 4	Basaltic andesite	Good	W wall – Inner part, h 102 cm
PV FN 5	Basaltic andesite	Good	Inner part of the Fortress, ground level
<i>Convento de la Compañía de Jesus</i>			
PV JC 1	Breccia	Good/ Slightly good (previously covered by plaster), bush-hammered	W façade, internal side, inner part of the arch, h 345 cm
PV JC 2	Breccia	Biological colonisation (algae), probably bush-hammered	W façade, internal side, inner part of the arch, h 300 cm
PV JC 3	Breccia	Good	Near the N façade, ground level
PV JC 4	Breccia	Good	W wall, h 293 cm
<i>Hospital de San Juan de Dios</i>			
PV SJdD	Altered volcanic rock	Biological colonisation (lichens) and white patina on the internal surface	Wall facing the old Via Cincuentenario, h 120-130 cm
<i>Torre de la Catedral</i>			
PV TC 3	Tuffite	Exfoliation	W wall, h 109 cm
PV TC 4	Tuffite	Biological colonisation (black algae)	S wall, h 127 cm
PANAMA VIEJO - Outcrops			
PV Q 1	Breccia	Blackening - biological colonisation (black algae?)	Outcrop near Casa Reales
PV Q 2	Basaltic andesite		Quarry near the Santo Domingo Convent
PV vic. CR	Basaltic andesite		Outcrop near Casa Reales - Location: Lat. 9°0'20.720'' - Long. -79°29'0728''

### *Fortín de la Natividad*

The Fort, built during the XVII century, arises in the eastern side of the archaeological site, close to the Puente del Matadero. Nowadays, it is located in proximity to the new *Vía Cincuentenario* and just in front of a gas station (Fig. 2.1.1.2a). Its masonry is characterized by the presence of yellowish breccias, mainly distributed in the lower part of the masonry (till more or less 1.40 m of height), both in the outer and in the inner part; while the upper part is largely composed by volcanic rocks, ascribable to basaltic andesite, showing a darker colour (Fig. 2.1.1.2b). The presence of different rocks in the masonry can be attributable to diverse supply of raw materials due to two distinct periods of construction, this fact was observed also in others buildings.

Therefore, four samples of the different materials were collected as described below (Fig. 2.1.1.3).

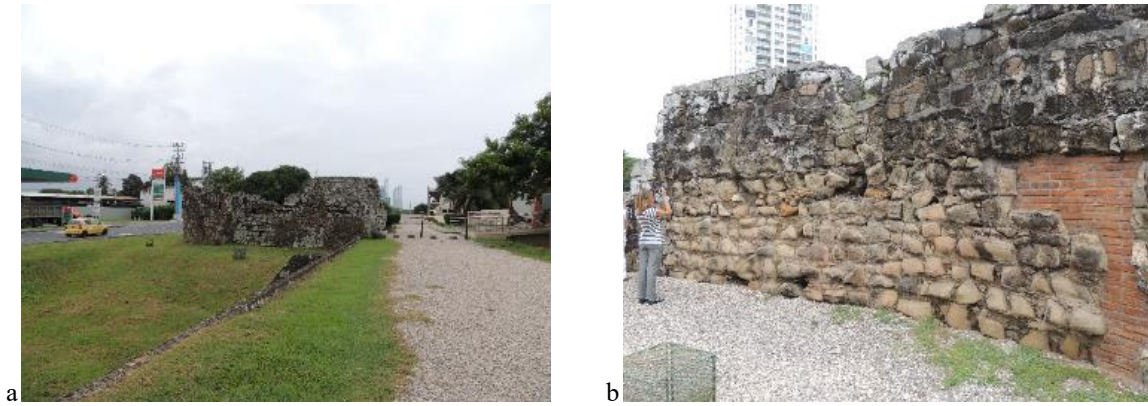


Figure 2.1.1. 2 Fortín de la Natividad: a. western wall; b. Southern wall.

It is clearly visible the different materials utilized for the lower and upper part.

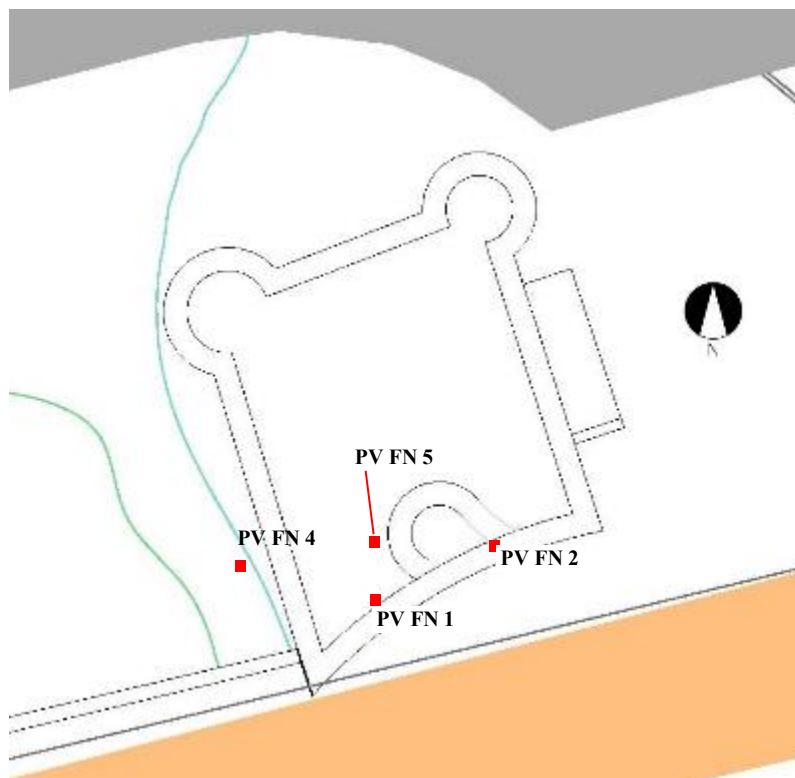


Figure 2.1.1. 3. Plan of the Fortín de la Natividad and sampling points (Plans are Courtesy of the Patronato de Panamá Viejo).

Two fragments of breccia were sampled from the external part of the Southern wall. PV FN 1 sample showed biological colonization, with a darker colour on the external surface, and exfoliation phenomena, moreover, the decohesion phenomenon conferred to the stone low hardness (Fig. 2.1.1.4). Instead, the second one, PV FN 2 sample, presented a better state of conservation (Fig. 2.1.1.5).





Figure 2.1.1. 4. Fortín de la Natividad, outer part of the Southern wall, PV FN 1 sampling.



Figure 2.1.1. 5. Fortín de la Natividad, outer part of the Southern wall, PV FN 2 sampling.

While two fragment of basaltic andesite were sampled: one from the Western wall of the inner part of the Fort (PV FN 4 sample, Fig. 2.1.1.6), and another one from the ground within the Fort (PV FN 5 sample, Fig. 2.1.1.7).



Figure 2.1.1. 6. Fortín de la Natividad, inner part of the Western wall, PV FN 4 sampling.



Figure 2.1.1. 7. Macroscopic picture of sample PV FN 5.

### *Convento de San Francisco*

The Convento de San Francisco, as the previous one, is located in the eastern side of the archaeological site close to the new *Vía Cincuentenario*.

In this structure two mainly typologies of stones can be observed in the masonry. Yellowish and greyish breccias are the mostly utilized (two varieties of the same outcrop), and sporadic blocks of creamy altered volcanic rock showing an aphyric texture, which can be considered due to later additions.

Observing the texture of the masonry of the wall facing East and the construction technique, the alternation of the two varieties is clearly visible, noticeable by the different hue, enhancing the hypothesis of belonging to the same outcrop (Fig. 2.1.1.8). The description of the sampling is reported below (Fig. 2.1.1.9)



Figure 2.1.1. 8. Overview of the San Francisco masonry mainly composed by yellowish-grey breccias.

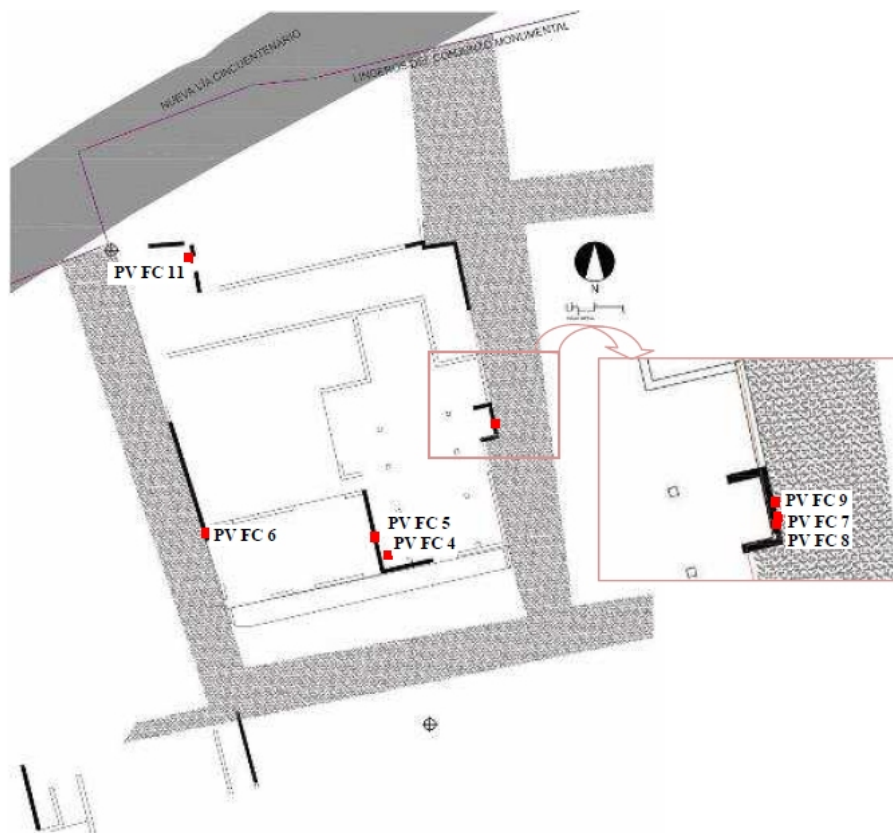


Figure 2.1.1. 9. Plan of the Convento de San Francisco and sampling points (Plans are Courtesy of the Patronato de Panamá Viejo).

The yellowish breccia was sampled from the masonry exposed to West, PV FC 8 sample (Fig. 2.1.1.10). This stone was deteriorated, showing exfoliation phenomena, and blackening. Another

sample was collected from the ground, near the eastern wall of the navy, PV FC 4 (Fig. 2.1.1.11). From the eastern wall of the navy was collected PV FC 5, another volcanoclastic stone block in the masonry (Fig. 2.1.1.12). It showed deterioration phenomena, as presence of lichens and biological black patina. Moreover, PV FC 7 was sampled from the Eastern wall, above a putlog hole, and near the PV FC 8 sample (Fig. 2.1.1.13). Finally, another sample showing a greyish-green hue and showing blackening, was sampled from the wall closest to the new Via Cinquantanerio, exposed to North, from the S-W side (PV FC 11, Fig. 2.1.1.14).

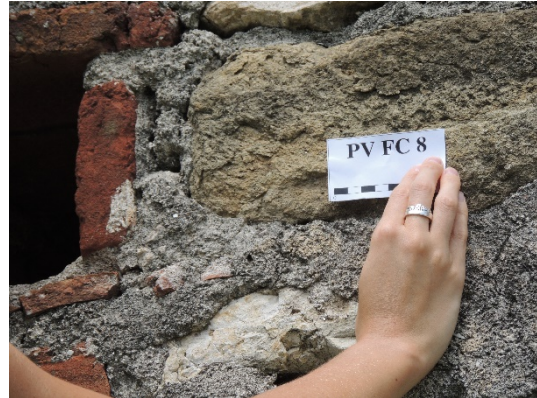


Figure 2.1.1. 10. Sampling of the yellowish breccia, PV FC 8 specimen.



Figure 2.1.1. 11. Sampling of the yellowish breccia, PV FC 4 specimen.



Figure 2.1.1. 12. Sampling of the breccia PV FC 5, showing a more reddish hue.



Figure 2.1.1. 13. Sampling of the breccia PV FC 7.



Figure 2.1.1. 14. Sampling of the breccia PV FC 11.

Concerning the creamy altered volcanic rocks they were sampled from two opposite walls: PV FC 6 from the base, near the south corner, of the Western wall (Fig. 2.1.1.15) and PV FC 9 sampled near PV FC 7 and PV FC 8, from the Eastern wall (fig. 2.1.1.16). This latter one showed deterioration phenomena as exfoliation, conchoidal fracture, due to differential erosion, and partial biological blackening.



Figure 2.1.1. 15. Sampling of the creamy altered volcanic rock PV FC 6.



Figure 2.1.1. 16. Sampling of the creamy altered volcanic rock PV FC 9.

### *Hospital de San Juan de Dios*

Another sample of the just mentioned creamy, aphyric altered volcanic rock was collected from the wall of the Hospital de San Juan de Dios, facing the old Via Cincuentenario (Fig. 2.1.1.17). This kind of rock in this building seems to realize a horizontal line in the masonry, similar to a string course. PV SJdD sample is shown in Figure 2.1.1.18.



Figure 2.1.1. 17. Wall of the complex of the Hospital de San Juan de Dios, facing the old Via Cincuentenario.



Figure 2.1.1. 18. Macro photographs of sample PV SJdD.

### *Convento de las Monjas de la Concepción*

This complex is mainly composed by green and yellow breccias, as observed at Convento de San Francisco, and bricks (Fig. 2.1.1.19). Sampling points are highlighted in Figure 2.1.1.20.



Figure 2.1.1. 19. Pictures of the Convento de las Monjas de la Concepción.



Figure 2.1.1. 20. Plan of the Convento de las Monjas de la Concepción and sampling points (Plans are Courtesy of the Patronato de Panamá Viejo).

Three samples of breccias were collected respectively from the North side of the chapel (PV CC 4, Fig. 2.1.1.21), showing differential erosion. From the North wall of the nave, PV CC 5, showed a greenish-grey colour, presenting high decay, exfoliation phenomena and high biological growth; moreover, it was located near areas affected by water percolation (Fig. 2.1.1.22). The latter sample, PV CC 6 (Fig. 2.1.2.23), collected from the outer wall of the Church, near an eaves, faced S and exposed to the old Via Cinquantenario, has a greenish hue and it is highly altered (exfoliation and biological growth).



Figure 2.1.1. 21. Sampling of PV CC 4 specimen.



Figure 2.1.1. 22. Sampling of PV CC 5 specimen.

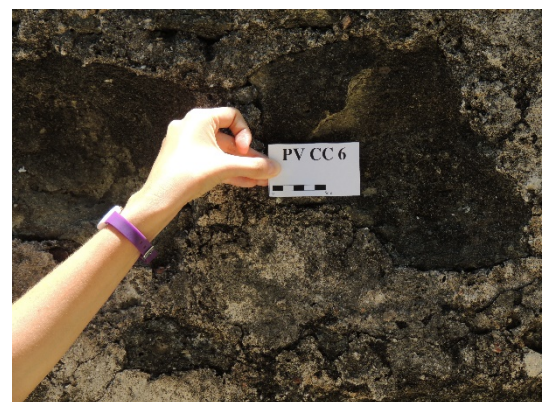


Figure 2.1.1. 23. Sampling of PV CC 6 specimen.

## Convento de la Compañía de Jesus

The breccia observed at this complex showed, in general, less exfoliation than the others aforementioned, on the other hand, the blackening, probably due to biological action, is still present. Moreover, in several rocks it is clearly visible the passage between the two different levels of the deposition, showing the two difference hues, the yellowish and the greyish-greenish (Fig. 2.1.1.24); nevertheless the variety mainly present is the yellow one. The sampling points are shown in Figure 2.1.1.25.



Figure 2.1.1. 24. Particular of a block of breccia, showing both greyish-greenish and yellowish colour.

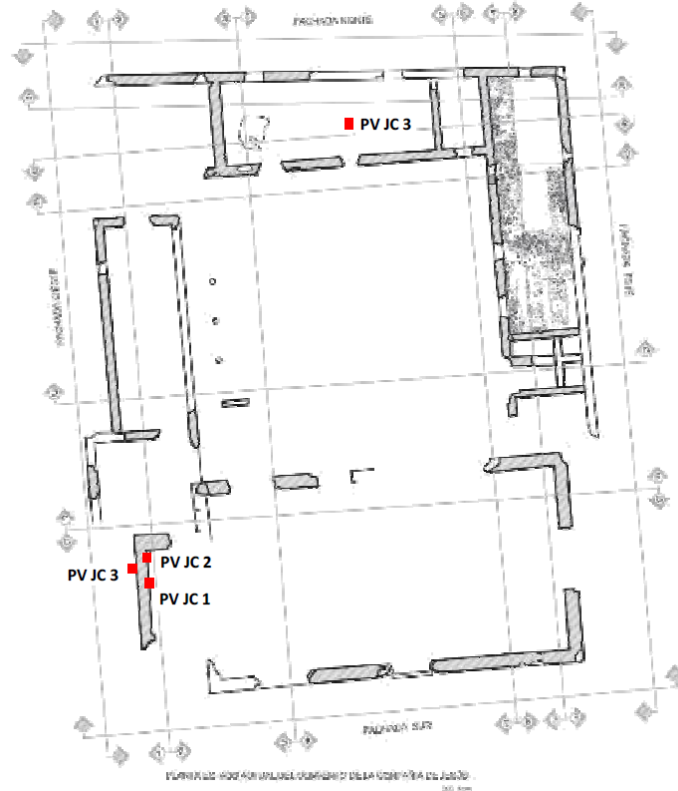


Figure 2.1.1. 25. Plan of the Convento de la Compañía de Jesus and sampling points (Plans are Courtesy of the Patronato de Panamá Viejo).

From the wall of the western façade, internal side, PV JC 1 and PV JC 2 was sampled. In particular, PV JC 1, was collected from the inner part of the arch, where in the past it can be protected by a plaster, nowadays no longer present (Fig. 2.1.1.26). Near the sampling point, a lime injection mortar plus 10% of Primal, were injected in 2008 (Arroyo, 2011).

Moreover, the surface of the rock showed stains. Regarding the PV JC 2 sample, it was collected from the same wall, and same side, but where there was blackening (Fig. 2.1.1.27).

Considering PV JC 3 specimen, it was sampled from the ground, in the setting near the N façade (Fig. 2.1.1.28).

Finally, PV JC 4 was sampled from the W wall, from the external side (Fig. 2.1.1.29).





Figure 2.1.1. 26. Sampling of PV JC 1 sample.



Figure 2.1.1. 27. Sampling of PV JC 2 sample.

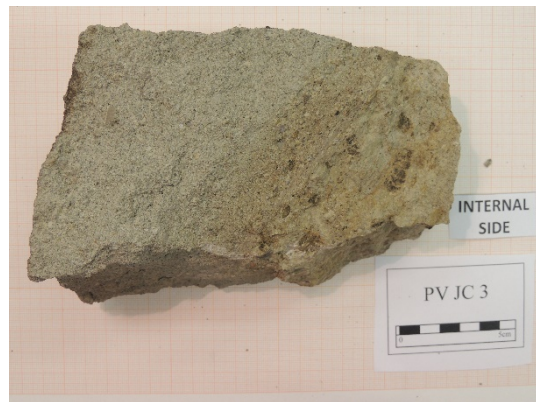


Figure 2.1.1. 28. PV JC 3 sample.



Figure 2.1.1. 29. Sampling of PV JC 4 sample.

### *Casa Terrín*

A wall near Casa Terrín was sampled, since it is characterized by only one stone typology, observed here exclusively, that is a volcanic rock, showing aphyric texture and chromatic alteration, presenting a reddish hue (Fig 2.1.1.30). The location of the two samples collected is displayed in Figure 2.1.1.31.



Figure 2.1.1. 30. Wall near the Casa Terrín, showing a reddish chromatic alteration.

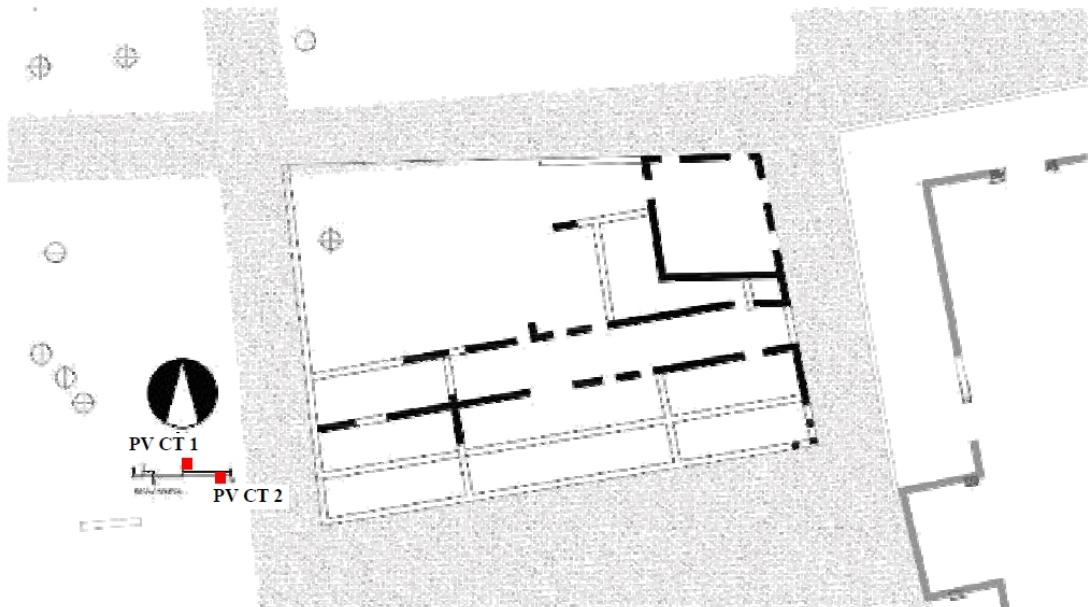


Figure 2.1.1. 31. Plan of the Casa Terrín and sampling points (Plans are Courtesy of the Patronato de Panamá Viejo).

PV CT 1 sample was collected from the North side of the wall; it showed high chromatic alteration, also in the inner part of the rock, furthermore, on the surface there was lichens presence (Fig. 2.1.1.32)

The second sample, PV CT 2, was collected from the ground near the S-E corner of the wall (Fig. 2.1.1.33). It also showed chromatic alterations, but with smaller thickness.



Figure 2.1.1. 32. Sampling of PV CT 1 specimen.



Figure 2.1.1. 33. PV CT 2 sample.

### Torre de la Catedral

The Cathedral Tower is mainly composed by a probable pyroclastic rock, ascribable to tuffite, showing alteration phenomena as alveolization and powdering, especially on the Western wall. In addition, this stone is highly affected by biological blackening on the Southern wall.

The sampled part (Fig.2.1.1.34) belongs to the area without interventions, indeed the restoration works interested only the upper part of the tower (from the first floor to the roof).

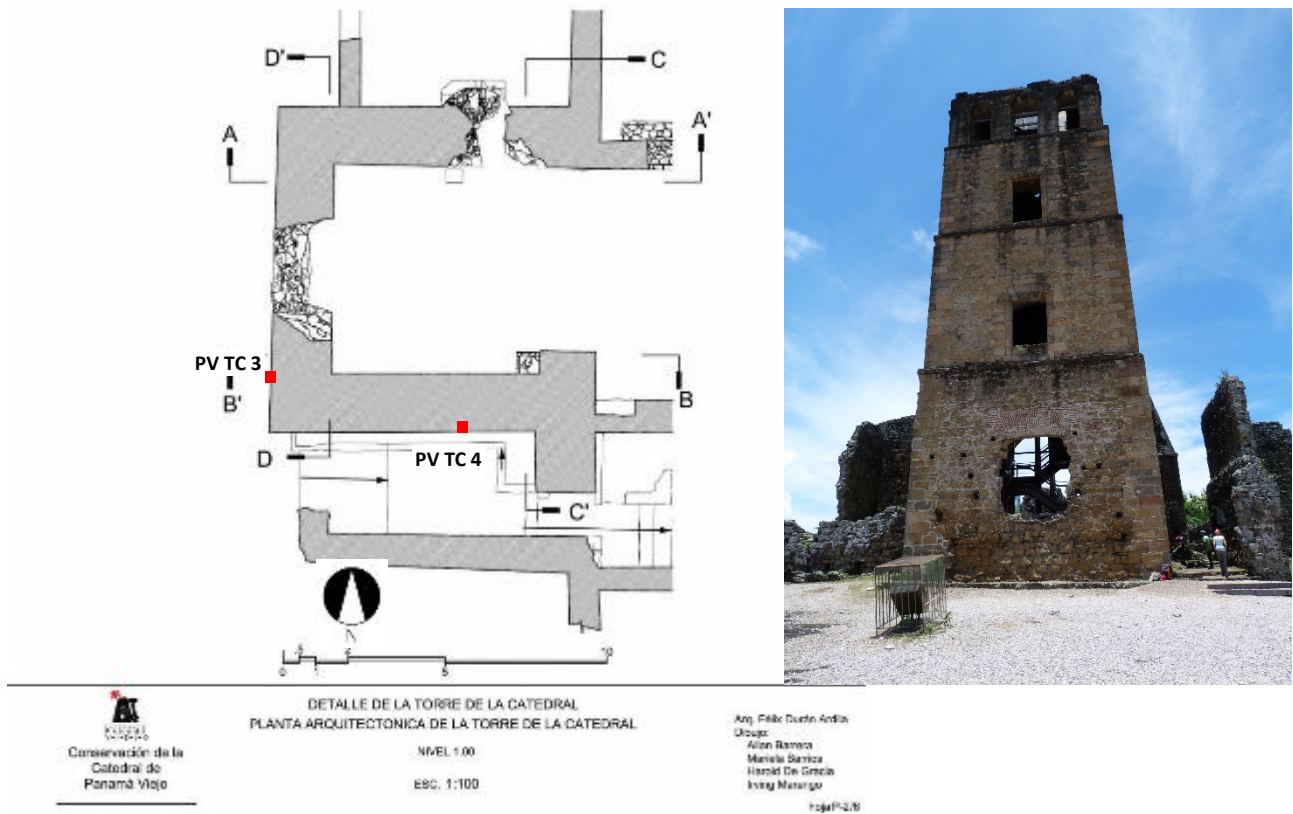


Figure 2.1.1. 34. Plan of the Cathedral Tower, sampling points and a picture of the West side of the Tower (Plans are Courtesy of the Patronato de Panamá Viejo).

One sample of tuffite, showing exfoliation, was sampled from the W wall (PV TC 3, Fig. 2.1.1.34). From the Southern it was collected the second specimen (PV TC 4), showing high blackening (biological) (Fig. 2.1.1.36).



Figure 2.1.1. 35. Sampling of PV TC 3 specimen, W wall.

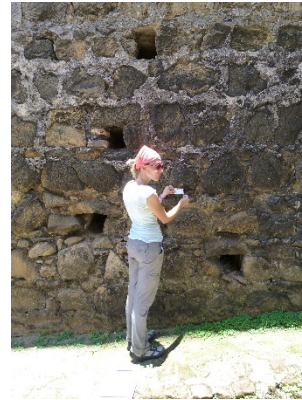


Figure 2.1.1. 36. Sampling of PV TC 4 specimen, S wall.

*Casas Reales*

This complex was directly exposed to the sea erosion due to tidal variations, and the effects of the marine action is still clearly visible on the masonry surface (Fig. 2.1.1.37).



Figure 2.1.1. 37. Effects due to the marine erosion.

It is mainly composed by the breccia, presenting high alteration phenomena, showing both yellowish and greenish hue. Sampling points are indicated on the map in Figure 2.1.1.38.

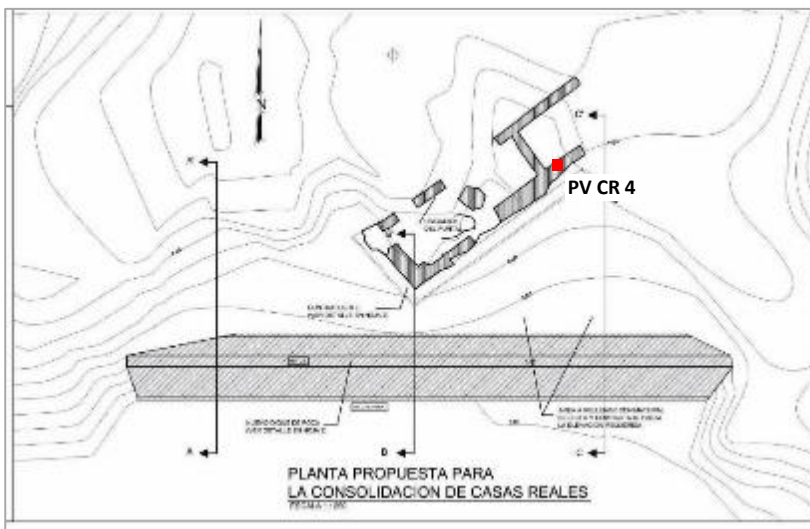


Figure 2.1.1. 38. Plan of the Casas Reales, sampling points and an image of one monument (Plans are Courtesy of the Patronato de Panamá Viejo).

Specimen PV CR 4 was sampled from the Southern wall, facing the sea side and showing elevated blackening due to biodeterioration (Fig. 2.1.1.39).

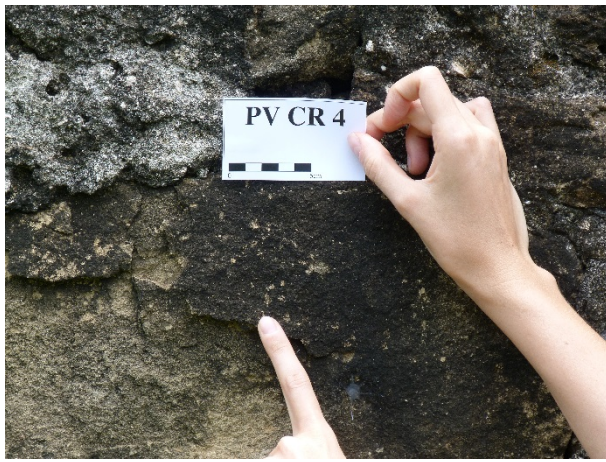


Figure 2.1.1. 39. Sampling of PV CR 4 specimen.

*Outcrops near the Casas Reales*

In proximity of Casas Reales complex, thus near the sea side, two outcrops have been sampled, in the area where Grajales Saavedra (2012) identified andesite and agglomerates outcrops. Indeed, the two samples resulted an outcrop of volcanic rock ascribable to andesite (Fig. 2.1.1.40), respectively PV vic CR (Fig. 2.1.1.41a) and PV Q 1 (Fig. 2.1.1.41b).

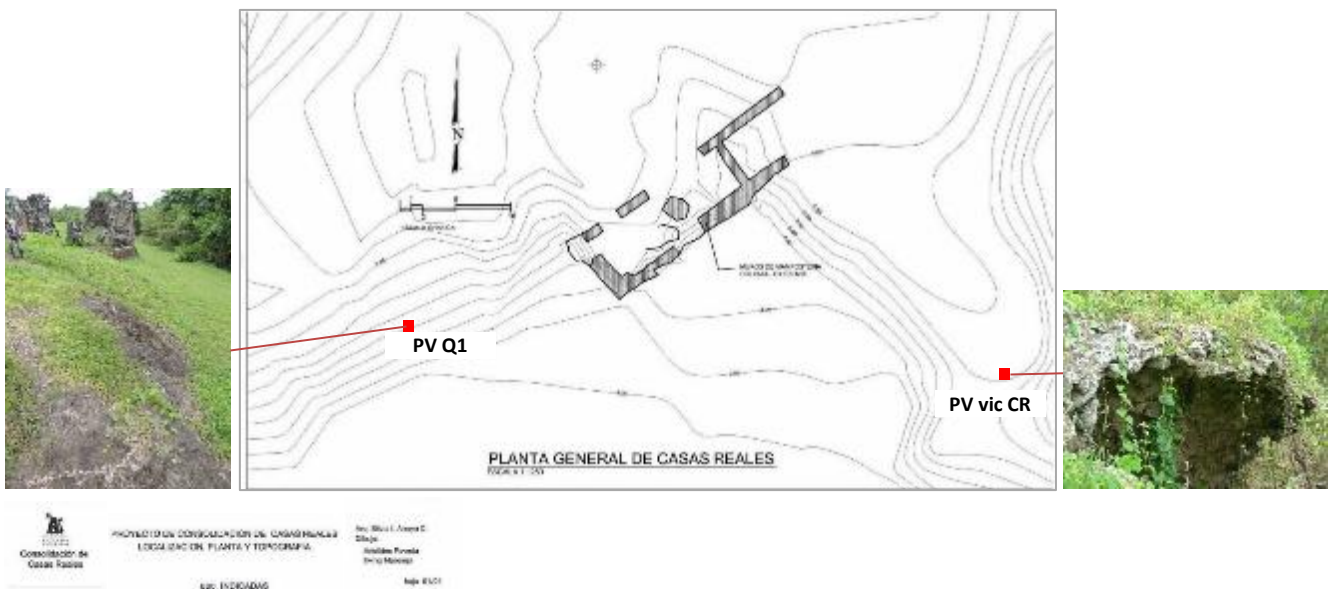


Figure 2.1.1. 40. Outcrops near the Casas Reales and sampling points (Plans are Courtesy of the Patronato de Panamá Viejo).



Figure 2.1.1. 41. a. PV vic CR sample; b. PV Q 1 sample.

*Outcrop near the Convento de Santo Domingo*

This quarry, near the Santo Domingo Convent, is obtained by an outcrop of breccia, which shows tracks of quarrying (Fig. 2.1.1.42).



Figure 2.1.1. 42. Sampling of PV Q 2 specimen. On the left image, with a red dotted line the tracks of quarrying are highlighted.



## 2.1.2 Portobelo

At Portobelo Bay, three fortifications have been sampled, two on the Southern coast of the bay and one the Northern part. In particular, 19 samples have been collected, 16 of them are rock materials belonging to the masonries; two are salt encrustations and one it was sampled at an outcrop. They are listed and described below (Tab. 2.1.2.1).

Table 2.1.2. 1 Samples, lithotypes, state of conservation and location of sampling  
(for the description of the Fort elements Spiteri, 1994).

Sample	Lithotype	State of conservation	Sampling location
<b>PORTOBELLO - Masonries</b>			
<i>Fort San Jeronimo</i>			
PB FSJ 1	Coral limestone (+ jointing mortar)	Biological colonisation (moss...)	External side of the W wall of the Lower Battery, distant 60 cm to the 5th embrasure (counted from the S wall to the N one), h 120 cm (from the water edge)
PB FSJ 4	Sandstone	Biological colonisation (algae?)	Corner of the external side of the W wall of the Lower Battery, near the 5th embrasure (counted from the S wall to the N one). H 110 cm (from the water edge)
PB FSJ 7	Coral limestone (+ mortar)	Biological colonisation	3rd parapet (counted from the bastion) with a distance of 120 cm from the 2nd embrasure, h 115 cm, from the upper level of the banquette
PB FSJ 8	Sandstone	During the tidal rise, it undergoes the seawater intrusion.	Stair of the 2nd banquette (counted from the bastion). Ground level
<i>Fort de Santiago</i>			
PB FdS 2	Sandstone	Exfoliation	Column on the left of the arch (of the external part of the <i>Camera de la inspeccion</i> ), h 250 cm
PB FdS 3	Salt encrustation	The masonry is characterized by several salt encrustations, even in the vault. Under the salt layer it was present a whitish plaster.	Internal part of the <i>Camera de la inspeccion</i> , distant 50 cm from the opening and h 135 cm
PB FdS 5	Sandstone	Biological colonisation (black algae)	Sampled from a corner (S-E) of a internal wall (exposed to S). Distant 56 cm from the corner, h 170 cm
PB FdS 6	Coral limestone	Biological colonisation (black algae + moss)	From S wall, near the PB FdS 5 sample. H 115 cm
PB FdS 8	Coral limestone	Biological colonisation (black algae? + lichens?)	External N side wall of the Fort, facing the sea, distant 660 cm from the E corner, h 80 cm
PB FdS 9	Sandstone		External N-W corner of the Fort, facing the sea, distant 35 cm from the corner and h 90 cm
PB FdS 10	Tuffite	Biological colonisation (moss)	Inner corner of the 3 <sup>rd</sup> embrasure of the W wall. H 70 cm (from the sole)
<i>Fort San Fernando</i>			
PB SF 1	Grainstone/Pack stone (+ mortar)	Biological colonisation (algae?) high decay	W-N wall, 2° embrasure (counted from the N side), h ≈ 140 cm (from the sole) h 125 cm (from the sole) - 60 cm from the external right corner of the mouth
PB SF 2	Coral limestone	Biological colonisation (algae + moss)	W-N wall, 2° embrasure (counted from the N side) S cheek, h 130 cm (from the sole) - 230 cm from the external left corner of the mouth
PB SF 5	Salt encrustation		Moat, west wall, between 6°-7° embrasure (counted from the N side). N cheek, h 125 - 130 cm from the 6° embrasure
PB SF 6	Basaltic andesite	Biological colonisation (algae?)	External part of the Fort, at the entrance by the sea, ground level
PB SF ramp	Andesite	Detachment	Belonging to the upper part of the ramp, ground level

Sample	Lithotype	State of conservation	Sampling location
PB SF 7	Basaltic andesite	Biological colonisation (algae?)	Both from the masonry in the area called "Nave para artilleria y para la guardia" Respectively, h 120 cm - 270 cm from the N wall
PB SF 8	Coral limestone	Biological colonisation (moss)	
PORTOBELO - Outcrops			
PB SF 11	Basaltic andesite		Eastern outer part of the Lower Battery

### *Fuerte San Jeronimo*

The Fort arises directly on the sea shore (Fig. 2.1.2.1a), on the Southern-East part of the Portobelo Bay, embedded in the village of Portobelo, surrounded by residential buildings (Fig. 2.1.2.1b).



Figure 2.1.2. 1 Fuerte San Jeronimo a. View from the sea side; b. View of the Portobelo village.

At this fortification, four samples of natural stone have been collected at the Western wall of the Lower Battery, in order to distinguish the different kind of stone present at the site (Fig. 2.1.2.2).

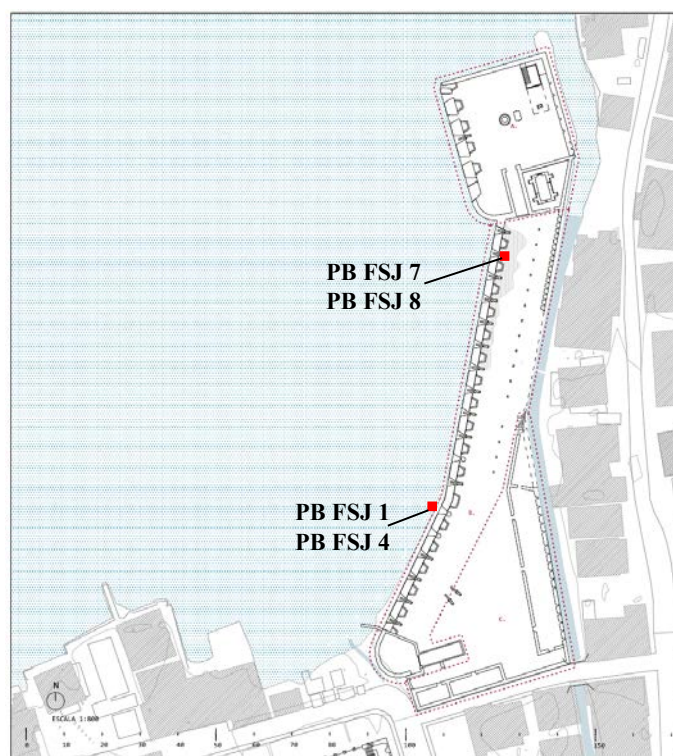


Figure 2.1.2. 2. Plan of the Furte San Jeronimo and sampling points (Plans belongs to the Emergency Plan for Property C135 Fortifications on the Caribbean Side of Panama: Portobelo – San Lorenzo). Point 1: PB FSJ 1, 4; Point 3: PB FSJ 7, 8.

In particular, two coral limestones have been collected at the external side of the wall (PB FSJ 1, Fig. 2.1.2.3a), also showing a jointing mortar, while the other one was sampled from the third parapet (counted from the bastion) of the internal side (PB FSJ 7, Fig. 2.1.2.3b). As the previous one, this latter sample shows mortar, probably always jointing mortar.

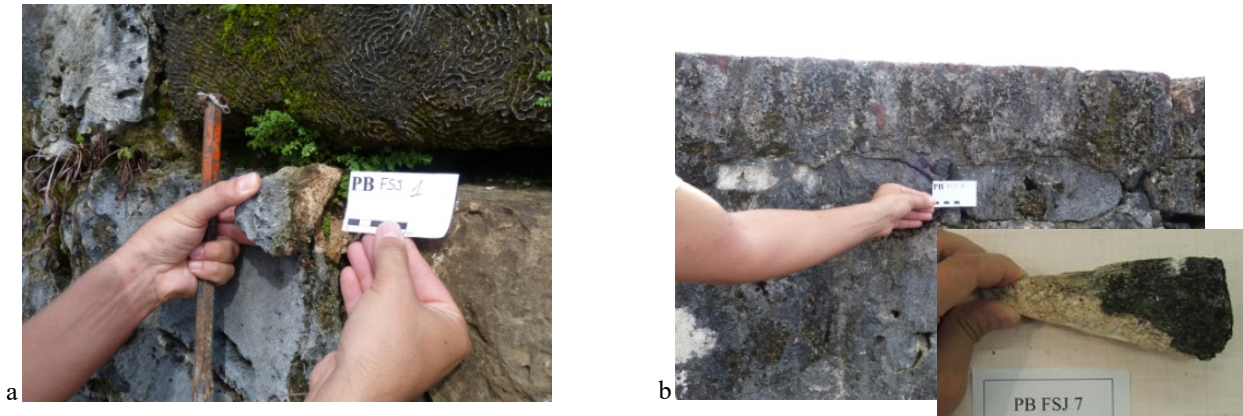


Figure 2.1.2. 3. a. Sampling of PB FSJ 1 specimen; b. Sampling of PB FSJ 7.

Moreover, two yellowish sandstones have been sampled. PB FSJ 4 specimen have been collected from the corner of the external side of the Western wall, near the 5<sup>th</sup> embrasure (counted from the Southern wall to the Northern one) (Fig. 2.1.2.4a), while, PB FSJ 8 belonged to the stairs of the 2<sup>nd</sup> banquette (counted from the bastion), since at ground level. It has to be underlined that this part during the tidal rise undergoes the water intrusion (Fig. 2.1.2.4b).

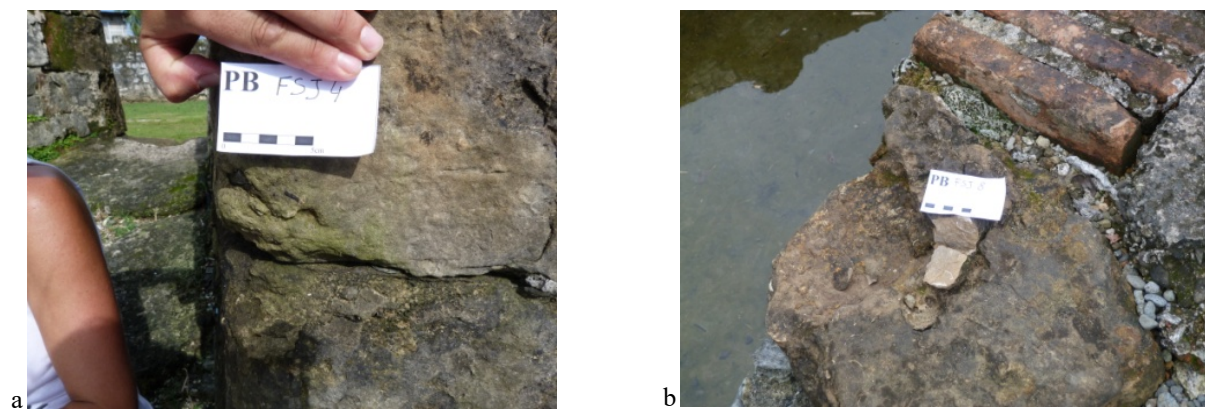


Figure 2.1.2. 4. a. Sampling of PB FSJ 4 specimen; b. Sampling of PB FSJ 8 specimen.

### *Fuerte de Santiago de la Gloria*

This fort has been erected on the Southern coast of the Portobelo Bay, near the village and next to the street, which reaches the hamlet (Fig.2.1.2.5).



Figure 2.1.2. 5. a. View of the Fuerte de Santiago de la Gloria from the Upper Battery; b; human settlements in a part of the Lower Battery.

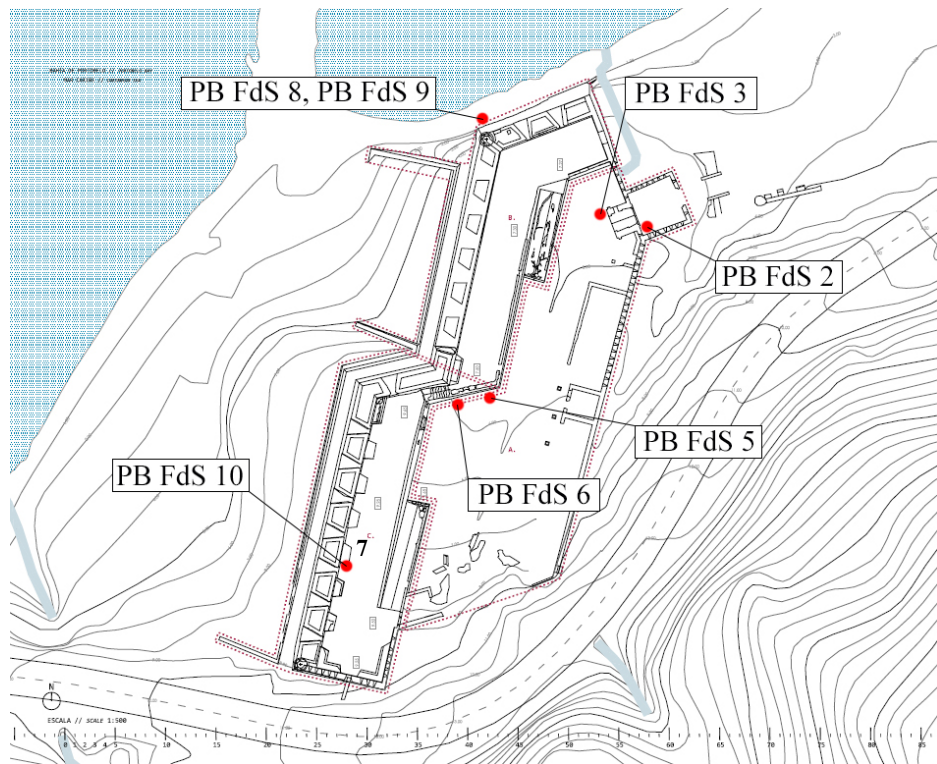


Figure 2.1.2. 6. Plan representing the Fuerte de Santiago de la Gloria and sampling points (Plans belongs to the Emergency Plan for Property C135 Fortifications on the Caribbean Side of Panama: Portobelo – San Lorenzo).

Three samples of yellowish sandstone were collected respectively at: the column on the left of the arch of the external part of the *Camera de la inspeccion* (PB FdS 2, Fig. 2.1.2.7); the S-E corner of the wall of the internal part of the banquette, so exposed to South (PB FdS 5, Fig. 2.1.2.8); from the external western corner of the banquette, near the sea shore (PB FdS 9, Fig. 2.1.2.9). Generally, this kind of stone has been observed utilized in the corners in this Fort. Moreover, it has to be underlined the W internal wall is the most affected by the biodeterioration phenomenon.



Figure 2.1.2. 7. Sampling of PB FdS 2 specimen.



Figure 2.1.2. 8. Sampling of PB FdS 5 specimen.



Figure 2.1.2. 9. Sampling of PB FdS 9 specimen.

Furthermore, two samples of coral limestone were collected respectively one at the S-E corner of the wall of the internal part of the banquette, so near to the PB FdS 5 sample (Fig. 2.1.2.10); while the other one was sampled near the external northern side wall of the Fort, facing the sea (PB FdS 8 sample, Fig. 2.1.2.11). This kind of rock showed a grey colour when exposed, probably due to a biological patina, while the inner part resulted with an ivory hue.



Figure 2.1.2. 10. Sampling of PB FdS 5 specimen.



Figure 2.1.2. 11. Sampling of PB FdS 8 specimen.

Finally, a tuffite was sampled at the inner corner of the 3<sup>rd</sup> embrasure of the western wall of the banquette; it resulted covered by green biological patina (PB FdS 10, Fig. 2.1.2.12).

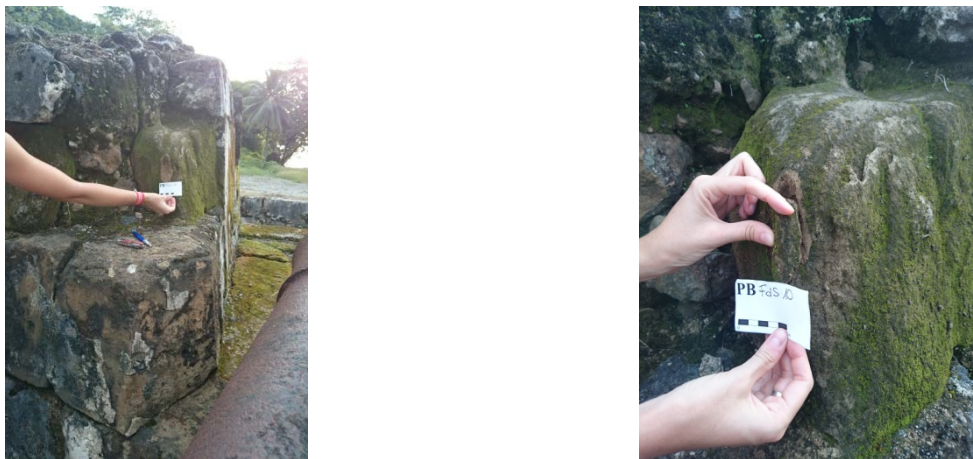


Figure 2.1.2. 12. Sampling of PB FdS 10 specimen.

At the entrance of the Fort, at the *Camera de la inspeccion*, the masonry resulted affected by several salts efflorescences and encrustations, even in the vault (Fig. 2.1.2.13a). A sample of salt encrustation was collected at the internal side of the *Camera de la inspeccion*, moreover, it was noticed a whitish plaster under the salt layers (PB FdS 5, Fig. 2.1.2.13b).



a



b

Figure 2.1.2. 13. a. Salts efflorescences and encrustations in the vault of the *Camera de la inspeccion*; b. Sampling of PB FdS 5, specimen of salt encrustations.

## Fort San Fernando

The construction is settled on the northern side of the bay of Portobelo and it is formed by a Fort, made up of a Lower and an Upper Battery (Fig. 2.1.2.14), and a Hilltop Stronghold. Natural stone materials belonging to the masonries were collected only from the Fort structures. The sampling points are reported in Figure 2.1.2.15 (Lower Battery) and Figure 2.1.2.22 (Upper Battery).



Figure 2.1.2. 14. Fuerte San Fernando: a. Lower Battery; b. Upper Battery.

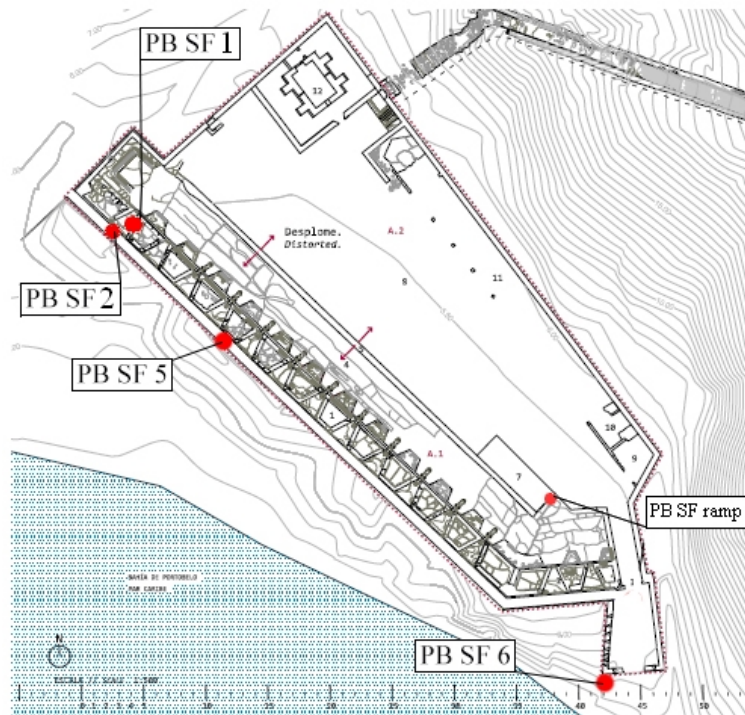


Figure 2.1.2. 15. Plan representing the Lower Battery of Fuerte San Fernando and sampling points (Plans belongs to the Emergency Plan for Property C135 Fortifications on the Caribbean Side of Panama: Portobelo – San Lorenzo).

In particular, at the Lower Battery, a specimen of grainstone/packstone was sampled from the N-W wall, at the right corner of the mouth of the 2<sup>nd</sup> embrasure (counted from the N side). It showed a plaster covering and a high decay (Fig. 2.1.2.16).





Figure 2.1.2. 16. Sampling of PB SF 1 specimen.

Moreover, coral limestones are utilized in the masonry, in particular in specific zones like cheeks and the neck soles of the embrasures (Fig.2.1.2.17); in addition, it was observed at the Fort entrance, specifically in the centreline of the pavement (Fig. 2.1.2.18). Indeed, a sample of this boundstone, PB SF 2, was collected at the 2<sup>nd</sup> embrasure, left cheek (facing West) (Fig. 2.1.2.19). As observed in the previous fort, this stone shown an outer greyish hue, probably due to a biological patina.

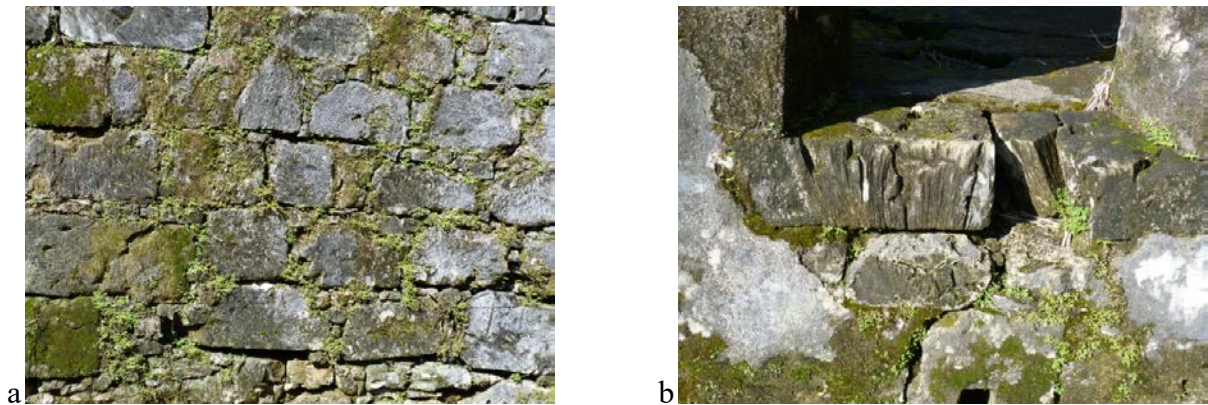


Figure 2.1.2. 17. Coral limestone utilized in the masonry: a. in a wall; b. in the neck soles of the embrasures.



Figure 2.1.2. 18. Coral limestone utilized at the Fort entrance in the centreline of the pavement pavements.



Figure 2.1.2. 19. Sampling of PB SF 2 specimen.

Finally, two volcanic rock, attributable to basaltic andesites, utilized in the pavements of the Lower Battery were collected on the upper part of the ramp, PB SF ramp sample (Fig. 2.1.2.20) and at the entrance of the Fort, PB SF 6 sample (Fig. 2.1.2.21).

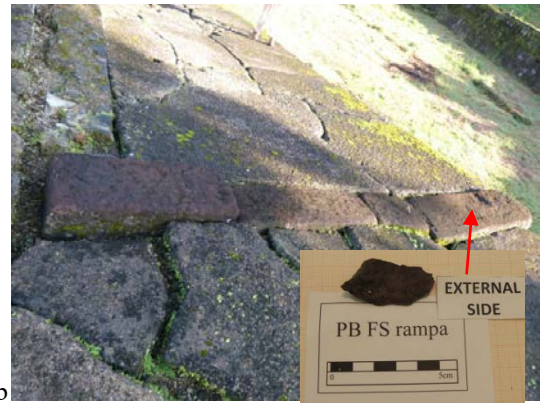


Figure 2.1.2. 20. a. Basaltic andesite utilized in the pavement at the Fort Entrance; b. Sampling of PB SF ramp specimen.



Figure 2.1.2. 21. Sampling of PB SF 6 specimen.

Moreover, salt encrustations were present in the internal wall of the moat, in particular a sample of them was collected from the inner west wall of it, PB SF 5 sample (Fig. 2.1.2.22).

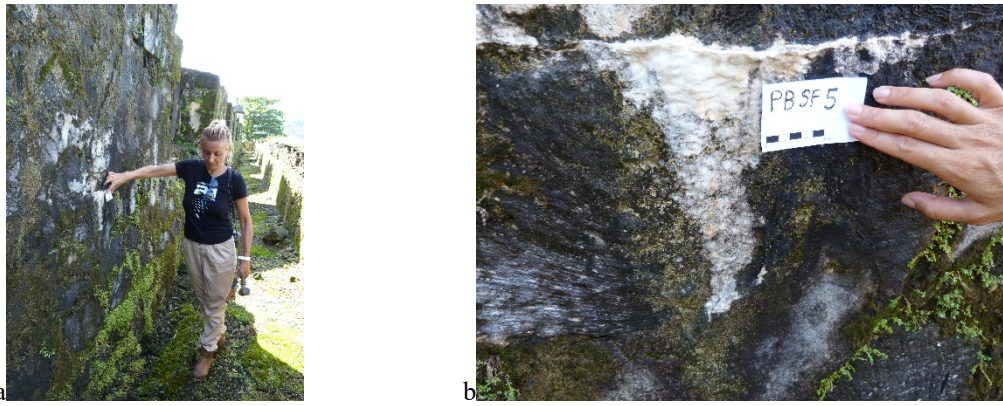


Figure 2.1.2. 22. a. View of the inner part of the moat, particular of the salt encrustations; b. Sampling of PB SF 5 specimen.

The same rock typology of the latter samples was observed also in the Upper Battery (Fig. 2.1.23), utilized in the masonry, especially in the sole of the embrasures (Fig. 2.1.2.24). It was sampled in the N-E masonry of the area called "*Nave para artillería y para la guardia*", PB SF 7, showing oxidation and high hardness (Fig. 2.1.2.25).

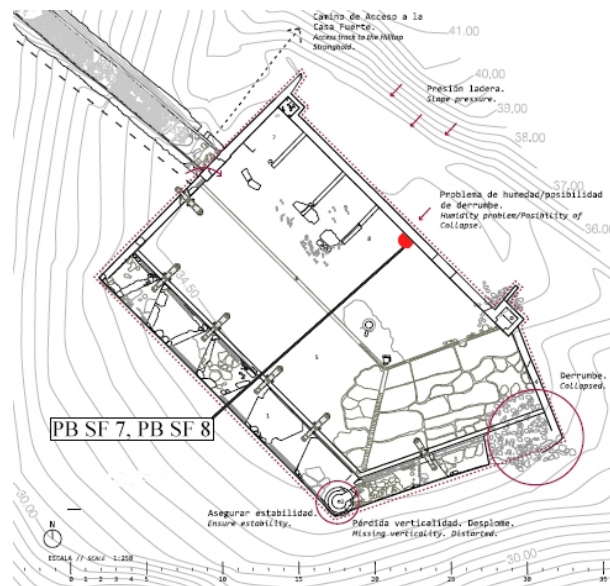


Figure 2.1.2. 23. Plan of the Upper Battery of Fuerte San Fernando and sampling points (Plans belongs to the Emergency Plan for Property C135 Fortifications on the Caribbean Side of Panama: Portobelo – San Lorenzo).



Figure 2.1.2. 24. Examples of volcanic rock utilized in the sole of the embrasures neck.



Figure 2.1.2. 25. Sampling of PB SF 7 specimen.

In the same masonry of the previous sample, next to it a coral limestone was collected (PB SF 8, Fig. 2.1.2.26). It is different from the species of the other one, which is the most diffused. Nevertheless, as the other one it showed a greyish external colour, but the inner part show the natural ivory hue.



Figure 2.1.2. 26. Sampling of PB SF 8 specimen.

### *Outcrop*

Near the entrance of the Fort, on the East part, just near the sea side, was discovered an outcrop of volcanic rock ascribable to basaltic andesite, possible quarry of raw materials utilized in the different part of the fortification (Fig. 2.1.2.27). Indeed, this complex is the only Fort of Portobelo, which presents this kind of rock utilized in the masonry.



Figure 2.1.2. 27. a. Outcrop of basaltic andesite; b. PB SF 11 sample.

### 2.1.3 San Lorenzo

Surrounded by the forest in the San Lorenzo Protected Area, the fort arises on a promontory beside the Chagres River mouth, on the Atlantic shore of Panama (Fig. 2.1.3.1).

Observing the building macroscopically in situ, the first deterioration phenomena observed are the presence of biomass, including insects, moss, algae, as well as vascular plants (see Table 2.1.1).



Figure 2.1.3. 1. Two views of Fort San Lorenzo.

The samples collected at the fort are localized on the map represented in Figure 2.1.3.2, listed in Table 2.1.3.1 and described below.

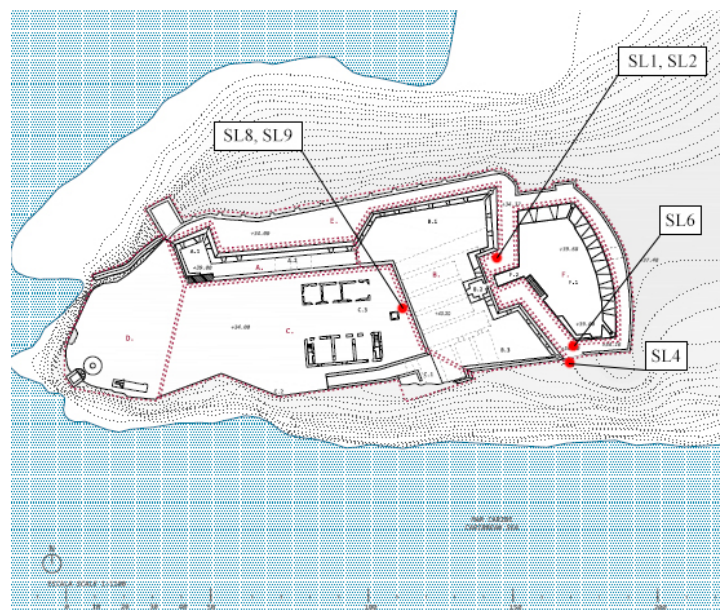


Figure 2.1.3. 2. Plan representing Fuerte San Lorenzo and sampling points (Plans belongs to the Emergency Plan for Property C135 Fortifications on the Caribbean Side of Panama: Portobelo – San Lorenzo).

Table 2.1.3. 1. Samples, lithotypes, state of conservation and location of sampling

(for the description of the Fort elements Spiteri, 1994).

Sample	Lithotype	State of conservation	Sampling location
SAN LORENZO - Masonries			
SL 4	Tuffite	High decohesion	S corner of the bastion; h 190 cm
SL 6	Tuffite	High decohesion and fracturing	S corner of the exterior terreplain, moat side.; h ≈130-140cm
SL 8	Grainstone	Slightly good	Inner part of the bastion; base ornamental blocks of the portal
SL 9	Tuffite	High decohesion and powdering	Wall of the inner part of the bastion; h ≈140-150cm
SAN LORENZO - Outcrops			
SL 1	Sandstone/tuffite	Slightly good	Below the bastion (moat area)
SL 2	Sandstone/tuffite	High decohesion	Below the bastion (moat area)
SL 13	Grainstone	Covered by vegetation	Distant 5 km from the Fort

The Fort masonries are mainly formed by a tuffite/sandstone sampled in several parts of the fortification. Specifically, SL 4 sample was collected at the South corner of the bastion (quoins) (Fig. 2.1.3.3). SL 6 specimen was always sampled from a corner of the exterior part of the terreplain, at the moat side (Fig. 2.1.3.4). SL 9 sample was collected from the wall of the inner part of the bastion, between the 2<sup>nd</sup> and the 3<sup>rd</sup> opening-vault, moreover, it showed a partial jointing mortar and probably a finishing mortar (Fig. 2.1.3.5). They all show high decohesion and fracturing, covered by a black biological patina.



Figure 2.1.3. 3. Sampling of SL 4 specimen.



Figure 2.1.3. 4. Sampling of SL 6 specimen.



Figure 2.1.3. 5. Sampling of SL 9 specimen.

In the inner part of the bastion, blocks of grainstone compose parts showing bossage, forming the ornamental parts of the portal and the base blocks (Fig. 2.1.3.6a). In particular, this latter part was sampled, near the third opening-vault, SL 8 sample (Fig. 2.1.3.6b). This kind of rock shows high hardness, indeed it results better preserved than the previous one, in particular, showing less superficial biological colonization.



a



b

Figure 2.1.3. 6. a. Grainstone forming the ornamental parts of the portal and the base blocks; b. Sampling of SL 8 specimen.

### *Outcrops*

Two outcrops were sampled at Fort San Lorenzo, one at the site, collected from the bastion foundation (Fig. 2.1.3.7), formed by sandstone/tuffite SL 1 and SL 2 samples (Fig. 2.1.3.8). They show high decohesion and differential erosion, however, SL 1 showed more cohesion than SL 2 sample.



Figure 2.1.3. 7. Outcrop of sandstone/tuffite forming the bastion foundation.



Figure 2.1.3. 8. a. Sampling of SL 1 specimen; b. Sampling of SL 2 specimen.

Finally, another outcrop was indicated by the personnel of Portobelo and San Lorenzo Patronage distant 5 km from the Fort and 1 km from the entrance in the San Lorenzo area (Fig. 2.1.3.9a). It was an outcrop of grainstone, thus sampled (SL 13 sample, Fig. 2.1.3.9b).



Figure 2.1.3. 9. a. Outcrop of grainstone; b. sampling of SL 13 specimen.



## 2.2 Analyses Performed

In order to characterize and evaluate the state of preservation of these materials, the following analyses were performed.

### *Stereomicroscope observations*

An Optika SZ6745TR, equipped with a webcam, MOTICAM 2005 5.0 Mp, and Moticam Image Plus 2.0 software, was utilized for performing preliminary analyses of the bulk samples.

### *Polarized Light Microscopy (PLM) investigations*

They have been utilized for the analysis of uncovered thin sections, partially polished for performing observations in both transmitted and reflected light, using an Olympus BX 51 microscope, equipped with scanner and the MICROMAX software “Primoplus\_32” vers. 8.11.02. In order to evaluate the state of conservation, the thin sections were realized through transversal cut from the external to the inner part of the samples.

### *X-Ray Powder Diffraction (XRPD) analysis*

For determining the mineralogical phases present, through a Philips PW 1730 diffractometer equipped with a copper anticathode and a nickel filter. The measurement conditions have a diffraction interval of  $2\theta$ , between  $5^\circ$  and  $50^\circ$ , and a  $2^\circ/\text{minute}$  step at 40kV voltage and 30 mA current intensity. In addition, further analysis have been performed in order to verify the clay minerals present in several samples, utilizing a Bruker AXS D8, in Bragg-Brentano geometry, equipped with a X-Ray tube and a SolX solid state detector, working in low-temperature through Peltier cooling system.

The samples for this techniques underwent powdering process, utilizing two mills, firstly a jaw crushers and secondly a mortar grinder with agate jar and pestle. For materials showing high hardness the process was finished by manual grinding with an agate mortar. Moreover, in order to examine in detail the clay minerals with the second diffractometer, analyses were repeated three times for each sample: the first one on the random mount sample (measurement conditions: time=2h14'; slits=1, 1, 0.2); then on iso-oriented powder (measurement conditions: time=1h33'; slits=0.6, 0.6, 0.2;  $2\theta=2^\circ-30^\circ$ ) and finally, this latter one underwent ethylene glycol solvation (measurement conditions: time=1h33'; slits=0.6, 0.6, 0.2;  $2\theta=2^\circ-30^\circ$ ).

### *Environmental Scanning Electron Microscopy and micro-chemical investigations (ESEM-EDX)*

Analyses were carried out to determine the elemental composition of specific areas of interest, already observed by Stereomicroscope and PLM investigation, therefore on both bulk and thin sections. The instrument utilized is a ZEISS EVO LS 10 with LaB6 source.

### *X-ray fluorescence (XRF)*

Performed on powder pellets (see XRPD section for powdering process), pressed with boric acid powder as binder, using a wavelength-dispersive automated ARL Advant'X spectrometer. Accuracy and precision for major elements are estimated 2-5%; for trace elements (above 10 ppm) are better than 10 %.

### *Mercury Intrusion Porosimetry (MIP)*

For understanding the porosimetry features of the materials, also index of their state of conservation, specimens that showed enough material (~1x1x1 cm – 2x2x2 cm) were selected and analysed by a porosimeter “PASCAL 240, THERMO SCIENTIFIC”.

### *Ion Chromatography (IC)*

In order to evaluate the possible presence of soluble salts present in the masonry, IC analyses have been performed on samples showing particular patina or superficial alteration phenomena. The selected specimens, powdered (see XRPD section for powdering process), were investigated by a DIONEX ICS 900. Anions analysis: Column S23 Pre-column G23; Cations analysis: Column CS12 Pre-column CG12.

## 2.3 Selection of Monitoring Stations and Climate Models

Monitoring stations have been selected in order to obtain climate parameters in the surroundings of the Monumental Site of Panama Viejo, the Portobelo and San Lorenzo areas. Specifically, the stations have been chosen among the network of the Panama Canal Authority (ACP) and the Empresa de Trasmision Electrica S.A. (ETESA). It has to be underlined that the ACP data have been downloaded from the Smithsonian Tropical Research Institute (STRI) and ETESA websites. They are listed and localized in the following Table 2.3.1 and Figure 2.3.1. Considering the stations of Cristobal, Cocosolo and Limon Bay, they will be expressed as an unique monitoring station, as STRI suggests, since the three stations are from the same area and represent a single data series.

Table 2.3. 1. Monitoring stations selected as the closest to the sites of interest, respectively: in grey to Panama Viejo; in blue to Portobelo and in green to San Lorenzo.

Name	Label	Province	Elevation (m)	Latitude	Longitude	Starting date	Final date	Operated by
Hato Pintado	HP	Panama	45	9° 00' 33" 9.009167	79° 30' 52" -79.511444	1/07/1987	still active	E.T.E.S.A.
Tocumen	T	Panama	18	9° 03' 56" 9.065556	79° 23' 31" -79.391944	1/01/1970	1/01/2013	E.T.E.S.A.
Balboa FAA	B-FAA	Panama	10	8° 58' 08" 8.968889	79° 32' 58" -79.5494	1/01/1908	still active	A.C.P.
Portobelo	Pb	Colon	2	9° 33' 42" 9.561667	79° 40' 00" -79.666666	1/05/1908	1/01/2004	E.T.E.S.A.
Gatun Rain Z.C.	G	Colon	31	9° 16' 06" 9.268333	79° 55' 14" -79.920556	1/01/1905	still active	A.C.P.
Cristobal	CCL	Colon	8.5	09° 21'	79° 54'	1/10/ 1862	30/09/ 1979	A.C.P.
CocoSolo			4.6	09° 22'	79° 53'	1/09/1980	30/06/1996	
Limon Bay			3	09° 21' 20" 9.355556	79° 54' 53" -79.914722	1/11/1996	still active	
Fort Sherman	FS	Colon	9	9° 22' 00" 9.366667	79° 57' 00" -79.950000	24/04/1997	14/10/2014	A.C.P.
Pina	P	Colon	3	9° 16' 00" 9.266667	80° 02' 00" -80.033333	1/12/1970	1/11/1998	E.T.E.S.A.

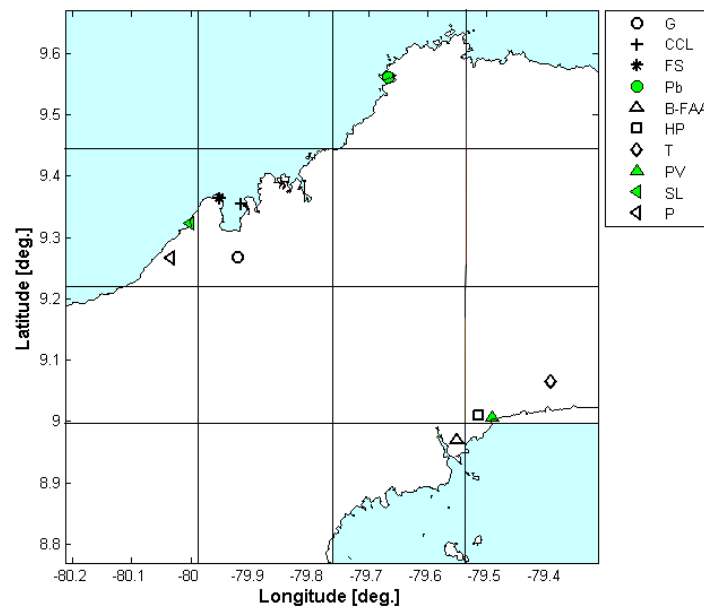


Figure 2.3. 1. Particular of the central area of the Panamanian isthmus. On the right the legend of the markers, in green the sites under study: PV=Panama Viejo; SL=San Lorenzo; P=Portobelo. This latter one coincides with a location of the Portobelo monitoring station. The white symbols indicate the monitoring stations, respectively: G=Gatun Rain Z.C., CCL=Cristobal-Cocosolo-Limonbay, FS=Fort Sherman, Pb=Portobelo, B-FAA=Balboa-FAA, HP=Hato Pintado, T=Tocumen, PV=Panamá Viejo, SL=San Lorenzo, P=Pina.

The climate parameters collected are rainfall, relative humidity and air temperature. As follows, they have been respectively extracted from:

1. Rainfall :

- a. Near Panama Viejo: Balboa FAA (operated by ACP but downloaded from STRI website); Hato Pintado and Tocumen (operated and downloaded by ETESA)
- b. Near Portobelo: Portobelo (operated and downloaded by ETESA)
- c. Near San Lorenzo: Cocosolo, Limonbay and Sherman (operated by ACP but downloaded from ETESA website) and Gatun (operated by ACP but downloaded from STRI website), Pina (ETESA)

2. Relative Humidity:

- a. Near Panama Viejo: Balboa FAA (operated by ACP but downloaded from STRI website) and Tocumen (operated and downloaded by ETESA)
- b. Near San Lorenzo: Cocosolo, Limonbay, Gatun and Sherman (operated by ACP but downloaded from STRI website)

3. Air Temperature:

- a. Near Panama Viejo: Balboa FAA (operated by ACP but downloaded from STRI website) and Tocumen (operated and downloaded by ETESA)
- b. Near Portobelo: Portobelo (operated and downloaded by ETESA)
- c. Near San Lorenzo: Cocosolo, Limonbay, Gatun and Sherman (operated by ACP but downloaded from STRI website)

(Dirección de Hidrometeorología, Empresa de Transmisión Eléctrica S.A.; Meteorological and Hydrological Branch of the Panama Canal Authority; Physical Monitoring Program of the Smithsonian Tropical Research Institute).

Concerning the climate simulations, two models have been elected: Arpege and EC-Earth. The first one is a global and spectral general circulation model developed by Meteo France (Déqué, 2010), the resolution of the experiment utilized is of 50 km (so covering areas of 50 km per side), with a historical simulation referred to the period 1950-2005, called FN1, while the period of future scenarios corresponds to 2006-2100. These future predictions represent three of the Representative Concentration Pathways (RCPs), specifically, RCP8.5, called FN2, RCP4.5 called FN3 and RCP2.6 called FN4.

In order to represent mainly the zones under study, four areas of the models have been extracted, with the following central points: Long.-79.50; Lat.9.74 (Portobelo area); Long.-80.00; Lat: 9.24 (San Lorenzo area); Long.-79.50; Lat.8.74 (near Panama Viejo area) and -79.50; Lat.9.24 (Panama Viejo area), as showed in Figure 2.3.2.

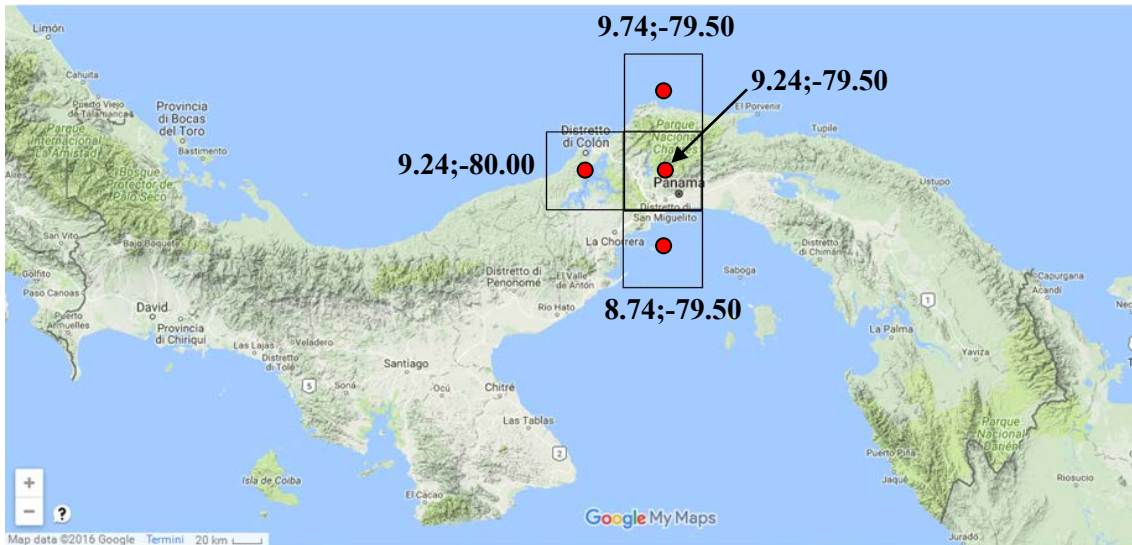


Figure 2.3. 2. Black squares represent the area extracted from the Arpege model overlapped the Panamanian region of interest.

The other model is a recent earth-system model developed by a consortium of European research institutions and researchers, based on state-of-the-art models for the atmosphere, the ocean, sea ice and the biosphere (Davini et al., 2016). The experiment adopted for this study is the t799, with a resolution of 25 km. The historical period of reference (hab3) is of 30 years, 1979-2008; the future period (hfb3), always of 30 years, corresponds to 2039-2068, representing only one RCP and, in particular, the RCP 8.5.

The resolution of the model has allowed us to obtain a grid of 4x4 areas, covering the central part of the isthmus with longitude values between 279.9 and 280.573 by 0.225 °E and latitude within 9.55653 and 8.88195 °N. For the comparison with the monitoring stations data and Arpege model series, the following points have been extracted: Long.79.45; Lat.9.1 (Panama Viejo area); Long.-79.6; Lat. 8.9 (near Panama Viejo area), Long.-79.85; Lat. 9.3 (near San Lorenzo area); Long.-80.05; Lat. 9.3 (San Lorenzo area) and Long. -79.65, Lat. 9.55 (Portobelo area), reported in Figure 2.3.3.

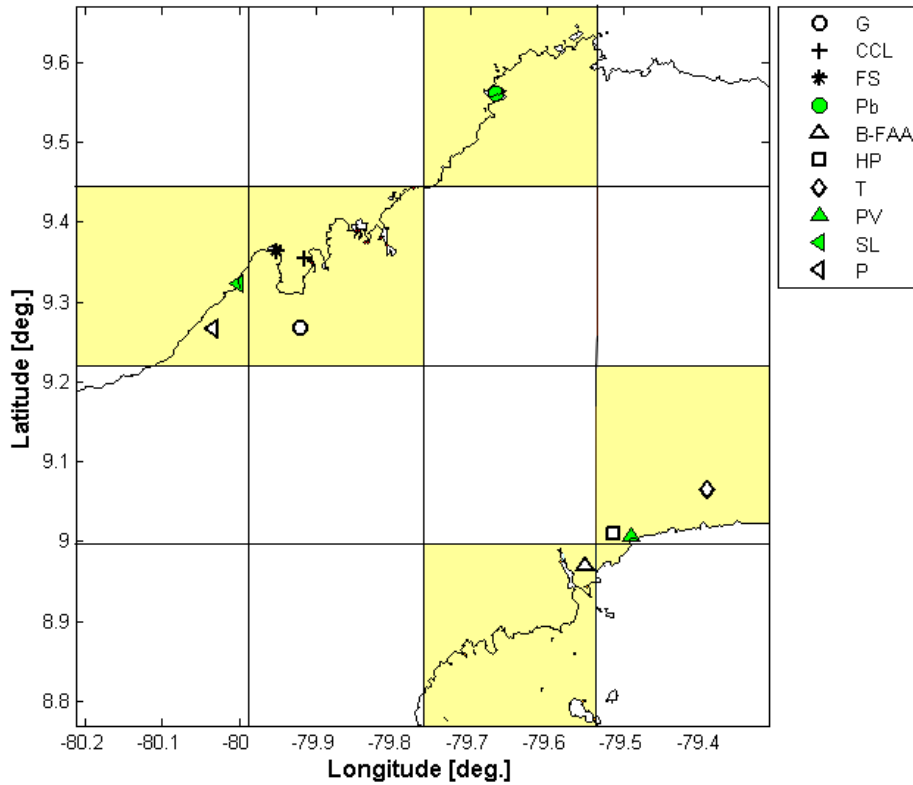


Figure 2.3. 3. Grid areas of EC-Earth model. In yellow are highlighted the zones which overlap or are near of the sites of interest. On the right the legend of the markers, the white symbols indicate the monitoring stations, the green markers the sites, respectively: G=Gatun Rain Z.C., CCL=Cristobal- Cocosolo-Limonbay, FS=Fort Sherman, Pb=Portobelo(both monitoring station and site), B-FAA=Balboa-FAA, HP=Hato Pintado, T=Tocumen, PV=Panamá Viejo, SL=San Lorenzo, P=Pina.

As it can be noticed from the previous maps (Figs. 2.3.2-3), Panamá Viejo and San Lorenzo sites result close to the border of EC-Earth grid area, while Panama Viejo it is close to the border also of the Arpege model area. For that reason, the areas selected to be investigated in detail and compared with the monitoring stations data are respectively four for Arpege simulation and five for EC-Earth model, as previously described, including also the surroundings of Panamá Viejo and San Lorenzo. Finally, from both models the climate parameters extracted are: the amount of daily rainfall (mm), the average of daily temperature (°C) and the average of daily relative humidity (RH). It has to be underlined that these latter two parameters have been calculated in the case of Arpege model, since it showed the temperature data as daily minumun and maximun, while the relative humidity presented four "measures" per day, so every 6 hours.

### 3. Chapter 3 - Materials Characterization and Damage Evaluation

#### 3.1. Observation of thin sections by Polarized Light Microscopy (PLM)

##### 3.1.1. Panama Viejo

###### Material characterization

Polarized light microscopy (PLM) observation was performed on twenty-seven thin sections and specifically on the samples listed as follows, in Table 3.1.1.1:

Table 3.1.1.1. List of samples belonging to Panama Viejo and their related lithotypes and provenance analysed through PLM observations of thin sections.

<b>Monuments</b>	<b>Samples</b>	<b>Lithotype</b>
<i>Convento de las Monjas de la Concepción</i>	PV CC 4, PV CC 5, PV CC 6	Breccia
<i>Casas Reales</i>	PV CR 4	Breccia
<i>Casa Terrin</i>	CT 1, CT 2	Rhyolite
<i>Convento de San Francisco</i>	PV FC 4, PV FC 5, PV FC 7, PV FC 8, PV FC 11 PV FC 6, PV FC 9	Breccia Altered volcanic rock
<i>Fortín de la Natividad</i>	PV FN 1, PV FN 2 PV FN 4, PV FN 5	Breccia Basaltic andesite
<i>Convento de la Compañía de Jesus</i>	PV JC 1, PV JC 2, PV JC 3, PV JC 4	Breccia
<i>Hospital de San Juan de Dios</i>	PV SJdD	Altered volcanic rock
<i>Torre de la Catedral</i>	PV TC 3, PV TC 4	Tuffite
<b>Outcrops location</b>	<b>Samples</b>	<b>Lithotype</b>
Near <i>Casas Reales</i>	PV Q 1 PV vic. CR	Breccia Basaltic andesite
Near <i>Convento de Santo Domingo</i>	PV Q 2	Basaltic andesite

Analyses performed on samples belonging to masonries revealed predominantly the presence of volcanic stones, mainly composed by sedimentary processes of volcanoclastic deposits, forming polygenic and volcanic breccias and tuffites. Furthermore, lava stones were detected such as basaltic andesites and rhyolites. Finally, altered volcanic rocks have been identified in different monuments.

In order to compare in detail the several stones present at Panama Viejo sites, the results will be presented divided by the different lithology.

###### *Breccia*

Considering the complexes of the *Convento de las Monjas de la Concepción*, *Casas Reales*, *Convento de la Compañía de Jesus* and, partially, of the *Convento de San Francisco* and of the *Fortín de la Natividad*, samples analysed reveal that masonries are built with breccias of polygenic formation. The main composition is due to volcanic deposits, nevertheless, numerous fragments of sedimentary rocks were also observed.

Specifically, at the *Convento de las Monjas de la Concepción*, PV CC 5 shows trachyte and carbonate rocks fragments (Fig. 3.1.1.1), while PV CC 4 shows basalt/andesite and pomiceous fragments (Fig. 3.1.1.2), amygdales, due to hydrothermal activity (Fig. 3.1.1.3), whereas PV CC 6 exhibits fossils, limestones and andesite fragments (Fig. 3.1.1.4).

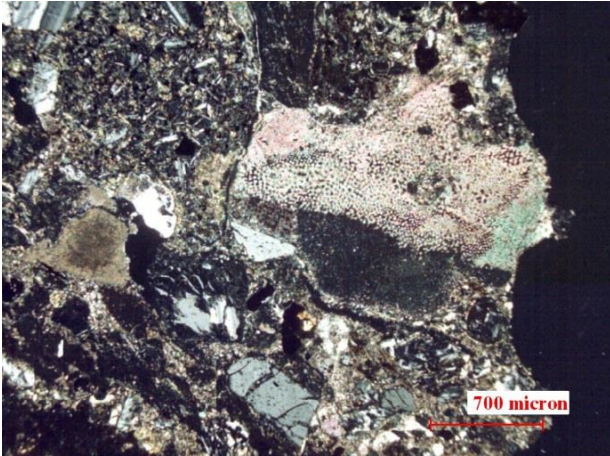


Figure 3.1.1. 1. Photomicrograph of PV CC 5 breccia sample (xpl, 4x). Particular of a carbonate fragment.



Figure 3.1.1. 2. Photomicrograph of PV CC 4 breccia sample (xpl, 10x). a. Basalt/andesite fragments.

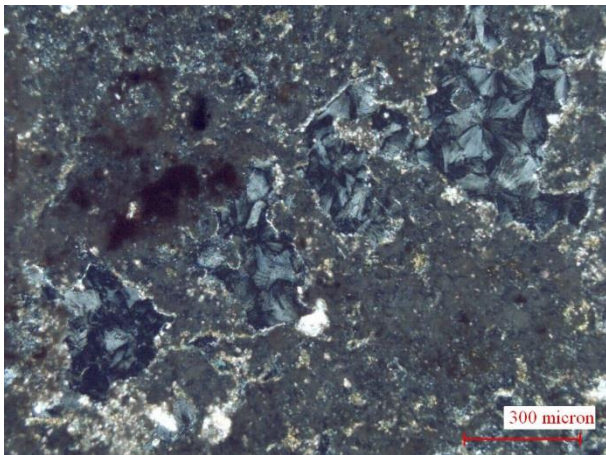


Figure 3.1.1. 3. Photomicrograph of PV CC 4 breccia sample (xpl, 10x). Particular of amygdales filled with zeolites.

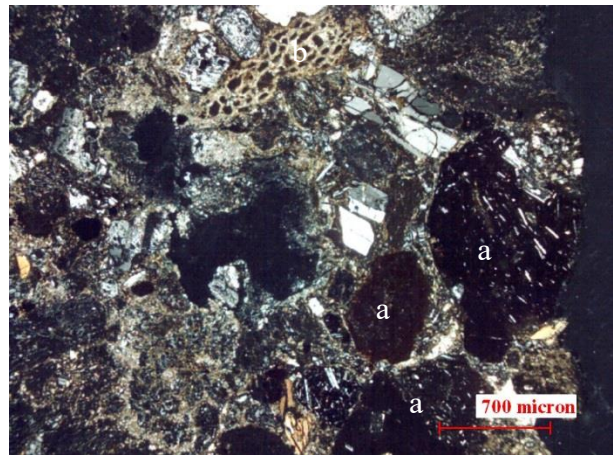


Figure 3.1.1. 4. Photomicrograph of PV CC 6 breccia sample (xpl, 4x). a. Basalt/andesite fragments; b. fossil.

One rock sample has been analyzed, belonging to Casas Reales' masonries, PV CR 4, a polygenic breccia similar to the previous ones, with fragments of basalts, andesites, and zeolitized parts (Figs. 3.1.1.5 – 3.1.1.6).

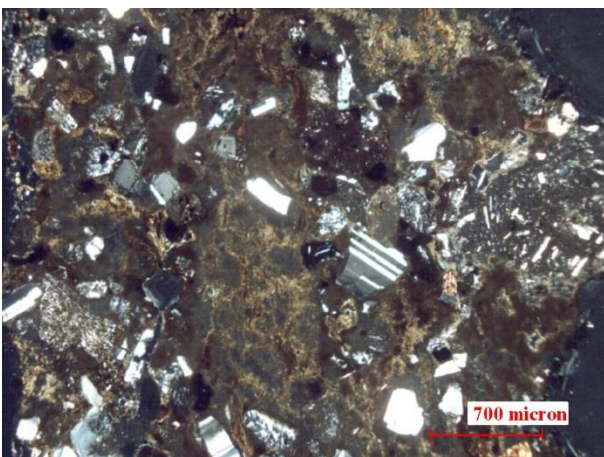


Figure 3.1.1. 5. Photomicrograph of PV CR 4 breccia sample (xpl, 4x).

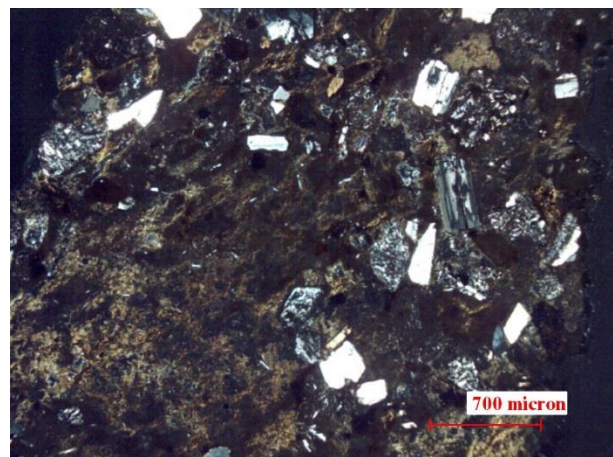


Figure 3.1.1. 6. Photomicrograph of PV CR 4 breccia sample (xpl, 4x).

Even in samples belonging to the *Convento de la Compañía de Jesus* fragments of micritic limestones, trachytes, basalts were detected. In particular, PV JC 1 shown a coarser and a finer part, while PV JC 2 exhibits presence of fossils and zeolitized parts (Fig. 3.1.1.7), these latter ones are



observed also in PV JC4, which are located in reddish parts rich in iron oxides. Finally, PV JC 3 presents also probable pomiceous and glass fragments (Fig. 3.1.1.8).

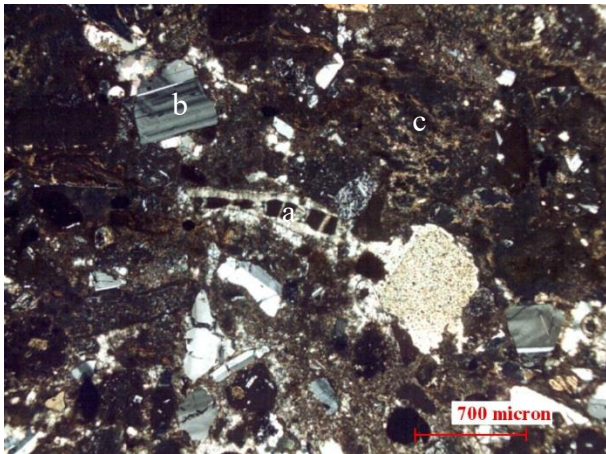


Figure 3.1.1. 7. Photomicrograph of PV JC 2 breccia sample (xpl, 4x), showing a. foraminifera; b. plagioclases and c. zeolitized parts.

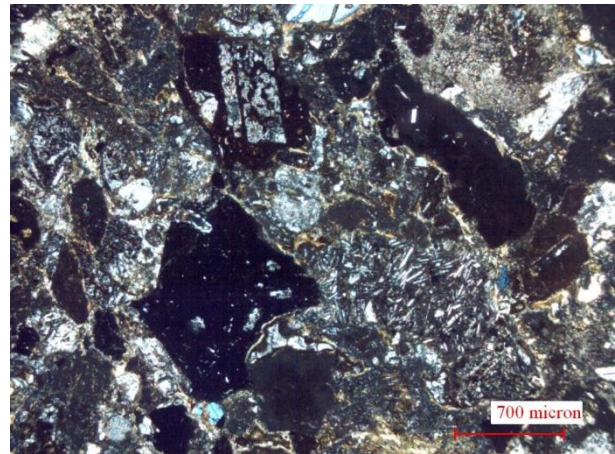


Figure 3.1.1. 8. Photomicrograph of PV JC 3 breccia sample (xpl, 4x).

At the *Convento de San Francisco*, polygenic breccias and altered volcanic rocks have been observed utilized in the masonry.

Regarding the first ones, they have been identified in samples PV FC 4, PV FC 5, PV FC 7, PV FC 8 and PV FC 11, showing basalt/andesite fragments, with rounded/subrounded shapes (Figs. 3.1.1.9, 3.1.1.10), indicating reshuffle of them by transport. Furthermore, the stones exhibits clear signs of being underwent to a remelting process, validated by the presence of magmatic pebbles showing inner devetrification and altered minerals of sanidine, quartz and zoned plagiase (Figs. 3.1.1.9-3.1.1.10). Moreover, samples PV FC 4, PV FC 8 and PV FC 11 showed a diffused zeolitization (Fig. 3.1.1.12).

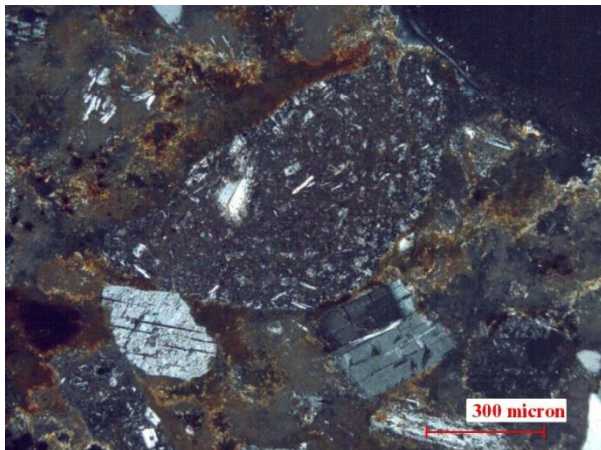


Figure 3.1.1. 9. Photomicrograph of PV FC 4 breccia sample (xpl, 10x), showing subrounded basalt/andesite fragment.

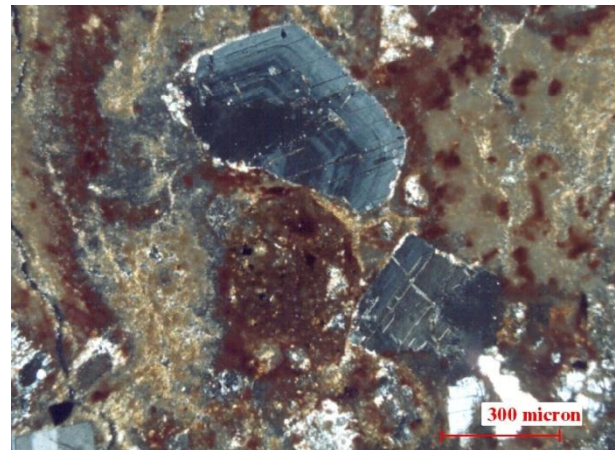


Figure 3.1.1. 10. Photomicrograph of PV FC 5 breccia sample (xpl, 10x) showing altered zoned plagioclase.

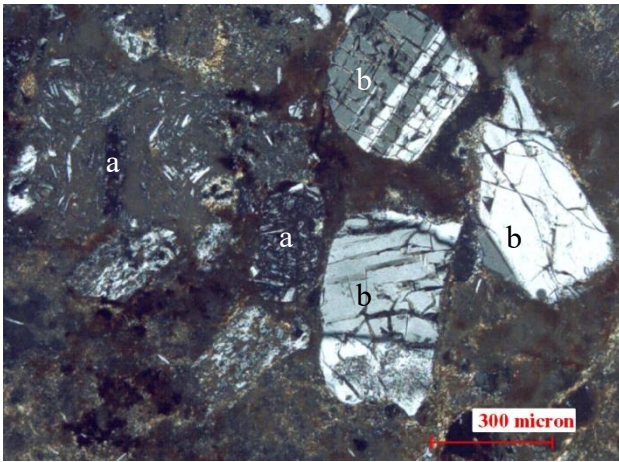


Figure 3.1.1. 11. Photomicrograph of PV FC 4 breccia sample (xpl, 10x) a. Basalt/andesite fragments; b. devitrified plagioclases.

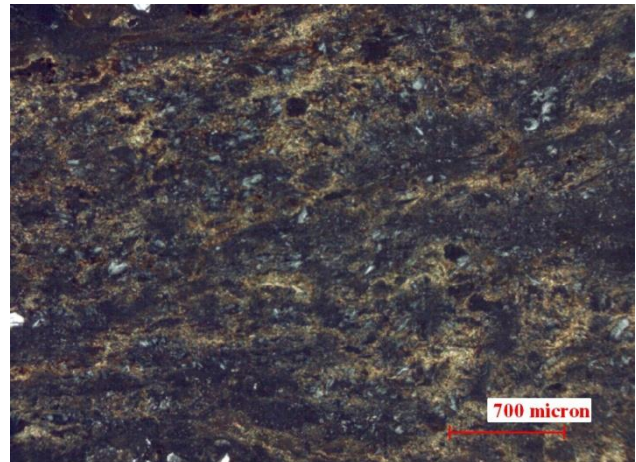


Figure 3.1.1. 12. Photomicrograph of PV FC 4 breccia sample (xpl, 4x) showing diffused zeolitization.

In addition, in PV FC 11 fragments of chert (Fig.3.1.1.13) and ironstone were detected; the latter one shown an alteration state (Figs. 3.1.1.14-3.1.1.15); moreover amygdales filled with zeolites have been observed (Figs. 3.1.1.15-3.1.1.16) .

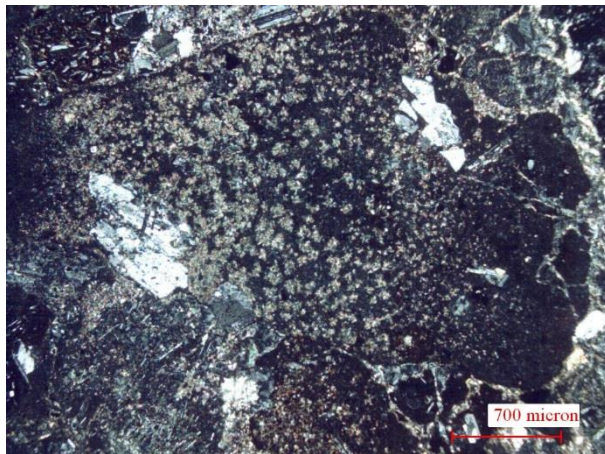


Figure 3.1.1. 13. Photomicrograph of PV FC 11 breccia sample (xpl, 4x) showing a chert fragment.

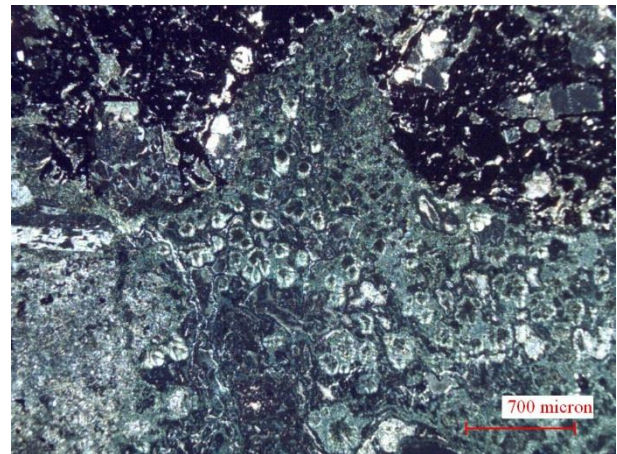


Figure 3.1.1. 14. PV FC 11 breccia sample (xpl, 4x), particular of the ironstone.



Figure 3.1.1. 15. Photomicrograph of PV FC 11 breccia sample (xpl, 10x), particular showing the ironstone and an amygdale filled with zeolites.



Figure 3.1.1. 16. Photomicrograph of PV FC 11 breccia sample (xpl, 40x), particular of zeolites filling an amygdale.

Concerning sample PV FC 7, it is noticeable the presence of fossils as macro-foraminifera. Moreover there is a silicate component, mainly represented by sanidine crystals, also as microcrystals, due to fluidal structures, and by angular and subangular quartz minerals and zeolitized

part (Fig. 3.1.1.17), thus with a magmatic origin. Several vitric structures and metal oxides were also identified (Fig. 3.1.1.18).

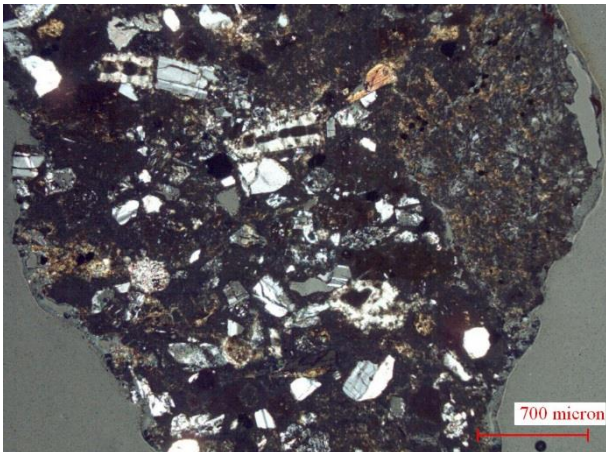


Figure 3.1.1. 17. Photomicrograph of PV FC 7 breccia sample, present several foraminifera and a zeolitized part (on the right).

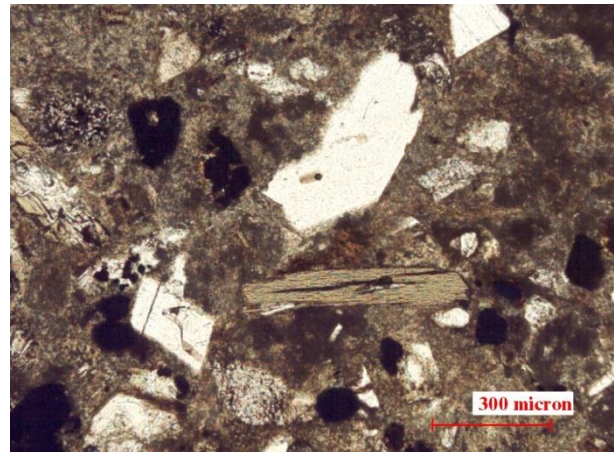


Figure 3.1.1. 18. Photomicrograph of PV FC 7 breccia sample (ppl, 10 x). Particular of the presence of metal oxides.

Considering the *Fortino de la Natividad*, it can be highlighted that volcanic rocks were widely utilized. In particular, PV FN 1 and PV FN 2 have been characterized as polygenic breccias. These rocks are characterized by 90% of magmatic origin and 10% derived by marine remolding, showing the presence of several carbonates fragments (Fig. 3.1.1.19), iron oxides such as magnetite and hematite, while, basalt/andesite fragments (Fig. 3.1.1.20), probable glass rests (Fig.3.1.1.21), sanidine crystals and zoned plagioclases (Fig. 3.1.1.22), were noted in the magmatic phase. In addition, both samples shows zeolitized parts, shown in Figures 3.1.1.23, 3.1.1.24.

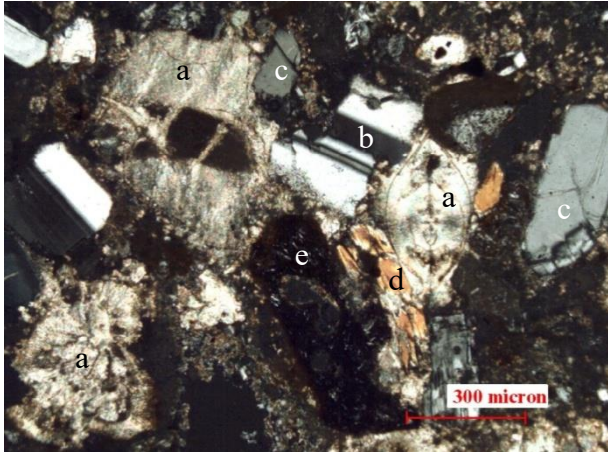


Figure 3.1.1. 19. Photomicrograph of PV FN 1 breccia sample (xpl, 10x): a. carbonate fragments; b. plagioclase; c. quartz, d. pyroxenes; e. volcanic fragment.

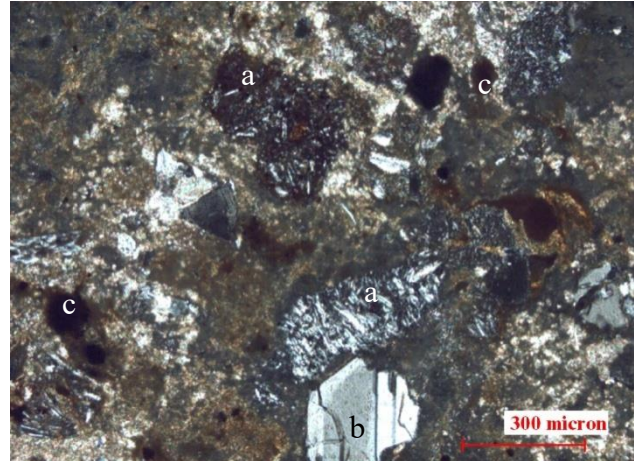


Figure 3.1.1. 20. Photomicrograph of PV FN 1 breccia sample (xpl, 10x), a. basalt/andesite fragments; b. altered plagioclase; presence of iron oxides.

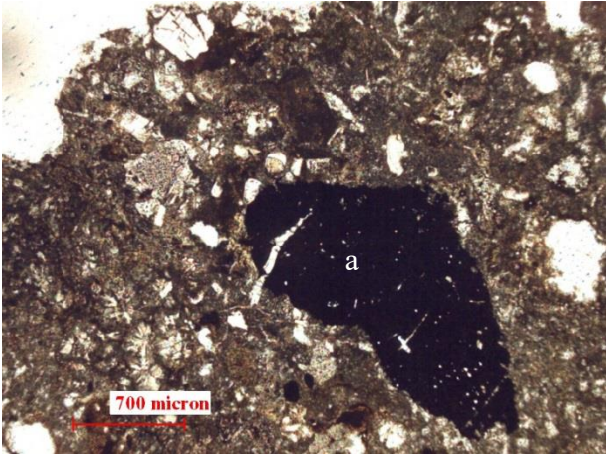


Figure 3.1.1. 21. Photomicrograph of PV FN 1 breccia sample (ppl, 4x). Particular of a probable glass fragment (a.).

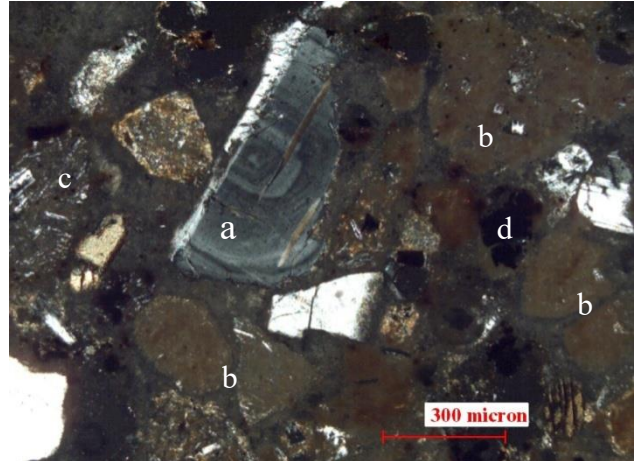


Figure 3.1.1. 22. Photomicrograph of PV FN 2 breccia sample (xpl, 10x), a. zoned plagioclase; b. rounded - subrounded carbonate fragments; c. basalt fragment and d. iron oxides.

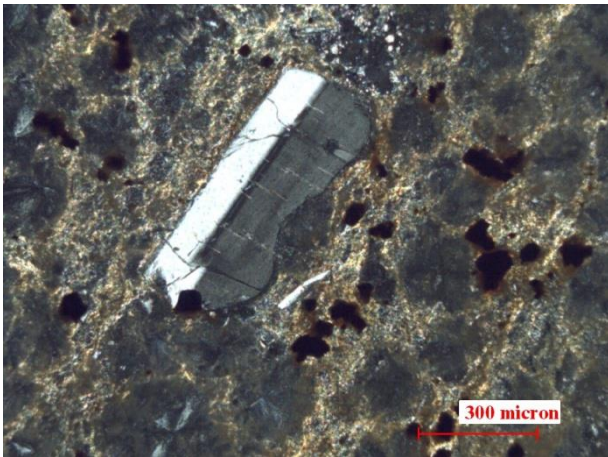


Figure 3.1.1. 23. Photomicrograph of PV FN 1 breccia sample (xpl, 10x) plagioclase surrounded by zeolites.

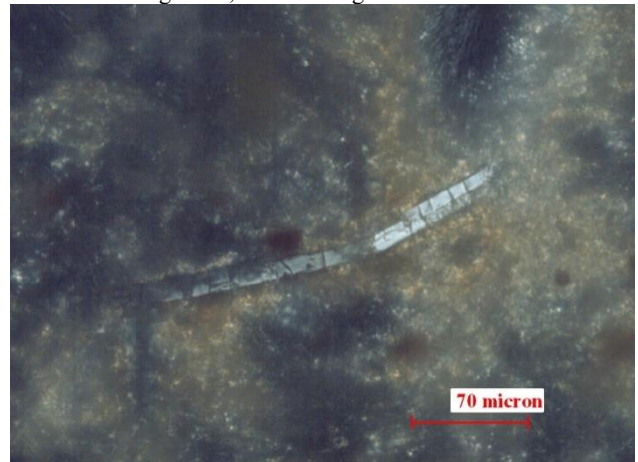


Figure 3.1.1. 24. Photomicrograph of FN 1 breccia sample (xpl, 40x), altered sanidine in the zeolitized part.

Taking into account the outcrops, PV Q 1 specimen, sampled near Casas Reales complex, it presented a structure predominantly attributable to volcanoclastic breccia, showing pyroxenes clusters (Fig. 3.1.1.25) and amygdales filled with secondary minerals due to hydrothermal phases (Fig. 3.1.1.26).

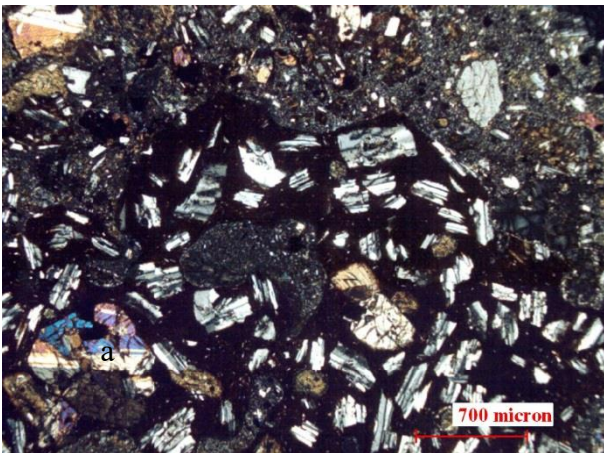


Figure 3.1.1. 25. Photomicrograph of PV Q1 breccia sample (xpl, 4x), particular of melting inclusion and presence of pyroxenes clusters (a).

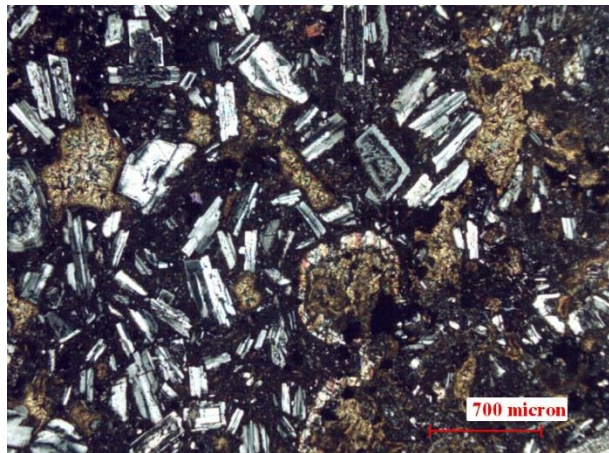


Figure 3.1.1. 26. Photomicrograph of PV Q1 breccia sample (xpl, 4x), amygdales.

### Basaltic Andesite

Whereas basaltic andesite have been observed at the *Fortín de la Natividad*, in samples PV FN 4 and PV FN 5 (Fig. 3.1.1.27). They show several melt inclusions, as amygdales filled with secondary minerals, due to hydrothermal activity (Fig. 3.1.1.28). Furthermore, PV FN 5 exhibits a glomeroporphyritic texture, with clusters of mafic minerals (pyroxenes) which reveal interaction with magma, showing dissolved parts (Figs. 3.1.1.29-30).

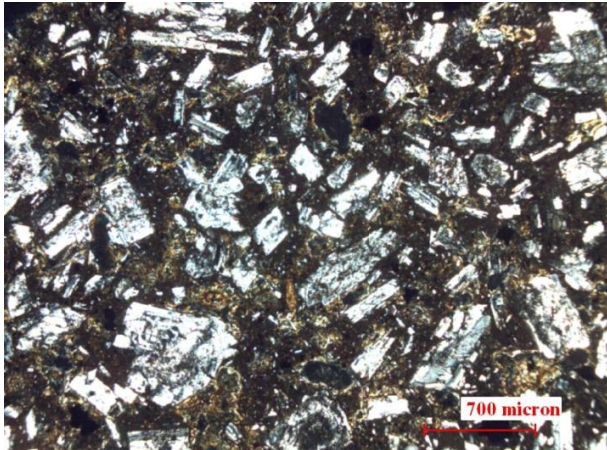


Figure 3.1.1. 27. Photomicrograph of PV FN 4 basaltic andesite sample (xpl, 4x).

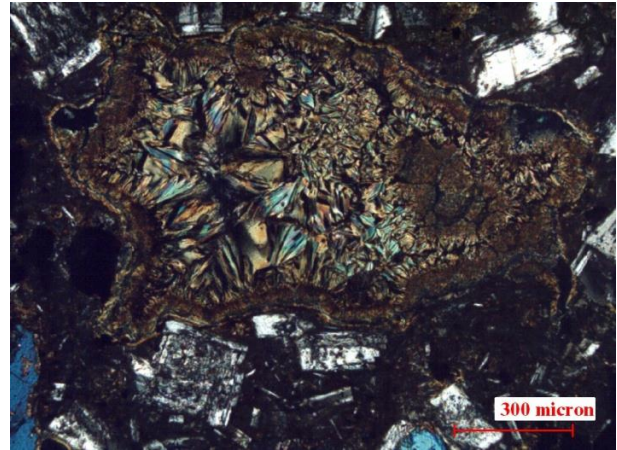


Figure 3.1.1. 28. Photomicrograph of PV FN 4 basaltic andesite sample (xpl, 10x), amygdales filled with secondary minerals.

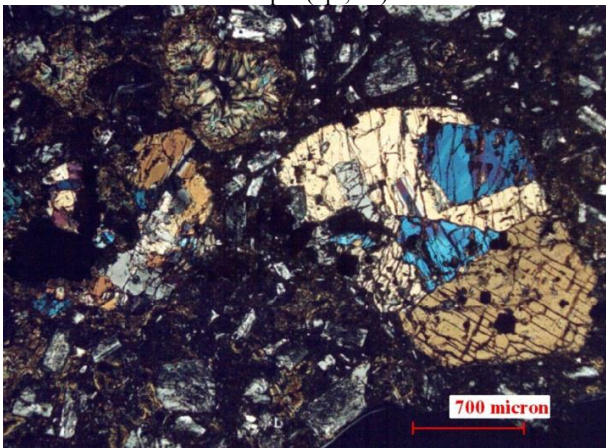


Figure 3.1.1. 29. Photomicrograph of PV FN 4 basaltic andesite sample (xpl) pyroxenes glomerocrysts and amygdales.

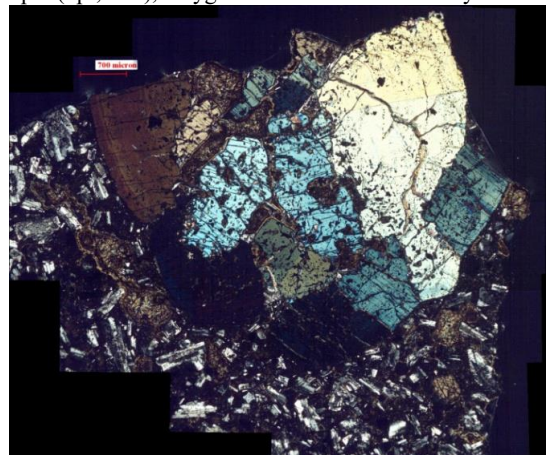


Figure 3.1.1. 30. Photomicrograph of PV FN 5 basaltic andesite sample (xpl), large pyroxenes glomerocryst showing a beginning of melting process.

In addition, basaltic andesite have been identified at two outcrops, one near *Casas Reales*, PV vic. CR sample, and the other one near the *Convento de Santo Domingo*, PV Q 2. They show an aspect similar to the previously observed ones, with the presence of zoned plagioclase (Figs. 3.1.1.31-32) and several amygdales, traces of hydrothermal activity.



Figure 3.1.1. 31. Photomicrograph of PV vic. CR basaltic andesite sample (xpl, 4x). Presence of zoned plagioclase.

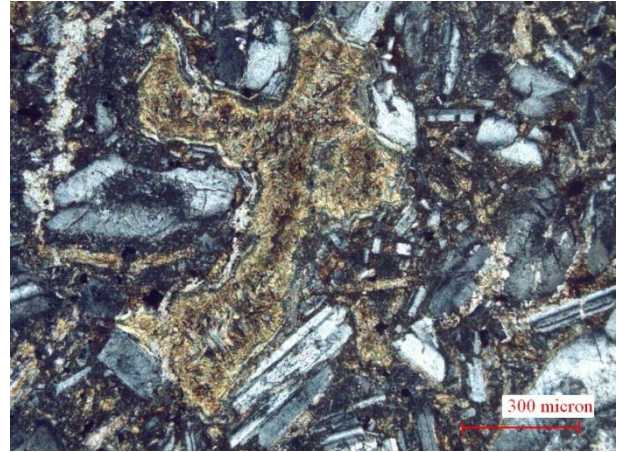


Figure 3.1.1. 32. Photomicrograph of PV Q 2 basaltic andesite sample (xpl, 10x). Particular of an amygdale.

### *Tuffite*

Considering the masonry of the *Torre de la Catedral*, tuffite was observed. In samples PV TC 3 and PV TC 4, presence of quartz, pomiceous/glass fragments, and also a great amount of different fossils (Fig.3.1.1.33), as foraminifera and echinoderms have been detected. It can be presumed that the rock underwent hydrothermal activity, demonstrated by the presence of zoned plagioclase and zeolitized areas (Fig.3.1.1.34).



Figure 3.1.1. 33. Photomicrograph of PV TC 4 tuffite sample (xpl, 4x), particular of foraminifera fossil.

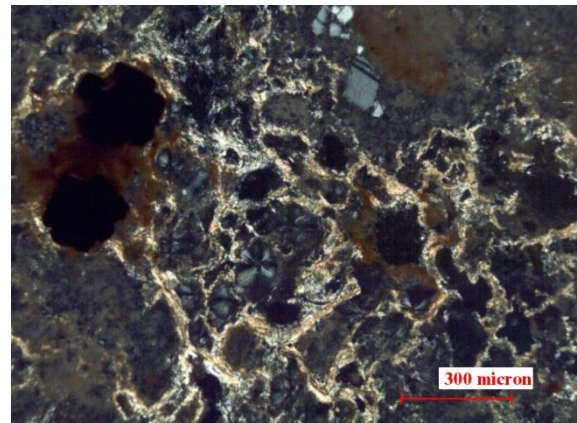


Figure 3.1.1. 34. Photomicrograph of PV TC 3 tuffite sample (xpl, 10x), zeolitized area.

### *Altered volcanic rock*

Samples PV FC 6 and PV FC 9 are altered volcanic rock, showing reddish areas due to iron oxides (Fig. 3.1.1.35). PV FC 6 present also two superficial layers: the inner one whitish and the external one, which exhibits a reddish hue, composed by iron oxides (Figs. 3.1.1.36-38). Although PV FC 9 present a coarser part ascribable to a superficial mortar layer (Fig. 3.1.1.39).



Figure 3.1.1. 35. Photomicrograph of PV FC 9 altered volcanic rock sample (xpl, 10x). Clearly evident a chalcedony crystal surrounded by iron oxides.

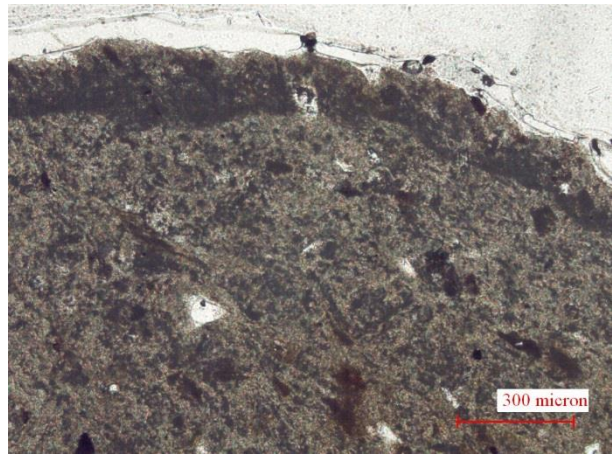


Figure 3.1.1. 36. Photomicrograph of PV FC 6 altered volcanic rock sample (ppl, 10x); particular of superficial whitish "patina".

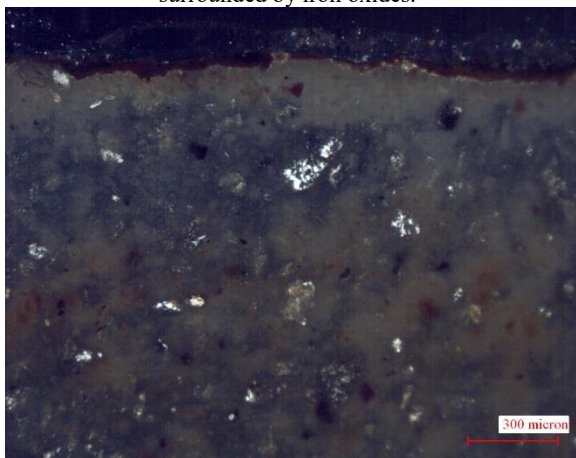


Figure 3.1.1. 37. Photomicrograph of PV FC 6 altered volcanic rock sample (xpl, 10x) Particular of the superficial reddish "patina".

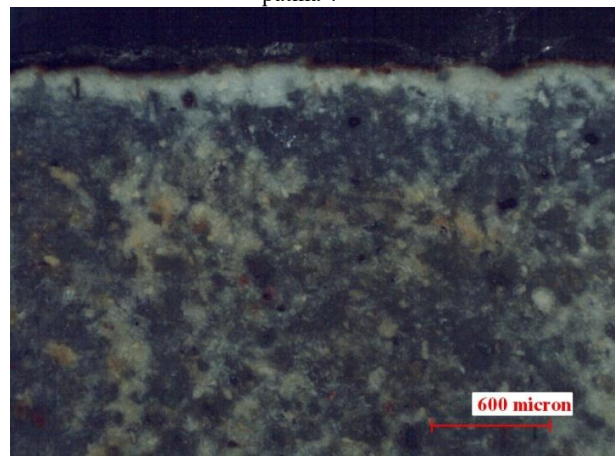


Figure 3.1.1. 38. Photomicrograph of PV FC 6 altered volcanic rock sample (10x), reflected light. Particular of the superficial "patina".

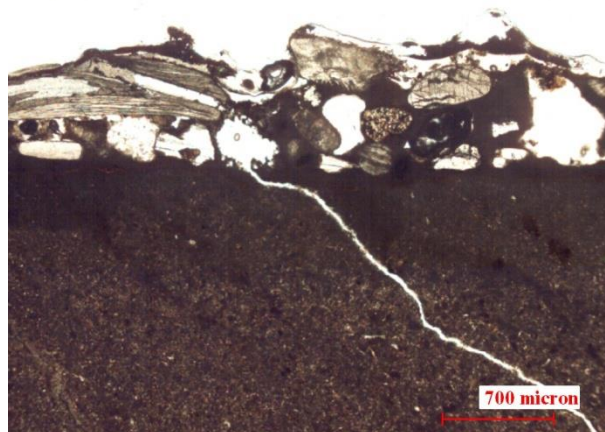


Figure 3.1.1. 39. Photomicrograph of PV FC 9 altered volcanic rock sample (ppl, 4x); particular of the superficial mortar layer.

Another altered volcanic rock was identified in PV SJdD sample, collected at the *Hospital de San Juan de Dios*. The similarity with samples PV FC 6 and PV FC 9, aforementioned, is highlighted also by the presence of iron hydroxides and oxides (Fig. 3.1.1.40), principally located in proximity of the external and internal surfaces. This latter one shows also a layer formed by calcite crystallization (Fig.3.1.1.41) and reddish superficial fragment of layer, ascribable to an organic pigment.

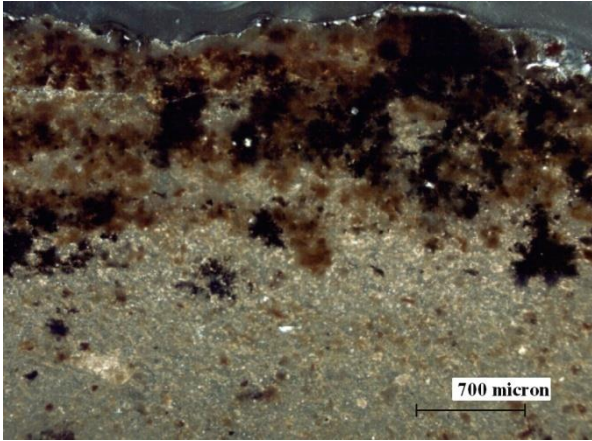


Figure 3.1.1. 40. Photomicrograph of PV SJdD altered volcanic rock sample (xpl, 4x); particular of the reddish external patina.

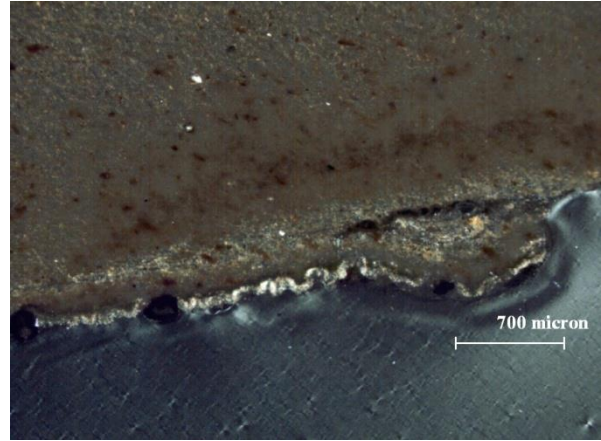


Figure 3.1.1. 41. Photomicrograph of PV SJdD altered volcanic rock sample (xpl, 4x); particular of the inner whitish patina.

### *Rhyolite*

Finally, the wall sampled near *Casa Terrin*, showed a stone completely different from the previous ones observed. Optical microscopy analysis on PV CT 1 and PV CT 2 samples revealed that this rock is a rhyolite, confirming the previous investigations carried out by Sanchez Nava (2000). The two specimens are principally composed by feldspars, specifically plagioclase and sanidine crystals (Fig.3.1.1.42). In addition, the rock shows a superficial chromatic alteration due to iron oxides and hydroxides (hematite and limonite). This phenomenon is present also in the core of the stone, but here it is concentrated in amygdales and, reaching the external part its presence increase in the rock matrix (Fig.3.1.1.43).

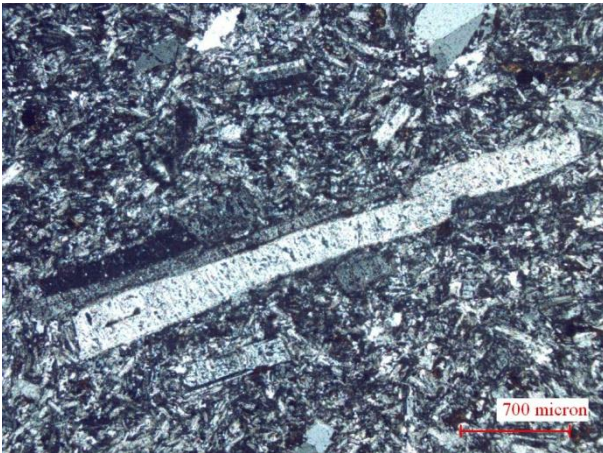


Figure 3.1.1. 42. Photomicrograph of PV CT 2 rhyolite sample (xpl, 4x). Particular of a sanidine crystal.

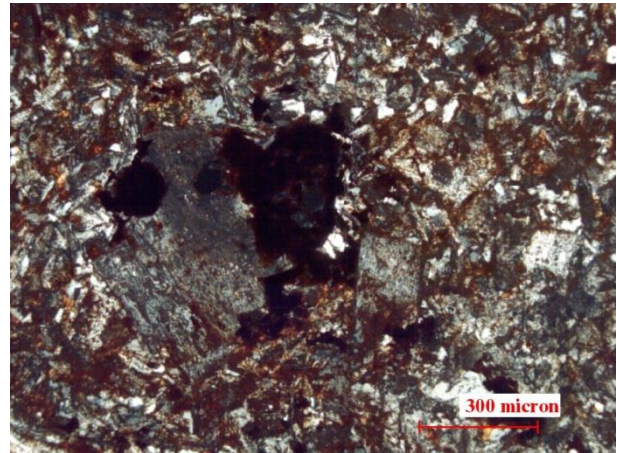


Figure 3.1.1. 43. Photomicrograph of PV CT 1 rhyolite sample (xpl, 10x). Plagioclase and iron oxides.

### Evaluation of the state of Conservation

In general, macroscopic observations revealed as main deterioration phenomena detachments, flaking, exfoliation phenomena, pulverization, presence of biomass on the surfaces, chromatic alterations. Microscopic analyses showed several inner alterations, which can be correlated with the aforementioned ones identified, as plagioclase and sanidine alteration, the presence of iron oxides or hydroxides, and porosity, which can be a point of stone weakness.

Generally, considering iron oxides or hydroxides, they have been observed concentrated in the external part of the stones (Figs. 3.1.1.44-45). According to Sanchez Nava (2000), these areas are supposed to undergo differential deterioration phenomena, since they show different physical-chemical features in comparison with the core. In any case, they represent an aesthetical damage.



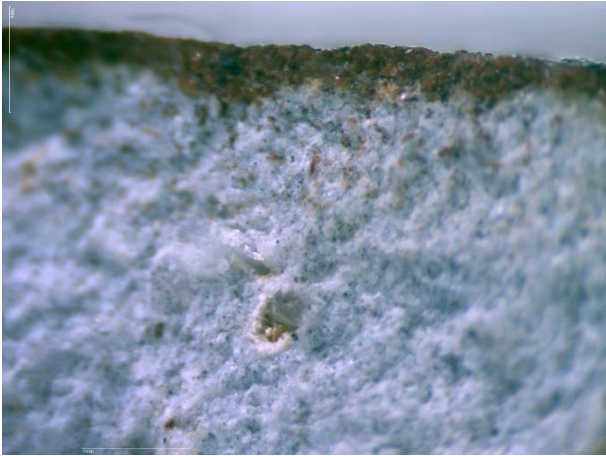


Figure 3.1.1. 44. Stereomicroscope micrograph of PV CT 2 rhyolite sample, showing the iron (hydr)oxides concentrated on the external surface.

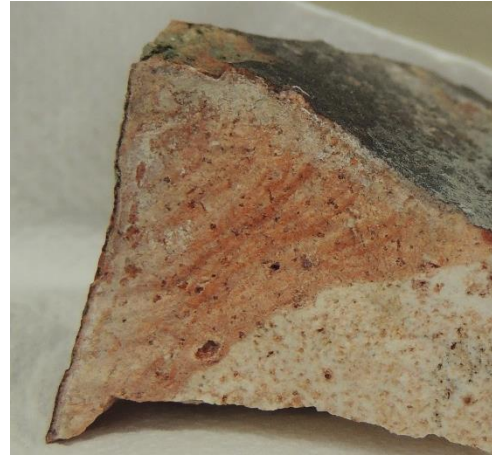


Figure 3.1.1. 45. Macrograph of PV CT 1 rhyolite sample. The increasing of iron (hydr)oxides near the external surfaces is clearly visible.

A special mention has to be given to the zeolitization process. This phenomenon is largely spread in the whole archaeological site. Specifically, it is shown in the following samples of volcanoclastic stones: *Fortino de la Natividad* in PV FN 1, *Convento de San Francisco* in PV FC 4, PV FC 8, PV FC 11, *Convento de la Concepción de las Monjas* in PV CC 4, in both samples of Torre de la Catedral PV TC 3 and PV TC 4, *Convento de la Compañía de Jesus* PV JC 2 and PV JC 4 and *Casas Reales* PV CR 4. Analysis revealed that zeolitized areas are concentrated both on the external and internal parts, these latter ones with a depth within tens of millimetres. In order to study deeper these areas, samples underwent also SEM-EDX analyses, described in sub-chapter 3.3. They can be affected by the humidity cycles, contributing to cause the macroscopic phenomena observed such as cracks, flaking, etc. (Figs. 3.1.1.46-47)

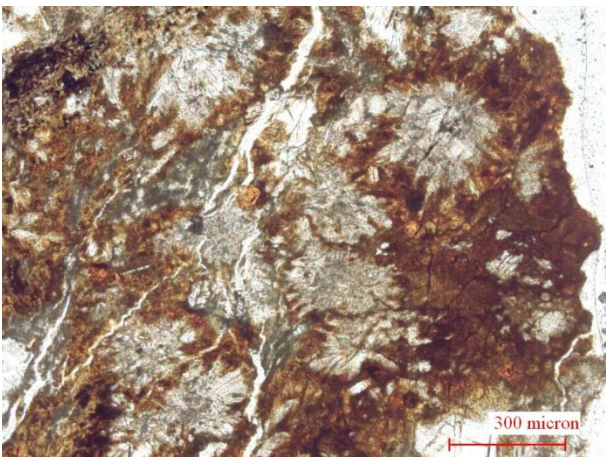


Figure 3.1.1. 46. Photomicrograph of PV JC 4 breccia sample (ppl, 10x). Particular of a zeolitized part showing several cracks.



Figure 3.1.1. 47. Photomicrograph of PV TC 4 tuffite sample (ppl, 4x). Cracks presence in proximity of a zeolitized area.

### 3.1.2. Portobelo and San Lorenzo

#### Material characterization

Considering the Caribbean Fortifications, eighteen samples have been selected from Portobelo Fortresses masonries (plus two samples of salt encrustations) and four from Fort San Lorenzo masonries, for being investigated through optical microscopy. In addition, four samples from outcrops have been analysed with the same technique, respectively one sample from Fort San Fernando and three belonging to Fort San Lorenzo area (table).

Table 3.1.2. 1. List of samples belonging to Portobelo and San Lorenzo and their related provenance and lithotypes analysed through PLM observations of thin sections.

<b>Monuments</b>	<b>Samples</b>	<b>Lithotype</b>
<i>Fort San Jeronimo</i>	PB FSJ 1, PB FSJ 7	Coral boundstone
	PB FSJ 4, PB FSJ 8	Sandstone
<i>Fort Santiago</i>	PB FdS 2, PB FdS 5, PB FdS 9	Sandstone
	PB FdS 6, PB FdS 8	Coral boundstone
	PB FdS 10	Tuffite
	PB FdS 3	Salt encrustation
<i>Fort San Fernando</i>	PB SF 1	Grainstone/packstone
	PB SF 2, PB SF 8,	Coral boundstone
	PB SF 6, PB SF 7, PB SF rampa	Basaltic andesite/andesite
	PB SF 5	Salt encrustation
<i>Fort San Lorenzo</i>	SL 4, SL 6, SL 9	Tuffite
	SL 8	Grainstone
<b>Outcrops location</b>	<b>Samples</b>	
Near <i>Fort San Fernando</i>	PB SF 11	Basaltic andesite
Near <i>Fort San Lorenzo</i>	SL 1, SL 2	Sandstone/tuffite
	SL 13	Grainstone

Thin sections observation of these specimens is described in the following paragraph, dividing them according to the diverse lithotypes.

#### *Sandstone*

This lithotype has been identified at Portobelo, specifically at Fort San Jeronimo (PB FSJ 4 and PB FSJ 8 sample), Fort de Santiago (PB FdS 2, PB FdS 5 and PB FdS 9).

Observing in detail the specimens, PB FSJ 4 sample is a yellow fine sandstone, with carbonate cement. Grains show a quite good sorting, ranging from 60 microns to 200 microns, with mainly angular shapes, formed by the following minerals listed in order of abundance: quartz, plagioclase and scarce micas (Fig.3.1.2.1). The grains volume % estimation is between 35 and 50%. In addition, several metal oxides, showing rounded shapes, have been detected. Furthermore numerous fossils (brachiopods, foraminifera, algae) are present (Fig.3.1.2.2), having dimensions until thousands micron; some of them show neomorphism. Samples show in general a scarce porosity.

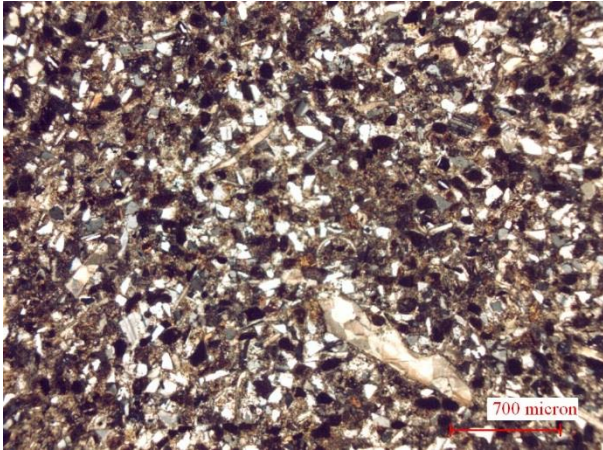


Figure 3.1.2. 1. Photomicrograph of PB SFJ 4 sandstone sample (ppl, 4x).



Figure 3.1.2. 2. Photomicrograph of PB SFJ 4 sandstone sample (ppl, 40x). Particular of globigerina filled by metal oxides.

Even PB FSJ 8 sample is a yellow fine sandstone, with scarce carbonate cement (grains volume estimation about 50%), well sorted, with grains ranging from 50 to 150 microns, both angular and rounded shapes (Fig. 3.1.2.3). The first ones are formed by the following minerals, listed in order of abundance: quartz, plagioclases, pyroxenes and micas, while the rounded shapes, are due to metal oxides.

Several fossils are present (foraminifera, algae), showing sizes similar to the aforementioned grains, to macrofossils having centimetric dimensions (brachiopods), and occasionally showing neomorphism (Fig. 3.1.2.4). Scarce porosity.

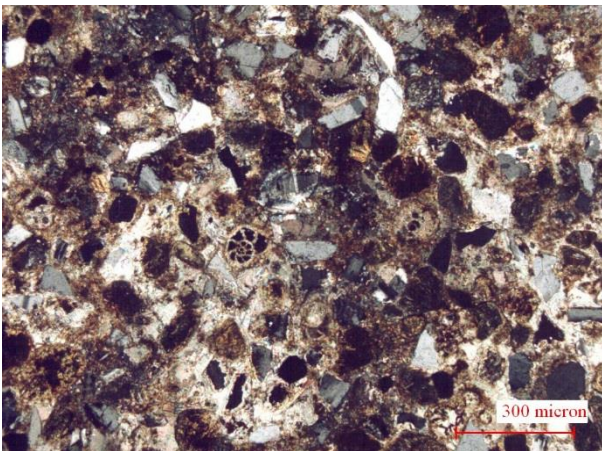


Figure 3.1.2. 3. Photomicrograph of PB SFJ 8 sandstone sample (xpl, 10x).

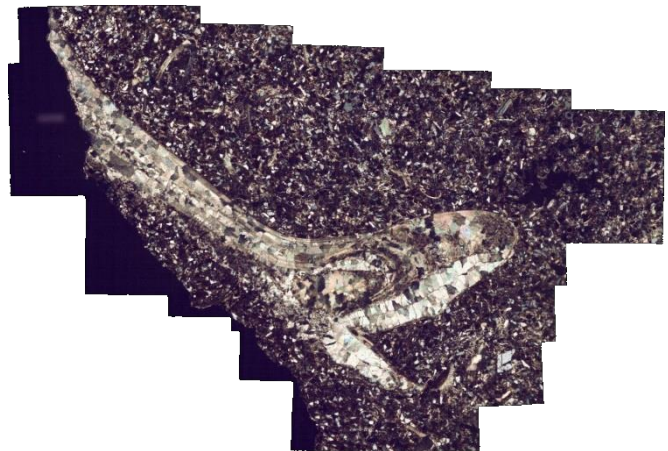


Figure 3.1.2. 4. Photomicrograph of PB SFJ 8 sandstone sample (xpl, 4x). Particular of a macrofossil presenting neomorphism.

While, considering samples belonging to *Fuerte de Santiago*, they are all yellow fine calcite cemented sandstone, with grains ranging from tens to hundreds of microns, and formed mainly by angular crystals of quartz and plagioclases, followed by micas and rare pyroxenes; scarce porosity. They show several bioclasts, as bivalves, showing neomorphism in particular in PB FdS 5 sample, algae, foraminifera and corals. In addition, in PB FdS 5 and PB FdS 9 samples rounded grains of metal oxides have been detected (Fig. 3.1.2.5-10).

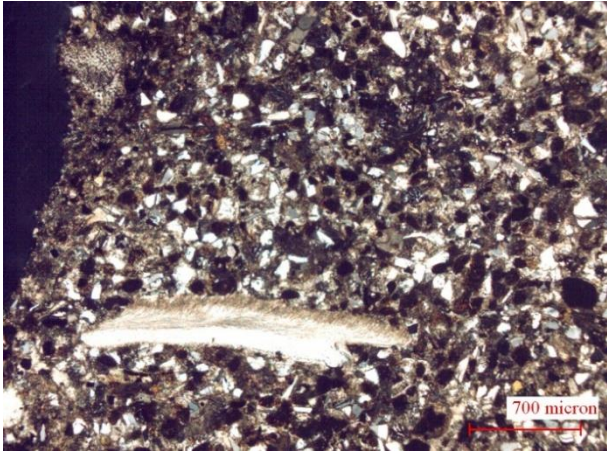


Figure 3.1.2. 5. Photomicrograph of PB FdS 2 sandstone sample (xpl, 4x).

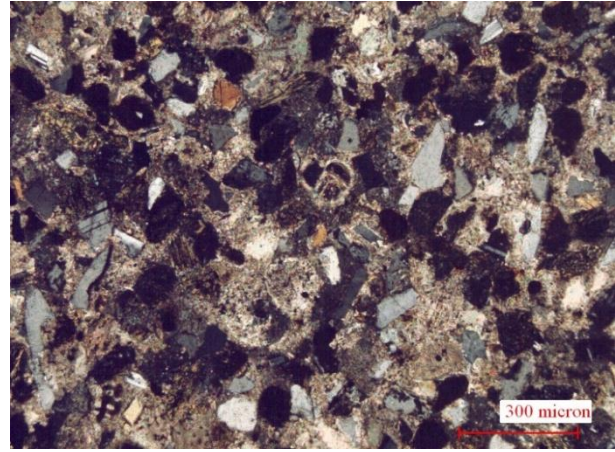


Figure 3.1.2. 6. Photomicrograph of PB FdS 2 sandstone sample (xpl, 10x).

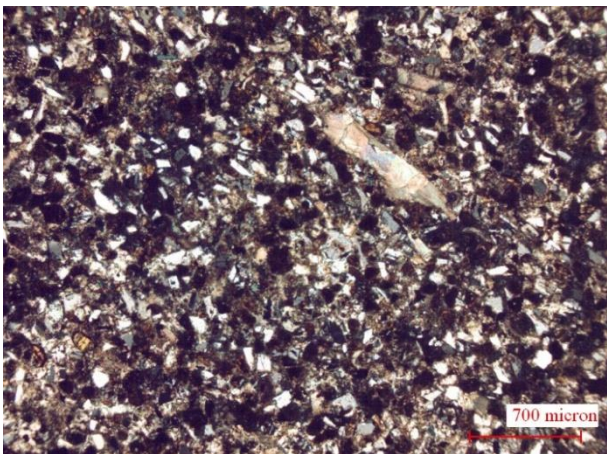


Figure 3.1.2. 7. Photomicrograph of PB FdS 5 sandstone sample (xpl, 4x).

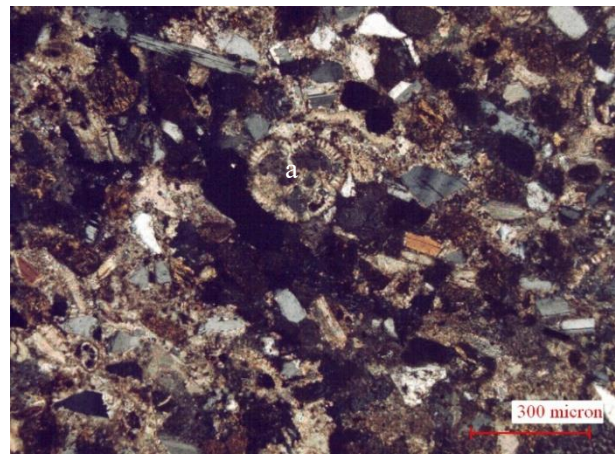


Figure 3.1.2. 8. Photomicrograph of PB FdS 5 sandstone sample (xpl, 10x). a. particular of a globigerina.

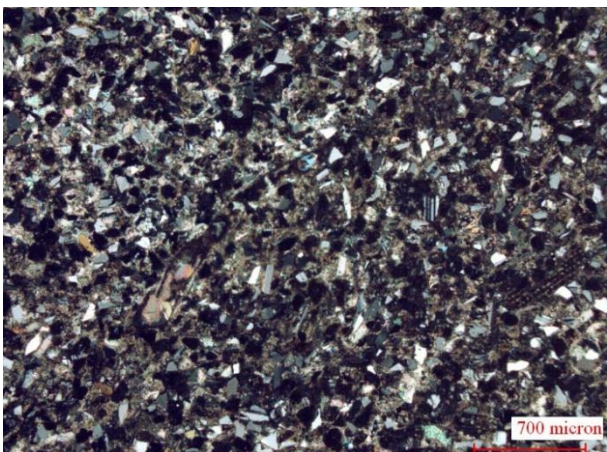


Figure 3.1.2. 9. Photomicrograph of PB FdS 9 sandstone sample (xpl, 4x).

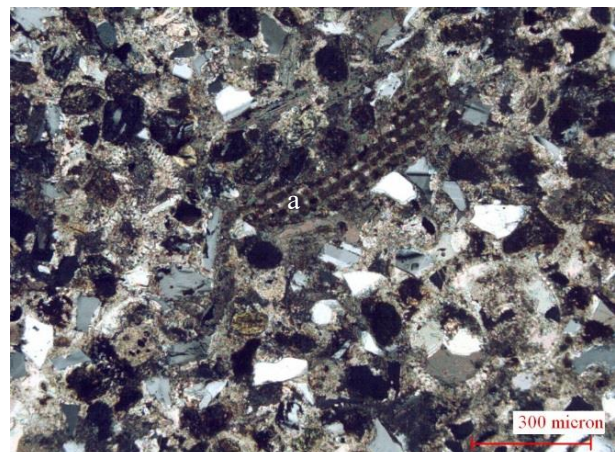


Figure 3.1.2. 10. Photomicrograph of PB FdS 9 sandstone sample (xpl, 10x). a. particular of a coral fragment.

### *Tuffite*

Tuffites showing granulometry between sandstone until grainstone has been observed at *Fuerte de Santiago*, in PB FdS 10 sample, and also at *Fuerte San Lorenzo*, in SL 1, SL 2, SL 4, SL 6 and SL 9 samples.

In particular, PB FdS 10 is rich in bioclasts (as bivalves, corals, algae, foraminifera, echinoderms), sub-angular grains of quartz, plagioclase, pyroxenes, measuring hundreds microns (100-500

microns), moderately/poorly sorted, so showing parts more ascribable to a grainstone (Figs. 3.1.2.11-12).

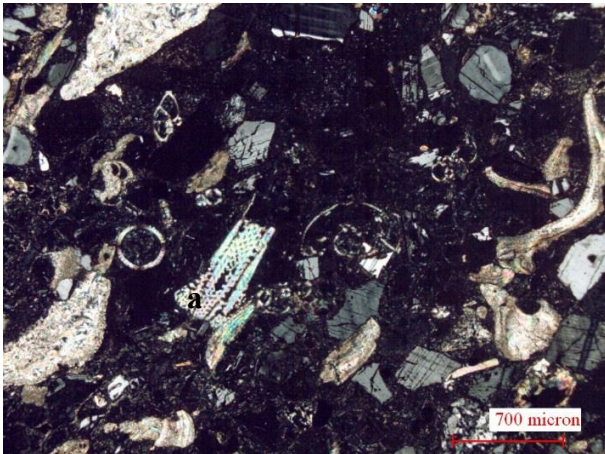


Figure 3.1.2. 11. Photomicrograph of PB FdS 10 tuffite sample (xpl, 4x), particular of the cineritic matrix and the bioclasts (a. coral fragment).



Figure 3.1.2. 12. Photomicrograph of PB FdS 10 tuffite sample (xpl, 10x), particular of the cineritic matrix and the bioclasts (a. globigerina; b. amphistegina).

While samples belonging to *Fuerte San Lorenzo* present a sandstone grain-size distribution. Moreover, SL 1 sample was formed by an external and an internal part, this latter one showing higher hardness. In particular, SL 1 sample (external part) shows angular grains of quartz, plagioclase, and several bioclasts, as foraminifera (Fig. 3.1.2.13). Within several of them, it is noticeable the presence of metal oxides, probably ascribable to sulphurs (Fig. 3.1.2.14). In addition, there is the presence of volcanic clasts and glass, showing angular shapes.

Considering the inner part of SL 1, it also shows angular grains of quartz, plagioclase (sometimes underwent argillation), pyroxene (showing an alteration rim), amphibole, olivine and other mafic minerals not identifiable since highly altered, and several bioclasts, as foraminifera and echinoids (Fig. 3.1.2.15). Within several of them, it is noticeable the presence of metal oxides, probably ascribable to sulphurs. In addition, there is the presence of volcanic ash having diffused cracks (Fig.3.1.1.16).

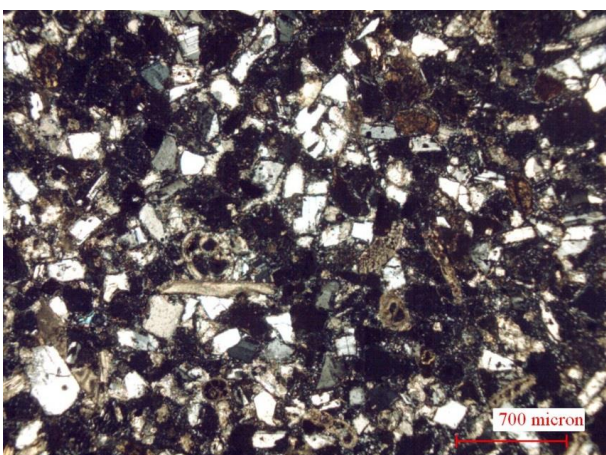


Figure 3.1.2. 13. Photomicrograph of SL 1 sandstone/tuffite sample (external part) (xpl, 4x).

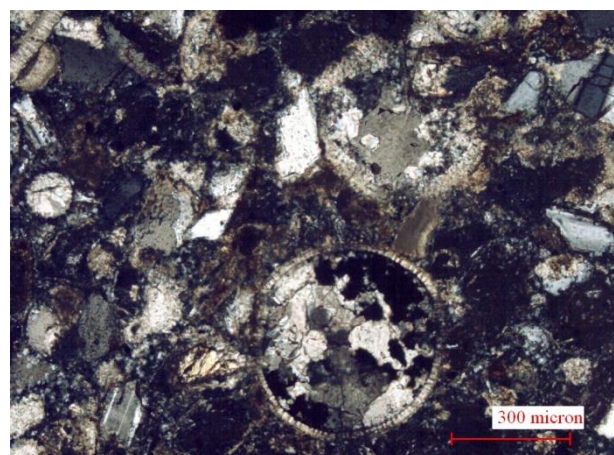


Figure 3.1.2. 14. Photomicrograph of SL 1 sandstone/tuffite sample (external part) (xpl, 10x). Presence of metal oxides within a bioclast.

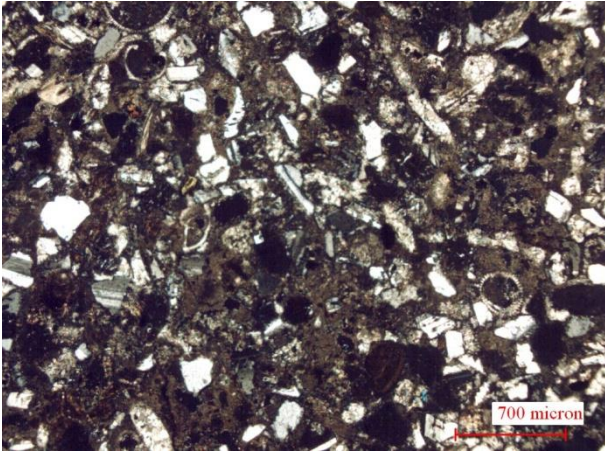


Figure 3.1.2. 15. Photomicrograph of SL 1 sandstone/tuffite sample (internal part) (xpl, 4x).

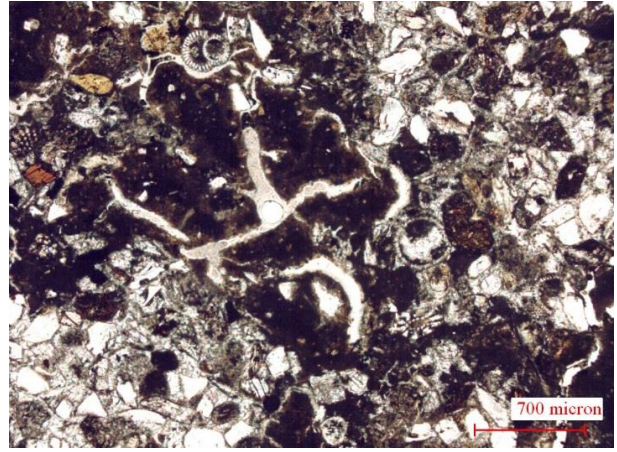


Figure 3.1.2. 16. Photomicrograph of SL 1 sandstone/tuffite sample (internal part) (ppl, 4x). Volcanic ash showing cracks.

SL 2 sample is similar to the previous ones, also presenting volcanic ash with diffused cracks (Fig.3.1.2.17), but having a coarser aggregate and numerous bioclasts filled with sulphurs and metal oxides (Figs. 3.1.2.18). It also show a better preservation state than the previously observed.

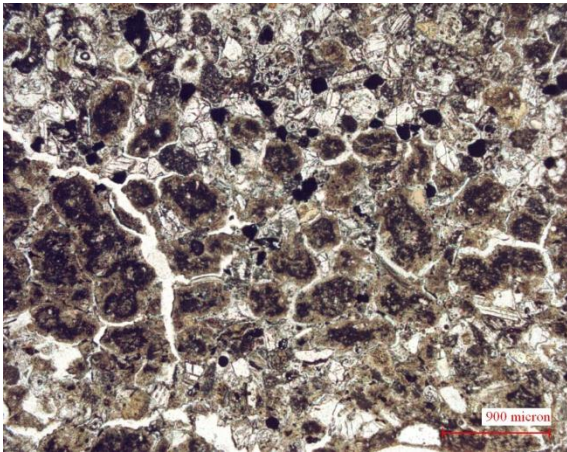


Figure 3.1.2. 17. Photomicrograph of SL 2 sandstone/tuffite sample (xpl, 4x) Volcanic ash showing cracks.



Figure 3.1.2. 18. Photomicrograph of SL 2 sandstone/tuffite sample (xpl, 10x). Particular of the bioclasts present in the sample (a. brachiopod spine; b. gastropod) filled with silicates.

SL 4 sample is a tuffite with a silicate component mainly due to quartz and plagioclase grains and basalt/andesite fragments; in addition, bioclasts as bryozoan and foraminifera have been identified (Figs.3.1.2.19-20). Several bioclasts are filled with silicate minerals.

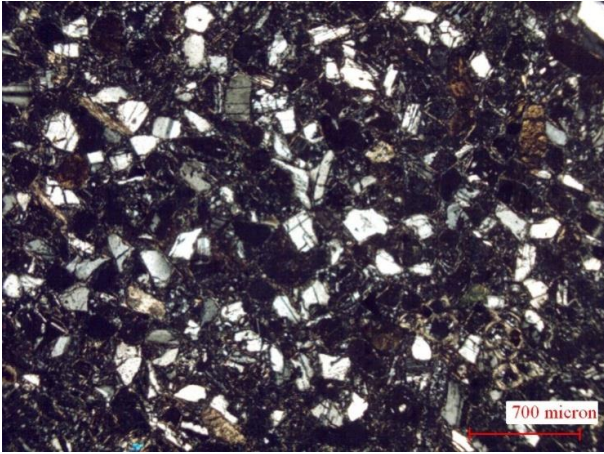


Figure 3.1.2. 19. Photomicrograph of SL 4 tuffite sample (xpl, 4x).

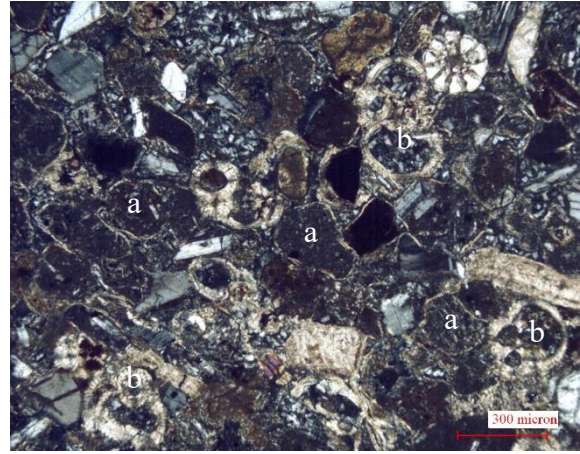


Figure 3.1.2. 20. Photomicrograph of SL 4 tuffite sample (xpl, 10x). a. basalt/andesite fragments; b foraminifera fragments filled with silicates.

Considering SL 6 sample, effusive rocks clasts and fossils, as foraminifera, gastropods and echinoderms, form it (Fig.3.1.2.21). Moreover, fossils present a re-crystallization of calcite on the external part, index of the magmatic erosion/action (Fig.3.1.2.22). The groundmass is rich of volcanic glass.

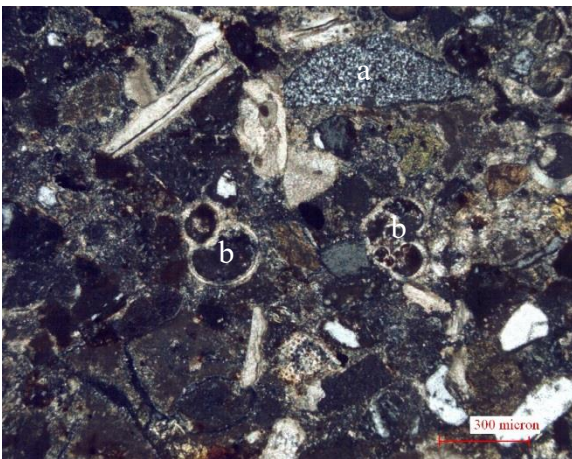


Figure 3.1.2. 21. Photomicrograph of SL 6 tuffite sample (xpl, 10x). a. volcanic rock fragment; b. foraminifera fragments.

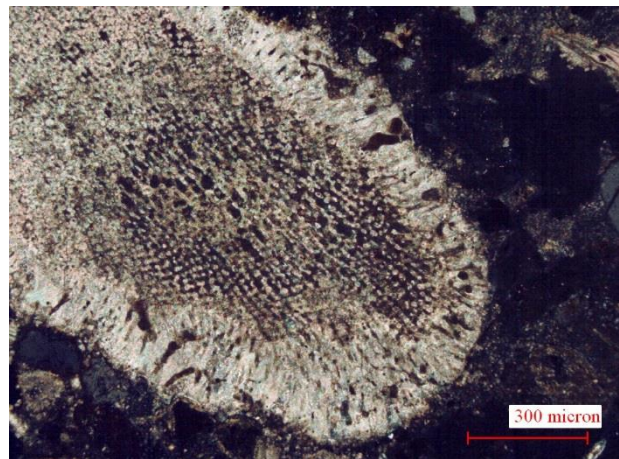


Figure 3.1.2. 22. Photomicrograph of SL 6 tuffite sample (xpl, 10x). Particular of a coral showing a re-crystallization of calcite on the external part.

Finally, SL 9 tuffite is highly deteriorated, showing cracks and exfoliations phenomena (Fig.3.1.2.23). The granulometry of the volcanic part is finer than the marine-sedimentary one (Fig.3.1.2.24). Fragments of volcanic glass are observed. Moreover, it shows a high decohesion, evident in Fig. 3.1.2.23.

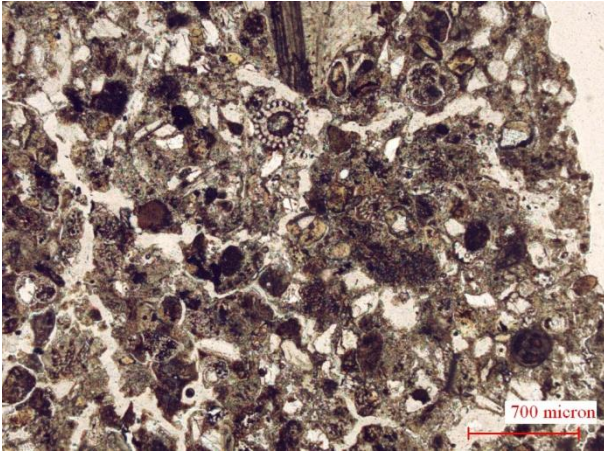


Figure 3.1.2. 23. Photomicrograph of SL 9 tuffite sample (ppl, 4x). Diffused cracks are clearly visible.

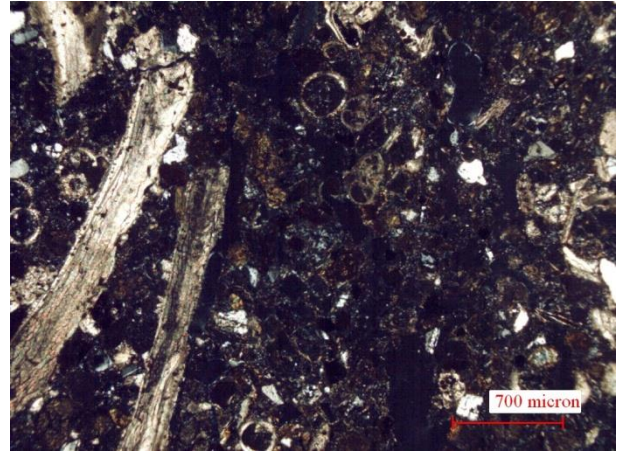


Figure 3.1.2. 24. Photomicrograph of SL 9 tuffite sample (xpl, 4x). Different granulometry between the bioclasts and the volcanic part.

### *Coral boundstone*

Coral boundstones have been largely observed in the masonries belonging to all the fortresses at Portobelo.

Specifically, at *Fuerte San Jeronimo*, PB FSJ 1 and PB FSJ 7 samples have been characterized as coral boundstones. In particular, in PB FSJ 1 the external surface was covered by a lime mortar, showing also a biological patina (Fig.3.1.2.25). It can be observed an evident presence of calcite crystallization in the interface between the mortar and the substrate (Fig.3.1.2.26). In addition, it is detectable a substantial intragranular porosity (Fig.3.1.2.27).

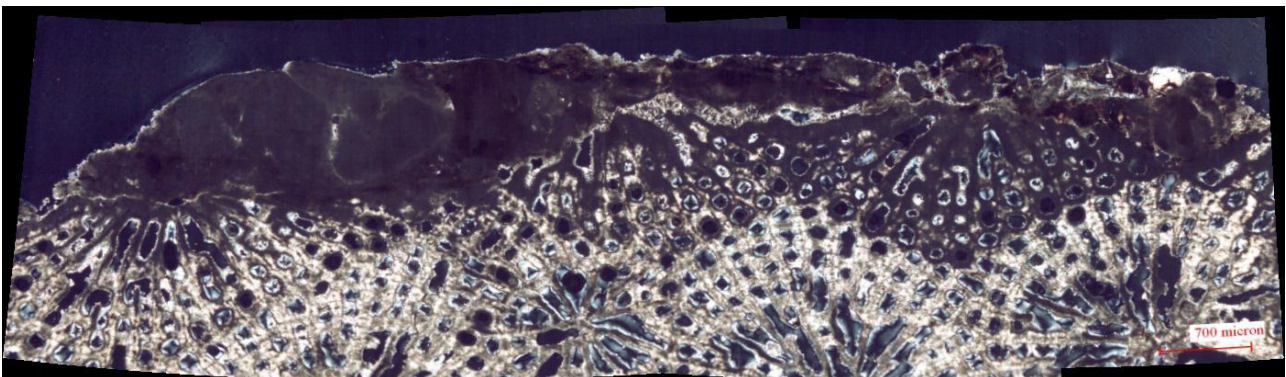


Figure 3.1.2. 25. Photomicrograph of PB FSJ 1 coral boundstone sample (xpl, 4x).



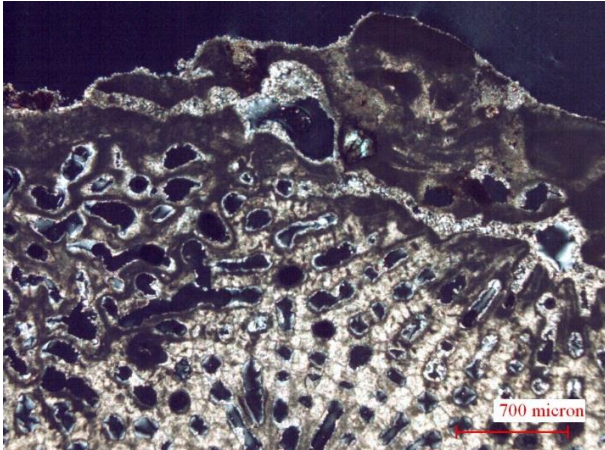


Figure 3.1.2. 26. Photomicrograph of PB FSJ 1 coral boundstone sample (xpl, 4x). Particular of the biological patina.

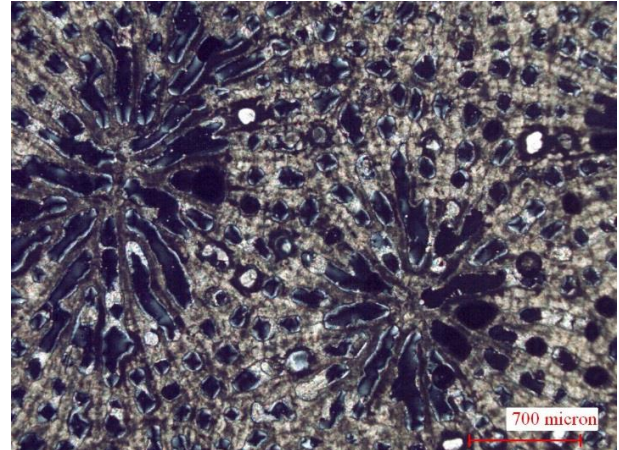


Figure 3.1.2. 27. Photomicrograph of PB FSJ 1 coral boundstone sample (xpl, 4x). Particular of the porosity.

On the external surface PB FSJ 7 sample shows a layer of mortar, with abundant lime binder and scarce carbonate aggregate. It is also characterized by intragranular porosity (Fig. 3.1.2.28).

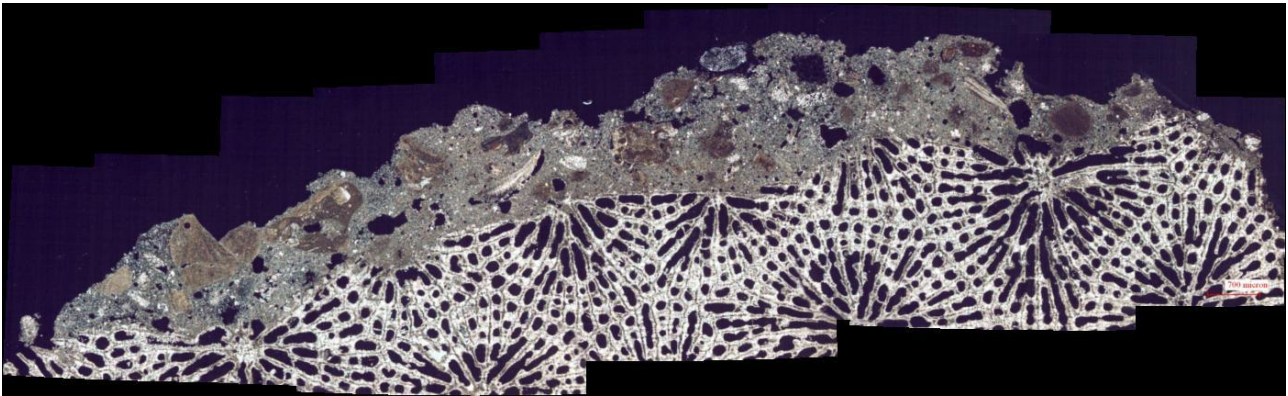


Figure 3.1.2. 28. Photomicrograph of PB FSJ 7 coral boundstone sample (xpl, 4x). Particular of the structure and the mortar layer.

At *Fuerte de Santiago*, PB FdS 6 shows a partial calcite crystallization within the pores of the structure (Fig. 3.1.2.29). In addition, remains of embedding mortar can be observed (Fig.3.1.2.30).

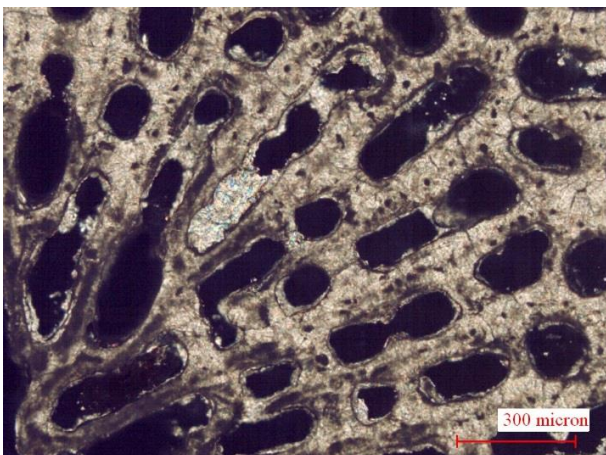


Figure 3.1.2. 29. Photomicrograph of PB FdS 6 coral boundstone sample (xpl, 10x) calcite re-crystallization within the pores of the structure.

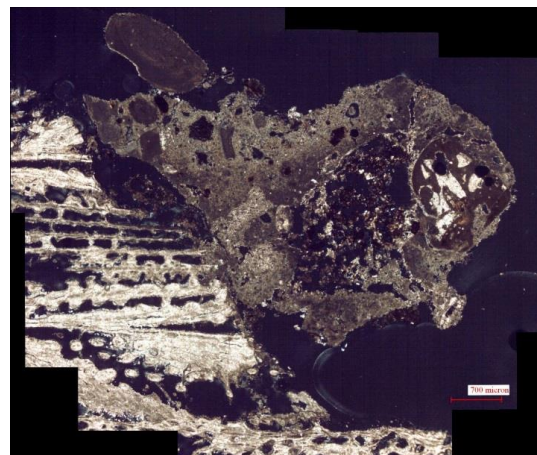


Figure 3.1.2. 30. Photomicrograph of PB FdS 6 coral boundstone sample (xpl, 4x), mortar remains.

Even PB FdS 8 sample presents a partial calcite crystallization within the pores of the structure (Fig. 3.1.2.31), moreover the external side show a biological patina (Fig. 3.1.2.32).

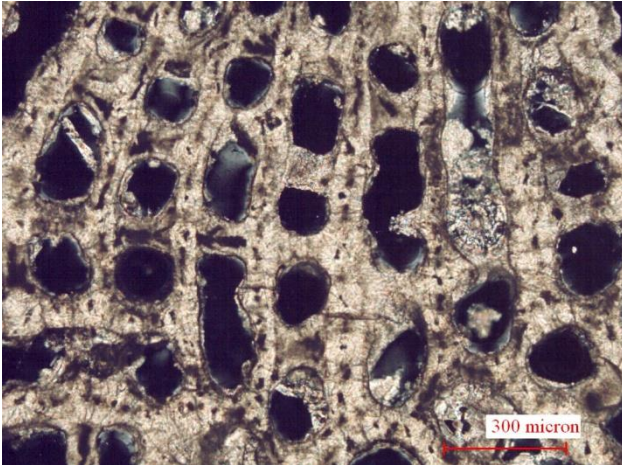


Figure 3.1.2. 31. Photomicrograph of PB FdS 8 coral boundstone sample (xpl, 10x) calcite crystallization within the pores of the structure.

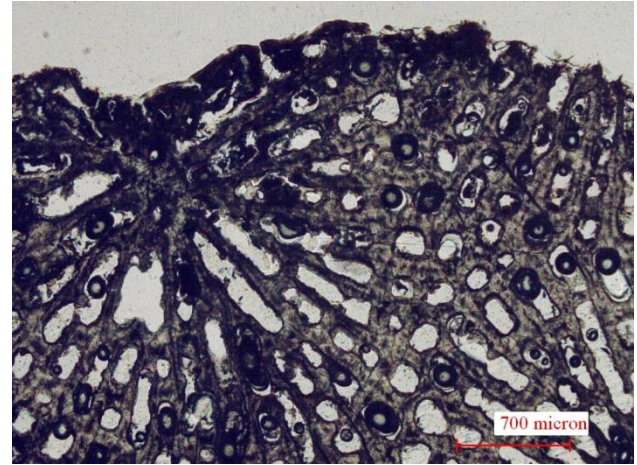


Figure 3.1.2. 32. Photomicrograph of PB FdS 8 coral boundstone sample (xpl, 4x), biological patina.

At *Fuerte San Fernando* PB SF 2 and PB SF 8 are coral boundstones, in particular SB SF 8 is a meandrina coral boundstone. They both show partial calcite crystallization within pores (Figs. 3.1.2.33-34) and diffused intragranular porosity (Figs.3.1.2.35-36).

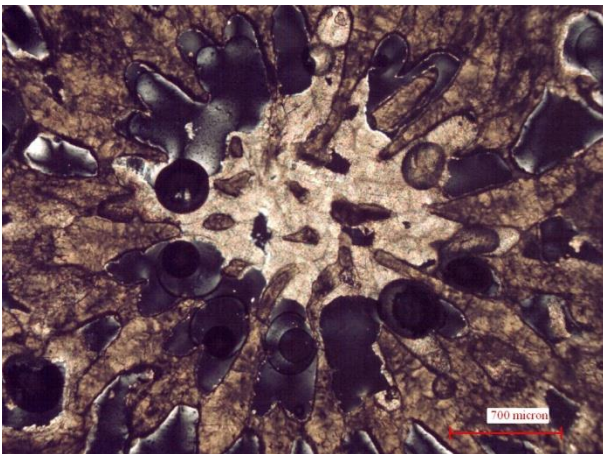


Figure 3.1.2. 33. Photomicrograph of PB SF 2 coral boundstone sample (xpl, 4x). Particular of calcite crystallization within the pores.



Figure 3.1.2. 34. Photomicrograph of PB SF 8 coral boundstone sample (xpl, 4x). Particular of calcite crystallization within the pores.



Figure 3.1.2. 35. Photomicrograph of PB SF 2 coral boundstone sample (xpl, 4x). Particular of the porosity.

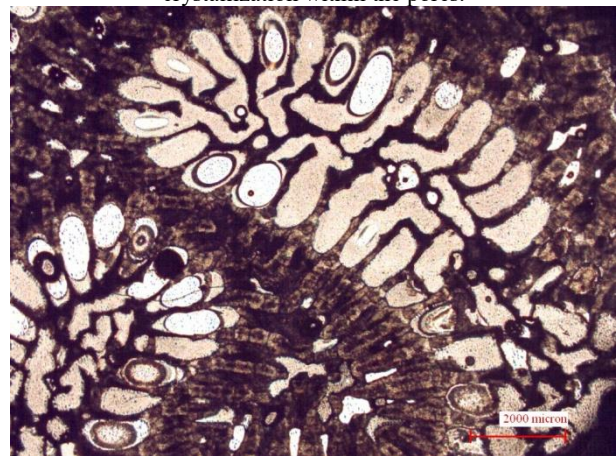


Figure 3.1.2. 36. Photomicrograph of PB SF 8 coral boundstone sample (xpl, 4x). Particular of the porosity.

### Grainstone/Packstone

Grainstone and Packstone (Dunham, 1962) have been detected at Fuerte San Lorenzo and Fuerte San Fernando. In particular, at Fuerte San Lorenzo in SL 8 sample, belonging to the masonry. It is a grainstone, showing also a packstone part, with bryozoans, echinoderms, bivalves and plankton foraminifera (Fig.3.1.2.37). Rich in manganese oxides and presenting high intragranular and intergranular porosity. Volcanic ejecta are also identified (Fig.3.1.2.38).



Figure 3.1.2. 37. Photomicrograph of SL 8 grainstone sample (ppl, 4x). a. Bryozoan fragment.

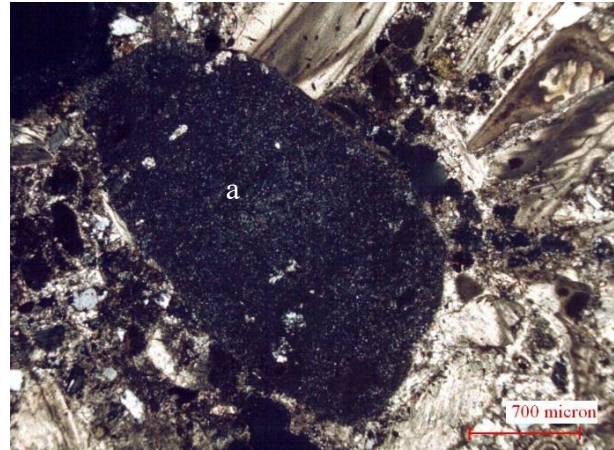


Figure 3.1.2. 38. Photomicrograph of SL 8 grainstone sample (xpl, 4x). a. Volcanic ejecta fragment.

Considering SL 13 sample, it was collected in an outcrop near *Fuerte San Lorenzo* and it showed the same structure of SL 8 sample. This grainstone is mainly formed by an association of bryozoans, echinoids, showing a preliminary diagenesis phase due to the presence of cement surrounding the echinoderm fragments (Figs.3.1.2.38-39). There are also fragments of bivalves not clearly identifiable. Extended porosity, both intragranular and itergranular.

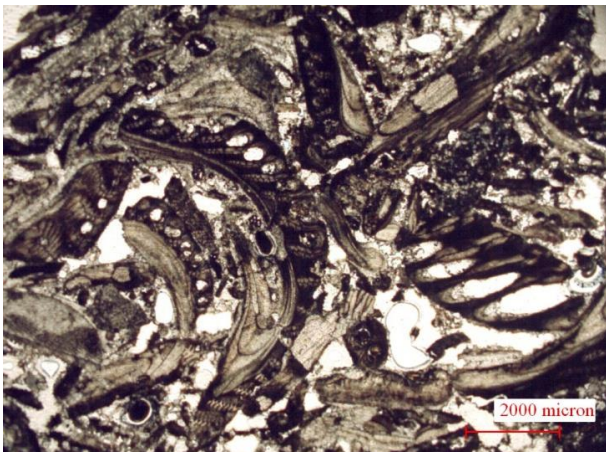


Figure 3.1.2. 39. Photomicrograph of SL 13 grainstone sample (ppl, 4x). Bryozoan fragments.

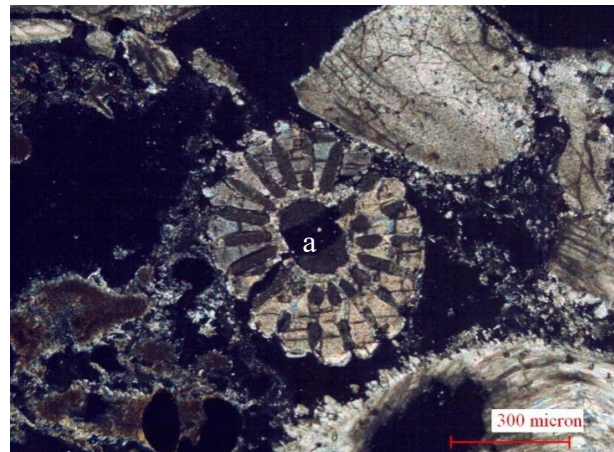


Figure 3.1.2. 40. Photomicrograph of SL 13 grainstone sample (xpl, 4x). a. Echinoid fragment.

Finally, considering PB SF 1 sample, belonging to the masonry of *Fuerte San Fernando*, it shows a texture from grainstone to packstone, mainly characterized by bryozoans, bivalves echinoids, rare coral fragments and planktonic foraminifera (Figs. 3.1.2.41-42). Several manganese oxides are present and diffused porosity was observed, both intragranular and itergranular.

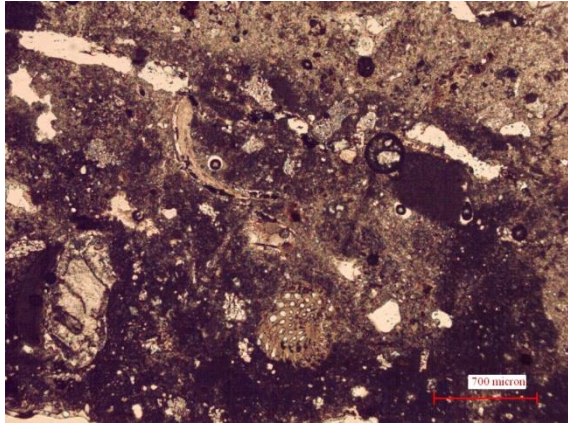


Figure 3.1.2. 41. Photomicrograph of PB SF 1 grainstone/packstone sample (xpl, 4x), particular of the packstone part.



Figure 3.1.2. 42. Photomicrograph of PB SF 1 grainstone/packstone sample (xpl, 4x), particular of the grainstone part. a. Bryozoans; b. Echinoids.

### *Basaltic Andesite*

Igneous rocks were observed at *Fuerte San Fernando*. In particular, in the samples belonging to the masonries of the Upper Battery PB SF 6 and PB SF 7 and PB SF 11 sample, belonging to the outcrop present next to the entrance of the Lower Battery. PLM observations carried out on the three samples, revealed mainly plagioclases, often in sericitization, followed by pyroxenes as phenocrysts and amygdales filled with zeolites (Figs. 3.1.2.43-48). In addition, metals (e.g. iron) oxides are also present. Furthermore, PB SF 7 sample clearly shows the presence of a fluid circulation (Fig. 3.1.2.44).

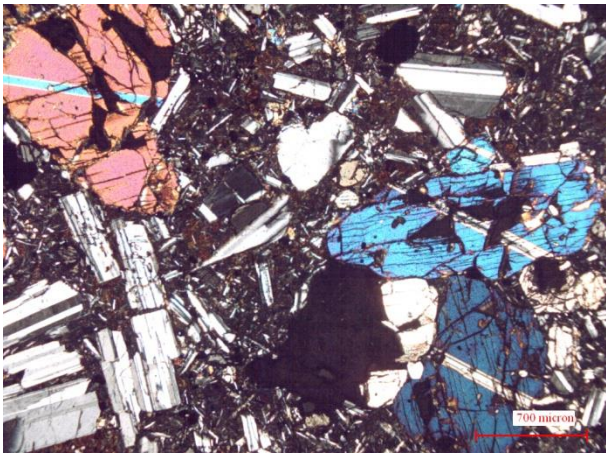


Figure 3.1.2. 43. Photomicrograph of PB SF 6 basaltic andesite sample (xpl, 4x). Particular of pyroxenes and plagioclases.

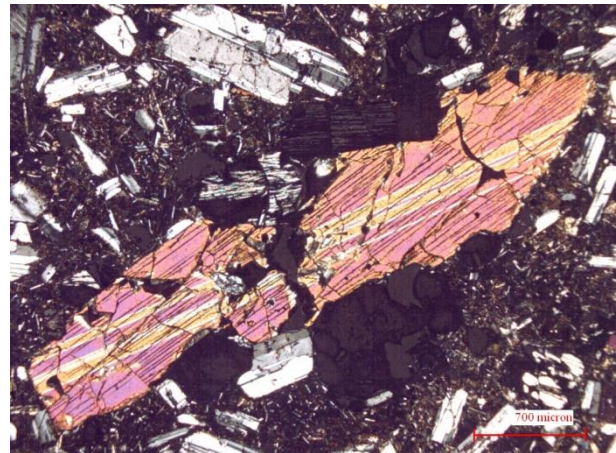


Figure 3.1.2. 44. Photomicrograph of PB SF 7 basaltic andesite sample (xpl, 4x). Augite crystal.

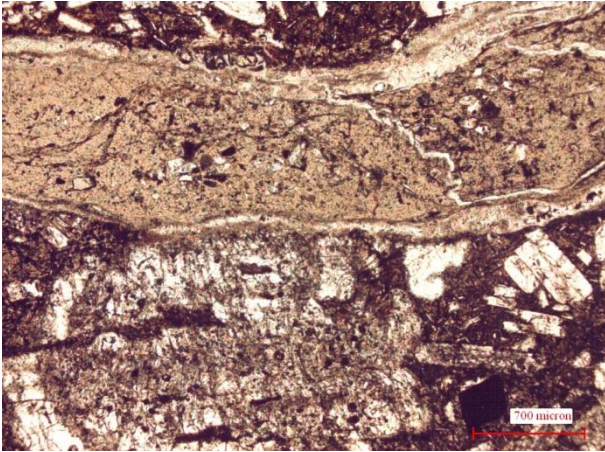


Figure 3.1.2. 45. Photomicrograph of PB SF 7 basaltic andesite sample (ppl, 4x). Particular of fluid circulation and iron oxides.

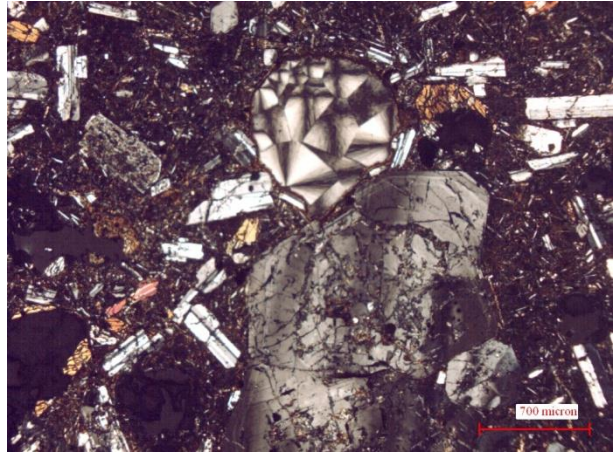


Figure 3.1.2. 46. Photomicrograph of PB SF 7 basaltic andesite sample (xpl, 4x). Particular of the sericitization of plagioclases and amygdales filled by zeolites.

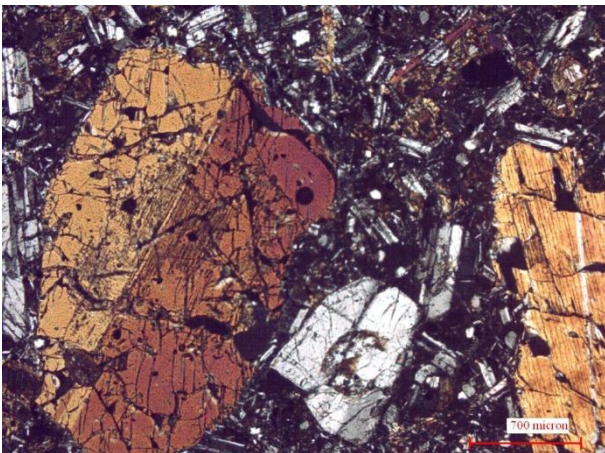


Figure 3.1.2. 47. Photomicrograph of PB SF 11 basaltic andesite sample (xpl, 4x). Particular of augite crystals.

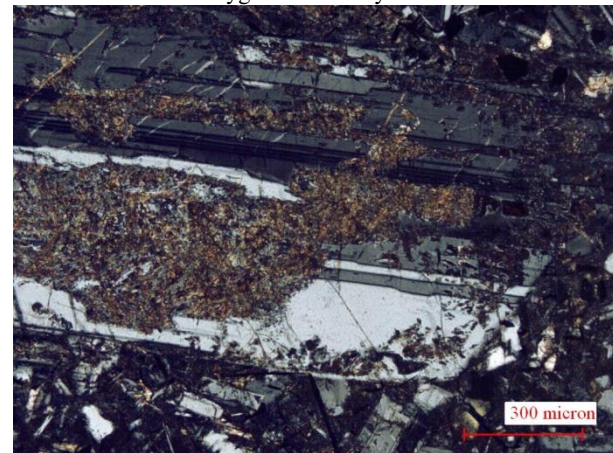


Figure 3.1.2. 48. Photomicrograph of PB SF 11 basaltic andesite sample (xpl, 4x). Particular of the sericitization of plagioclases.

### Evaluation of the state of Conservation

Considering the state of conservation of the sedimentary rocks, especially coral boundstones and grainstones/packstones they show a very high intergranular and intragranular porosity. While considering the sandstones and tuffites, they are more compact, but affected by cracks. In addition, coral boundstones present biological patina.

In proximity of carbonate stone masonries, salts encrustations have been identified, sampled at *Fuerte de Santiago* and *Fuerte San Fernando*, in Portobelo. Respectively PB FdS 3 and PB SF 5 samples are calcite salts encrustation showing several different layers, with micritic and sparitic crystals (Figs. 3.1.2.49-52). Therefore, the process of calcite crystallization has been obtained in several steps, with a different duration, understandable thanks to the diverse size of the minerals belonging to the layers.

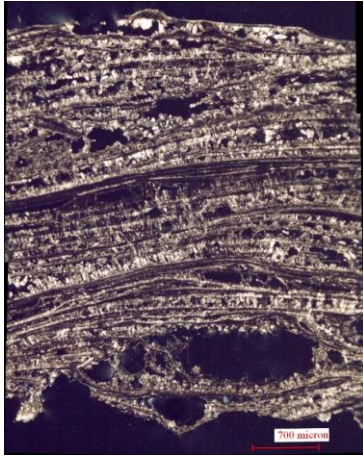


Figure 3.1.2. 49. Photomicrograph of PB FdS 3 salt encrustation sample (xpl,4x). Particular of several calcite layers.

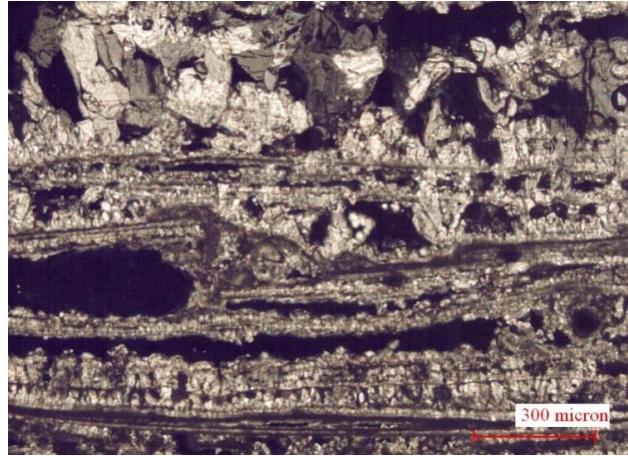


Figure 3.1.2. 50. Photomicrograph of PB FdS 3 salt encrustation sample (xpl, 10x). Particular of micritic and sparitic crystals of calcite.

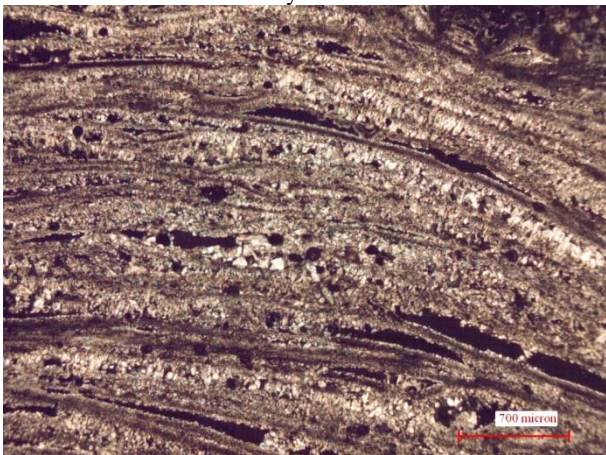


Figure 3.1.2. 51. Photomicrograph of PB SF 5 salt encrustation sample (xpl,4x). Particular of several calcite layers.

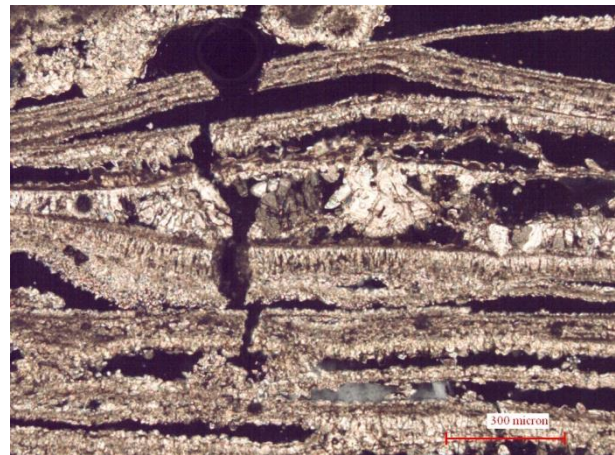


Figure 3.1.2. 52. Photomicrograph of PB SF 5 salt encrustation sample (xpl, 10x). Particular of micritic and sparitic crystals of calcite.

Finally, basaltic andesites are characterized by iron oxides and sericitization of plagioclases, which can be points of weakness of the stone.

### Final remarks

PLM observation of thin sections allowed us to identify several lithotypes in the areas under study. The materials utilized in both sites are mainly ascribable to sedimentary rocks of volcanogenic and marine sediments. In addition, the presence of igneous rocks was observed.

In particular, considering Panama Viejo masonries, the rocks detected are: polygenic breccias, basaltic andesites, tuffites, altered volcanic rocks and rhyolites. Regarding the Fortresses of Portobelo and San Lorenzo, sandstones, tuffites, coral boundstone, grainstones/packstones and basaltic andesites have been identified.

Considering the outcrops, recognised in proximity of the archaeological area of Panama Viejo, volcanic breccias and basaltic andesites have been detected. A basaltic andesite outcrop was analysed also in Portobelo, specifically near the Fort of San Fernando; while, at San Lorenzo Fortress, a grainstone outcrop was identified.

Concerning the state of conservation at Panama Viejo site, microscopic analyses showed several inner alterations as plagioclase and sanidine alteration, the presence of iron oxides or hydroxides, and porosity which can be a point of stone weakness. Generally, considering iron oxides or hydroxides, they have been observed concentrated in the external part of the stones. These areas represent an aesthetical damage; moreover, they can undergo to differential deterioration phenomena, since they show different physical-chemical features in comparison with the core of the rock. In addition, the alteration process due to diffused zeolitization was detected largely spread in the entire archaeological site and, specifically, it is shown by samples of volcanoclastic stones. These parts can be affected by the humidity cycles, contributing to cause the macroscopic phenomena observed such as cracks, flaking, etc.

At Portobelo and San Lorenzo, especially coral boundstones and grainstones/packstones show a very high intergranular and intragranular porosity. While considering the sandstones and tuffites, they are more compact, but affected by cracks. In addition, coral boundstones present biological patina. Moreover, in proximity of carbonate stone masonries, salts encrustations have been identified, showing a process of calcite crystallization developed in several steps, with a different duration, understandable thanks to the alternation of sparitic and micritic minerals belonging to different layers.

### 3.2. X-Ray Powder Diffraction Analysis (XRPD)

Diffraction analysis has been performed on almost all samples, discarding only specimens which shown an insufficient material quantity for carrying out all the analyses planned. Nevertheless, each rock typology has been investigated, thus we obtained a complete representation of the mineralogy of the lithotypes under study.

Therefore, considering the diverse stone types, different crystalline phases have been detected and described below in detail; however, the complete series of diffractograms are reported in Annex 1. In order to have a clearer comparison among the several samples, they have been assembled according to lithology.

#### *Breccias*

For analysing polygenic breccias, samples have been powdered without performing a separation of the fragments and the matrix, but choosing the most representative parts, in order to obtain the most realistic composition of the different specimens. As noticeable in Table 3.2.1, the majority of samples shows silicates as main component (PV CC 4, PV CC 5, PV CC 6, PV CR 4, PV FC 4, PV FC 5, PV FC 8, PV FC 11, PV FN 2, PV JC 3, PV JC 4a and PV JC 4b). In addition, calcite has been detected, as abundant and dominant phase, in several rocks due to the presence of carbonate fragments, already identified under microscope observation (PV CC 4, PV CC 5, PV CC 6, PV FC 7, PV FC 11, PV FN 1, PV FN 2, PV JC 1, PV JC 2 and SL 6). Moreover, it is confirmed the zeolitization process, aforementioned in the subchapters 3.1 and 3.2, detecting zeolite minerals as Clinoptilolite and Mordenite. Finally, traces of chlorite and clay expanded minerals, as Montmorillonite and Vermiculite, have been identified and confirmed by comparing the diffractograms obtained by the following different preparations: randomly oriented, oriented and saturated with glycol. This process has been performed only on one representative sample, as shown in Figure 3.2.1.



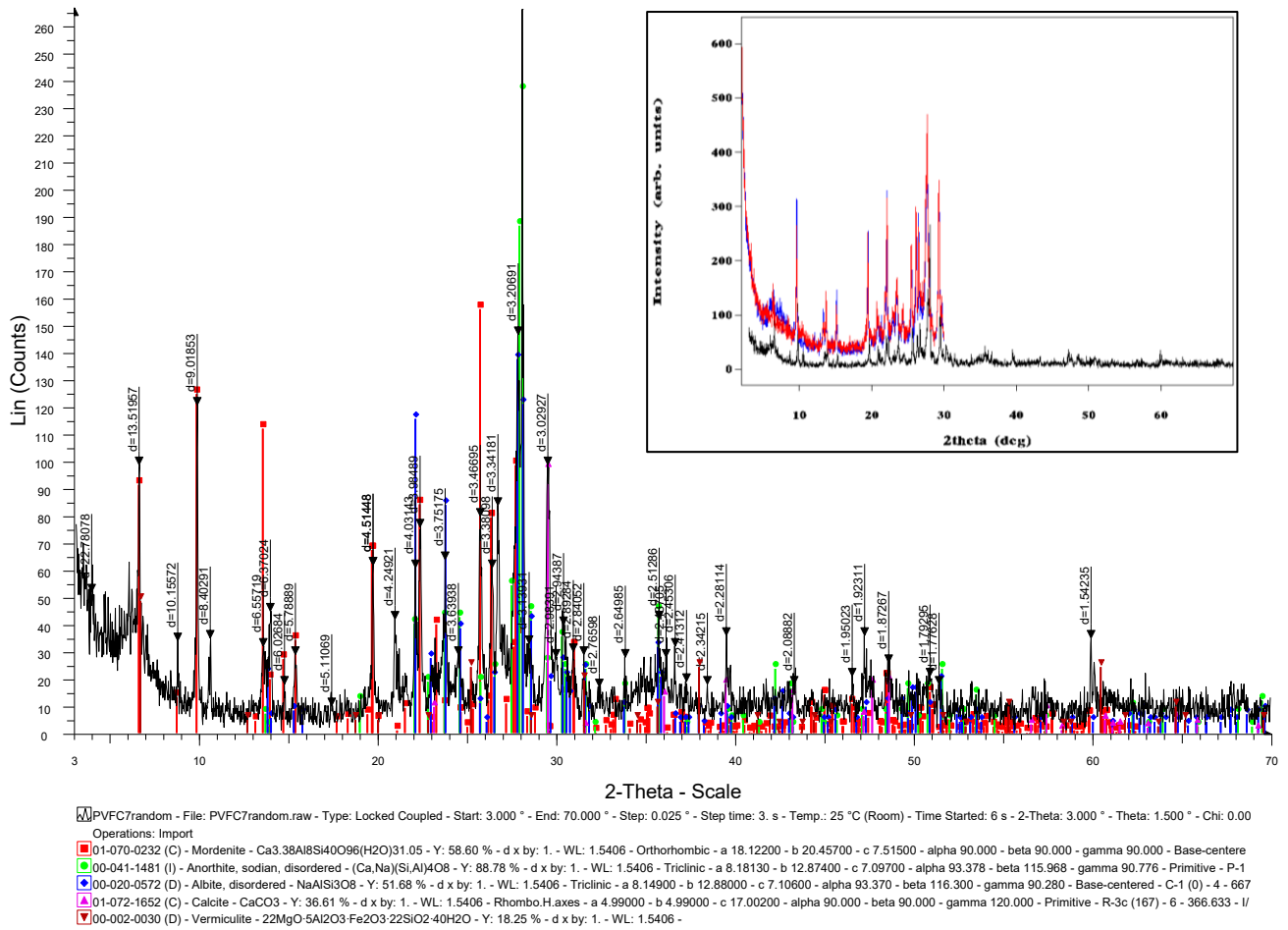


Figure 3.2. 1. Randomly oriented diffractogram of PV FC 7 sample. On the right, diffractograms of PV FC 7 sample, in randomly oriented (black), oriented (blue) and saturated with glycol (red) state.

Table 3.2. 1. Legend: Cal: Calcite; Qtz: Quartz; Fsp: Feldspar; Px: Pyroxenes; Zeo: Zeolite (CPL = Clinoptilolite; MOR = Mordenite); Chl= Chlorite; Mnt: Montmorillonite; Vrm: Vermiculite.  
 +++ = dominant; ++ = abundant; + = present, traces; - = absent  
 N.B. PV JC4a (interior part) e PV JC4b (external part)

Sample	Cal	Qtz	Fsp	Px	Zeo	Chl	Mnt	Vrm
PV CC 4	+/++	+/++	+/+++	-	CPL +/++	tr	-	tr
PV CC 5	++	++	+++	-	CPL +/++	tr	-	tr
PV CC 6	+/+++		+++	-	CPL +	tr	-	tr
PV CR 4	-	tr	++	-	MOR tr	-	-	-
PV FC 4	-	+/++	++	-	MOR tr	-	-	-
PV FC 5	-	++	+/+++	-	MOR ++	-	-	-
PV FC 7	+++	+	++	-	MOR ++	-	-	-
PV FC 8	-	++	+++	-	MOR ++	-	tr/+	-
PV FC 11	++	++	+++	-	CPL +	tr	-	tr
PV FN 1	+++	++	++	-	MOR +	-	-	-

Sample	Cal	Qtz	Fsp	Px	Zeo	Chl	Mnt	Vrm
<b>PV FN 2</b>	++	++	+++	-	MOR +	-	-	
<b>PV JC 1</b>	+++	+/++	+++	-	MOR tr	-	tr	tr
<b>PV JC 2</b>	+++	+	+	-	MOR +	?	tr	tr
<b>PV JC 3</b>	+	?	+++	-	CPL +	tr	-	-
<b>PV JC 4 a</b>	-	++	+++	tr?	MOR Tr/+	-	-	-
<b>PV JC 4 b</b>	-	++	++	+	MOR ++	-	-	-

### *Tuffite*

Considering tuffites, the dominant minerals present are feldspars, such as high albite and anorthite, in almost all samples. Regarding the two specimens belonging to the Panama Viejo site (PV TC 3 and PV TC 4), dominant feldspars are followed by abundant quartz, calcite and mordenite. While analysing the specimen of *Fuerte de Santiago* (PB FdS 10), it shows abundant calcite and traces of quartz, clinoptilolite and montmorillonite. Among San Lorenzo tuffites, SL 9 sample shows dominant calcite, presence of quartz, clinoptilolite and montmorillonite, followed by traces/presence of feldspars. SL 1, SL 2 and SL 4 specimens are characterized by dominant feldspars, traces/presence of quartz, calcite (except for SL 4, where it is absent), clinoptilolite and montmorillonite.

This information is summarize and listed in Table n.3.2.2.

Table 3.2. 2. Legend: Cal: Calcite; Qtz: Quartz; Fsp: Feldspar; Zeo: Zeolite (CPL = Clinoptilolite; MOR = Mordenite); Mnt: Montmorillonite. +++ = dominant; ++ = abundant; + = present, traces; - = absent

Sample	Cal	Qtz	Fsp	Zeo	Mnt
<b>PV TC 3</b>	++	+++	+++	MOR ++	-
<b>PV TC 4</b>	++	++	+++	MOR ++	-
<b>PB FdS 10</b>	++	Tr	+++	CPL tr	tr
<b>SL 1</b>	tr/+	tr	+++	CPL +	tr
<b>SL 2</b>	tr	tr	+++	CPL +	tr
<b>SL 4</b>	-	+	+++	CPL tr	+
<b>SL 6</b>	+++	+	++	CPL +	tr/+
<b>SL 9</b>	+++	+	tr/+	CPL +	+

### *Sandstone*

In this case, summarized in Table 3.2.3, the dominant phase is represented by calcite, followed by the presence/abundance of feldspars, except for PB FSJ 4 and PB FdS 9 samples, which show traces of them. Moreover, presence of quartz has been detected in samples from *Fuerte de Santiago*, PB FdS 5 and PB FdS 9, which respectively show also traces of clinoptilolite and chlorite. Traces of this latter one have been identified also in PB FdS 2 sample. Finally, traces/presence of clinoptilolite has been observed also in PB FSJ 8 sample.

Table 3.2. 3. Legend: Cal: Calcite; Qtz: Quartz; Fsp: Feldspar; Zeo: Zeolite (CPL = Clinoptilolite); Chl= Chlorite.  
 +++ = dominant; ++ = abundant; + = present, traces; - = absent

Sample	Cal	Qtz	Fsp	Zeo	Chl
<b>PB FSJ 4</b>	+++	tr	tr	-	-
<b>PB FSJ 8</b>	+++	tr/+	+ /+++	CPL tr/+	-
<b>PB FdS 2</b>	+++	?	+ /+++	-	tr
<b>PB FdS 5</b>	+++	+	++	CPL tr	-
<b>PB FdS 9</b>	+++	+	tr	-	tr

### *Basaltic andesite*

Dominant minerals in basaltic andesites are feldspars, followed by present/abundant pyroxenes. Moreover, samples belonging to the *Fortín de la Natividad*, PV FN 4 and PV FN 5, show abundant montmorillonite, confirmed also by carrying out X-Ray diffraction analysis on randomly oriented, oriented and saturated with glycol powder (Fig. 3.2.2). In PV FN 4, PV vic. CR and PB SF 11 quartz has been identified, respectively in traces, abundant and present. In addition, traces of vermiculite has been detected in PV Q 2 sample, while traces of magnetite have been identified in PV FN 4, PV FN 5 and PB SF 7 samples; finally, presence of calcite has been detected in PV vic. CR sample, as listed in Table 3.2.4.

Table 3.2. 4. Legend: Cal: Calcite; Qtz: Quartz; Fsp: Feldspar; Px: Pyroxenes; Mnt: Montmorillonite; Vrm: Vermiculite; Mag: Magnetite.  
 +++ = dominant; ++ = abundant; + = present, traces; - = absent

Sample	Cal	Qtz	Fsp	Px	Mnt	Vrm	Mag
<b>PV FN 4</b>	-	tr?	++ /+++	+	++	-	tr
<b>PV FN 5</b>	-	-	+++	++	++	-	tr
<b>PV Q 2</b>	-	-	+++	-	-	tr	-
<b>PV vic. CR</b>	+	++	+++	+ /+++	?	-	-
<b>PB SF 6</b>	-	-	+++	tr	-	-	?
<b>PB SF 7</b>	-	-	+++	tr/+	-	-	tr
<b>PB SF 11</b>	-	+	+++	+	-	-	-

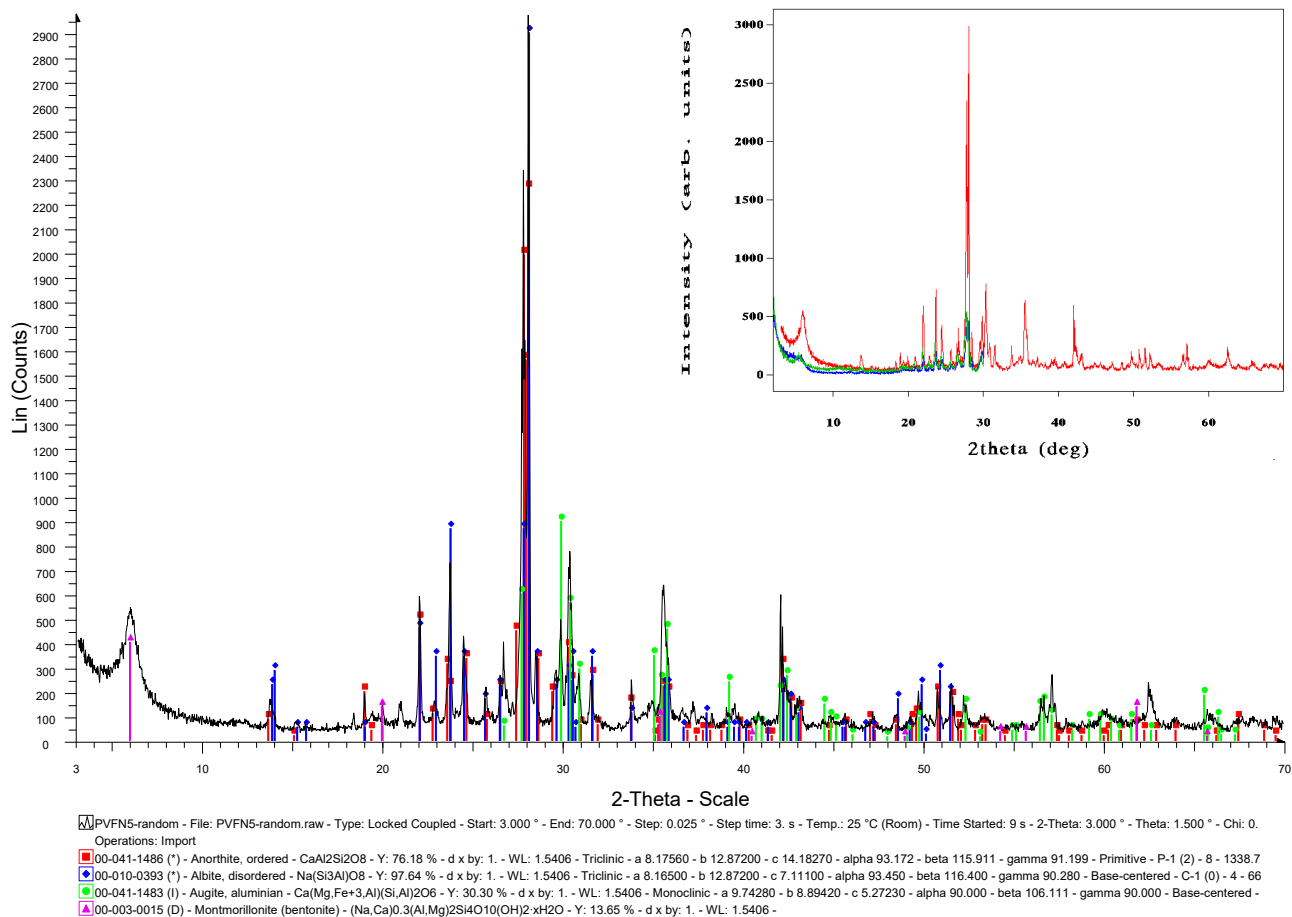


Figure 3.2. 2 Randomly oriented diffractogram of PV FN 5 sample. On the right, diffractograms of PV FN 5 sample, in randomly oriented (black), oriented (blue) and saturated with glycol (red) state.

### Coral boundstone

The three samples of coral limestone analysed, PB FSJ 7, PB SF 2, BF SF 8, belonging to Portobelo fortresses, are all characterized by dominant aragonite and presence or traces of calcite, as described below in Table 3.2.5.

Table 3.2. 5. Legend: Arg: Aragonite; Cal: Calcite.  
 +++ = dominant; ++ = abundant; + = present, traces; - = absent

Sample	Arg	Cal
<b>PB FSJ 7</b>	+++	tr/+
<b>PB SF 2</b>	+++	+
<b>PB SF 8</b>	+++	traces

### Grainstone/Packstone

Analysis on grainstone/packstone (PB SF 1, SL 8 and SL 13 samples), summarized in Table 3.2.6, detected as main mineral phase aragonite, followed by traces/presence of quartz. Specifically, SL 8 sample shows also presence of feldspar and traces of clinoptilolite and montmorillonite; while SL 13 sample has only montmorillonite in traces.

Table 3.2. 6. Legend: Cal: Calcite; Qtz: Quartz; Fsp: Feldspar; Zeo: Zeolite (CPL = Clinoptilolite); Mnt: Montmorillonite.  
 +++ = dominant; ++ = abundant; + = present, traces; - = absent

Sample	Cal	Qtz	Fsp	Zeo	Mnt
<b>PB SF 1</b>	+++	traces	-	-	-
<b>SL 8</b>	+++	tr/+	+	CPL tr	tr
<b>SL 13</b>	+++	tr	-	-	tr

### *Altered volcanic rock*

XRPD analysis allowed us to define this rock typology as “zeolitized rock”, since it is largely composed by zeolites. In particular, the dominant mineral is quartz, for each sample. Considering the single cases, PV FC 9 and PV SJD samples are characterized by another dominant phase: clinoptilolite; while PV FC 6 has mordenite as abundant phase, followed by the presence of feldspar, as reported in Table 3.2.7.

Table 3.2. 7. Legend: Qtz: Quartz; Fsp: Feldspar; Zeo: Zeolite (CPL = Clinoptilolite; MOR = Mordenite).  
+++ = dominant; ++ = abundant; + = present, traces; - = absent

Sample	Qtz	Fsp	Zeo
<b>PV FC 6</b>	+++	+	MOR ++
<b>PV FC 9</b>	+++	-	CPL ++/+++
<b>PV SJD</b>	++	-	CPL +++

### *Rhyolite*

The two samples of rhyolite, PV CT 1 and PV CT 2, are characterized by dominant quartz, abundant feldspar (albite and sanidine), traces of kaolinite and, only PV CT 1, traces of hematite (Table 3.2.8).

Table 3.2. 8. Legend: Qtz: Quartz; Fsp: Feldspar; Kln: Kaolinite; Hem: Hematite.  
+++ = dominant; ++ = abundant; + = present, traces; - = absent

Sample	Qtz	Fsp	Kln	Hem
<b>PV CT 1</b>	+++	++	tr	tr
<b>PV CT 2</b>	+++	++	tr	-

### *Salt encrustations*

Encrustations have been observed and sampled at *Fuerte de Santiago* and *Fuerte San Fernando*, respectively PV FdS 3 and PB SF 5 specimens. XRPD investigations revealed calcite as unique mineralogical phase present (Table 3.2.9).

Table 3.2. 9. Legend: Cal: Calcite. +++ = dominant; ++ = abundant; + = present, traces; - = absent

Sample	Cal
<b>PB FdS 3</b>	+++
<b>PB SF 5</b>	+++

### *Final remarks*

X-Ray powder diffraction analysis allowed us to identify the mineral phases present in the different samples, confirming and/or clarifying the previous investigations performed.

In particular, the zeolitization process observed in several stone typologies, such as breccia, tuffite and sandstone, has been confirmed, detecting clinoptilolite in all sites (Panama Viejo, Portobelo and San Lorenzo), while mordenite zeolite has been identified only at Panama Viejo. In addition, the PV FC 6, PV FC 9 and PV SJD samples, which macroscopically and microscopically shown a mud-limestone-like aspect, have been recognized as altered volcanic rocks, thus with totally silicate composition. The presence of clay expanded minerals, such as montmorillonite and vermiculite, has been detected, thus identifying a possible co-responsible of the detachment and exfoliation processes observed macroscopically.

Finally, XRPD analysis allowed us to determine the composition of the encrustations sampled, revealing calcite as unique mineralogical phase present.

### 3.3. Environmental Scanning Electron Microscopy Analysis (ESEM-EDS)

Environmental Scanning Electron Microscopy (ESEM) equipped with an energy dispersive X-ray spectrometer (EDS) analyses have been performed on thin sections and bulk samples in order to investigate more in detail particular areas already investigated through PLM, macroscopic and stereomicroscopic observations and XRPD investigations.

#### 3.3.1. Materials Characterization

Through the PLM and XRD analysis, was possible to affirm the presence of zeolites, specifically mordenite  $(Ca,Na_2,K_2)Al_2Si_{10}O_{24} \cdot 7(H_2O)$  and clinoptilolite  $(Na,K,Ca)_{2-3}Al_3(Al,Si)_2Si_{13}O_{36} \cdot 12H_2O$ , in several samples. In order to confirm the zeolitization phenomenon, ESEM-EDS technique has been utilized to determine and confirm the composition of these areas.

Considering Panama Viejo, three polygenic breccias have been investigated: PV FN 1, PV FC 4 and PV FC 7 samples.

Analyses on the first one, PV FN 1 sample, have been carried out on the following points, firstly on a zeolitized part, highlighted in Figures 3.3.1.1-3.



Figure 3.3.1. 1. PLM photomicrograph of PV FN1 sample (xpl, 4x). Plagioclase crystal surrounded by zeolites; presence of brownish iron oxides.

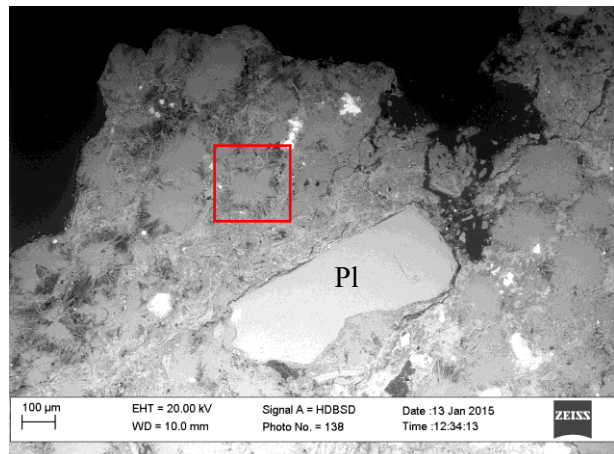


Figure 3.3.1. 2. BSD-ESEM photomicrograph of PV FN1 sample. Plagioclase crystal surrounded by zeolites. The area under investigation is highlighted by a red rectangle.

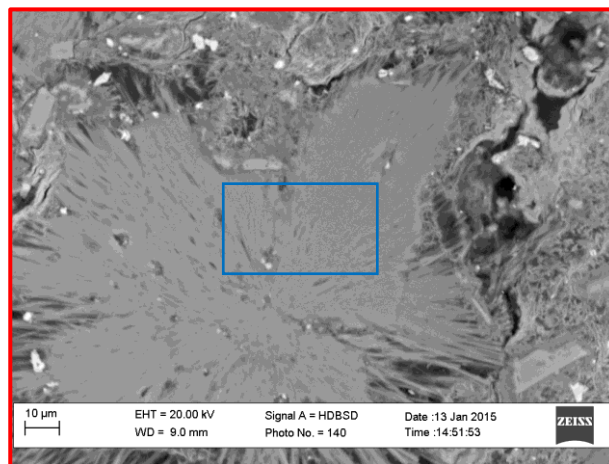


Figure 3.3.1. 3. BSD-ESEM photomicrograph of PV FN1 sample. The blue rectangle indicates the area of EDS investigation.

EDS investigations detected as major elements O, Si and C, followed by Al, Na, Fe, Ca, K and Mg. The composition revealed the presence of aluminosilicates, therefore confirming the zeolitization process, while the Fe can be ascribable to the iron oxides presence, visible also by PLM microscopy (Fig. 3.3.1.1).

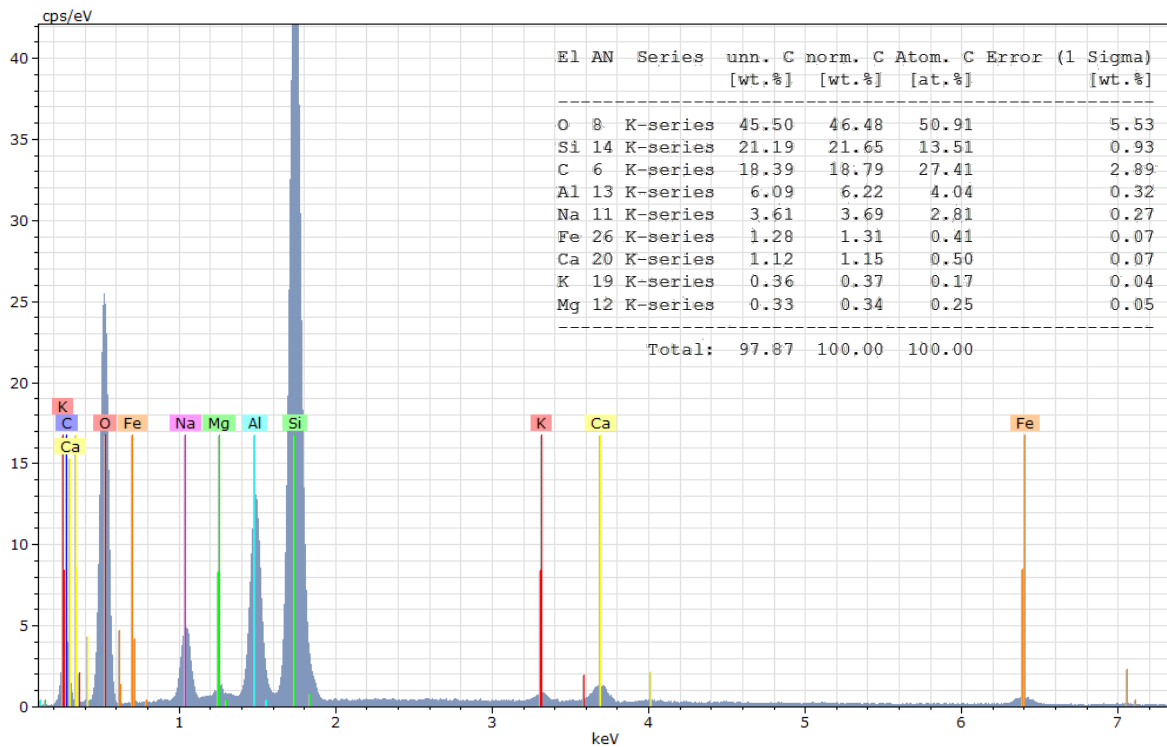


Figure 3.3.1. 4. ESEM-EDS spectrum of PV FN 1 sample, area shown in Fig. 3.3.1.3.

Another part showing the same structure has been analysed, as shown in Figs. 3.3.1.5-6; even in this case the composition results to be ascribable to zeolites associated to the presence of iron oxides, as it is demonstrated by the spectrum shown in Fig. 3.3.1.7.

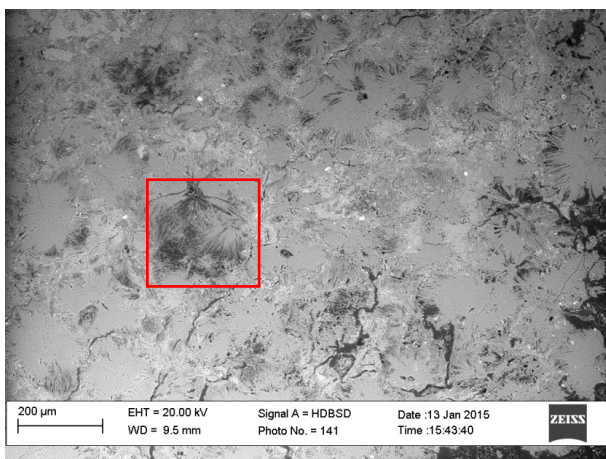


Figure 3.3.1. 5. BSD-ESEM photomicrograph of PV FN1 sample. The area under investigation is highlighted by a red rectangle.

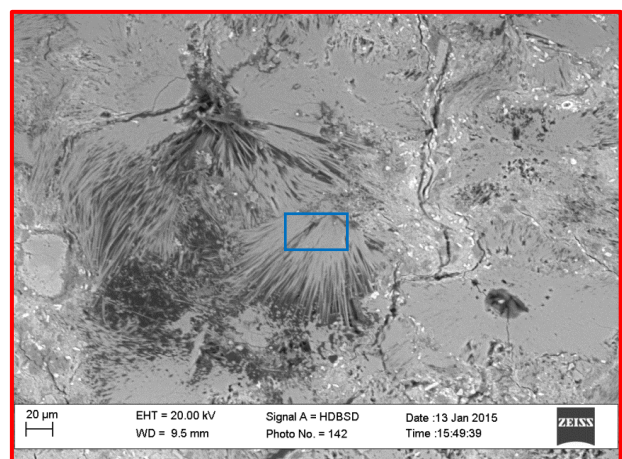


Figure 3.3.1. 6. BSD-ESEM photomicrograph of PV FN1 sample. The blue rectangle indicates the area of EDS investigation.

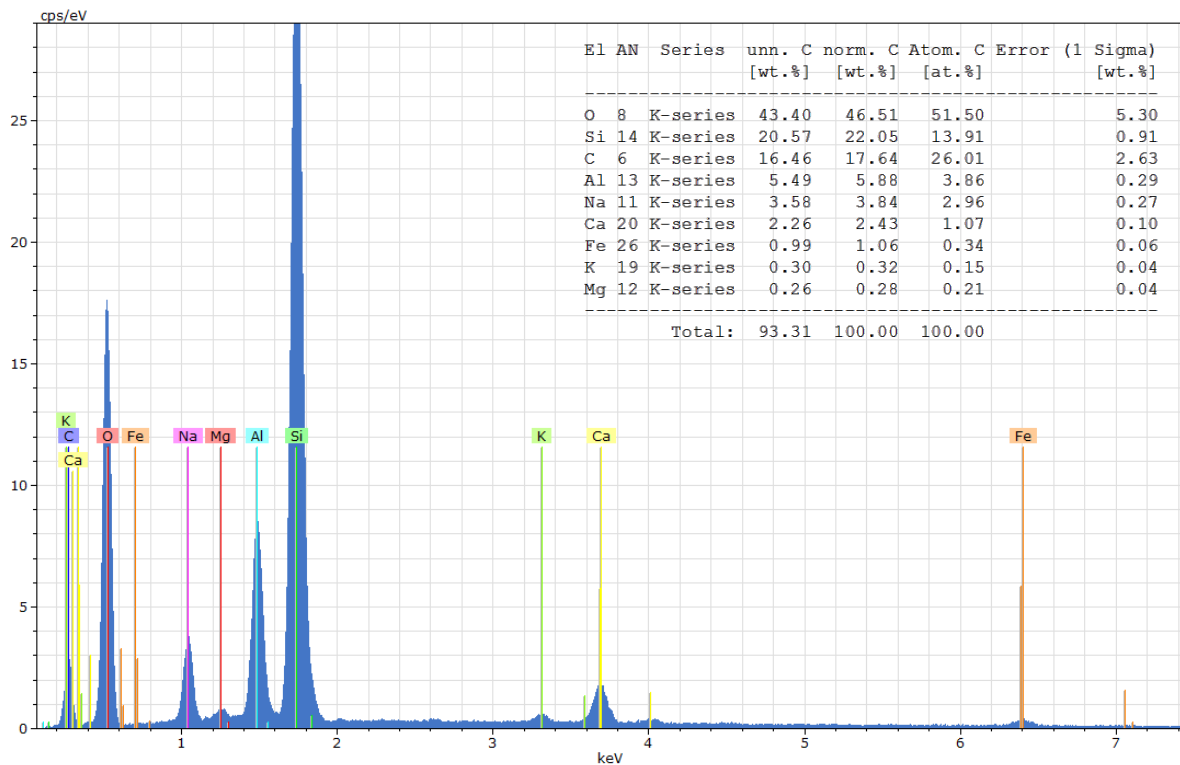


Figure 3.3.1. 7. ESEM-EDS spectrum of PV FN 1 sample, area shown in Fig. 3.3.1.6.

Moreover, crystals of metal oxides have been identified and analyzed as shown in Fig. 3.3.1.8. The spectrum reveals as major elements detected oxygen and iron, thus it is iron oxide, followed by C, Si, Al, Na, Ca, Mg and K (Fig. 3.3.1.9); these latter ones are due to the zeolites which surrounds the iron oxides minerals.

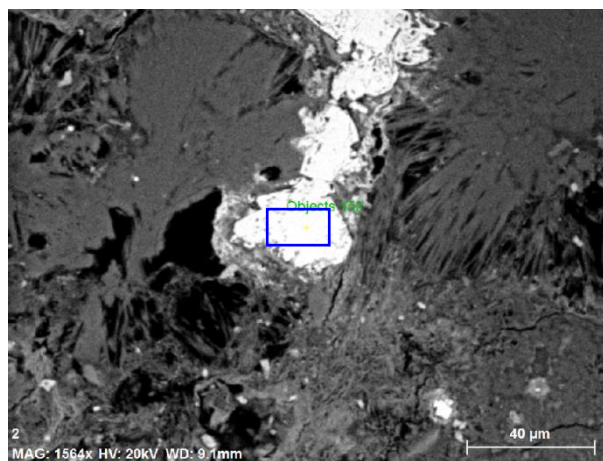


Figure 3.3.1. 8. BSD-ESEM photomicrograph of PV FN1 sample. The blue rectangle indicates the area of EDS investigation.



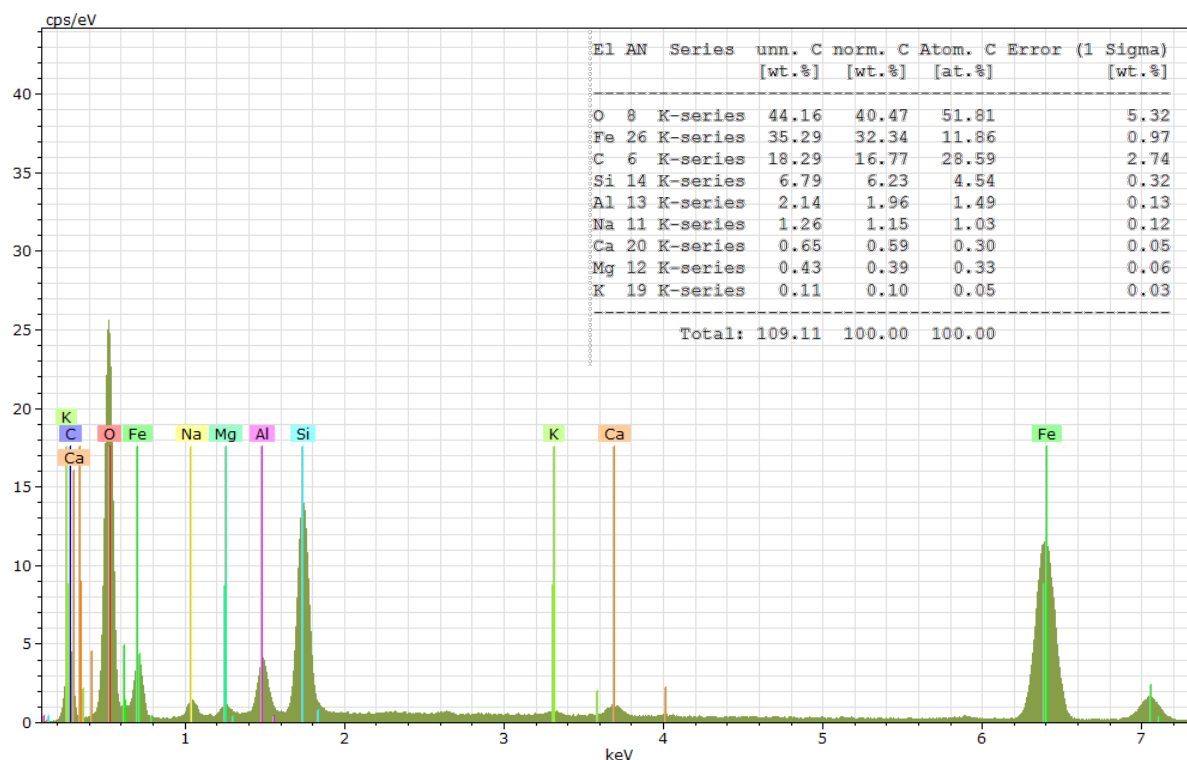


Figure 3.3.1. 9. ESEM-EDS spectrum of PV FN 1 sample, area shown in Fig. 3.3.1.8.

In PV FC 4 sample, the parts showing a yellowish-brownish hue present in the zeolitized areas, under PLM (Fig. 3.3.1.10), underwent ESEM observations (Figs.3.3.1.11-13) and EDS spectroscopy (Figs. 3.3.1.14-16). In particular, three points of analyses have been selected and shown in Figure 3.3.1.13.

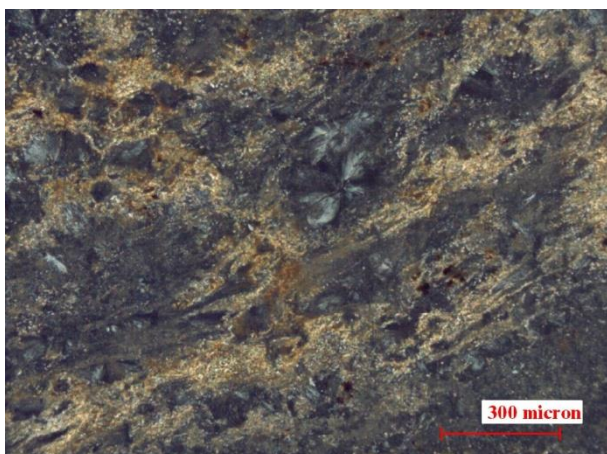


Figure 3.3.1. 10. PLM photomicrograph of PV FC 4 sample (xpl, 10x). Particular of yellowish-brownish parts present in the zeolitized areas.

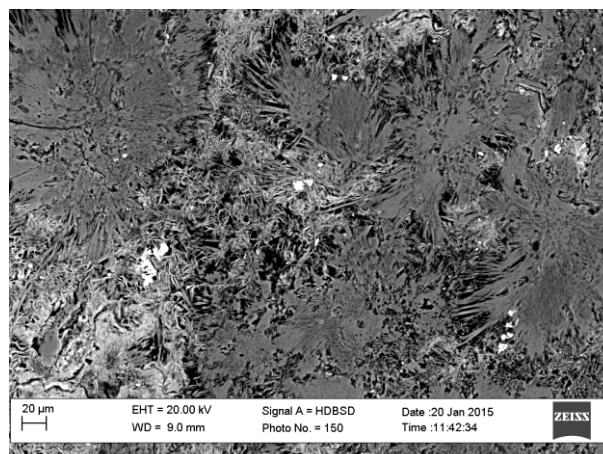


Figure 3.3.1. 11. BSD-ESEM photomicrograph of PV FC 4 sample. Particular of the yellowish-brownish parts present in the zeolitized areas.

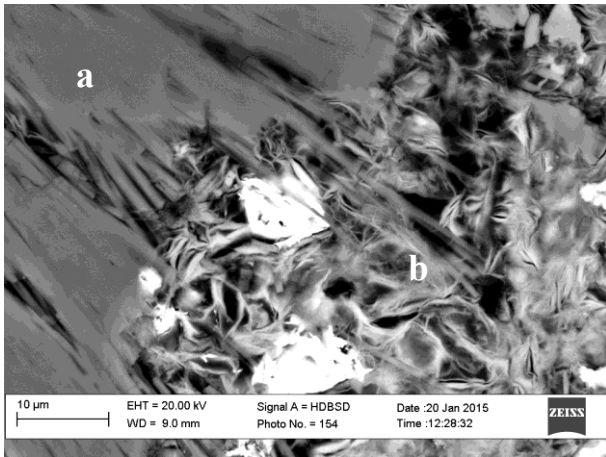


Figure 3.3.1. 12. BSD-ESEM photomicrograph of PV FC 4 sample. a. zeolite; b. Particular of the yellowish-brownish parts.

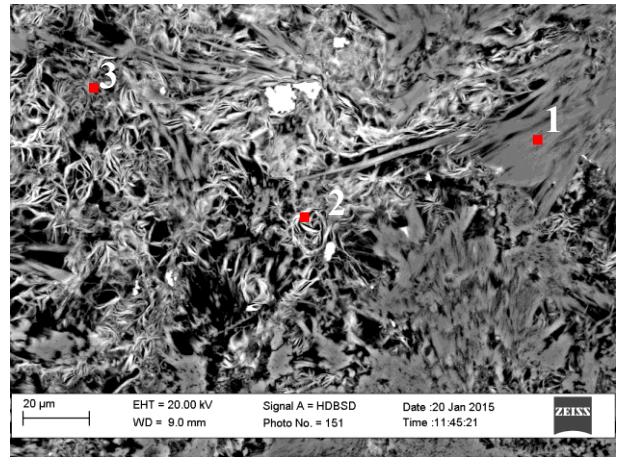


Figure 3.3.1. 13. BSD-ESEM photomicrograph of PV FC 4 sample. The 3 points of EDS analysis are indicated with red dots.

The analysis performed on zeolites confirmed the previous elemental composition detected (Fig. 3.3.1.14), while the EDS spectrum obtained on the yellowish-brownish areas surrounding the zeolites show higher presence of iron and magnesium, with an elemental composition formed by O, Si, C, Fe, Al, Mg, Ca, K and Na, listed in order of abundance (Figs. 3.3.1.15-16). It can be attributable to chlorite.

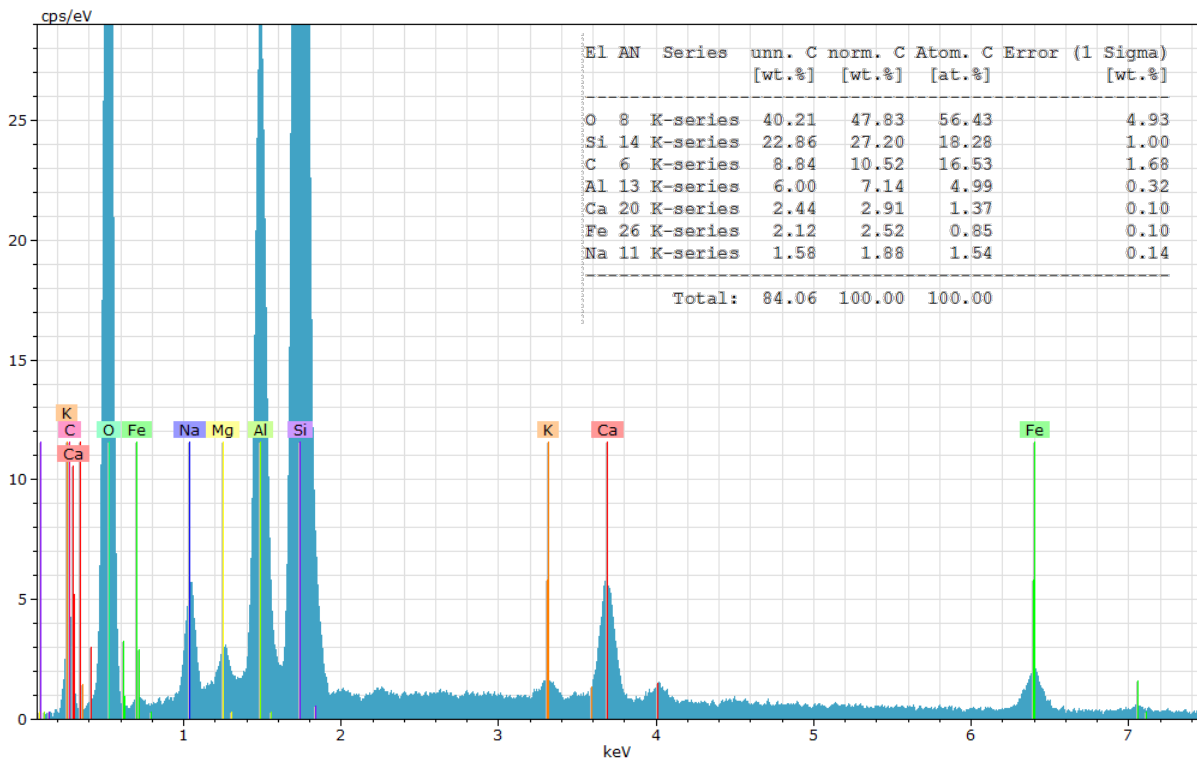


Figure 3.3.1. 14. ESEM-EDS spectrum 1 of PV FC 4 sample, area shown in Fig. 3.3.1.13.

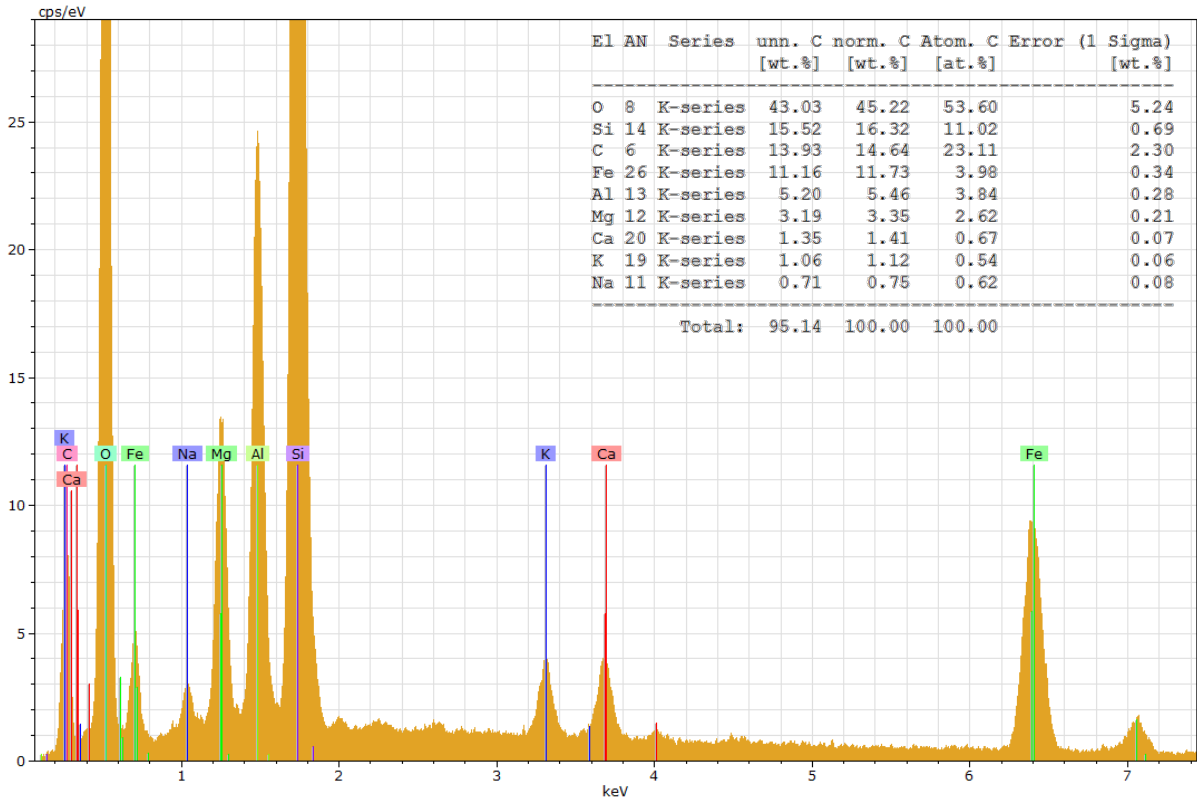


Figure 3.3.1. 15. ESEM-EDS spectrum 2 of PV FC 4 sample, area shown in Fig. 3.3.1.16.

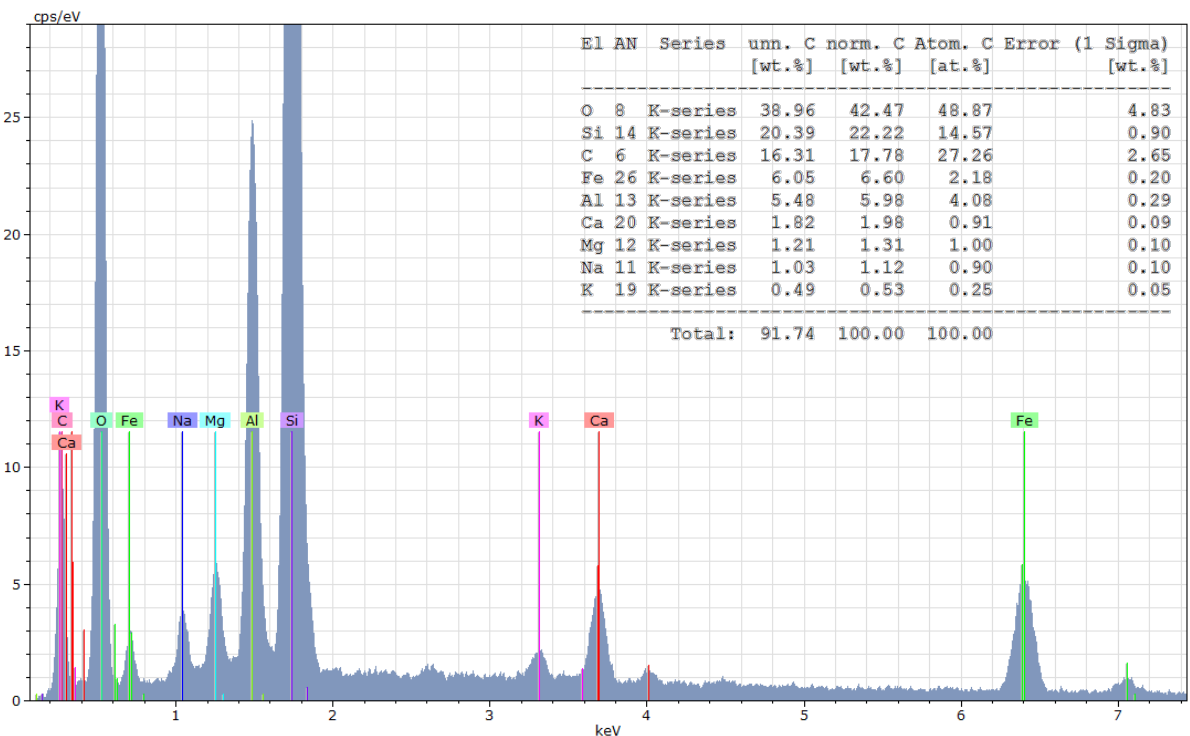


Figure 3.3.1. 16. ESEM-EDS spectrum 3 of PV FC 4 sample, area shown in Fig. 3.3.1.16.

Moreover, on PV FC 4 sample EDS-maps investigations have been performed in order to understand better the elements distributions. As shown in Figs. 3.3.1.17-18, the analysis has been carried out on a zeolitized area, near to a plagioclase. The spectrum obtained shows the same elements already observed (Fig. 3.3.1.19). Observing the EDS-maps is evident the presence of

silicates and aluminates of K, in correspondence of the fibrous zeolite, and Fe, Mg around them, probably due to chlorite (Fig. 3.3.1.20). In addition, the presence of Fe can be also ascribable to iron oxides.

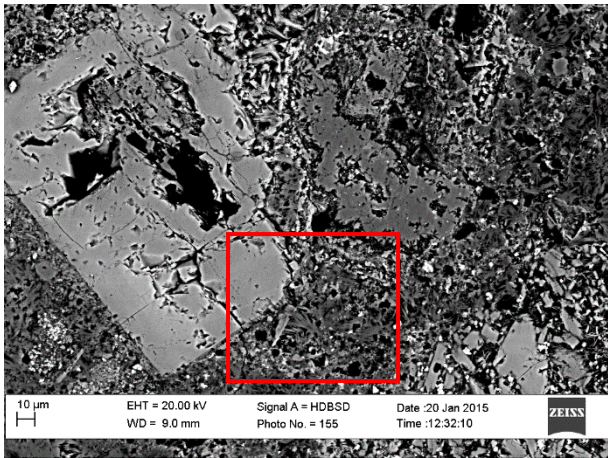


Figure 3.3.1. 17. BSD-ESEM photomicrograph of PV FC 4 sample. The area under investigation is highlighted by a red rectangle.

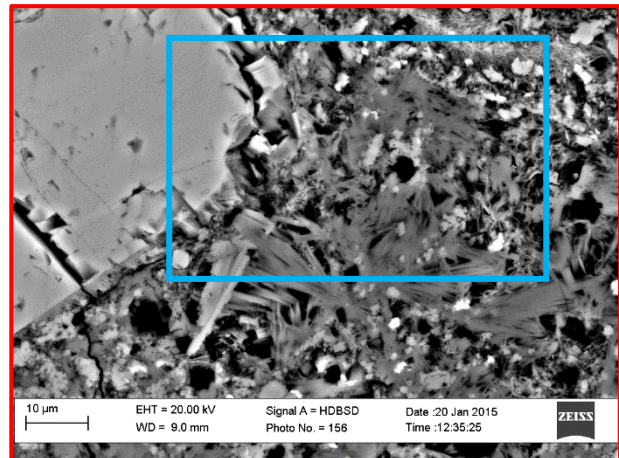


Figure 3.3.1. 18. BSD-ESEM photomicrograph of PV FC 4 sample. The EDS-Maps analysis has been performed on the area within the blue rectangle, so including also a plagioclase (on the left).

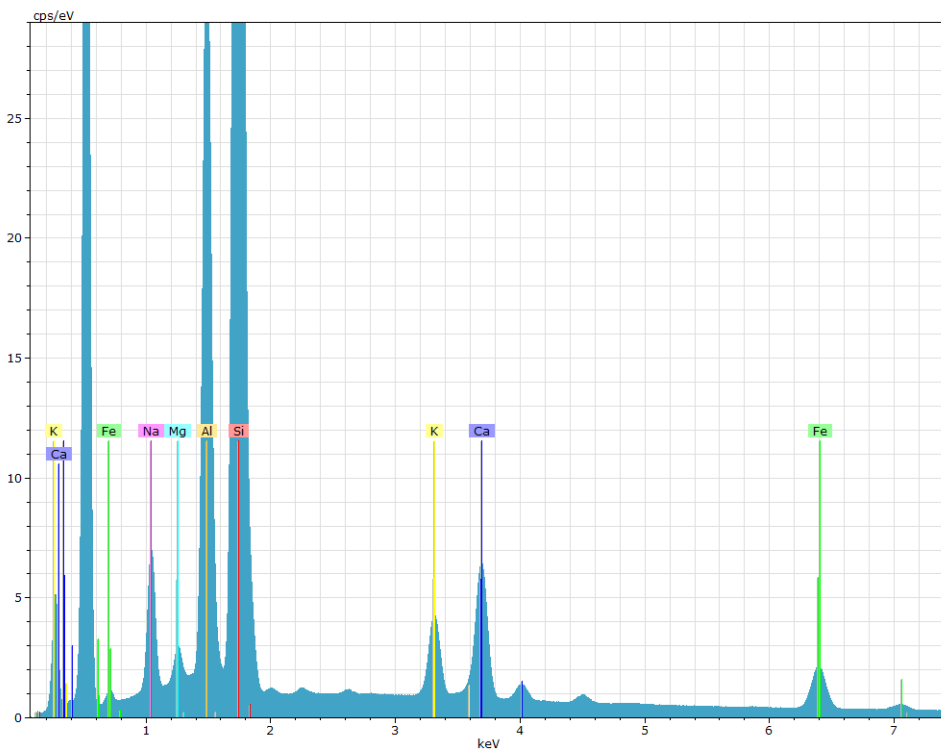


Figure 3.3.1. 19. ESEM-EDS spectrum of PV FC 4 sample, area shown in Fig. 3.3.1.18.

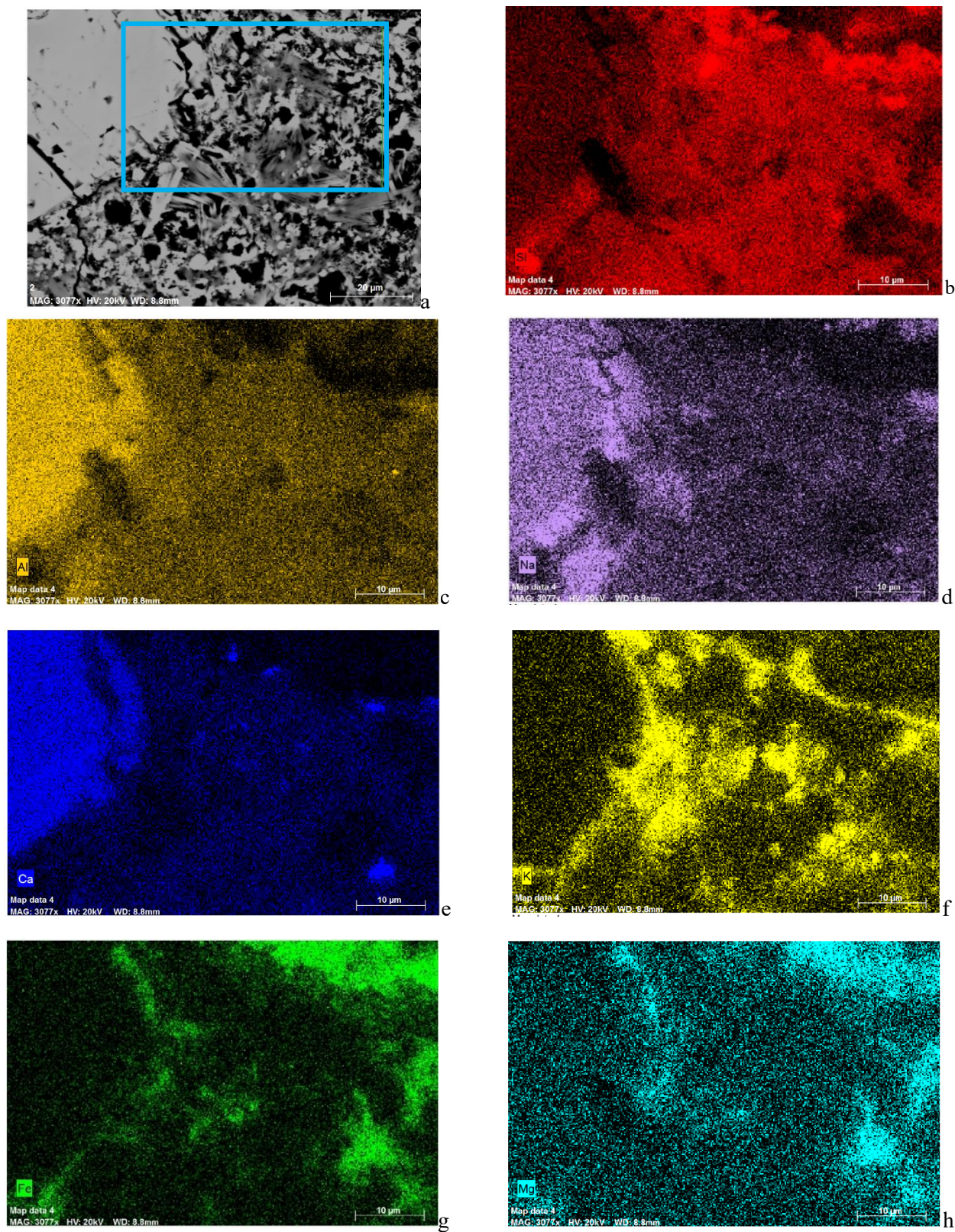


Figure 3.3.1. 20. Photomicrographs of PV FC 4 sample representing the EDS-maps analyses carried out on the area shown in a; b. EDS-map of Si; c. EDS-map of Al; d. EDS-map of Na; e. EDS-map of Ca; f. EDS-map of K; g. EDS-map of Fe; h. EDS-map of Mg.

Zeolitization process has been investigated also in sample PV FC 7 (Figs. 3.3.1.21-22), showing the same composition of the previously observed (Fig. 3.3.1.23).

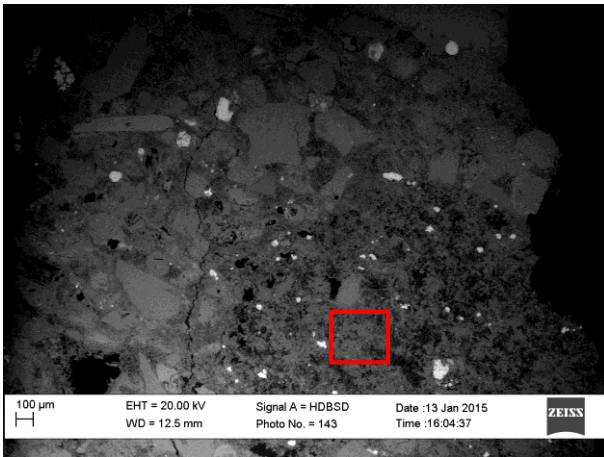


Figure 3.3.1. 21. BSD-ESEM photomicrograph of PV FC 7 sample. The area under investigation is highlighted by a red rectangle.

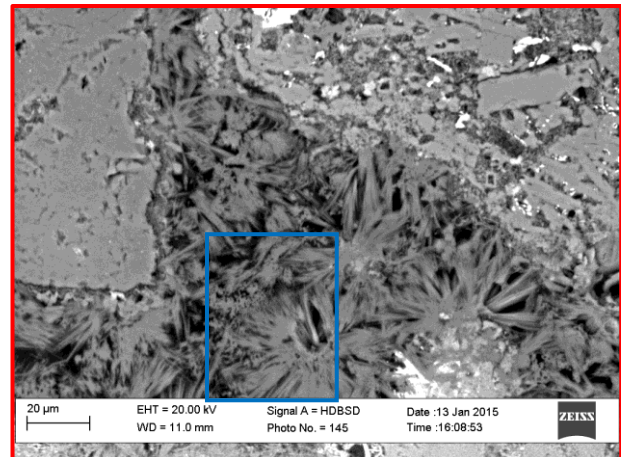


Figure 3.3.1. 22. BSD-ESEM photomicrograph of PV FC 7 sample. The blue rectangle indicates the area of EDS investigation.

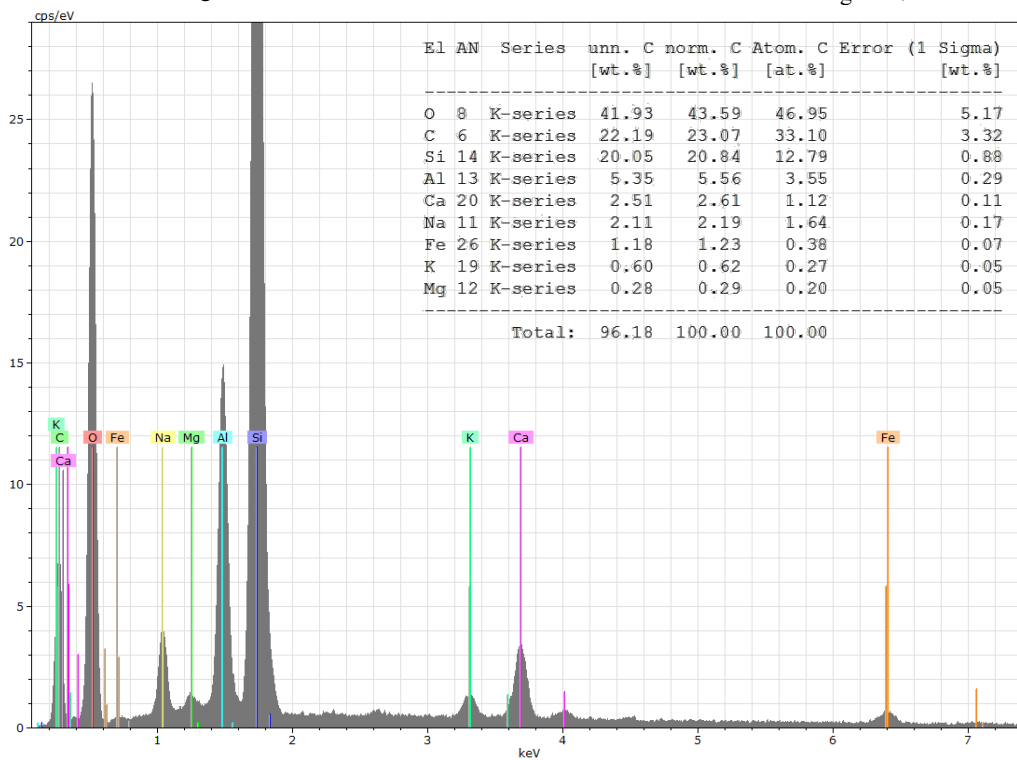


Figure 3.3.1. 23. ESEM-EDS spectrum of PV FC 7 sample, area shown in Fig. 3.3.1.18.

Considering the basaltic andesites at Panama Viejo, amygdales filled with secondary minerals have been observed under stereomicroscope (Fig. 3.3.1.24) and PLM (Figs. 3.3.1.25-26). Therefore, ESEM-EDS investigation was performed on PV FN 4 sample (Figs. 3.3.1.27-28), showing several of these structures.



Figure 3.3.1. 24. Stereomicroscope photomicrograph of PV FN 5 sample.

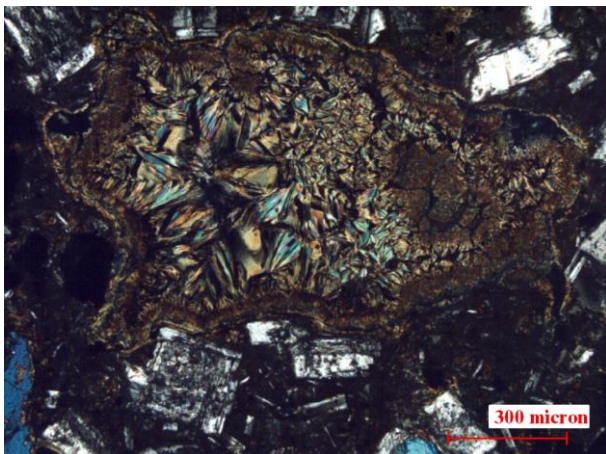


Figure 3.3.1. 25. Photomicrograph of PV FN 4 (xpl, 10x), amygdales filled with secondary minerals.

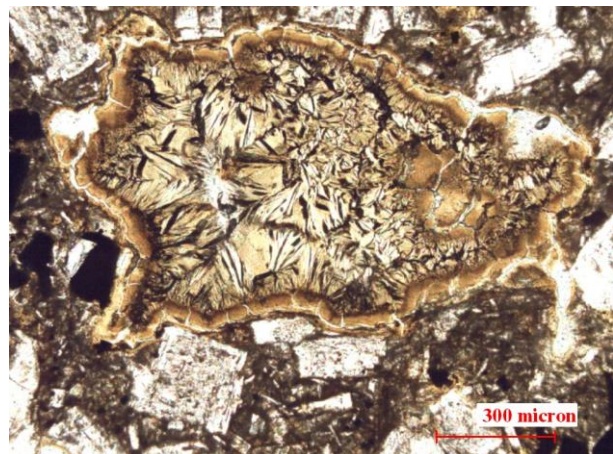


Figure 3.3.1. 26. Photomicrograph of PV FN 4 (ppl, 10x), amygdales filled with secondary minerals.

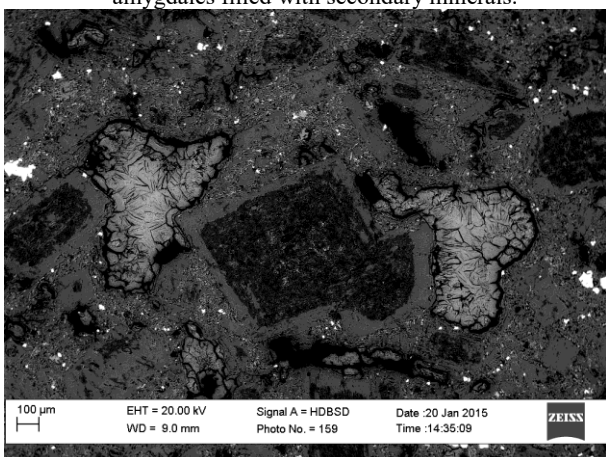


Figure 3.3.1. 27. BSD-ESEM photomicrograph of PV FN 4 sample showing amygdales filled with secondary minerals.

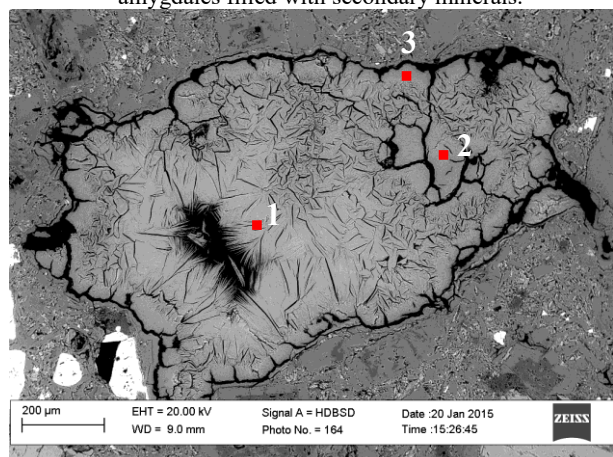


Figure 3.3.1. 28. BSD-ESEM photomicrograph of PV FN 4 sample.

Spectra highlight the following elemental composition: O, Si, Al, Mg, Fe, Ca, k and Na (Figs. 3.3.1.29-31), thus attributable to amygdales containing concentric structures of chlorite.

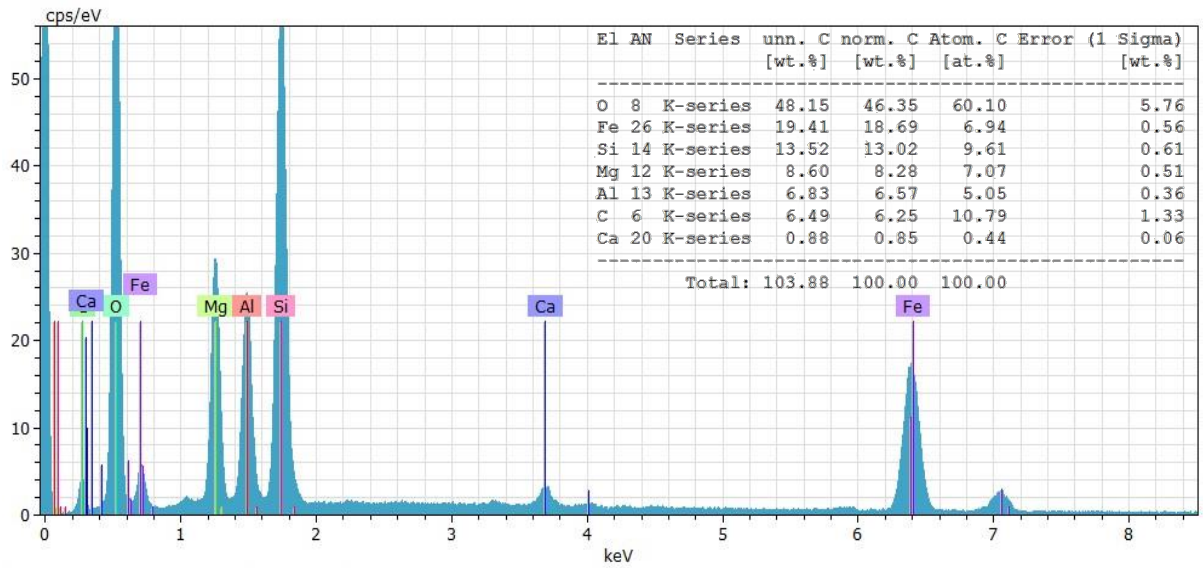


Figure 3.3.1. 29. ESEM-EDS spectrum 1 of PV FN 4 sample, point shown in Fig. 3.3.1.28.

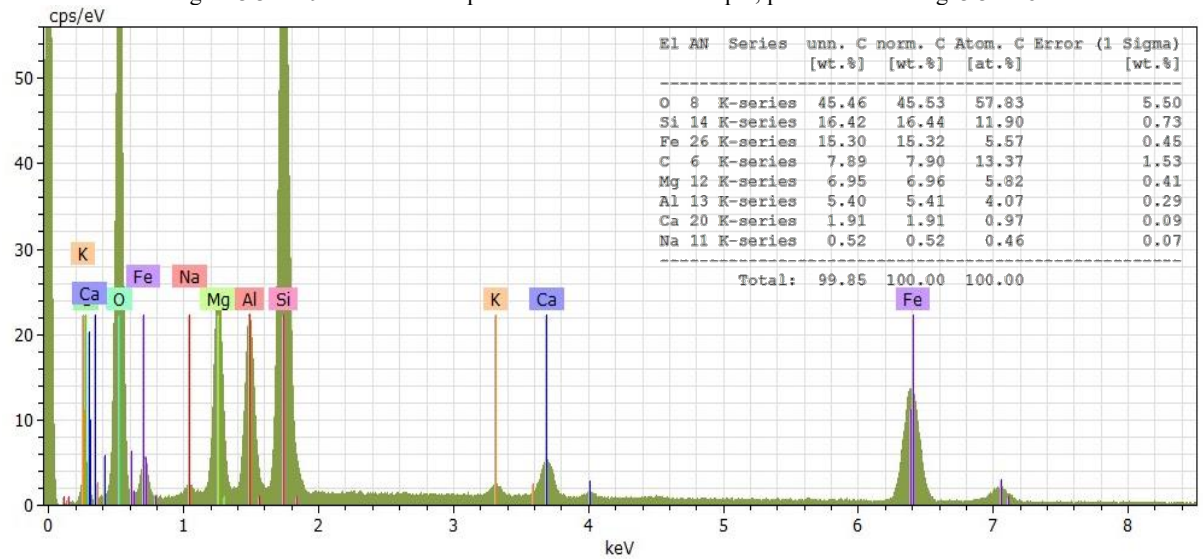


Figure 3.3.1. 30. ESEM-EDS spectrum 2 of PV FN 4 sample, point shown in Fig. 3.3.1.28.

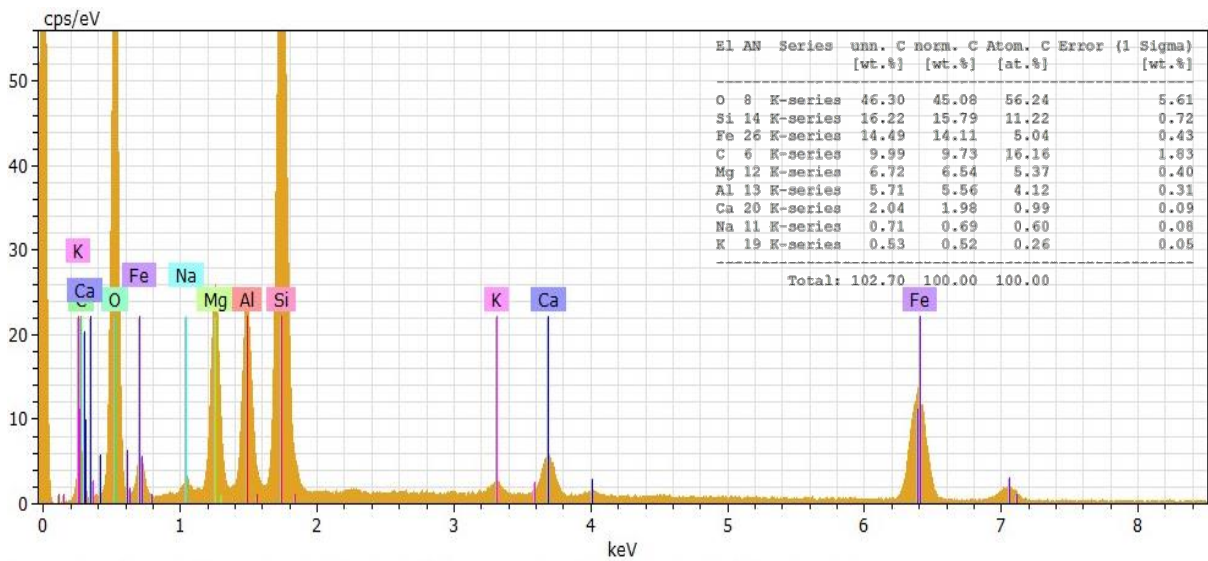


Figure 3.3.1. 31. ESEM-EDS spectrum 3 of PV FN 4 sample, point shown in Fig. 3.3.1.28.



Another structure underwent ESEM-EDS investigation, belonging to the same sample, reported in Figures 3.3.1.32-33.

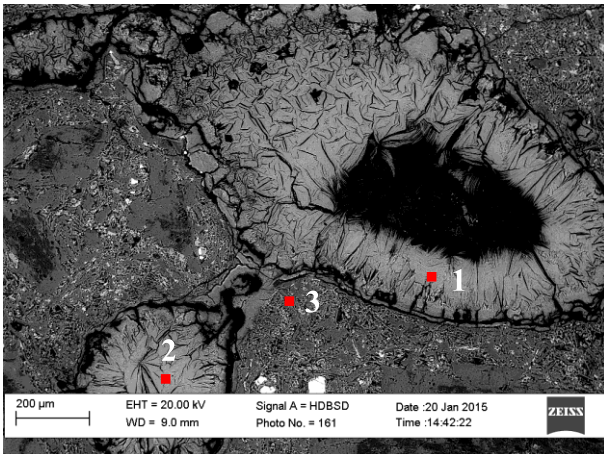


Figure 3.3.1. 32. BSD-ESEM photomicrograph of PV FN 4 sample showing an amygdale filled with secondary minerals. The red dots indicate the points of analysis.

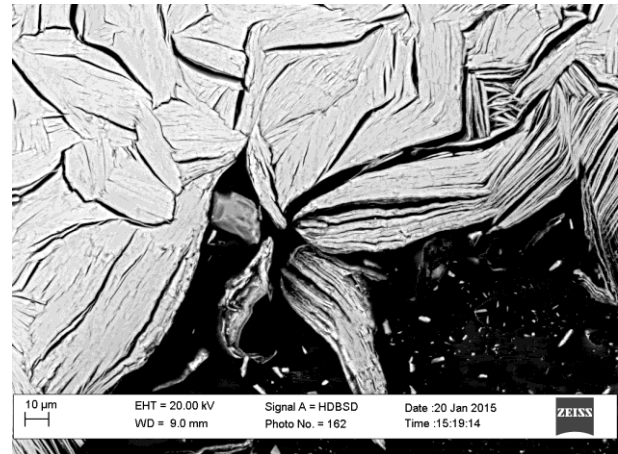


Figure 3.3.1. 33. BSD-ESEM photomicrograph of PV FN 4 sample. Particular of the fibrous structure of the minerals contained in the amygdale.

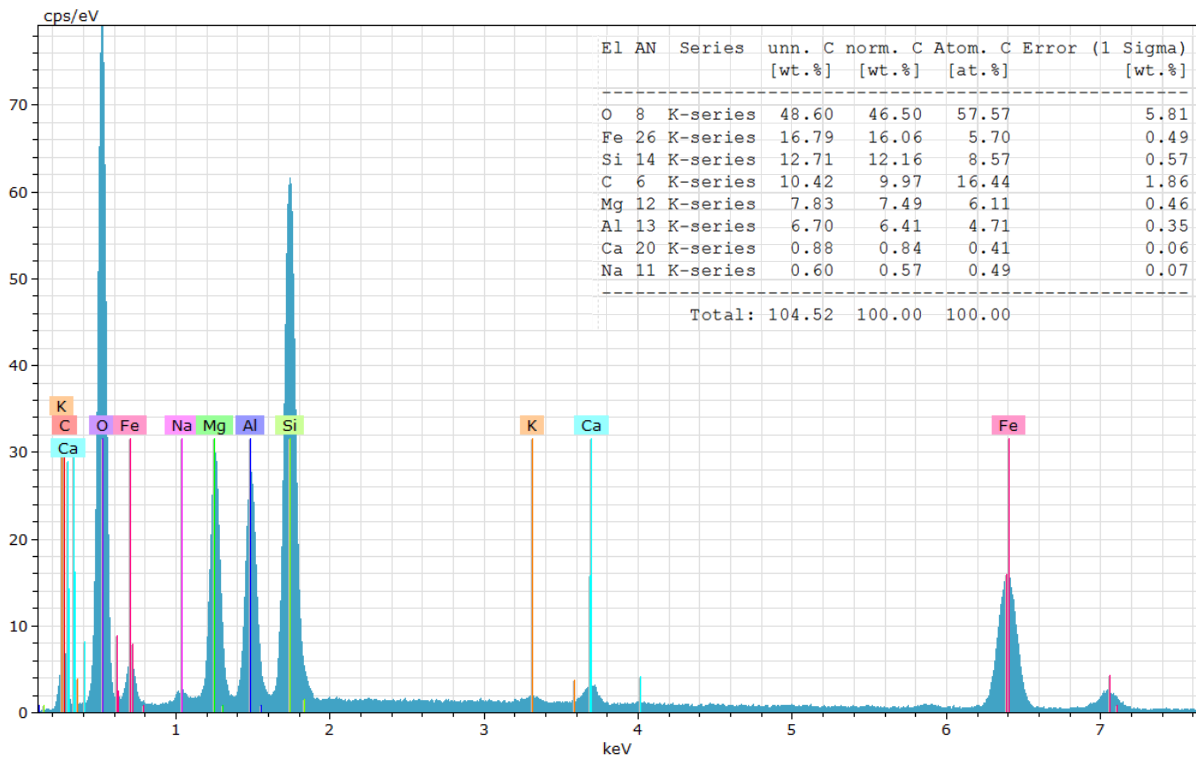


Figure 3.3.1. 34. ESEM-EDS spectrum 1 of PV FN 4 sample, point shown in Fig. 3.3.1.32.

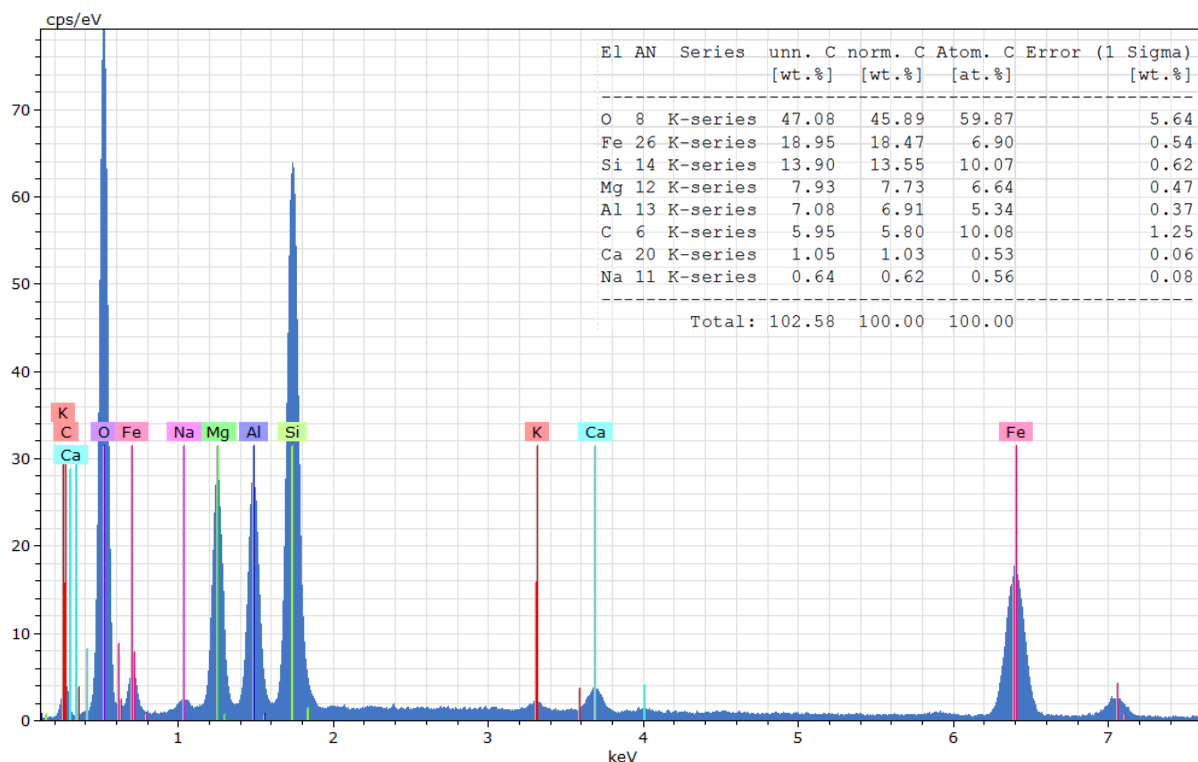


Figure 3.3.1. 35. ESEM-EDS spectrum 2 of PV FN 4 sample, point shown in Fig. 3.3.1.32.

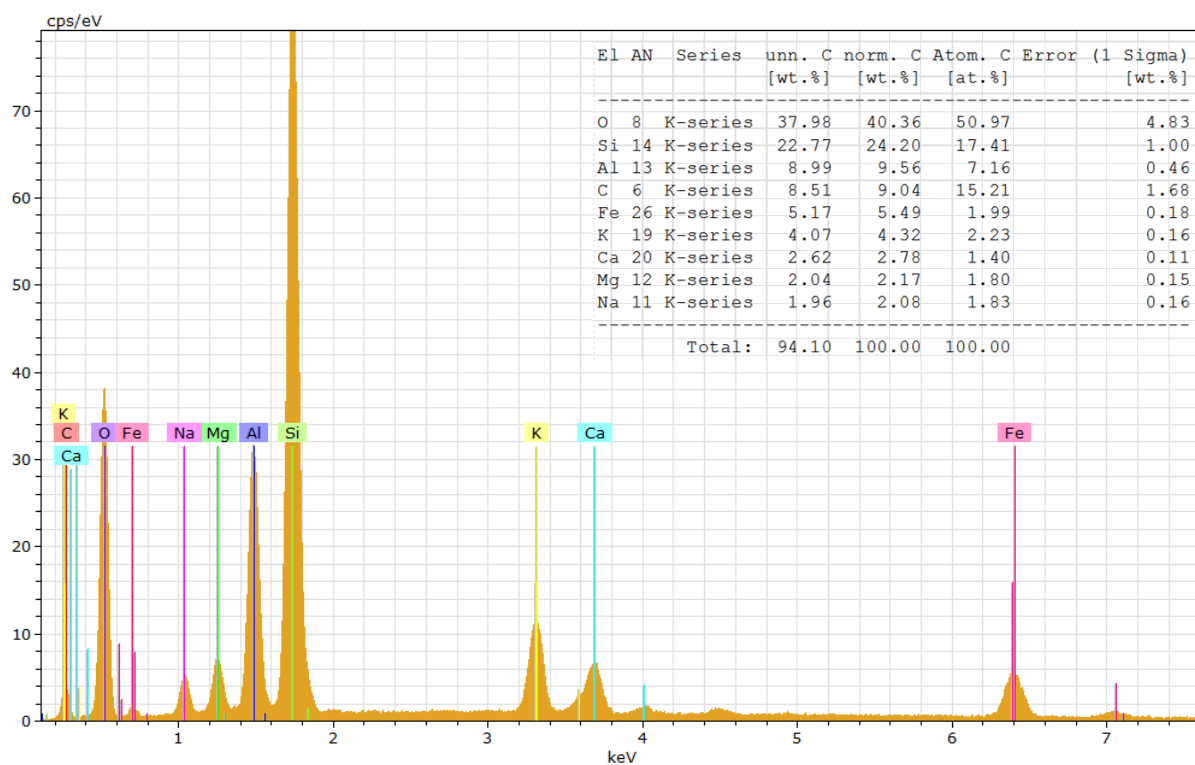


Figure 3.3.1. 36. ESEM-EDS spectrum 3 of PV FN 4 sample, point shown in Fig. 3.3.1.32.

Regarding Portobelo, even in the basaltic andesites detected at Fuerte San Fernando, amygdaloidal structures have been observed also under stereomicroscope, as shown in Figures 3.3.1.33-38 for PB SF 6 sample.



Figure 3.3.1. 37. Stereomicroscope photomicrograph of PB SF 6 sample showing an amygdale.



Figure 3.3.1. 38. Stereomicroscope photomicrograph of PB SF 6 sample showing an amygdale.

Analysing the amygdaloidal morphologies, observed under PLM through ESEM-EDS (Figs. 3.3.1.39-45), the different composition and the morphology aspect, in comparison to the previously observed in Panama Viejo site, is evident. Indeed, the spectra highlight an elemental composition mainly due to Si, O, followed by Al, Ca, K, Na, C and Mg.

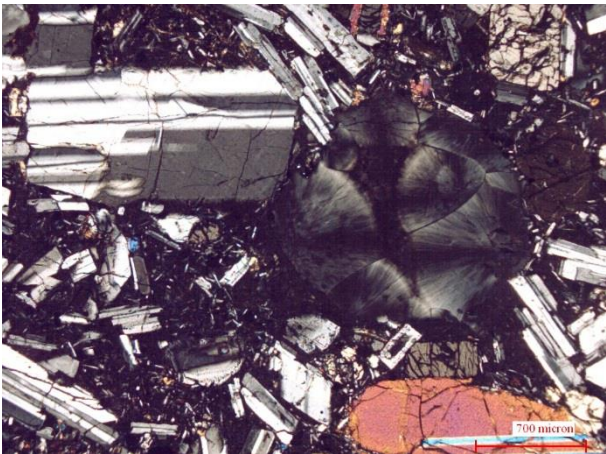


Figure 3.3.1. 39. PLM photomicrograph of PB SF 6 sample showing an amygdale between plagioclases and a pyroxene (right, bottom).

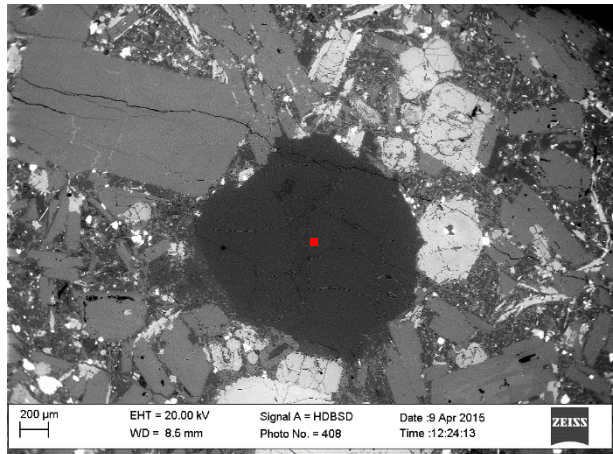


Figure 3.3.1. 40. BSD-ESEM photomicrograph of PB SF 6 represented in Fig. 3.3.1.39. The red dot represents the point of EDS analysis.

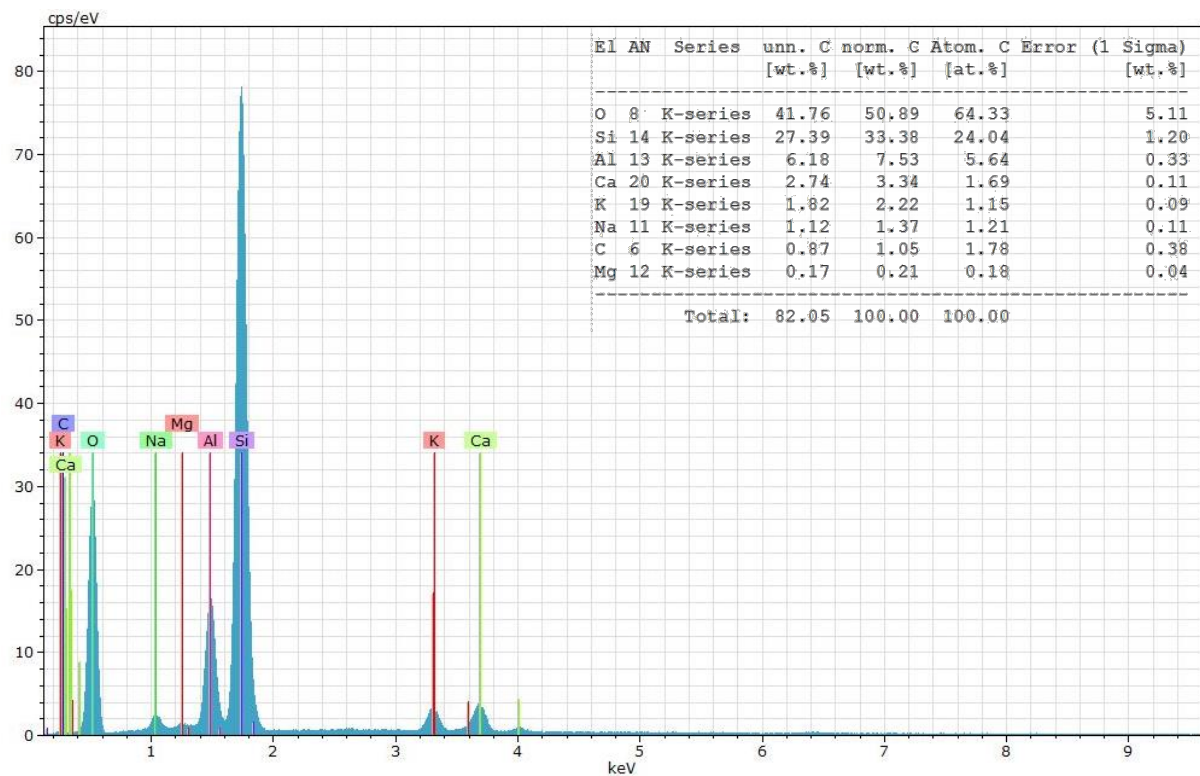


Figure 3.3.1. 41. ESEM-EDS spectrum of PB SF 6 sample, point shown in Fig. 3.3.1.40.

Considering the second point of analysis, represented in Figures 3.3.1.42-43, it is also evidenced the presence of iron sulfide, which is recognizable as the white spot in Figure 3.3.1.43 and through the corresponding spectrum (Fig. 3.3.1.45).

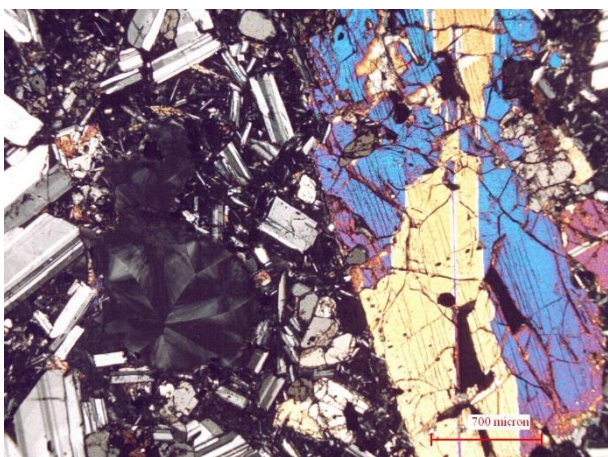


Figure 3.3.1. 42. PLM photomicrograph of PB SF 6 sample showing an amygdale between plagioclases and a pyroxene cluster (right).

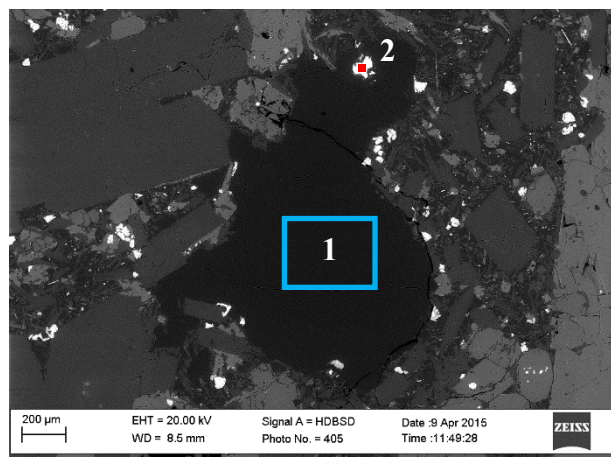


Figure 3.3.1. 43. BSD-ESEM photomicrograph of PB SF 6 represented in Fig. 3.3.1.42. The blue rectangle and the red dot represent respectively the area and the point of EDS analysis.

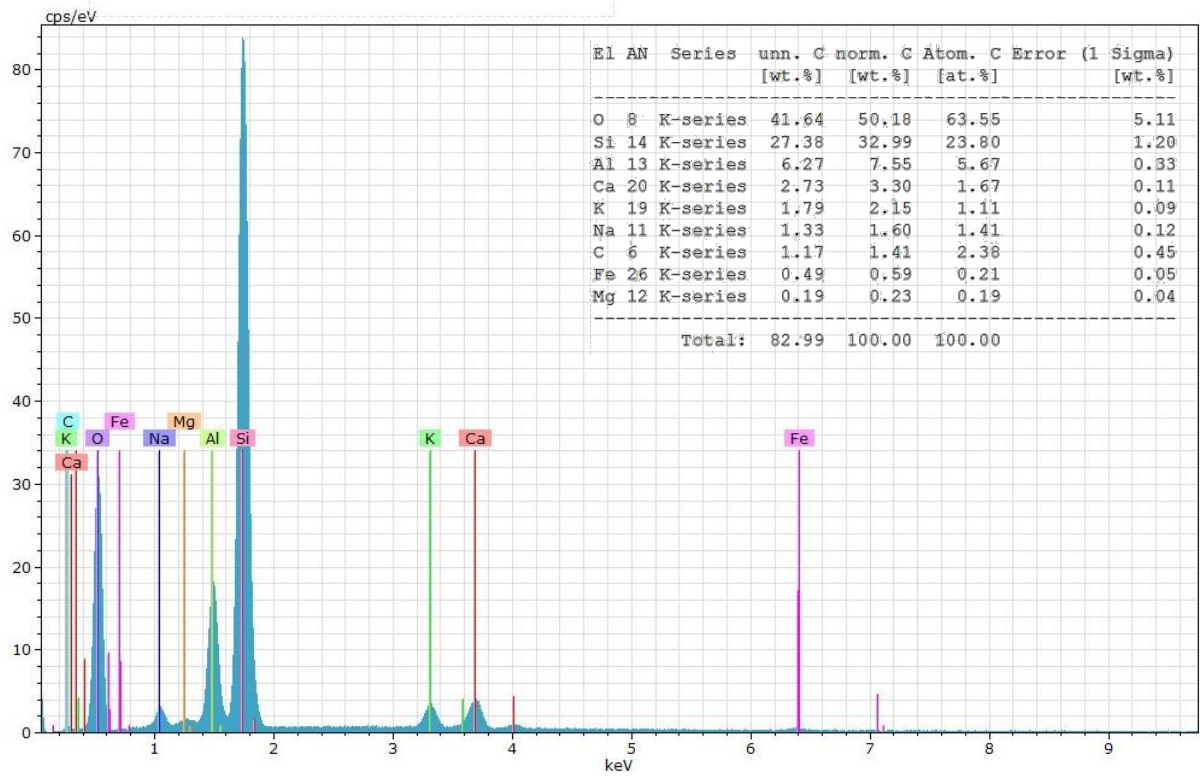


Figure 3.3.1. 44. ESEM-EDS spectrum 1 of PB SF 6 sample, area shown in Fig. 3.3.1.43.

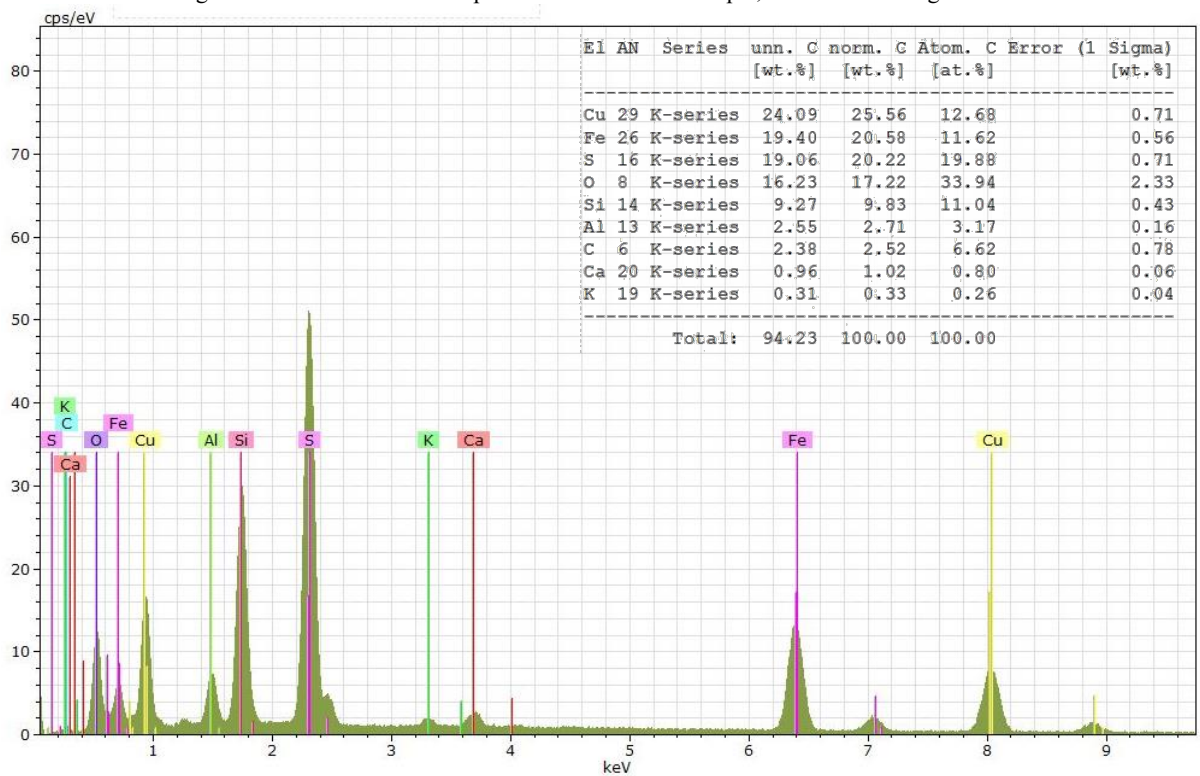


Figure 3.3.1. 45. ESEM-EDS spectrum 1 of PB SF 6 sample, point shown in Fig. 3.3.1.43.

PF SF 7 sample showed a similar structure observed both under PLM (Fig. 3.3.1.1.46) and under ESEM (Fig. 3.3.1.47).

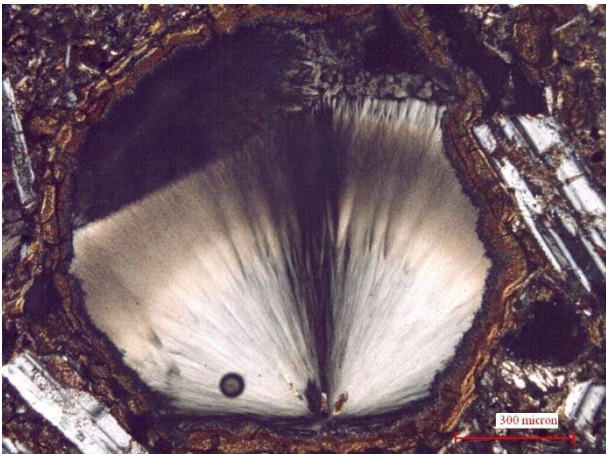


Figure 3.3.1. 46. PLM photomicrograph of PB SF 6 sample showing an amygdale.

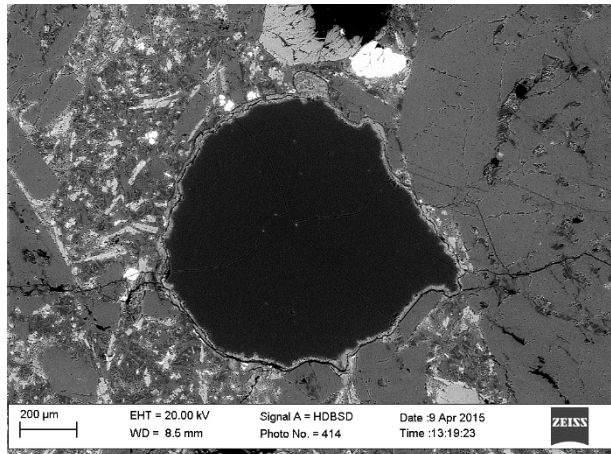


Figure 3.3.1. 47. BSD-ESEM photomicrograph of PB SF 6 represented in Fig. 3.3.1.46.

Performing an ESEM-EDS map on the border of this object, it can be highlighted the composition of the inner part of the amygdale, mainly formed by Si, O, Al, Ca and Na, and of the corona structure, presenting O, Fe and Mg, (Si, Al and K) as main elements (Figs. 3.3.1.48-49). Thus, the internal part can be attributable to chalcedony plus impurities, while the rim to metal oxides.

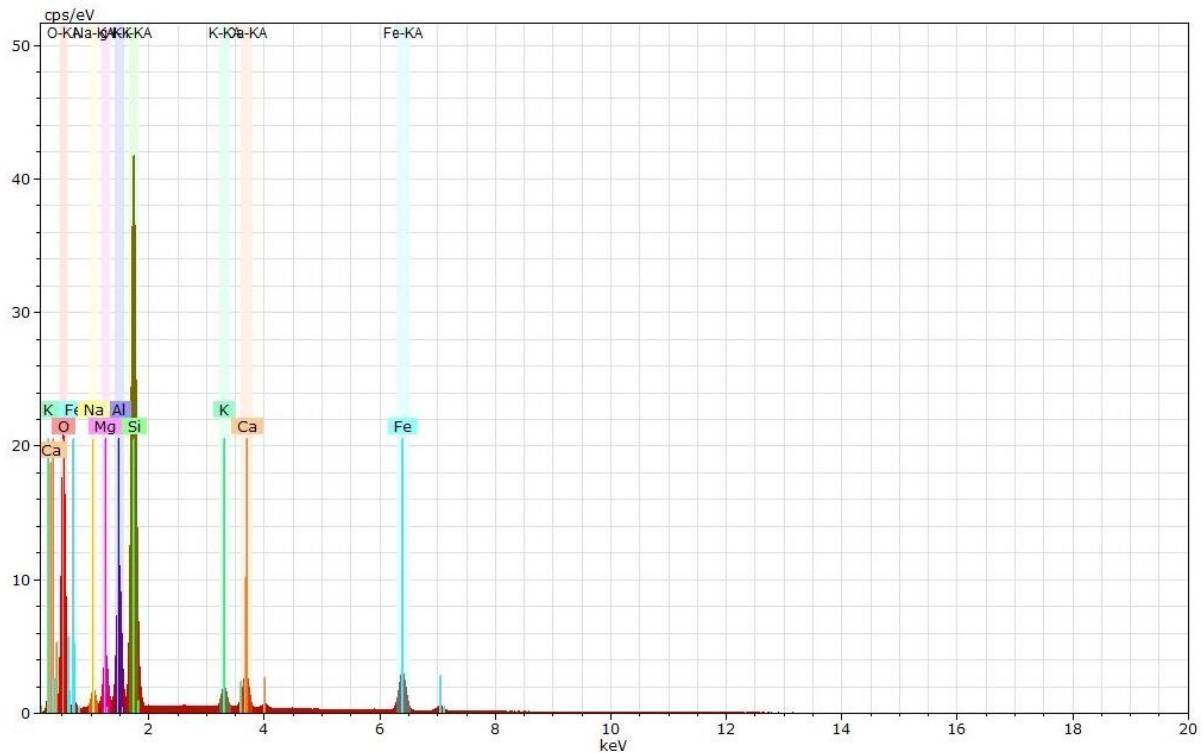


Figure 3.3.1. 48. ESEM-EDS spectrum of PB SF 7 sample, area shown in Fig. 3.3.1.49a.

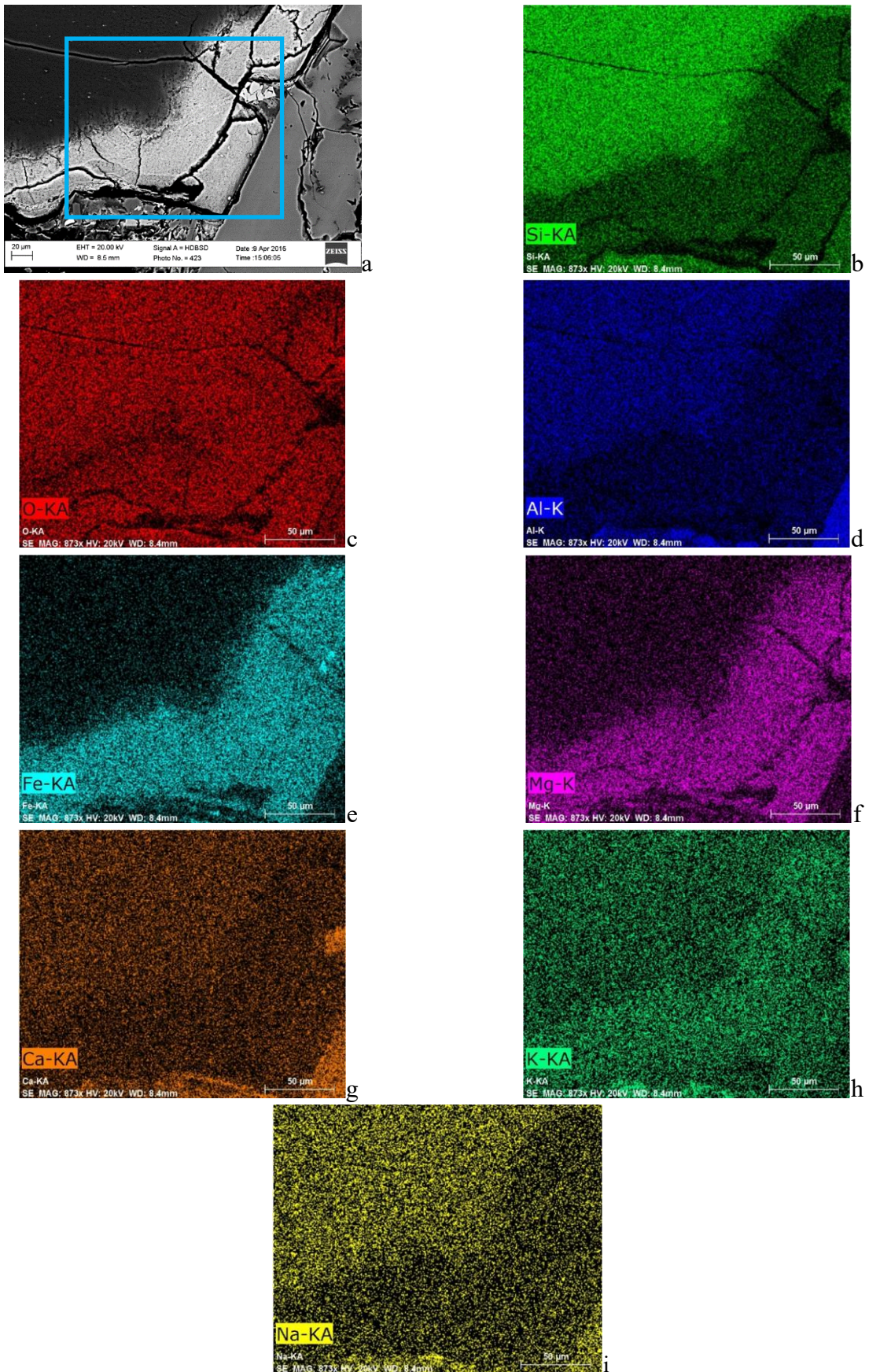


Figure 3.3.1. 49. Photomicrographs of PB SF 6 sample representing the EDS-maps analyses carried out on the area shown in a; b. EDS-map of Si; c. EDS-map of O; d. EDS-map of Al; e. EDS-map of Fe; f. EDS-map of Mg; g. EDS-map of Ca; h. EDS-map of K; i. EDS-map of Na.

Finally, on PB SF 11 sample EDS investigation has been carried out on the bulk specimen (Figs. 3.3.1.51). As clearly visible in the spectrum shown in Fig. 3.3.1.52, in this case calcite minerals fill the amygdale structure.



Figure 3.3.1. 50. Stereo photomicrograph of PB SF 11 bulk sample showing an amygdale.

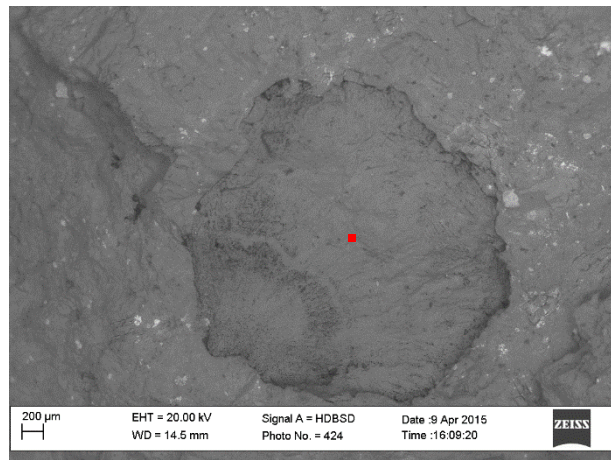


Figure 3.3.1. 51. BSD-ESEM photomicrograph of PB SF 11 bulk, represented in Fig. 3.3.1.50. The red dot represents the point of EDS analysis.

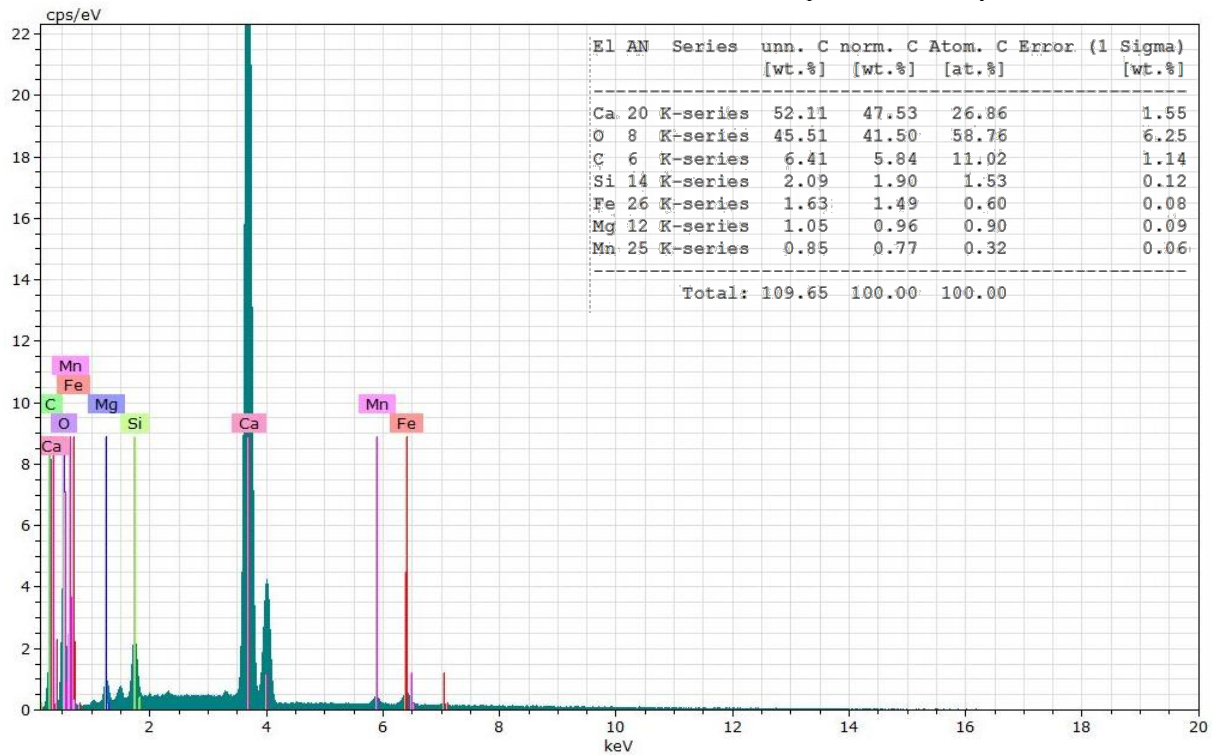


Figure 3.3.1. 52. ESEM-EDS spectrum of PB SF 11 bulk sample, area shown in Fig. 3.3.1.51.



Another case is represented by PV FN 1 sample, showing the presence of a black fragment, similar to obsidian under polarized light microscopy (Fig.3.3.1.53). Nevertheless, analyzing through EDS investigations it resulted mainly formed by carbon (Figs.3.3.1.54-55), thus due to an organic composition ascribable to coal fragment.

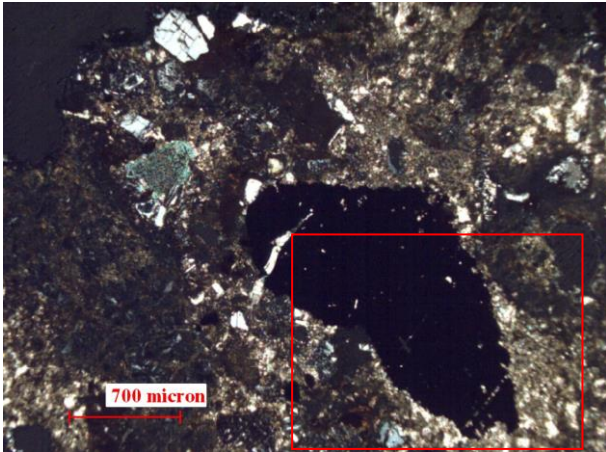


Figure 3.3.1. 53. PLM photomicrograph of PV FN1 sample (xpl, 4x). Particular of the black fragment.

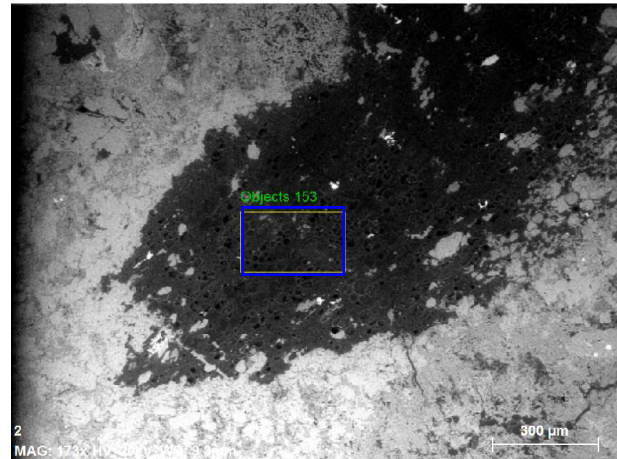


Figure 3.3.1. 54. BSD-ESEM photomicrograph of PV FN 1 sample. The blue rectangle indicates the area of EDS investigation.

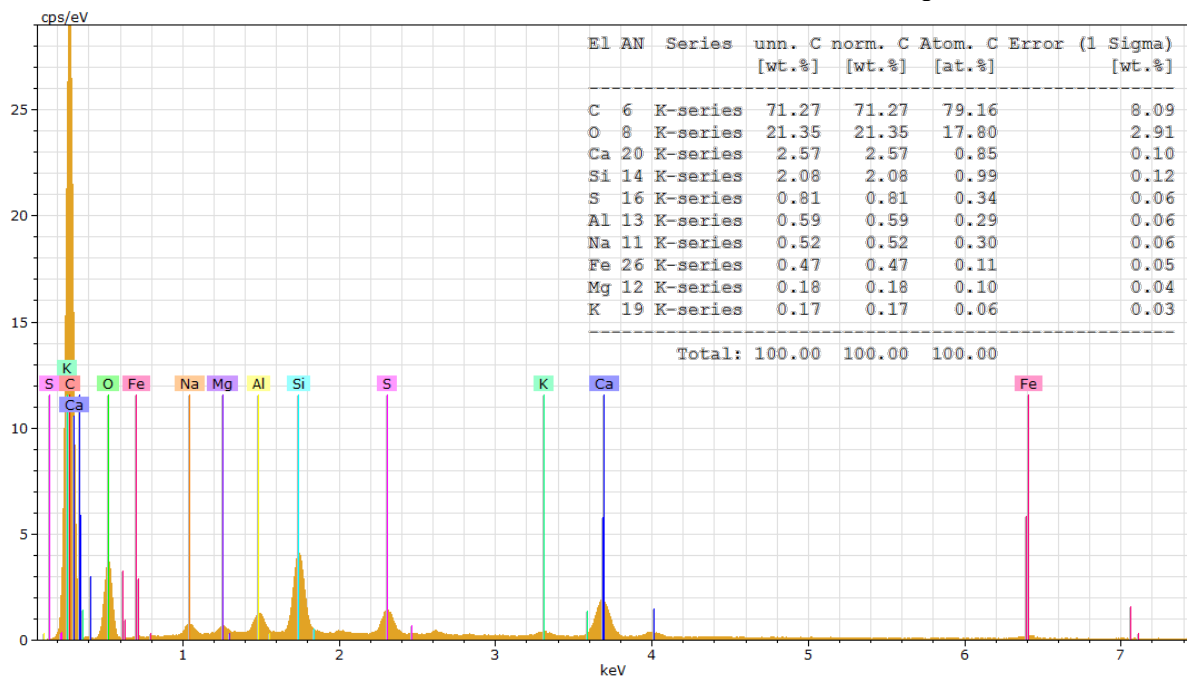


Figure 3.3.1. 55 ESEM-EDS spectrum of PV FN 1 sample, area shown in Fig. 3.3.1.54.

### 3.3.2. Evaluation of the State of Conservation

At Panama Viejo site two samples of altered volcanic rock, PV FC 6 and PV SJdD samples, showing reddish and whitish damage layers, have been investigated, in order to determine the composition of these formations.

Considering PV FC 6, the reddish patina, shown in Figures. 3.3.2.1-2, is due to iron oxides concentrated on the external part, while the inner part shows also the presence of silicates (Figs. 3.3.2.3-4).

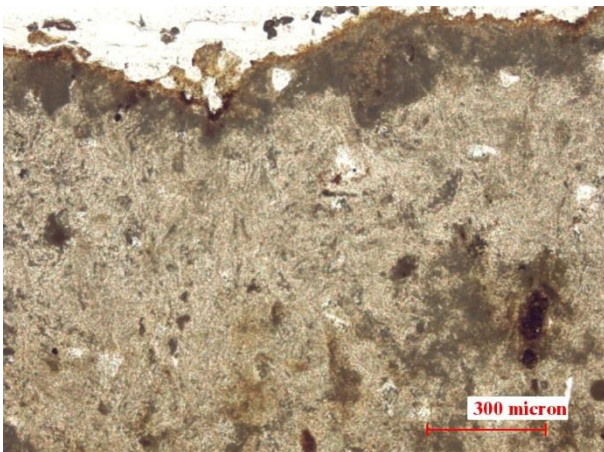


Figure 3.3.2. 1. PLM photomicrograph of PV FC 6 (ppl, 10x), particular of superficial reddish "patina".

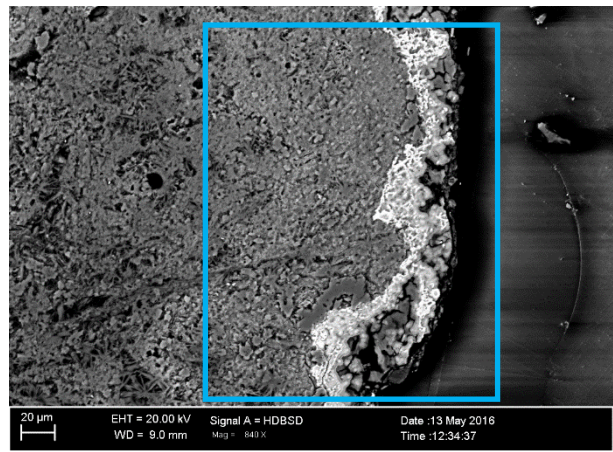


Figure 3.3.2. 2. BSD-ESEM photomicrograph of PV FC 6 sample. The blue rectangle indicates the area of EDS investigation.

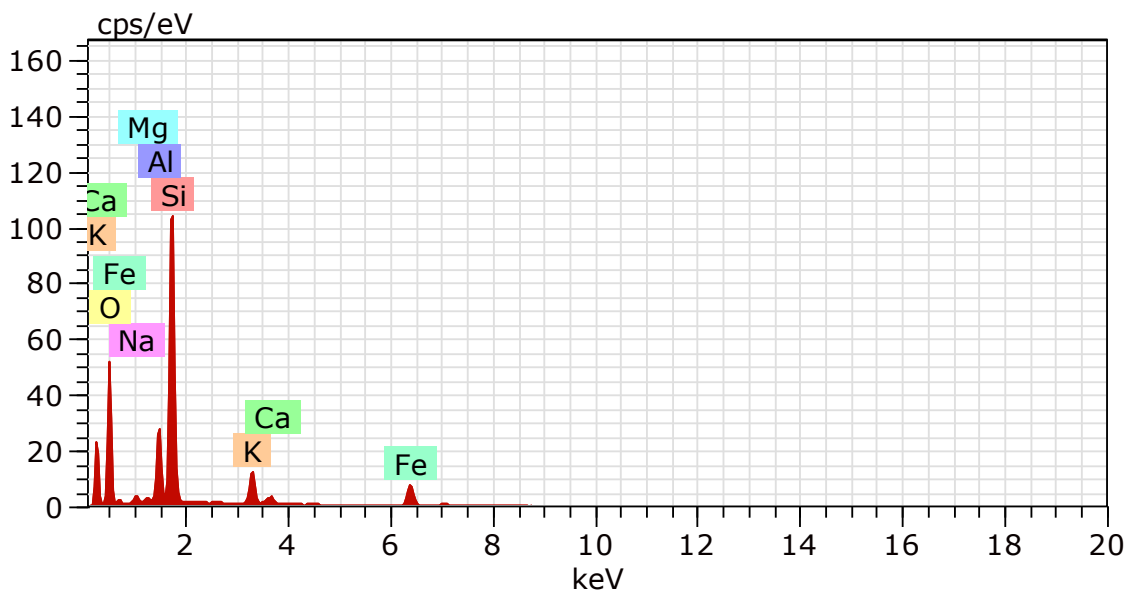


Figure 3.3.2. 3. ESEM-EDS spectrum of PV FC 6 sample, area shown in Figure 3.3.2.2.

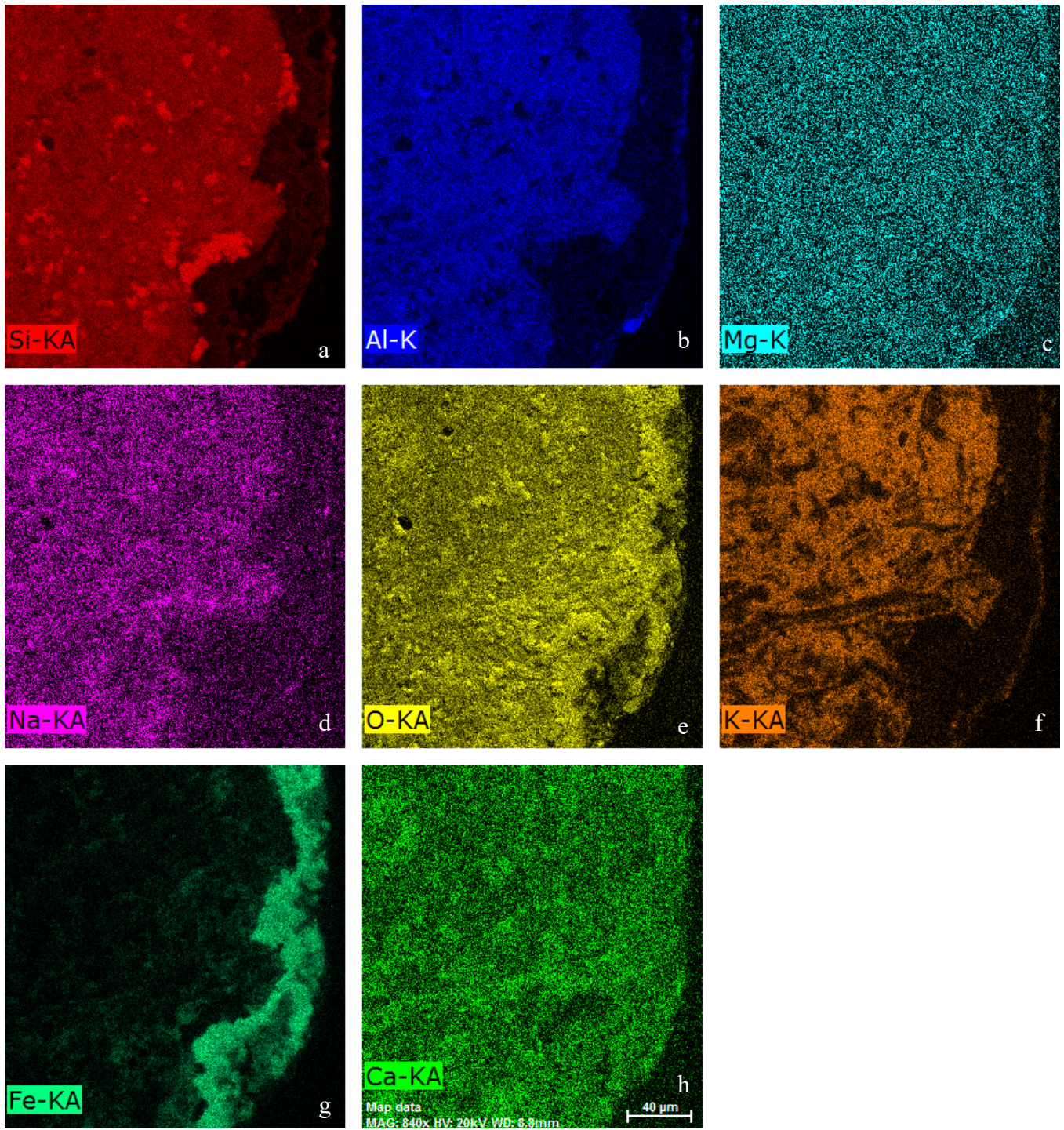


Figure 3.3.2. 4. Photomicrographs of PV FC 6 sample representing the EDS-maps analyses carried out on the area shown in Fig. 3.3.2.2 a. EDS-map of Si; b. EDS map of Al; c. EDS map of Mg; d. EDS map of Na; e. EDS map of O; f. EDS map of K; g. EDS map of Fe; h. EDS map of Ca.

While PV SJdD showed a whitish patina on the inner side, where the sample presented the detachment, represented in Figures. 3.3.2.5-6. According to the analysis, Ca and O mainly compose it, thus it is formed by calcite (Figs. 3.3.2.7-8)

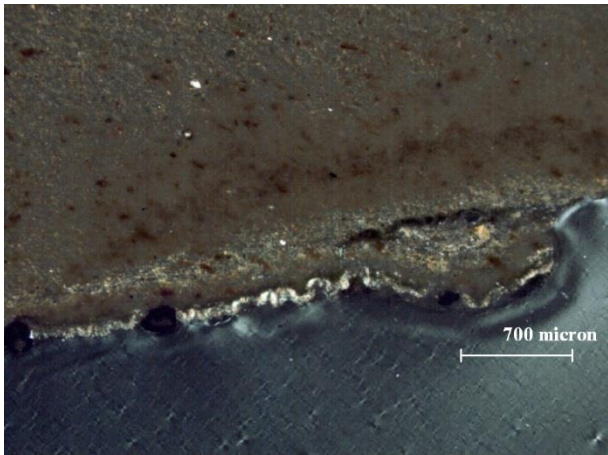


Figure 3.3.2. 5. PLM photomicrograph of PV SJdD sample (xpl, 4x), particular of superficial whitish "patina".

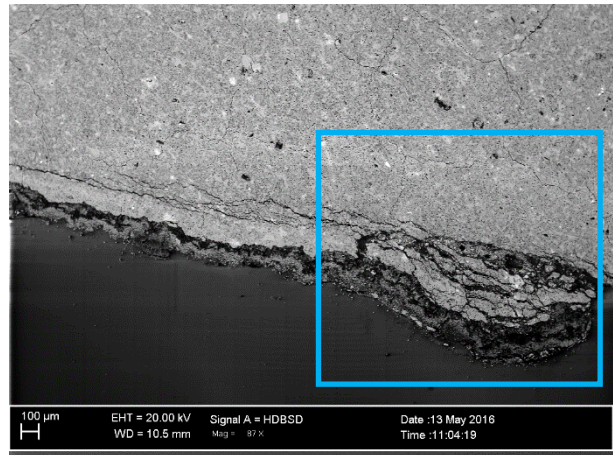


Figure 3.3.2. 6. BSD-ESEM photomicrograph of PV SJdD sample. The blue rectangle indicates the area of EDS investigation.

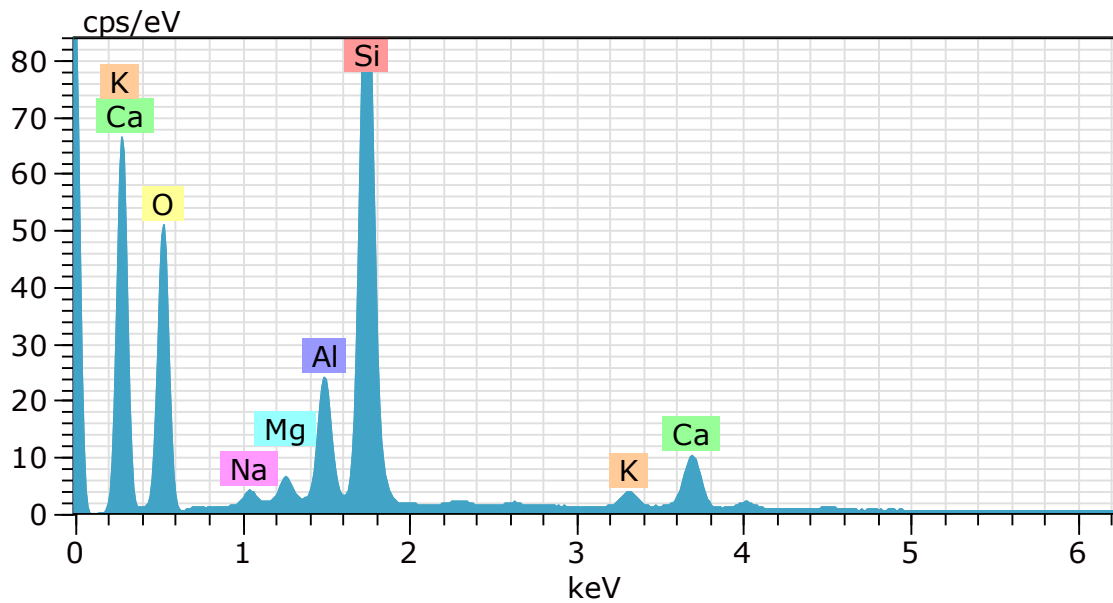


Figure 3.3.2. 7. ESEM-EDS spectrum of PV SJdD sample, area shown in Fig. 3.3.2.6.

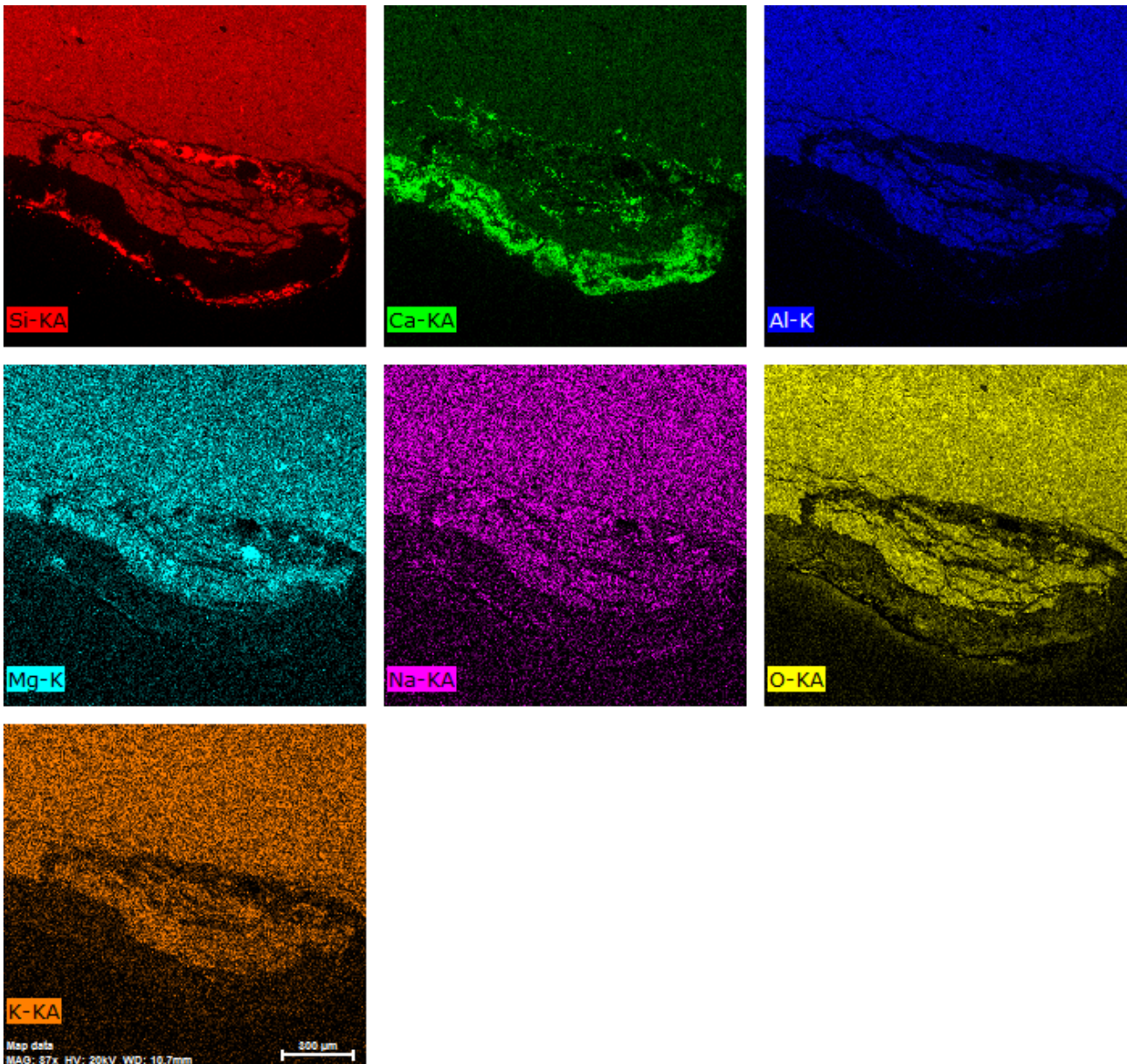


Figure 3.3.2. 8. Photomicrographs of PV SJDd sample representing the EDS-maps analyses carried out on the area shown in Fig. 3.3.2.6. a. EDS-map of Si; b. EDS map of Ca; c. EDS map of Al; d. EDS map of Mg; e. EDS map of Na; f. EDS map of O; g. EDS map of K.

Morphological analysis has been performed on samples showing biological patina, in order to investigate the possible presence of particles deposited due to particulate matter, soil dust, sea spray, etc.

PV TC 4, a tuffite sample, showed a black patina due to biological growth (Fig. 3.3.2.9). Through ESEM observation, it was possible to recognize a morphology attributable to cyanobacteria colonization, according to Torres Montes (1996) it can be *Oscillatoria sp.*. As mentioned in sub-chapter 1.4.1, Macedo et al. (2009) state that these organisms can colonize different kind of substrata, since the propensity of colonization is more conditioned by the physical characteristics of the stone surface, microclimate and environmental conditions than the lithotype composition. Indeed, this “black patina” was observed also on polygenic breccias belonging to other monuments at Panama Viejo site.

Moreover, a cubic crystal was observed on the surface, so probably due to sea-spray deposit of halite (Fig. 3.3.2.10).

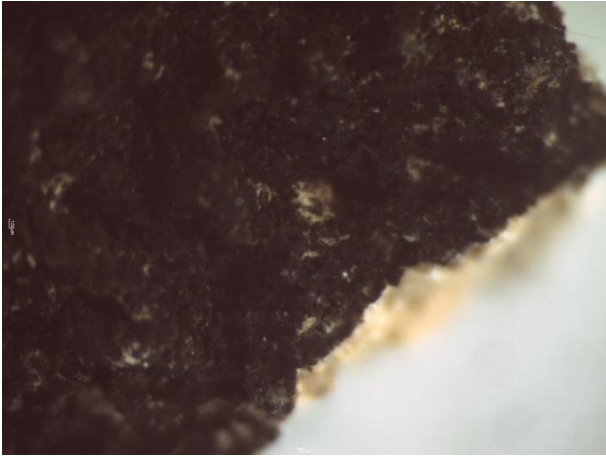


Figure 3.3.2. 9. Stereo photomicrograph of PV TC 4 sample, showing a superficial black algal patina.

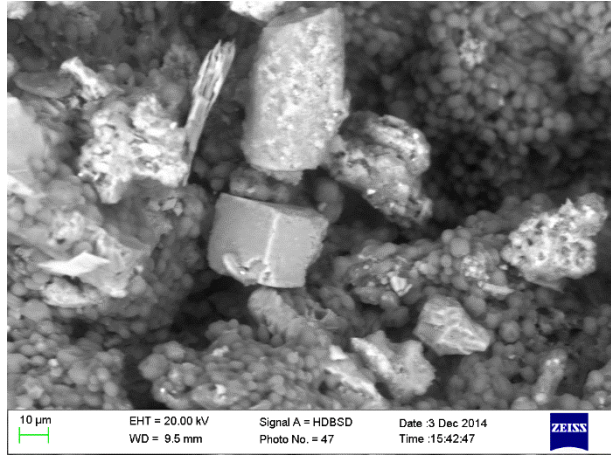


Figure 3.3.2. 10. BSD-ESEM photomicrograph of PV TC 4 sample. Particular of the superficial black algal patina and of a cubic crystal, probably ascribable to NaCl.

Several samples belonging to Portobelo Fortifications showed biological growth due to moss and/or algal presence. In Figures 3.3.2.11-12 it is possible to observe them, respectively on a coral limestone (PB SF 2 sample) and on a grainstone/packstone (PB SF 1 sample).

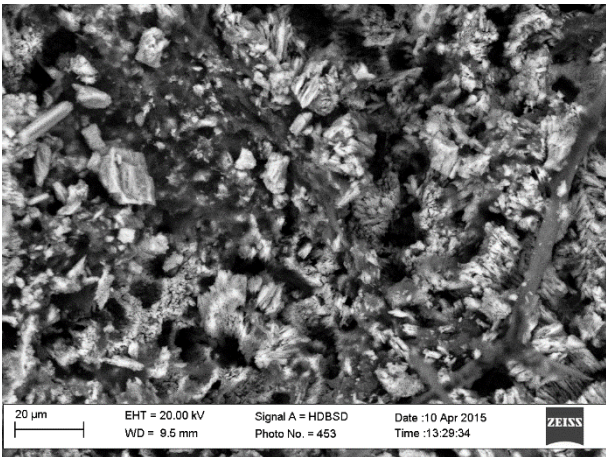


Figure 3.3.2. 11. BSD-ESEM photomicrograph of PB SF 2 showing moss filaments on coral limestone.

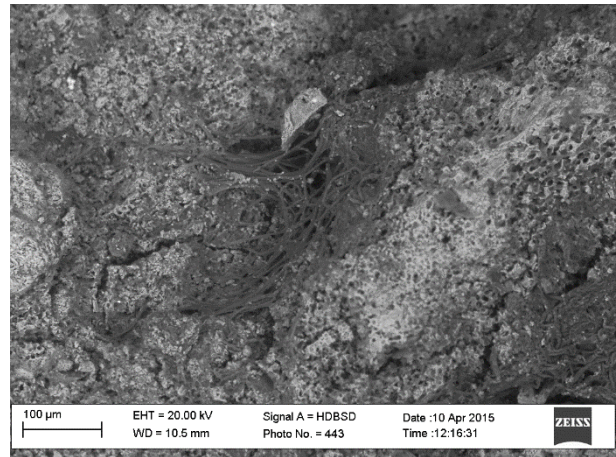


Figure 3.3.2. 12. BSD-ESEM photomicrograph of PB SF 1 showing moss filaments on grainstone/packstone.

On the latter one, PB SF 1 sample, was observed a cubic crystal (Figs.3.3.2.13-14); performing the EDX investigation it resulted being formed by Si, Al, Ca and K while the surrounding part is formed by calcite crystals (Figs.3.3.2.15-16).

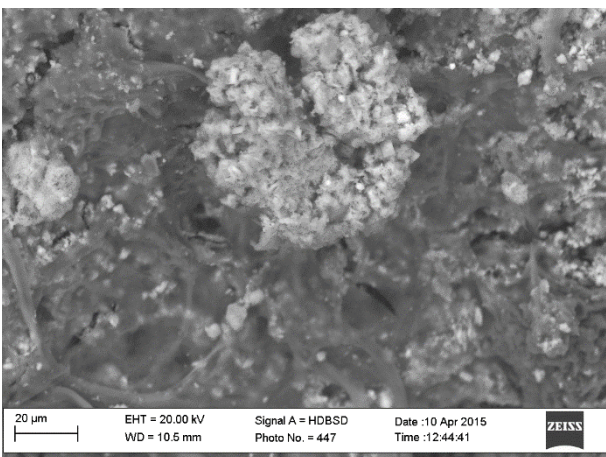


Figure 3.3.2. 13. BSD-ESEM photomicrograph of PB SF 1 showing moss filaments covering the surface except for the part in the middle.

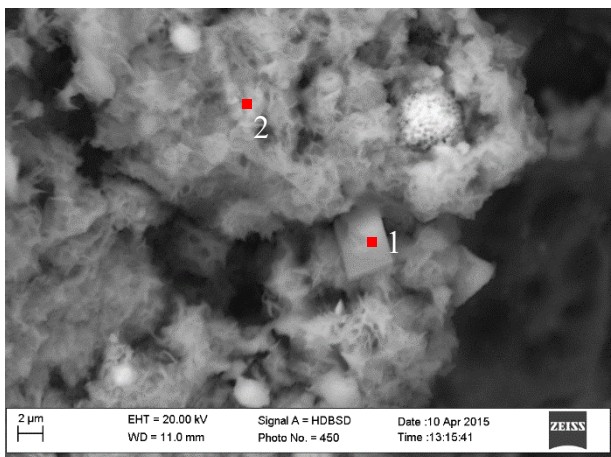


Figure 3.3.2. 14. BSD-ESEM photomicrograph of PB SF 1 showing the presence of a cubic crystal. The red dots show the EDS analysis points.

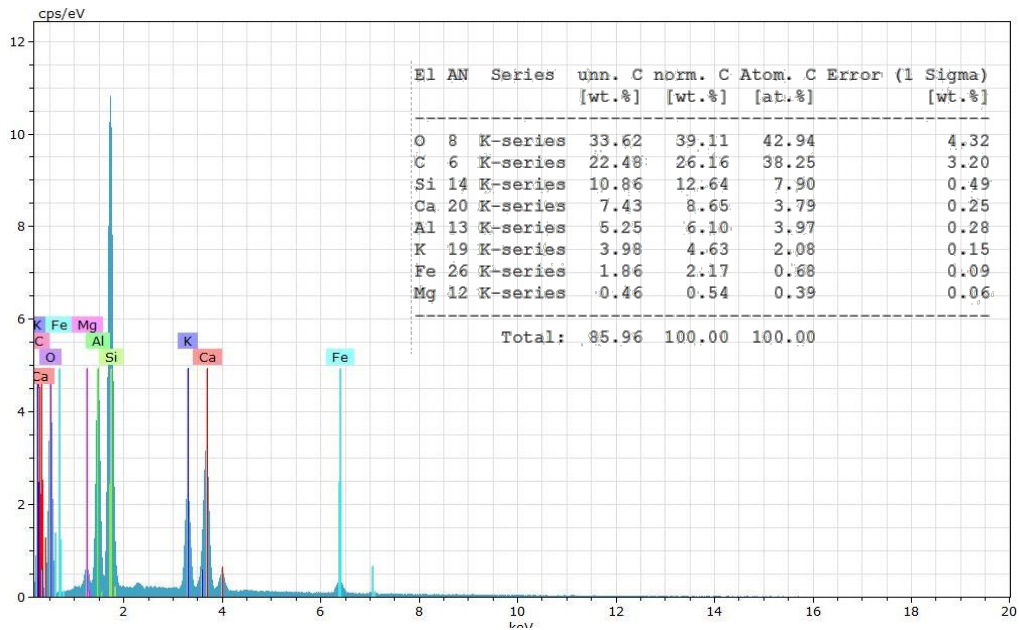


Figure 3.3.2. 15. ESEM-EDS spectrum 1 of PB SF 1 sample, area shown in Fig. 3.3.2.14.

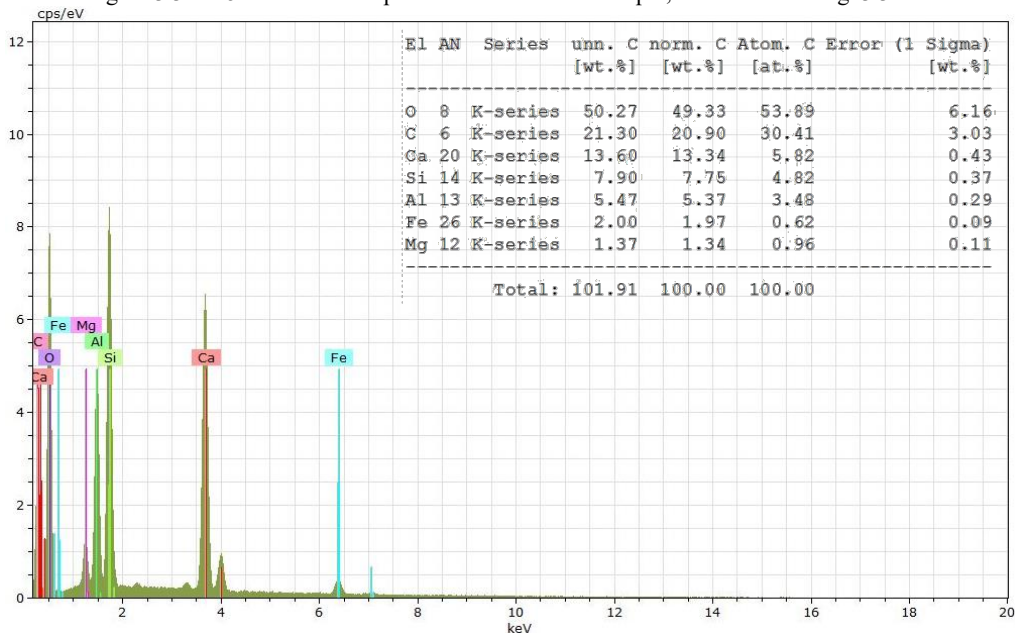


Figure 3.3.2. 16. ESEM-EDS spectrum 2 of PB SF 1 sample, area shown in Fig. 3.3.2.14.

Salt encrustations have been observed in all the sites and sampled at Portobelo fortifications. Specifically at Fuerte San Fernando, PB SF 5 sample, already investigated by PLM (sub-chapter 3.1.2) and XRD (sub-chapter 3.2), underwent ESEM-EDS analyses, showing a composition of calcite (Figs. 3.3.2.17-18), as already demonstrated in the previous analyses.

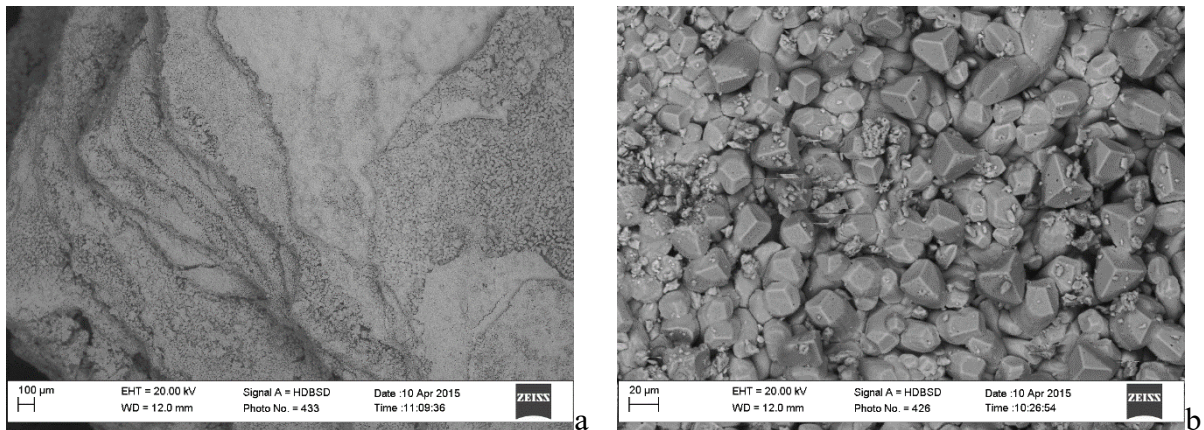


Figure 3.3.2. 17. BSD-ESEM photomicrographs of PB SF 5 calcite encrustation.

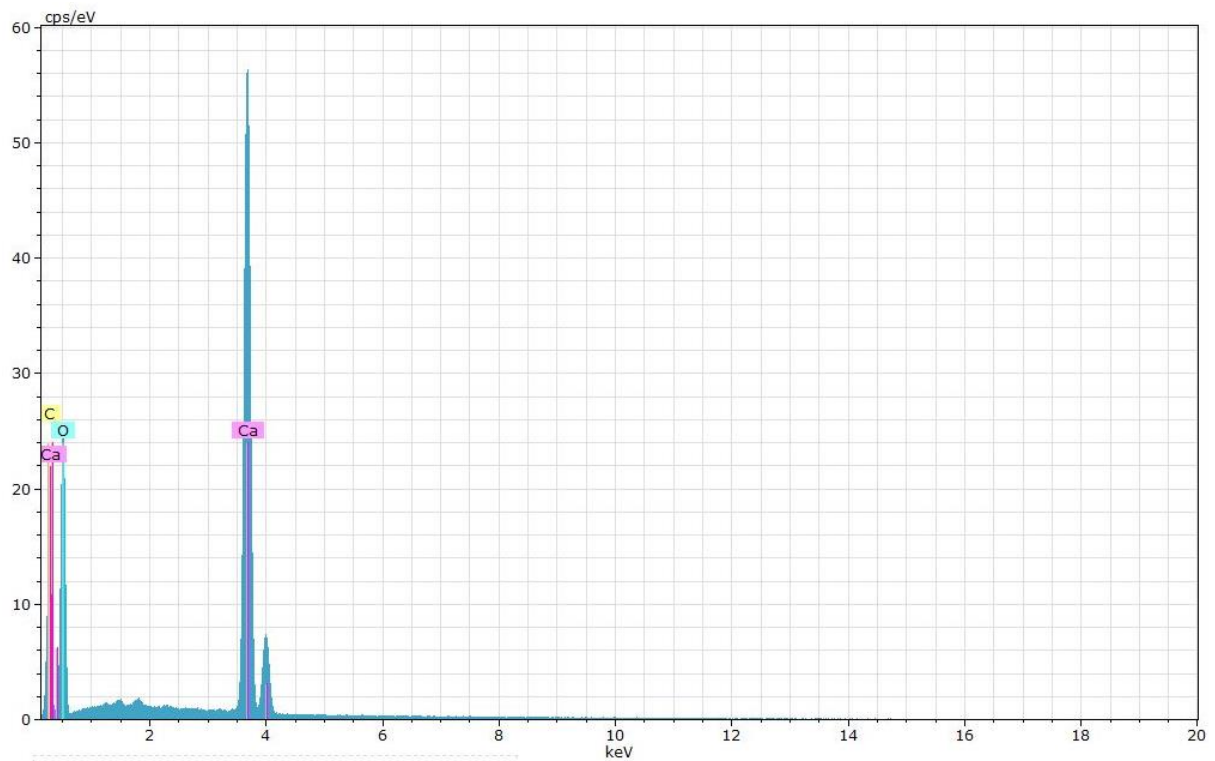


Figure 3.3.2. 18. ESEM-EDS one spectrum obtained by EDS analyses on of PB SF 5 sample, area shown in Fig. 3.3.2.17.

Furthermore, a black patina was observed, (Fig. 3.3.2.19) presenting a composition mainly ascribable to the calcium carbonate substrate of calcite encrustation, but also with Si, Al, S, Mg and Na elements (Figs. 3.3.2.20-21), thus due to biological activity and soil dust deposit.



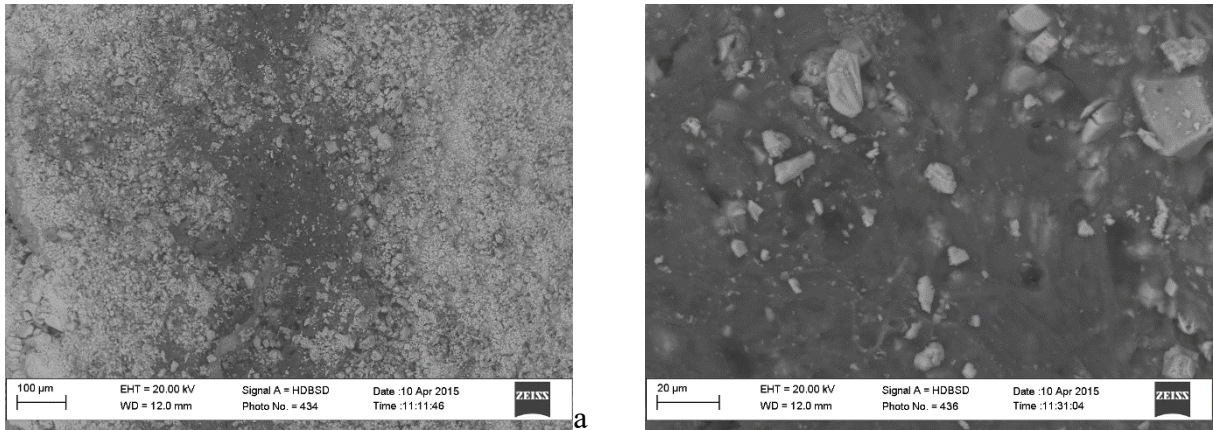


Figure 3.3.2. 19. BSD-ESEM photomicrographs of PB SF 5 calcite encrustation, showing a biological patina (a,b different zoom).

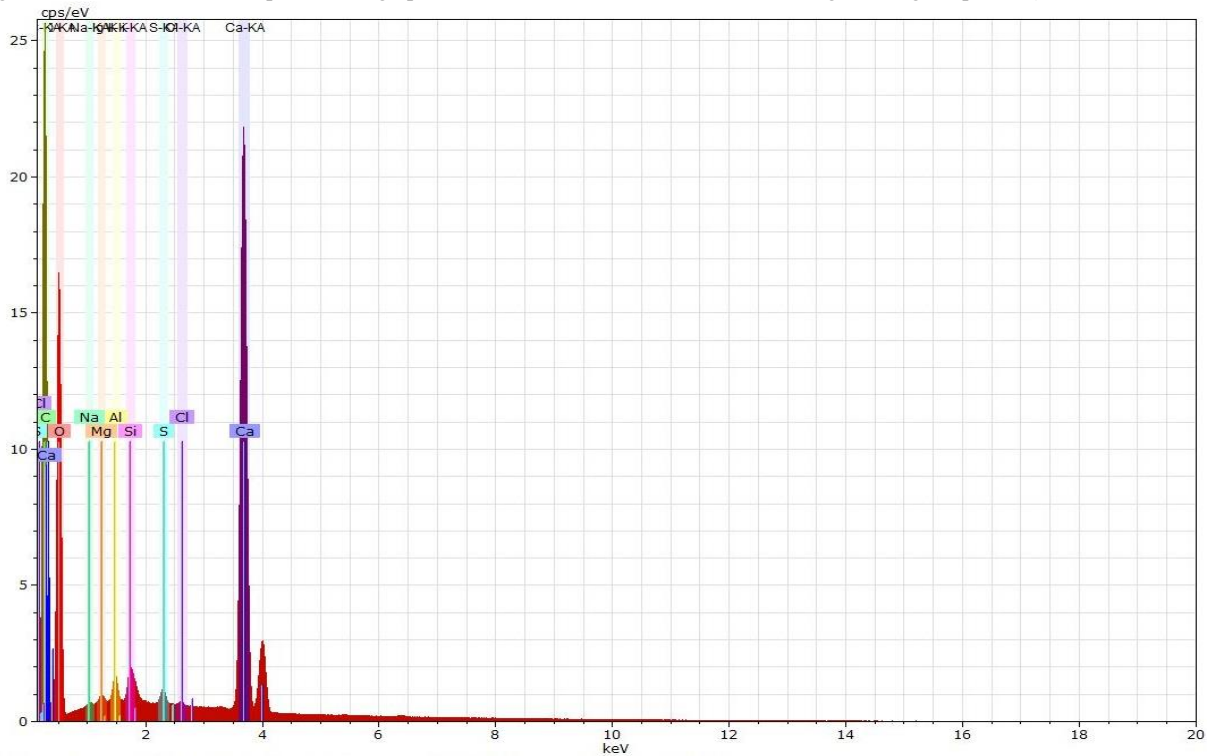


Figure 3.3.2. 20. ESEM-EDS spectrum of PB SF 5 sample, area shown in Fig. 3.3.2.19b.

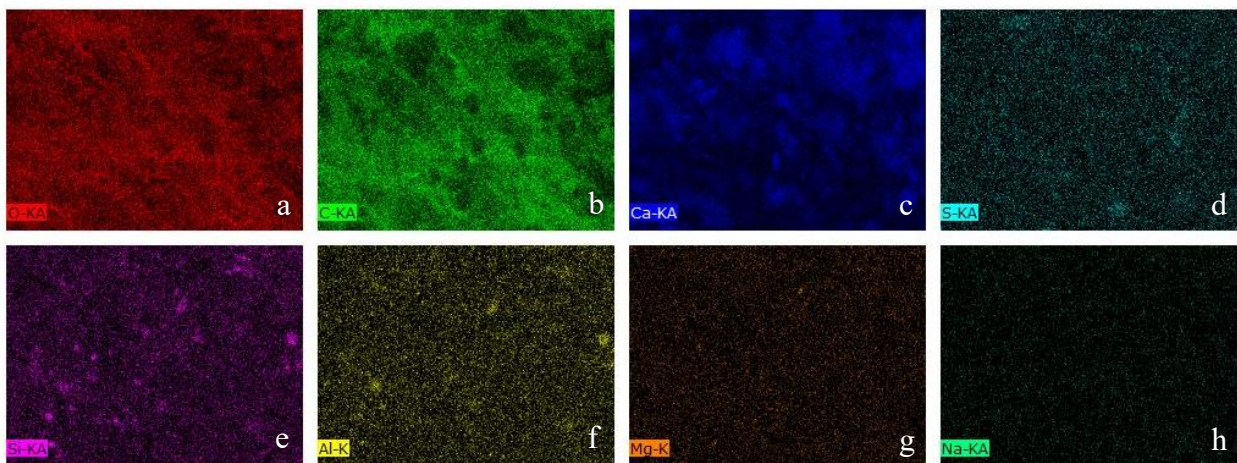


Figure 3.3.2. 21. Photomicrographs of PB SF 5 sample representing the EDS-maps analyses carried out on the area shown in Fig. 3.3.2.19b; a. EDS-map of O; b. EDS map of C; c. EDS map of Ca; d. EDS map of S; e. EDS map of Si; f. EDS map of Al; g. EDS map of Mg; h. EDS map of Na.

### Final remarks

Regarding the materials characterization, through ESEM-EDS analysis performed on thin sections, it was possible to investigate zeolitized areas, shown by several rocks at Panama Viejo site, confirming the previous results obtained by PLM observations and XRPD analysis. Moreover, in these areas, it has been possible to identify the presence of iron oxides and others silicates of Al, Mg, Fe attributable to chlorite.

In addition, amygdaloidal structures detected in the basaltic andesites, belonging to both Panama Viejo and Portobelo sites, have been investigated. Specifically, at Panama Viejo the structures resulted to be filled mainly by radial aggregate of chlorite. While, considering Portobelo, in particular *Fuerte San Fernando* samples, the amygdales can be filled by zeolites, but showing a different aspect respect the previous ones observed at Panama Viejo, surrounded by a rim of chlorite. Finally, the sample belonging to the outcrop showed vesicles filled by calcite.

Referring to the evaluation of the state of conservation, hematite patinas have been detected on altered volcanic rocks at Panama Viejo site. Furthermore, one of them showed also a whitish patina, on the inner surface, mainly made by calcite.

Concerning the biodeterioration, at Panama Viejo tuffite and polygenic breccias showed a black patina ascribable to cyanobacteria colonization. At Portobelo fortresses, the biological growth is mainly due to moss; in addition, encrustations have been analysed, confirming calcite as main component.

### 3.4 X-Ray Fluorescence Spectroscopy (XRF)

Through geochemical analysis, performed by XRF investigations, it has been possible to realize a better understanding of the composition of the different lithotypes and their classification.

#### *Breccias*

Silica and alumina are the major components of these rocks, followed by CaO, due to the carbonate fraction represented by bioclasts; then, Fe<sub>2</sub>O<sub>3</sub>, MgO, ascribable to the presence of chlorite, vermiculite and iron compounds. In addition, the detection of Na<sub>2</sub>O and K<sub>2</sub>O is attributable to the presence of albite plagioclase, zeolites, as clinoptilolite and mordenite, and to montmorillonite.

Among the trace elements, the highest values are recorded for Ba, Sr and V. Moreover, S was present in PV CC 4, PV FN 1, PV JC 4int, PV JC 1 and PV JC 2 samples. Analysing PV FN 1 and PV JC 4int samples by IC analysis, the presence of sulphates was detected (Tab. 3.4.1).

Table 3.4. 1. Bulk rock major (wt %) and trace (ppm) element analyses for breccias.

	PV CC 4	PV CC 5	PV CC 6	PV CR 4	PV FC 4	PV FC 7	PV FC 8	PV FC 11	PV FN 1	PV FN 2	PV JC 1	PV JC 2	PV JC 3	PV JC 4int
SiO <sub>2</sub>	48.96	45.45	47.77	54.71	60.37	54.97	57.59	48.16	48.99	57.71	46.85	43.54	47.89	59.47
TiO <sub>2</sub>	0.85	0.79	0.80	0.79	0.89	0.69	0.73	0.81	0.59	0.87	0.73	0.62	0.88	0.75
Al <sub>2</sub> O <sub>3</sub>	13.05	12.09	13.11	12.05	14.16	11.55	12.03	12.87	8.65	12.86	10.87	9.54	13.64	13.28
Fe <sub>2</sub> O <sub>3</sub>	8.53	7.82	7.96	8.19	8.98	5.70	7.40	8.52	3.52	5.19	8.26	5.54	9.34	5.52
MnO	0.16	0.17	0.14	0.09	0.20	0.09	0.15	0.17	0.13	0.13	0.28	0.20	0.17	0.05
MgO	5.79	5.67	5.18	5.31	2.59	2.86	3.81	5.79	1.55	1.44	3.04	3.21	5.69	2.01
CaO	8.71	11.06	9.23	5.02	4.45	8.39	4.49	9.13	13.89	4.58	12.59	16.68	7.95	3.44
Na <sub>2</sub> O	2.42	2.40	1.70	1.92	2.73	2.97	2.15	1.96	4.28	5.38	1.93	1.74	1.16	2.84
K <sub>2</sub> O	1.48	1.97	1.62	2.56	1.77	1.89	1.81	2.01	1.97	1.75	1.69	1.82	1.96	2.57
P <sub>2</sub> O <sub>5</sub>	0.23	0.23	0.22	0.19	0.21	0.18	0.25	0.30	0.19	0.23	0.17	0.15	0.24	0.16
LOI	9.82	12.36	12.27	9.18	3.65	10.71	9.59	10.27	16.23	9.87	13.59	16.96	11.08	9.91
Tot.	100	100	100	100	100	100	100	100	100	100	100	100	100	100
Anhyd.	90	88	88	91	96	89	90	90	84	90	86	83	89	90
Ba	534.30	499.50	1574.1	638.40	1054.7	728.70	708.60	553.40	744.80	955.70	488.10	471.50	679.30	839.40
Ce	24.60	19.00	20.00	20.40	38.80	27.40	28.90	22.90	33.90	45.40	23.10	16.40	22.40	32.30
Co	26.60	24.20	22.80	21.60	24.20	15.80	23.30	25.00	17.10	24.10	25.70	19.00	24.70	15.10
Cr	21.30	24.70	19.40	44.80	90.60	35.50	65.70	21.80	24.70	65.30	55.80	51.40	16.90	31.20
Cu	72.50	51.20	65.80	42.90	49.40	41.40	48.60	62.30	28.00	47.10	50.20	33.20	101.60	38.00
Ga	18.80	18.70	17.90	20.10	20.80	18.50	18.50	19.90	15.90	15.20	18.10	15.90	19.50	18.10
Hf	7.90	6.50	8.20	11.00	10.30	8.00	9.80	8.00	6.10	9.80	5.90	3.50	10.40	11.30
La	18.20	20.40	11.10	14.40	44.40	16.50	15.10	12.80	9.20	20.60	15.90	9.60	16.00	23.50
Nb	6.00	5.70	5.10	7.20	7.80	8.20	6.60	6.70	8.80	7.80	6.80	6.80	5.30	8.60
Nd	12.00	13.40	10.10	16.80	44.30	12.70	19.50	18.40	14.30	15.50	11.00	4.50	17.60	23.00
Ni	5.90	8.00	8.20	12.60	27.60	9.80	30.40	9.60	6.80	9.00	25.10	16.70	8.00	5.30
Pb	11.30	10.70	12.60	12.90	6.10	30.20	14.20	15.10	20.30	31.80	12.90	9.80	8.20	9.10
Rb	28.80	36.50	26.80	26.80	20.20	17.50	27.90	45.40	18.10	20.50	17.00	15.20	31.10	27.00
S	709.10	0.00	0.00	0.00	0.00	0.00	0.00	0.00	2632.4	0.00	143.80	328.30	0.00	1351.2
Sc	27.70	25.20	25.90	26.20	30.90	21.30	25.90	25.90	15.40	22.30	29.20	24.10	29.00	20.30
Sr	789.60	668.60	1589.9	379.50	488.20	490.30	679.50	784.90	378.90	510.10	389.70	356.30	2280.0	301.60
Th	3.60	3.50	3.50	4.70	4.10	4.40	3.70	3.30	4.00	4.80	2.90	3.30	3.10	6.10
V	241.60	220.90	221.90	182.30	203.50	163.50	177.20	211.40	123.20	190.90	200.30	153.20	249.40	130.80
Y	19.40	16.30	14.90	18.80	53.30	19.10	19.30	18.10	22.20	23.00	20.10	16.50	17.30	27.90
Zn	95.30	86.50	83.00	95.80	104.80	91.10	98.70	104.60	72.10	107.20	113.30	77.10	91.90	56.20
135.50	86.20	77.90	76.00	103.90	103.50	106.50	107.60	88.80	106.20	112.20	78.20	74.50	95.60	

## Tuffite and Sandstone

### Tuffite

Considering tuffite, the highest values are of SiO<sub>2</sub>, Al<sub>2</sub>O<sub>3</sub> followed by CaO, due to the presence of bioclasts, Fe<sub>2</sub>O<sub>3</sub> and MgO, as previously mentioned due to iron compounds and possible chlorite. Furthermore, Na<sub>2</sub>O and K<sub>2</sub>O is ascribable to the presence of albite plagioclase, zeolites, as clinoptilolite and mordenite, and to montmorillonite.

As dominant trace elements, Ba and Sr are the principal in all samples; nevertheless, S shows the highest values in PV TC 3 and PV TC 4. Investigating PV TC 4 sample through IC analysis high sulphate amounts were detected (Tab.3.4.2).

### Sandstone

In sandstones, silica and CaO show the highest weight percentage in all samples, followed by alumina, Fe<sub>2</sub>O<sub>3</sub> and MgO, respectively attributable to quartz, calcite, albite and chlorite. Considering the trace elements, Sr, Ba and Zr shows values greater than 100 ppm (Tab.3.4.2).

Table 3.4. 2. Bulk Bulk rock major (wt %) and trace (ppm) element analyses for tuffites.  
Highlighted in blue the samples belonging to outcrops.

	Tuffite									Sandstone				
	Panama Viejo		Portobelo	San Lorenzo					Portobelo					
	PV TC 3	PV TC 4	PB FdS 10	SL 1	SL 2	SL 4	SL 6	SL 9	PBFSJ4	PBFSJ8	PBFdS2	PBFdS5	PBFdS9	
SiO <sub>2</sub>	55.86	52.89	47.72	49.77	55.75	56.43	42.22	44.36	30.19	30.35	30.75	31.25	32.01	
TiO <sub>2</sub>	0.74	0.64	0.53	0.43	0.57	0.46	0.39	0.41	0.50	0.49	0.48	0.63	0.49	
Al <sub>2</sub> O <sub>3</sub>	11.45	11.13	11.14	12.09	13.76	14.89	8.98	10.76	7.03	7.07	7.04	7.06	7.22	
Fe <sub>2</sub> O <sub>3</sub>	6.42	6.36	6.58	4.34	6.01	7.07	5.66	5.90	4.67	5.06	4.89	5.33	4.36	
MnO	0.14	0.13	0.09	0.32	0.07	0.03	0.07	0.03	0.27	0.57	0.22	0.32	0.19	
MgO	2.15	2.18	6.35	2.60	3.61	5.60	2.36	2.58	3.65	2.91	3.60	3.28	3.24	
CaO	6.38	7.41	12.90	14.95	9.55	7.46	16.59	16.01	28.74	28.94	28.58	28.40	28.56	
Na <sub>2</sub> O	3.38	2.72	1.42	1.90	1.56	2.20	0.55	1.00	1.26	0.60	0.75	0.58	0.83	
K <sub>2</sub> O	1.45	1.83	0.78	0.90	1.04	0.91	1.14	1.03	0.82	0.55	0.93	0.68	0.99	
P <sub>2</sub> O <sub>5</sub>	0.17	0.16	0.20	0.14	0.14	0.14	0.27	0.33	0.12	0.11	0.11	0.12	0.11	
LOI	11.85	14.54	12.29	12.56	7.95	4.81	21.77	17.59	22.75	23.33	22.66	22.35	22.00	
Tot.	100.00	100.00	100.00	100.00	100.00	100.00	100.00	100.00	100.00	100.00	100.00	100.00	100.00	
Anhyd.	88	85	87.71	87.44	92.05	95.19	78.23	82.41	77.25	76.67	77.34	77.65	78.00	
Ba	646.90	719.10	337.30	328.80	362.60	369.30	307.50	282.40	253.10	261.70	262.60	233.60	369.30	
Ce	31.50	28.70	9.30	11.70	9.80	12.80	14.40	16.50	10.10	9.70	15.80	13.70	17.10	
Co	22.50	16.80	27.30	19.60	23.30	20.10	18.20	16.10	19.00	20.80	18.40	17.80	23.10	
Cr	46.40	36.30	62.80	68.80	75.70	66.20	62.10	87.10	56.60	58.80	42.10	62.30	54.60	
Cu	39.80	31.90	28.00	22.20	29.20	29.30	20.70	25.50	17.40	15.10	13.70	13.60	13.20	
Ga	16.90	16.40	16.40	15.70	16.50	19.50	13.70	14.20	12.80	11.80	13.50	11.50	12.30	
Hf	8.90	7.40	3.90	3.10	5.70	7.10	2.60	2.30	0.00	0.00	0.00	0.00	0.00	
La	10.10	21.20	8.50	3.80	11.60	6.70	5.60	8.90	2.70	8.40	7.70	9.30	6.90	
Nb	7.80	7.70	3.90	5.70	5.60	4.90	5.40	4.50	5.50	7.00	6.20	6.60	5.50	
Nd	12.60	12.10	3.20	5.60	4.20	5.20	6.40	2.60	2.70	3.10	4.50	4.30	5.30	
Ni	9.30	8.30	33.80	27.10	29.30	21.30	27.60	29.60	11.30	13.00	12.70	10.40	16.60	
Pb	17.00	13.60	7.80	7.00	7.00	7.30	10.30	5.90	8.40	5.10	8.20	7.80	7.50	
Rb	16.90	21.30	7.20	8.80	9.50	9.60	14.50	12.80	6.40	5.20	8.70	6.00	7.40	
S	9978.40	4483.40	0.00	0.00	0.00	0.00	0.00	0.00	0.00	0.00	0.00	0.00	21.20	
Sc	22.80	22.50	21.90	16.30	22.40	16.50	13.50	17.10	17.50	20.30	18.50	19.20	19.90	
Sr	427.90	533.50	1437.40	797.30	865.90	774.00	1653.00	2061.40	536.40	706.90	606.40	700.70	715.10	
Th	3.70	4.40	1.50	1.60	1.60	1.40	1.10	1.10	1.50	1.00	1.40	1.20	0.80	
V	153.90	124.50	104.10	84.50	120.10	82.80	95.20	100.10	81.50	80.80	76.90	92.20	70.60	
Y	17.70	19.10	6.50	7.10	6.90	4.60	6.60	5.30	7.30	8.00	9.50	7.80	8.50	
Zn	112.60	98.40	63.60	50.30	65.50	51.60	51.60	57.10	49.70	46.10	50.70	46.50	51.70	
Zr	106.00	112.20	51.20	47.20	57.20	59.10	53.50	52.70	123.20	110.50	111.50	306.10	119.50	

## Igneous rocks

### Basaltic Andesite

Analysing the results obtained, it is deducible that silica and alumina are the major components, followed by Fe<sub>2</sub>O<sub>3</sub> and CaO. Moreover, in samples PV FN 4, PV FN 5 and PV Q 2 also MgO is high, thus, together with the Fe<sub>2</sub>O<sub>3</sub>, it is attributable to chlorite and iron compounds.

Regarding the trace elements, Ba, Sr, V and Cu result the most abundant (Tab.3.4.3).

### Rhyolite

Rhyolites present as main compounds silica and alumina, while Ba, Zr and Sr show the highest values among the trace elements (Tab.3.4.3).

### Rhyodacite

In the volcanic altered rocks, the main compounds are silica and alumina, followed by Fe<sub>2</sub>O<sub>3</sub>, CaO, Na<sub>2</sub>O and K<sub>2</sub>O. Sr and Ba show the highest values among the trace elements, followed by Zr (Tab.3.4.3).

Table 3.4. 3. Bulk rock major (wt %) and trace (ppm) element analyses for igneous rocks.  
Highlighted in blue the samples belonging to outcrops.

	Basaltic andesite				Portobelo			Rhyolite		Rhyodacite	
	Panama Viejo				Portobelo			Panama Viejo		Rhyodacite	
	PV FN 4	PV FN 5	PV vic CR	PV Q 2	PB SF 6	PB SF 7	PB SF 11	PV CT 1	PV CT 2	PV FC 6	PV FC 9
SiO <sub>2</sub>	49.83	50.07	49.81	50.02	55.04	52.95	55.34	72.43	70.95	66.90	61.20
TiO <sub>2</sub>	1.09	1.13	1.15	1.13	0.68	0.80	0.70	0.52	0.53	0.49	0.52
Al <sub>2</sub> O <sub>3</sub>	13.34	13.96	14.91	12.51	15.56	14.86	14.82	16.15	15.84	12.47	11.01
Fe <sub>2</sub> O <sub>3</sub>	10.94	10.50	7.55	10.31	8.44	9.04	8.03	0.20	2.19	3.18	4.96
MnO	0.13	0.14	0.28	0.13	0.15	0.17	0.17	n.d.	n.d.	0.02	0.07
MgO	8.08	7.99	3.66	10.58	4.49	6.29	5.87	n.d.	n.d.	0.55	2.18
CaO	8.35	8.46	9.14	6.07	8.43	8.18	7.67	0.14	0.27	1.44	2.88
Na <sub>2</sub> O	2.08	2.14	3.34	1.84	2.49	2.32	3.03	7.45	6.82	1.47	2.21
K <sub>2</sub> O	1.05	1.10	1.60	1.29	1.32	1.43	2.18	2.05	2.24	5.50	0.65
P <sub>2</sub> O <sub>5</sub>	0.29	0.26	0.29	0.39	0.25	0.28	0.25	0.03	0.03	0.05	0.05
LOI	4.83	4.27	8.27	5.74	3.14	3.69	1.95	1.28	1.40	7.93	14.26
Tot.	100.01	100.02	100.00	100.01	99.99	100.01	100.01	100.25	100.27	100.00	99.99
Anhyd.	95.18	95.75	91.73	94.27	96.85	96.32	98.06	98.97	98.87	92.07	85.73
Ba	369.20	364.80	590.10	407.20	928.50	1003.80	937.20	835.80	850.30	1114.00	441.40
Ce	16.10	22.70	20.10	23.10	15.00	12.90	11.40	65.00	71.80	37.50	19.70
Co	39.50	40.00	27.90	29.90	29.40	33.00	28.50	2.80	4.10	7.70	13.30
Cr	59.00	75.60	24.10	8.30	90.40	113.20	98.10	0.00	0.00	4.00	27.60
Cu	100.60	113.40	58.00	59.00	207.70	142.00	50.50	3.20	3.10	23.00	47.50
Ga	19.70	20.20	22.40	23.10	16.50	16.70	16.60	17.90	19.20	12.80	17.40
Hf	7.50	7.20	7.20	8.10	6.80	7.30	7.50	16.90	16.90	13.70	10.70
La	16.40	15.70	10.90	16.00	11.70	9.30	8.40	40.10	38.10	13.90	20.60
Nb	5.50	5.60	8.30	9.40	4.60	8.80	4.40	16.00	14.60	10.30	5.70
Nd	12.70	11.60	13.70	17.40	5.70	5.20	3.20	34.90	44.00	19.50	18.50
Ni	16.60	17.90	8.50	2.50	21.70	39.30	22.70	0.00	0.00	6.00	8.00
Pb	10.40	5.10	14.60	10.30	7.80	8.80	9.50	6.60	8.10	8.30	15.20
Rb	10.60	10.80	24.40	21.70	14.30	18.60	35.30	39.00	46.20	67.10	19.40
S	0.00	0.00	0.00	0.00	0.00	0.00	0.00	0.00	0.00	0.00	697.80
Sc	40.20	40.60	31.80	33.00	26.30	28.80	28.70	8.60	11.60	14.10	17.80
Sr	390.30	399.40	469.40	572.20	633.20	769.40	513.40	200.70	353.30	255.50	1155.00
Th	1.90	2.00	3.10	3.30	2.10	2.70	2.20	7.90	6.50	8.60	2.40
V	366.50	379.60	321.70	245.60	289.40	295.10	285.60	2.60	2.90	67.90	62.50
Y	16.60	17.30	21.20	18.90	13.20	13.30	12.60	63.80	57.80	32.40	25.60
Zn	75.20	76.20	70.40	83.60	62.60	67.00	68.20	0.00	39.80	52.00	76.80
Zr	60.90	63.40	97.20	106.60	55.10	65.20	55.40	383.20	349.60	209.30	126.70

Utilising the alkali-versus-silica diagram, it is also possible to perform the classification of the igneous rocks, utilizing the Total Alkali Silica classification (Le Maitre, 1984). Thanks to this elaboration, it has been possible to classify precisely the basaltic andesite, belonging both to the masonries and to the outcrops, at Panama Viejo and Portobelo/San Fernando sites; moreover, samples collected at Casa Terrín resulted as rhyolite rocks (Tab. 3.4.4 and Fig. 3.4.1).

Table 3.4. 4 Bulk rock major (wt %) element analyses for magmatic rocks.  
Highlighted in blue the samples belonging to outcrops.

	Rhyolite		Basaltic Andesite						
	PV CT 1	PV CT 2	PV FN 4	PV FN 5	PV vic CR	PV Q 2	PBSF6	PBSF7	PBSF11
SiO <sub>2</sub>	73.18	71.76	52.35	52.29	54.3	53.06	56.83	54.97	56.43
TiO <sub>2</sub>	0.53	0.54	1.15	1.18	1.25	1.2	0.70	0.83	0.71
Al <sub>2</sub> O <sub>3</sub>	16.32	16.02	14.02	14.58	16.25	13.27	16.07	15.43	15.11
Fe <sub>2</sub> O <sub>3</sub>	0.2	2.22	11.49	10.97	8.23	10.94	8.71	9.39	8.19
MnO	n.d.	n.d.	0.14	0.15	0.31	0.14	0.15	0.18	0.17
MgO	n.d.	n.d.	8.49	8.34	3.99	11.22	4.64	6.53	5.99
CaO	0.14	0.27	8.77	8.84	9.96	6.44	8.70	8.49	7.82
Na <sub>2</sub> O	7.53	6.9	2.19	2.23	3.64	1.95	2.57	2.41	3.09
K <sub>2</sub> O	2.07	2.27	1.1	1.15	1.74	1.37	1.36	1.48	2.22
P <sub>2</sub> O <sub>5</sub>	0.03	0.03	0.3	0.27	0.32	0.41	0.26	0.29	0.25

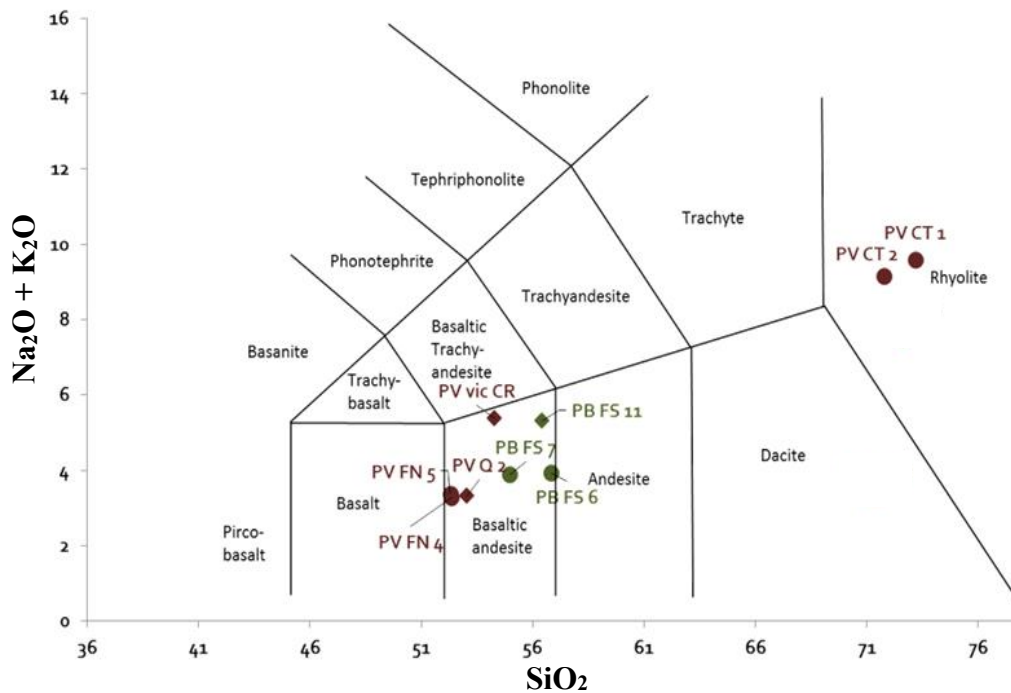


Figure 3.4. 1. TAS (Total Alkali/Silica) classification (Le Maitre, 1984). ○ = Masonry samples; ◇ = Outcrops samples.

In order to classify the volcanic altered rocks, the Winchester & Floyd (1977) diagram, using immobile trace elements, has been applied (Fig. 3.4.2). It allowed us to identify two rhyodacites.

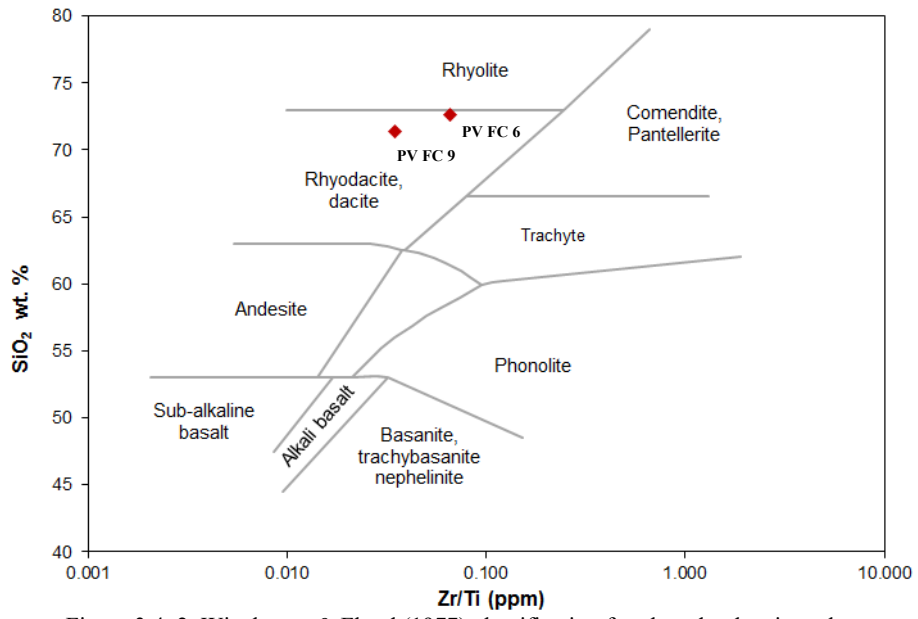


Figure 3.4. 2. Winchester & Floyd (1977) classification for altered volcanic rocks.

## Coral Limestone and Grainstone

### Coral Limestone

As expected, CaO represents the main component among the major elements, due to aragonite and calcite. While the highest values recorded among the trace elements are due to Sr and S (Tab.3.4.5).

### Grainstone

Even in this case CaO is the main component, followed by silica; moreover, alumina, Fe<sub>2</sub>O<sub>3</sub> and MgO have been detected. Among the trace elements, Sr is the main one, followed by S and Ba (Tab.3.4.5).

Table 3.4. 5. Bulk rock major (wt %) and trace (ppm) element analyses for coral boundstones and grainstone. Highlighted in blue the sample belonging to outcrops.

	Portobelo				San Lorenzo		
	Coral limestone				Grainstone		
	PB SF 2	PB SF 8	PB FSJ 7	PB FdS 8	PBSF1	SL8	SL13
SiO <sub>2</sub>	3.38	3.42	3.35	3.81	18.06	28.27	16.02
TiO <sub>2</sub>	0.00	0.00	0.00	0.01	0.16	0.36	0.13
AL <sub>2</sub> O <sub>3</sub>	0.38	0.39	0.37	0.52	3.60	5.96	2.62
Fe <sub>2</sub> O <sub>3</sub>	0.00	0.00	0.00	0.02	1.36	3.01	1.02
MnO	0.00	0.00	0.00	0.00	0.03	0.06	0.04
MgO	0.19	0.20	0.18	0.25	1.56	1.66	1.38
CaO	50.83	50.92	51.10	50.00	36.64	30.48	40.24
Na <sub>2</sub> O	0.55	0.60	0.57	0.53	0.19	0.86	0.24
K <sub>2</sub> O	0.02	0.02	0.02	0.02	0.47	0.63	0.45
P <sub>2</sub> O <sub>5</sub>	0.02	0.01	0.01	0.02	0.12	0.19	0.08
LOI	44.64	44.46	44.40	44.83	37.82	28.51	37.79
Tot.	100.00	100.00	100.00	100.00	100.01	100.00	100.01
Anhyd.	55.36	55.54	55.60	55.17	62.19	71.49	62.22
Ba	0.00	3.40	0.00	4.00	87.10	163.90	63.40
Ce	8.70	7.90	8.90	5.70	7.20	13.10	7.30
Co	4.10	3.80	4.60	4.90	10.20	12.20	9.90
Cr	0.00	1.70	0.00	0.00	19.70	52.40	10.80
Cu	5.60	5.70	7.10	7.30	11.10	17.80	7.60
Ga	2.50	2.00	2.50	2.30	6.20	9.60	5.00
Hf	0.00	0.00	0.00	0.00	0.00	0.00	0.00
La	2.30	1.50	0.00	0.00	1.60	3.50	2.70
Nb	2.40	2.30	2.80	2.20	3.90	5.10	3.00
Nd	0.00	0.00	0.00	0.00	2.00	2.00	0.00
Ni	0.00	0.00	0.00	0.00	6.00	21.20	3.40
Pb	8.50	7.40	6.10	8.30	8.80	6.90	9.80
Rb	0.00	0.00	0.00	0.00	1.40	4.20	1.50
S	148.70	184.60	126.10	198.90	405.50	601.40	408.70
Sc	0.00	0.00	0.00	0.00	3.40	10.10	2.10
Sr	8333.60	8216.90	8269.30	8038.70	1791.70	1534.50	1658.60
Th	0.00	0.00	0.00	0.00	0.10	0.80	0.20
V	1.70	3.10	0.10	4.90	55.40	101.60	43.40
Y	0.00	0.00	0.00	0.00	2.30	3.60	3.40
Zn	0.00	0.00	0.00	0.00	10.00	35.10	6.50
Zr	45.80	48.10	45.60	43.30	21.80	33.90	21.80



Plotting the data in binary diagrams, as alumina versus silica and calcium oxide versus silica (Figs. 3.4.3-4), is evident a correlation between the oxides, indeed, alumina and silica are directly proportional, while calcium oxide and silica are inversely proportional. Moreover, the distinction among the several rock typologies is clear; therefore, the samples showing the highest silica and alumina content are PV CT 1, 2, rhyolites, PV FC 6, 9, rhyodacites, followed by breccia, basaltic andesite and tuffite rocks, confirming the previous investigations.

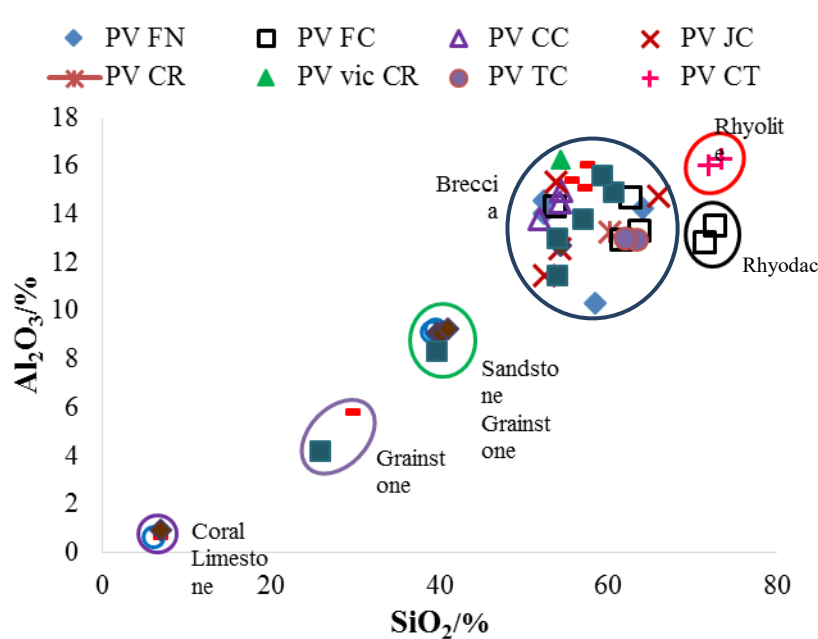


Figure 3.4. 3. Binary diagram alumina versus silica. The different sets identify the diverse rock typologies: coral limestone (violet line); grainstone (yellow line); sandstone and grainstone (green line); breccia, basaltic andesite and tuffite (blue line); rhyolite (red line); rhyodacite (black line).

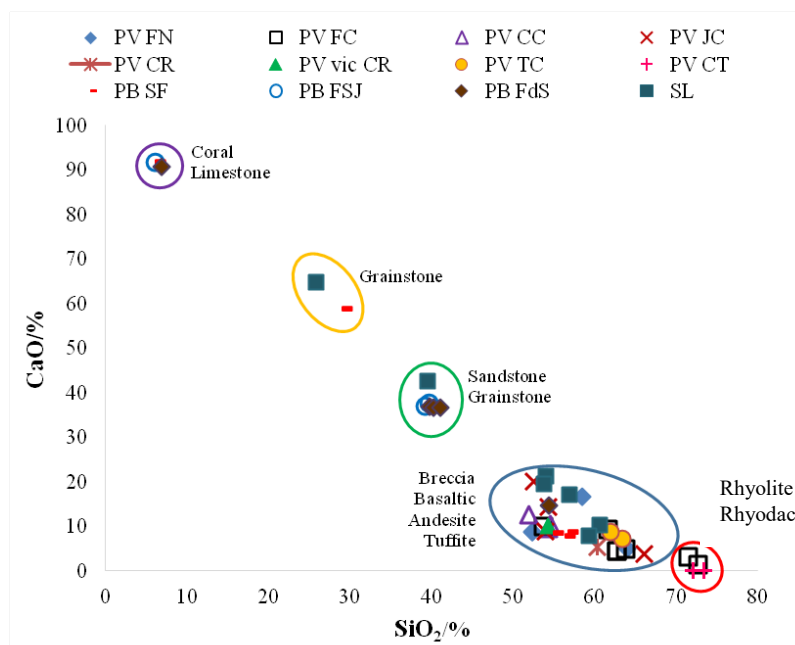


Figure 3.4. 4. Binary calcium oxide versus silica. The different sets identify the diverse rock typologies: coral limestone (violet line); grainstone (yellow line); sandstone and grainstone (green line); breccia, basaltic andesite and tuffite (blue line); rhyolite and rhyodacite (red line).

All the previous analyses detected the presence of iron oxides, indeed, except the coral limestone and PV CT 1, the rhyolite, all the other samples showed considerable percentage of  $Fe_2O_3$ , especially the basaltic andesite sampled at the Fortín de la Natividad (PV FN 4 and PV FN 5), followed by the other basaltic andesites, breccias and, finally, tuffites (Fig.3.4.5).

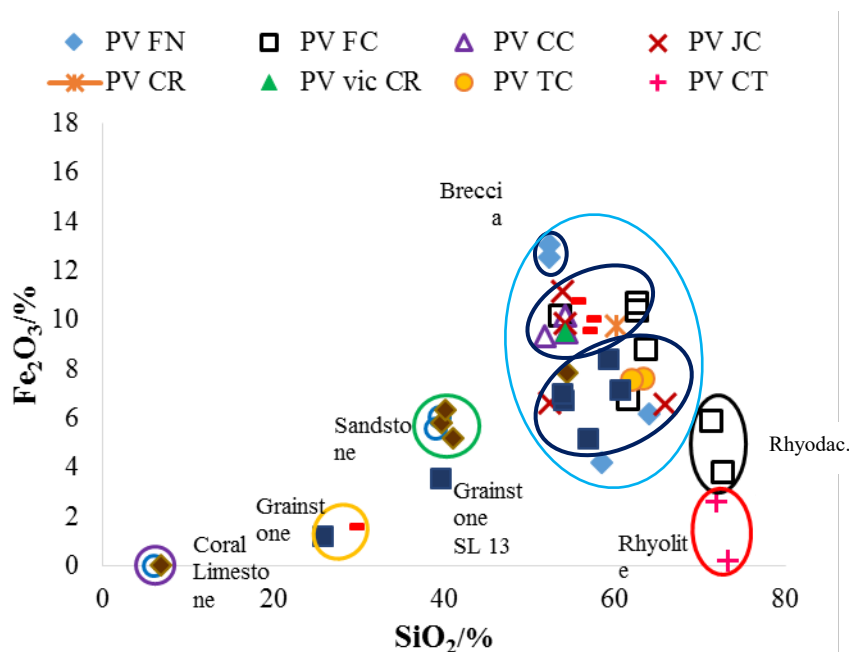


Figure 3.4. 5. Binary diagram iron oxide versus silica. The different sets identify the diverse rock typologies: coral limestone (violet line); grainstone (yellow line); sandstone and grainstone (green line); breccia, basaltic andesite and tuffite (blue lines); rhyolite (red line); rhyodacite (black line).

Taking into consideration the alkali versus silica diagram (Fig.3.4.6), the samples, which present the highest alkali percentage, confirm the feldspars detected with the previous analysis, especially the sodium members considering the rhyolites (PV CT 1 and PV CT 2), breccias (PV FN 4 and PV FN 5); while the rhyodacite PV FC 6 results richer in potassium (Fig.3.4.7).

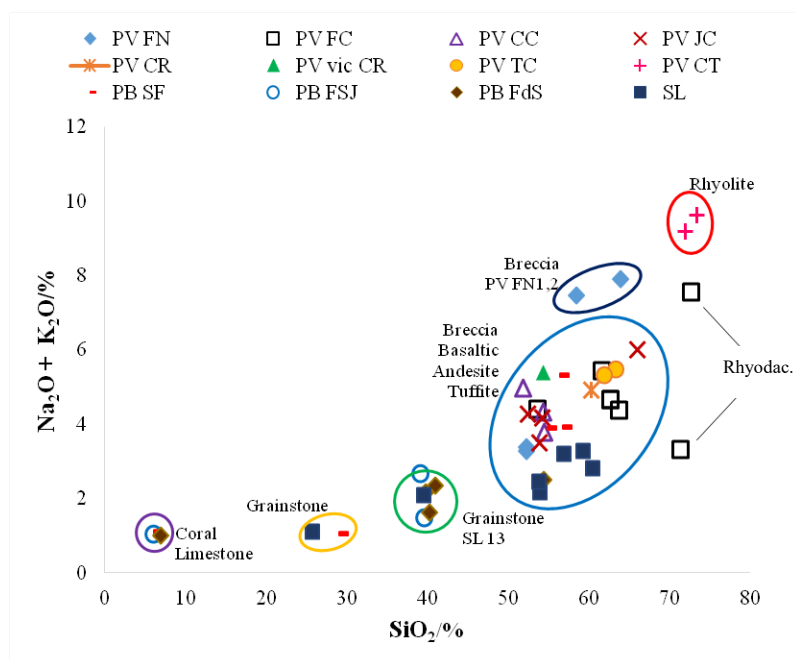


Figure 3.4. 6. Binary diagram alkali versus silica. The different sets identify the diverse rock typologies: coral limestone (violet line); grainstone (yellow line); sandstone and grainstone (green line); breccia, basaltic andesite and tuffite (blue lines); rhyolite (red line); rhyodacite (black line).

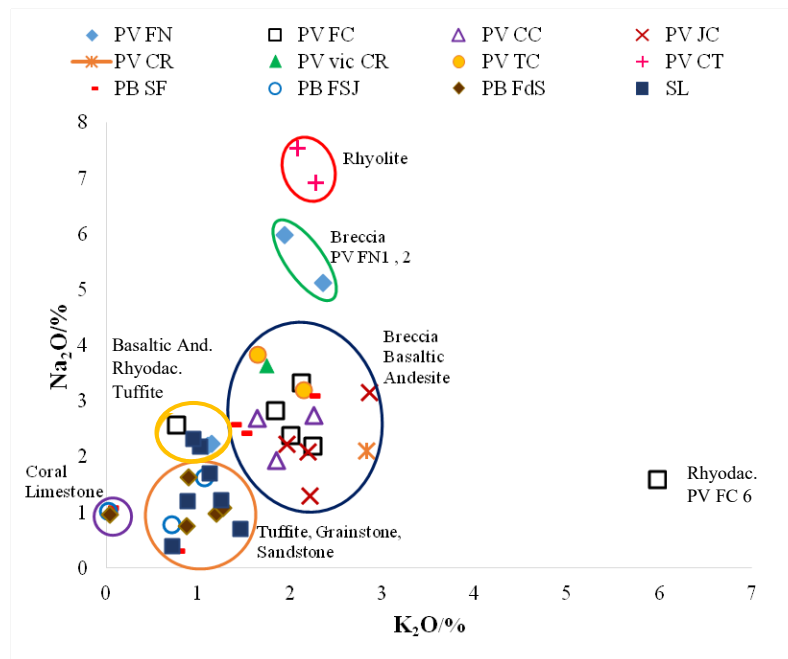


Figure 3.4. 7. Binary diagram sodium oxide versus potassium oxide. The different sets identify the diverse rock typologies: coral limestone (violet line); basaltic andesite (PV FN 4,5), rhyodacite (PV FC 9) and tuffite/sandstone (SL 1,4) (yellow line); grainstone, sandstone and tuffite (orange line); breccia and basaltic andesite (blue line); breccia (PV FN 1,2) (green line); rhyolite (red line).

### Final remarks

Through XRF analysis it was possible to define the major compounds and the trace elements present in the samples under study, confirming the presence of minerals previously detected by PLM, ESEM-EDS and XRD investigations, such as chlorite, zeolites and micas.

Moreover, igneous rocks have been classified by TAS classification, identifying basaltic andesites, both belonging to masonries and outcrops at Panama Viejo and Portobelo sites; finally, rhyolites have been detected at Casa Terrín. Utilizing Winchester & Floyd (1977) classification for altered volcanic rocks, it has been possible to identify rhyodacites in the altered volcanic rocks.

Finally, plotting the results in binary diagrams, the different compositions according to the diverse lithology is undoubtedly highlighted.

### 3.5 Mercury Intrusion Porosimetry Analysis (MIP)

Considering the porosimetry analysis, it is noticeable the highest values for accessible porosity in the coral limestones, tuffite, polygenic breccias and rhyodacites, followed by grainstones, sandstones, basaltic andesites and rhyolites (Table 3.5.1).

Regarding the pore diameter, it is included in a range of 0.01-10  $\mu\text{m}$ ; detailed descriptions are reported in the following paragraphs divided by rock typologies.

Table 3.5. 1. Porosity and pore diameter results divided by rock typology.

Lithotype	Sample	Accessible porosity	Inaccessible porosity	Average pore diameter	Median pore diameter	Modal pore diameter
		%	%	$\mu\text{m}$	$\mu\text{m}$	$\mu\text{m}$
Polygenic breccia	PV CC 4	21.21	0.16	0.1111	0.5957	3.3144
	PV FC 4	12.32	0.09	0.0564	0.0859	0.0466
	PV FN 2	25.90	0.05	0.1027	0.1916	0.1364
	PV JC 1	24.09	0.01	0.0829	0.1534	0.1899
	PV JC 3A	27.09	0.02	0.1136	0.6978	2.4389
	PV JC 3B	22.43	0.14	0.0611	0.1122	0.1344
	PV JC 4	15.96	0.33	0.0388	0.0538	0.0641
	PV Q 1	29.52	1.92	0.1318	0.3759	1.1640
Tuffite	PV TC 3	30.70	0.25	0.1008	0.3340	0.8158
	PV TC 4	26.50	1.11	0.1136	0.2699	0.4726
	PB FdS 10	25.79	0.03	0.1223	1.4301	4.5461
	SL 1	16.96	0.05	0.1628	0.5227	0.4507
	SL 2	26.93	0.15	0.1960	2.2229	3.0510
	SL 4	23.99	0.19	0.1368	1.1010	5.3738
	SL 6	27.76	0.12	0.1066	0.2159	0.1569
Basaltic andesite	PV FN 4	10.52	0.16	0.0638	0.1720	0.0435
	PV FN 5	12.14	0.08	0.0676	0.2236	0.2928
	PB SF 6	1.41	0.23	0.0233	0.0316	0.0074
	PB SF 11	2.60	0.25	0.0364	0.0380	0.0239
	PV Q 2	11.51	0.02	0.0522	0.1361	0.1979
	PV vic. CR	5.23	1.32	0.0543	0.0752	0.0638
Sandstone	PB FdS 2	9.05	0.04	0.0654	0.3002	0.4334
	PB FdS 5	10.11	0.23	0.0583	0.2562	0.3836
	PB FSJ 4	12.18	0.19	0.0946	0.6237	0.9288
	PB FSJ 8	12.36	0.08	0.0793	0.4215	0.6019
Grainstone	PB SF 1	15.90	0.06	0.0866	0.3040	0.0686
	SL 13	6.83	0.02	0.0956	0.7496	1.5103
Coral limestone	PB FSJ 7	19.13	0.58	0.8466	2.5148	2.6152
	PB SF 2	37.29	0.22	1.6475	3.0185	2.6694
Rhyolite	PV CT 1	11.57	0.23	0.1301	0.2024	0.2178
	PV CT 2	10.31	0.48	0.1048	0.1649	0.1738
Rhyodacite	PV FC 6	27.39	0.15	0.0451	0.0668	0.0642

## Breccia

Considering the different samples, all belonging to Panama Viejo site, accessible porosity is within 12% (PV FC 4 sample) and 29% (PV Q 1). The majority of the samples shows average, median and modal pores diameter lower than 0.2  $\mu\text{m}$ , threshold of micropores range. Except for PV CC 4, PV JC 3 and PV Q 1 samples, which present an average always lesser than 0.2  $\mu\text{m}$ , but with a median and a modal pore diameter higher, with the maximum value represented by PV CC 4 with a mode of 3  $\mu\text{m}$ . Predominantly, the distribution of the pore diameter is bimodal (Fig. 3.5.1), nevertheless, PV CC 4 curve is unimodal (Fig. 3.5.2) and PV JC 3B is approximable to unimodal too, both showing a right skew. Finally, PV Q 1 curve is multimodal.

Considering the apparent density, all samples are included in the range between 2.4 and 2.7  $\text{g}/\text{cm}^3$ .

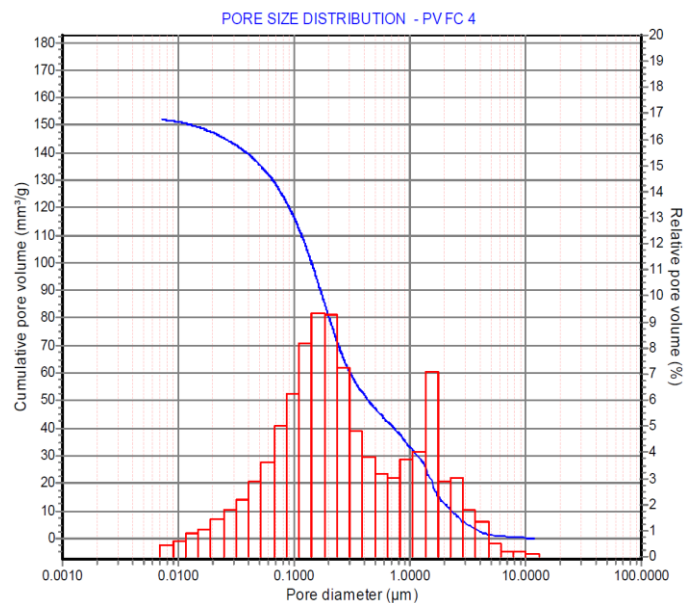


Figure 3.5. 1. Pore size distribution of polygenic breccia sample, PV FC 4, showing bimodal distribution.

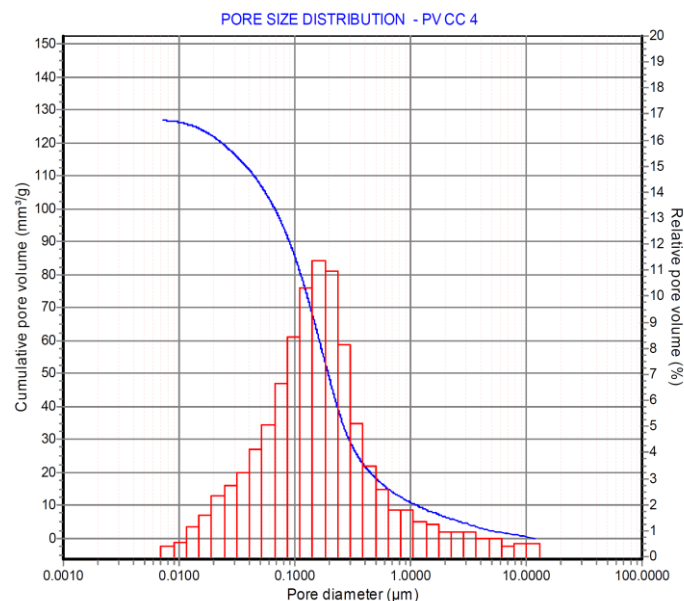


Figure 3.5. 2. Pore size distribution of polygenic breccia sample, PV CC 4, showing unimodal distribution.

## Tuffite

Most of the tuffites, belonging to the different sites, present similar values of accessible porosity, between 24% and 28%, with two extremities of 17% (SL 1 sample) and 31% (PV TC 3 sample). All samples has an average pore diameter lower than the 0.2  $\mu\text{m}$  threshold; nevertheless, considering the median and mode, we can divide the samples in two groups: one formed by PV TC 3, PV TC 4, SL 1 and SL 6, with similar values of average, median and modal pore diameter. While the second one shows different values in a range between 1 and 2  $\mu\text{m}$  for the median and 3 and 5  $\mu\text{m}$  for the mode, represented by PB FdS 10, SL 2 and SL 4.

Generally, the majority of the samples has a multimodal distribution of pore diameter (Fig. 3.5.3), quite symmetrical regarding the two PV samples and SL 1, while PB FdS 10 curve is skewed to the left (Fig. 3.5.4). SL 6 has a bimodal distribution and SL 2 is a unimodal left skewed curve, with a long tail.

Moreover, they all show an apparent density within 2.2 and 2.6  $\text{g}/\text{cm}^3$ .

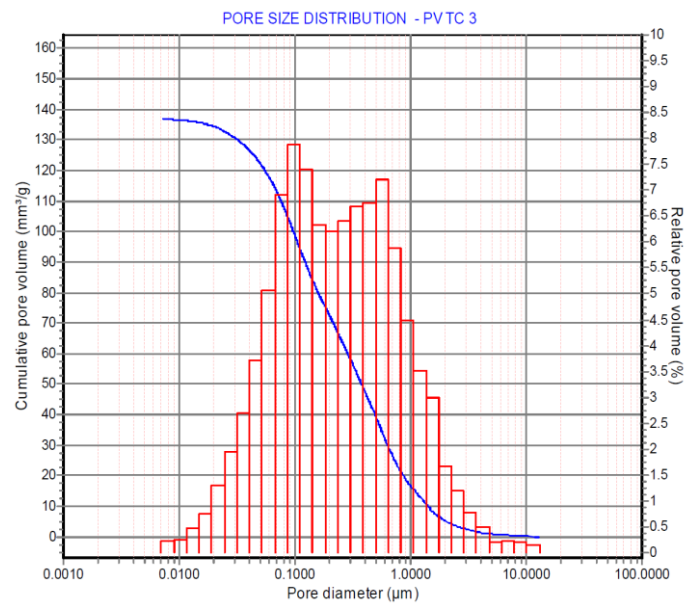


Figure 3.5. 3. Pore size distribution of tuffite sample, PV TC 3, showing symmetrical multimodal distribution.

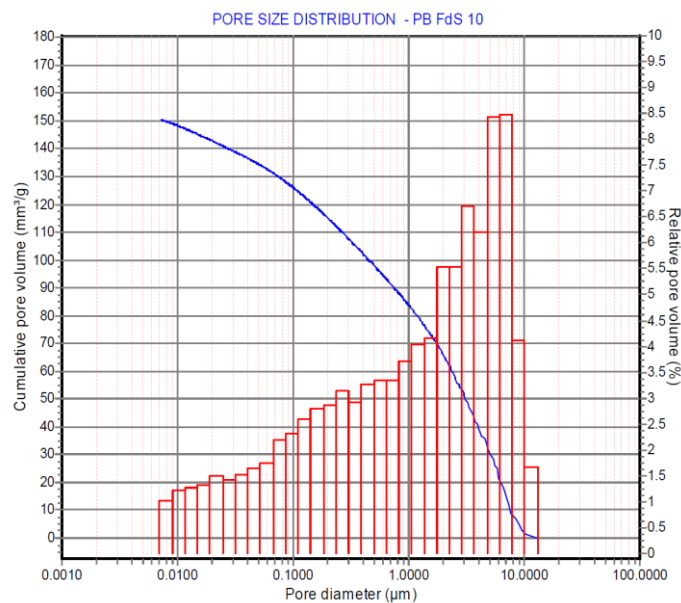


Figure 3.5. 4. Pore size distribution of tuffite sample, PB FdS 10, showing unimodal left skewed distribution.

*Basaltic andesite*

The samples belonging to Panama Viejo show values of accessible porosity higher than Portobelo, respectively within 5%, due to the outcrop sample PV vic CR, and 12%, of PV FN 5 belonging to the masonry, while PB SF 6 and PB SF 11 (outcrop), measure 1.41 and 2.60 %.

Regarding the average pore diameter, all the samples show very small pores average, median and mode, except for PV FN 5, which have the median corresponding to 0.2  $\mu\text{m}$  and the mode to 0.3  $\mu\text{m}$ . The distribution of the pores diameter is multimodal in PV FN 4 and PV FN 5 samples (Fig.3.5.5), while PB SF 6 is bimodal (Fig.3.5.6) and PB SF 11 unimodal, both showing a range predominantly between 0.01 and 1  $\mu\text{m}$  and a curve right skewed with a long tail.

Finally, they all present an apparent density of 2.7-2.8  $\text{g}/\text{cm}^3$ .

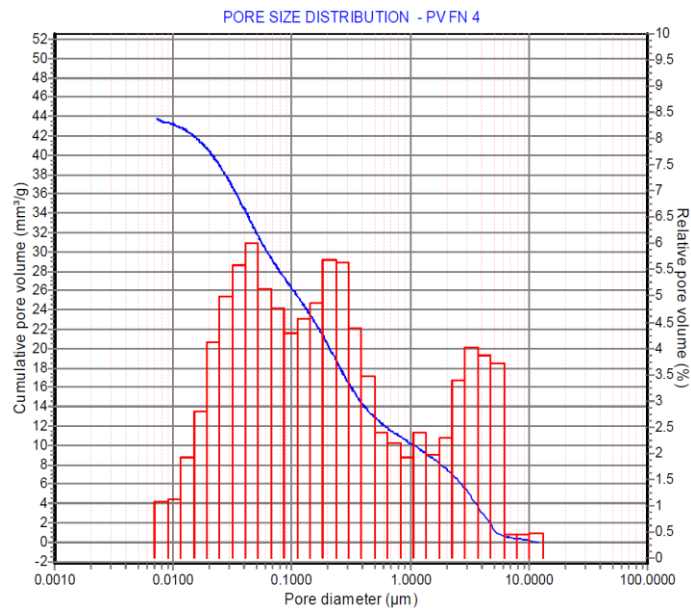


Figure 3.5. 5. Pore size distribution of basaltic andesite sample, PV FN 4 showing multimodal distribution.

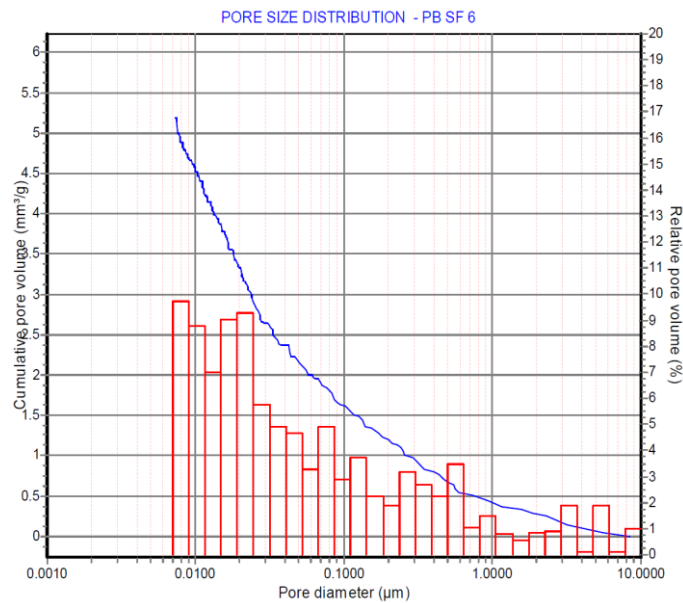


Figure 3.5. 6. Pore size distribution of basaltic andesite sample, PB SF 6 showing unimodal right skewed distribution.

## Sandstone

All samples show a quite low accessible porosity, according also with the PLM observation (Chap.3.1.2), included between 9 and 12%, with very similar values of apparent density, equal to 2.6-2.7 g/cm<sup>3</sup>. In addition, the average pore diameters is lower than 0.2 μm and the median values are within 0.26 and 0.62 μm. Considering the distributions of pore diameters, PB FdS 5 and PB FdS 2 curves are multimodal, this latter one can be similar to unimodal, as PB FSJ 4, which is bimodal, but approximable to unimodal. Finally, PB FSJ 8 present a bimodal curve (Fig. 3.5.7). Moreover, all the distributions show a left skew.

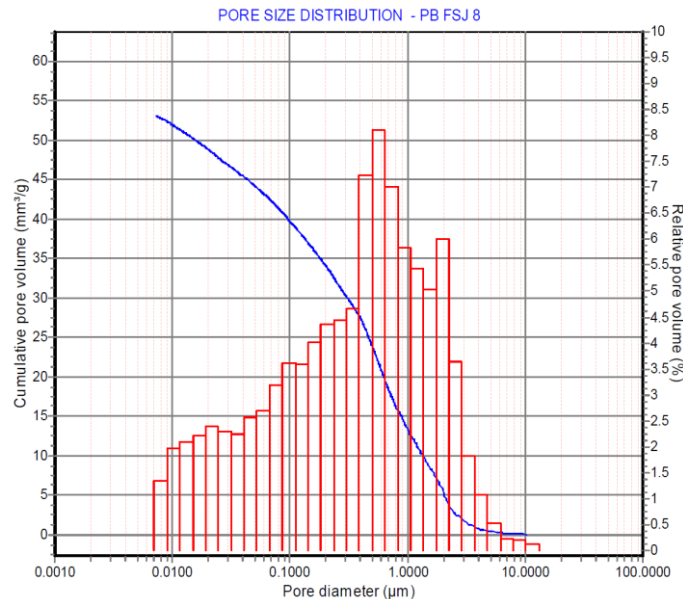


Figure 3.5. 7. Pore size distribution of tuffite sandstone sample, PB FSJ 8 showing bimodal left skewed distribution.

## Grainstone

The two samples, belonging to two different sites, show different features. Considering PB SF 1 it has an accessible porosity of 16%, average and modal pore diameter under the threshold of micropores, while the median is equal to 0.7 μm; the distribution is multimodal, quite symmetric (Fig.3.5.8). SL 13 sample, collected from an outcrop, shows a lower accessible porosity than the previous one, corresponding to 7%, with an average of pore diameter lower than 0.2 μm, but with a median pore of 0.7 μm, a mode of 1.5 μm and showing a multimodal distribution (Fig. 3.5.9). It is ascribable to the extended porosity identified also by PLM observations (Chap.3.1.2). Both show a similar apparent density of 2.4-2.5 g/cm<sup>3</sup>.



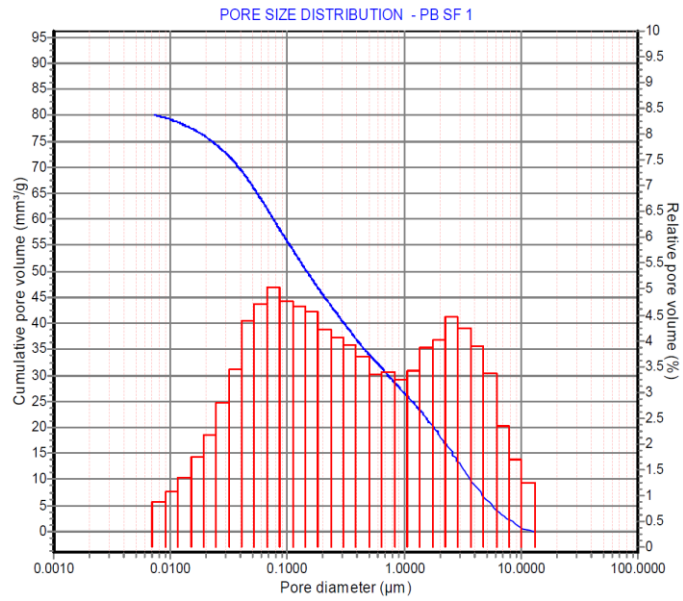


Figure 3.5. 8. Pore size distribution of grainstone sample, PB SF1, showing symmetric multimodal distribution.

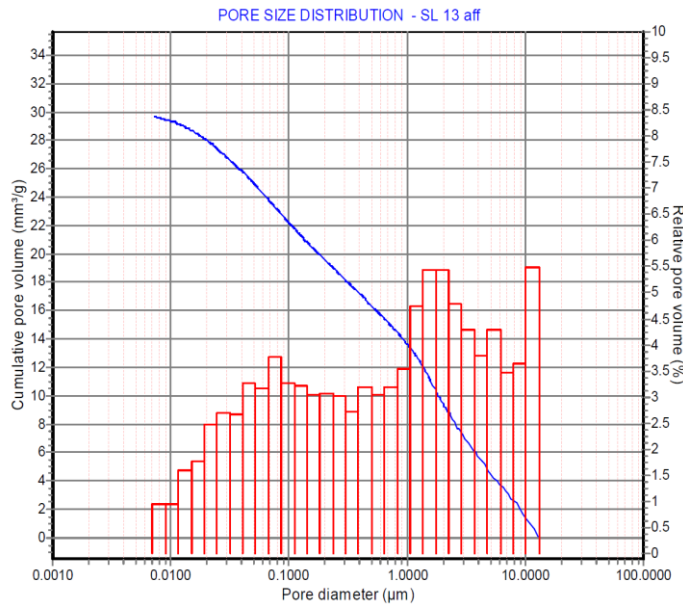


Figure 3.5. 9. Pore size distribution of grainstone sample, SL 13, showing multimodal distribution.

### *Coral limestone*

As already detected by PLM investigations (Chap.3.1.2), these boundstones present diffused porosity, measured by MIP with the following values: 19%, for PB FSJ 7 and 37% for PB SF 2. Both samples have average, median and modal value of pore diameter higher than the 0.2  $\mu\text{m}$  threshold, with a range mostly included between 1 and 10  $\mu\text{m}$ . Indeed the distributions, mostly unimodal, are left skewed with a long tail (Fig.3.5.10). Finally, the apparent density is around 2  $\text{g}/\text{cm}^3$ .

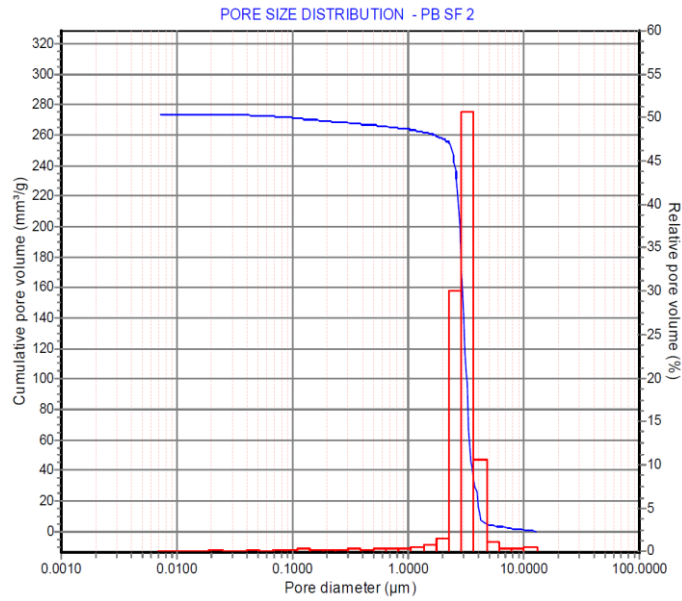


Figure 3.5. 10. Pore size distribution of boundstone sample, PB SF 2, showing unimodal, left skewed, distribution.

### *Rhyodacite*

Only one sample has been analysed, PV FC 6, presenting an accessible porosity of 27 %, and with the average, median and mode of pores diameter under the threshold of micropores.

Therefore, the distribution of the diameters shows a range mainly between 0.01 and 0.1 µm, the bimodal right skewed curve, has a predominant part with a peak corresponding to 0.06 µm (Fig.3.5.11). Furthermore, the apparent density is equal to 2.4 g/cm<sup>3</sup>.

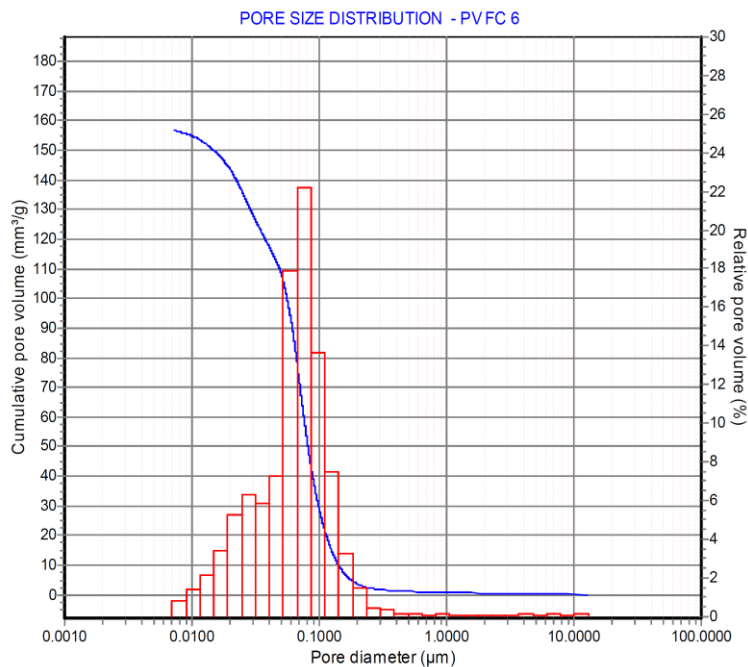


Figure 3.5. 11. Pore size distribution of a rhyodacite sample, PV FC 6, showing an approximately unimodal right skewed distribution. .

## Rhyolite

The two samples of rhyolite show an accessible porosity of 10-12%, with the majority of the size pore distribution range between 0.01 and 1  $\mu\text{m}$ , presenting an average pore diameter of 0.1  $\mu\text{m}$ , and median and modal equal to  $\sim 0.2 \mu\text{m}$ . Moreover, both samples has a symmetric unimodal distribution curve (Fig. 3.5.12).

The apparent density for both samples correspond to  $2.6 \text{ g/cm}^3$ .

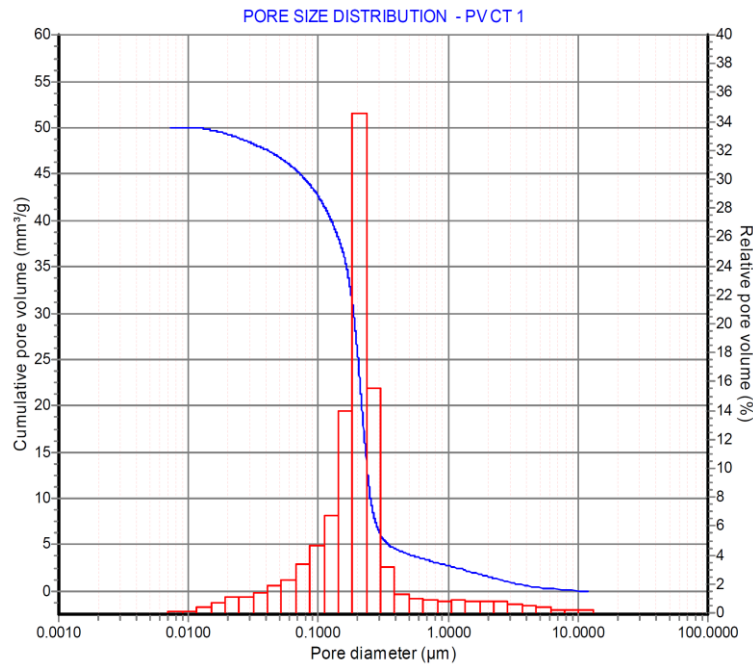


Figure 3.5. 12. Pore size distribution of a rhyolite sample, PV CT 1, showing a symmetric unimodal distribution.

### Final remarks

MIP analysis revealed that the majority of samples analysed present an average pore diameter lower than the 0.2  $\mu\text{m}$ , threshold of micropores. This has to be taken into account for the salts crystallization phenomenon, since, according to Camuffo (2013), in pores with radius  $> 0.1 \mu\text{m}$ , so  $\varnothing > 0.2 \mu\text{m}$ , contaminated by soluble salts (typically in marine environment, as our case of study), the condensation may occur at lower relative humidity (RH).

In general, all samples show a pore distribution ranging between 0.01 and 10  $\mu\text{m}$ , nevertheless, coral limestones have a predominance of the pore distribution towards to 10  $\mu\text{m}$ , while the rhyodacite and rhyolites tend to have the majority of pore diameters between 0.01 and 1  $\mu\text{m}$ .

Moreover, the investigation allow us to confirm the diffused porosity observed by PLM analysis on grainstones and boundstones.

### 3.6 Ion Chromatography Analysis (IC)

Through the ion chromatography analysis, it was possible to determine the soluble salts present in the materials under investigation.

All the samples, in each site, show calcium as the most abundant cation.

Considering specifically the site of Panama Viejo, the anions most abundant are sulphates, nitrates and chlorides. In addition, PV FC 9, a rhyodacite, shows high values of acetates (Table 3.6.1). While among the cations, after calcium, there are sodium, magnesium, potassium and ammonium, listed in order of abundance (Table 3.6.2).

Table 3.6. 1. Anions concentrations (ppm) in Panama Viejo samples.

Lithotype	Samples	C <sub>2</sub> H <sub>3</sub> O <sub>2</sub> <sup>-</sup>	PO <sub>4</sub> <sup>3-</sup>	C <sub>2</sub> O <sub>4</sub> <sup>=</sup>	CHO <sub>2</sub> <sup>-</sup>	NO <sub>2</sub> <sup>-</sup>	NO <sub>3</sub> <sup>-</sup>	SO <sub>4</sub> <sup>=</sup>	Cl <sup>-</sup>
Polygenic breccias	PV FN 1	87	0	2	68	11	1183	822	1112
	PV FC 5	7	0	319	37	0	258	576	499
	PV FC 8	6	42	24	42	0	129	443	565
	PV FC 11	14	0	0	53	1	67	173	640
	PV CC 6	17	7	0	37	0	115	572	382
	PV JC 4int	4	0	3	26	8	2926	11525	2931
	PV JC4 est	3	0	0	31	11	3551	2848	3821
	PV CR 4	6	0	12	25	6	39	162	579
Tuffite	PV TC 4	0	0	34	75	62	6352	3098	10675
Rhyodac.	PV FC 6	4	199	0	17	27	1033	775	1739
	PV FC 9	1088	143	0	41	26	1051	634	1334

Table 3.6. 2. Cations concentrations (ppm) in Panama Viejo samples.

Lithotype	Samples	NH <sub>4</sub> <sup>+</sup>	K <sup>+</sup>	Mg <sup>2+</sup>	Na <sup>+</sup>	Ca <sup>2+</sup>
Polygenic breccias	PV FN 1	57	325	343	10076	0
	PV FC 5	25	244	289	2077	2490
	PV FC 8	19	123	199	1178	3038
	PV FC 11	89	354	369	573	19930
	PV CC 6	0	224	1123	850	27884
	PV JC 4int	43	114	505	1834	4474
	PV JC4 est	0	0	15	287	341
	PV CR 4	27	314	823	2434	8845
Tuffite	PV TC 4	99	237	294	5306	33039
Rhyodac.	PV FC 6	25	250	288	1518	1787
	PV FC 9	35	244	353	3672	1775

Making a comparison among cations and anions concentration, illustrated in Figure 3.6.1, it can be noticed a correlation between Na<sup>+</sup> and Cl<sup>-</sup>, thus it can be supposed the risk of cycles of halite formation. Moreover, the high presence of sulphates and nitrates can cause an aggressive ambient, forming sulfuric and nitric acid, responsible of the corrosion in particular of carbonate stones.

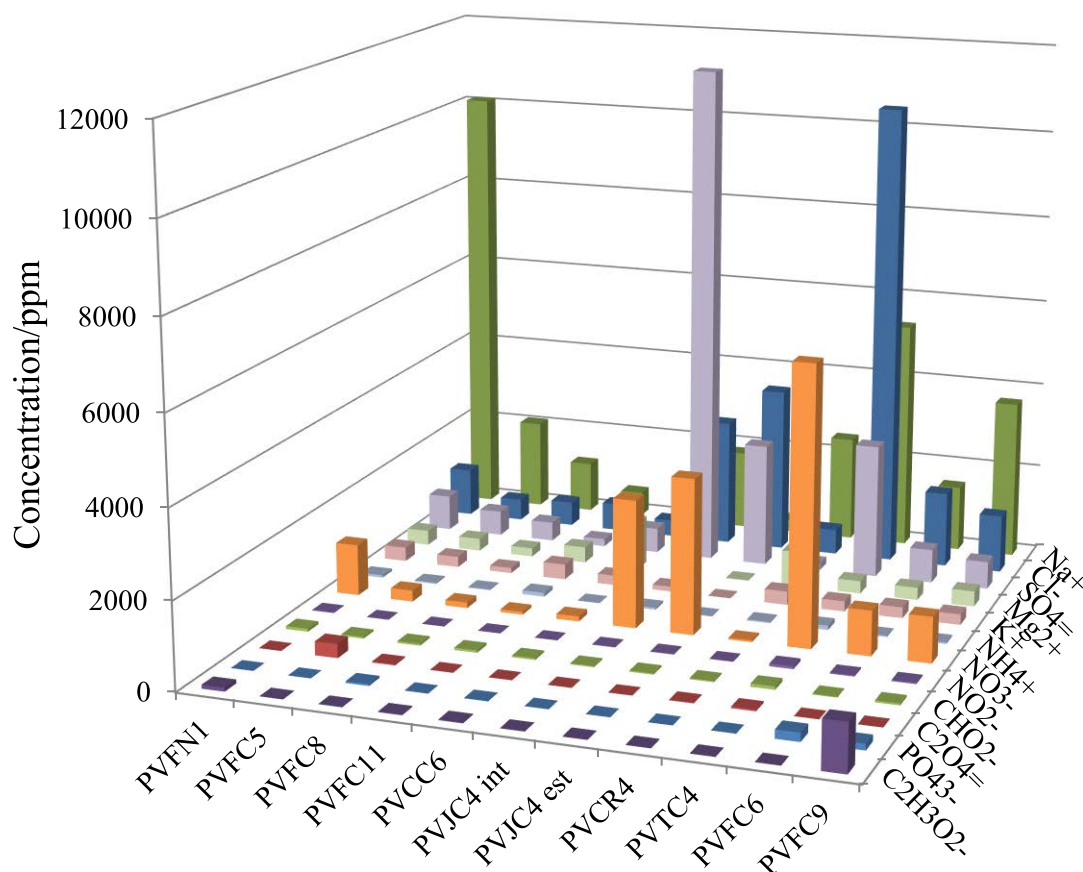


Figure 3.6. 1. Ion concentration in Panama Viejo samples, calcium is excluded in order to have a clearer visualization of the other ions.

Regarding the situation at Portobelo and San Lorenzo, among the anions the highest values are due to chlorides, followed by sulphates, nitrates, formates and nitrites (Tab. 3.6.3). While, after calcium, the most abundant cations are sodium, magnesium, potassium and ammonium.

Table 3.6. 3. Anions concentrations (ppm) in Portobelo and San Lorenzo samples.

Lithotype	Samples	C <sub>2</sub> H <sub>3</sub> O <sub>2</sub> <sup>-</sup>	PO <sub>4</sub> <sup>3-</sup>	C <sub>2</sub> O <sub>4</sub> <sup>=</sup>	CHO <sub>2</sub> <sup>-</sup>	NO <sub>2</sub> <sup>-</sup>	NO <sub>3</sub> <sup>-</sup>	SO <sub>4</sub> <sup>=</sup>	Cl <sup>-</sup>
Basaltic andesite	PBSF6	0	0	0	32	0	19	74	670
	PBSF7	0	0	0	103	29	61	169	617
	PBSF11	0	0	33	35	0	41	101	704
Tuffite	PB FdS10	0	0	0	56	20	94	251	1103
	SL 9	0	0	0	50	35	343	203	2802
	SL 6	12	0	0	49	12	58	326	729
Sandstone	PBFSJ4	16	52	0	15	0	35	222	1779
	PBFSJ8	1	0	0	39	0	76	132	316
	PB FdS2	0	67	0	50	0	369	191	828
Grainstone	PBSF1	15	0	20	22	43	21	362	700
Coral limestone	PBSF2	0	0	24	60	66	71	545	495
	PB FdS 8	1	0	0	38	13	71	408	508
	PBSF8	28	0	0	49	25	62	634	766

Table 3.6. 4. Cations concentrations (ppm) in Panama Viejo samples.

Lithotype	Samples	NH <sub>4</sub> <sup>+</sup>	K <sup>+</sup>	Mg <sup>2+</sup>	Na <sup>+</sup>	Ca <sup>2+</sup>
Basaltic andesite	PBSF6	30	406	318	789	2888
	PBSF7	23	313	633	873	0
	PBSF11	103	641	374	1377	2017
Tuffite	PB FdS10	163	267	604	472	33233
	SL 9	53	219	496	1217	32204
	SL 6	498	618	586	453	0
Sandstone	PBFSJ4	86	441	1208	2576	49087
	PBFSJ8	112	306	938	277	32356
	PB FdS2	85	1160	1052	1157	34490
Grainstone	PBSF1	52	158	652	452	48671
Coral limestone	PBSF2	0	0	0	0	34328
	PB FdS 8	221	311	209	846	59090
	PBSF8	255	148	231	790	49958

Even in this case it can be noticed a correlation between sodium and chloride, since the crystallization of halite may occur (Fig.3.6.2).

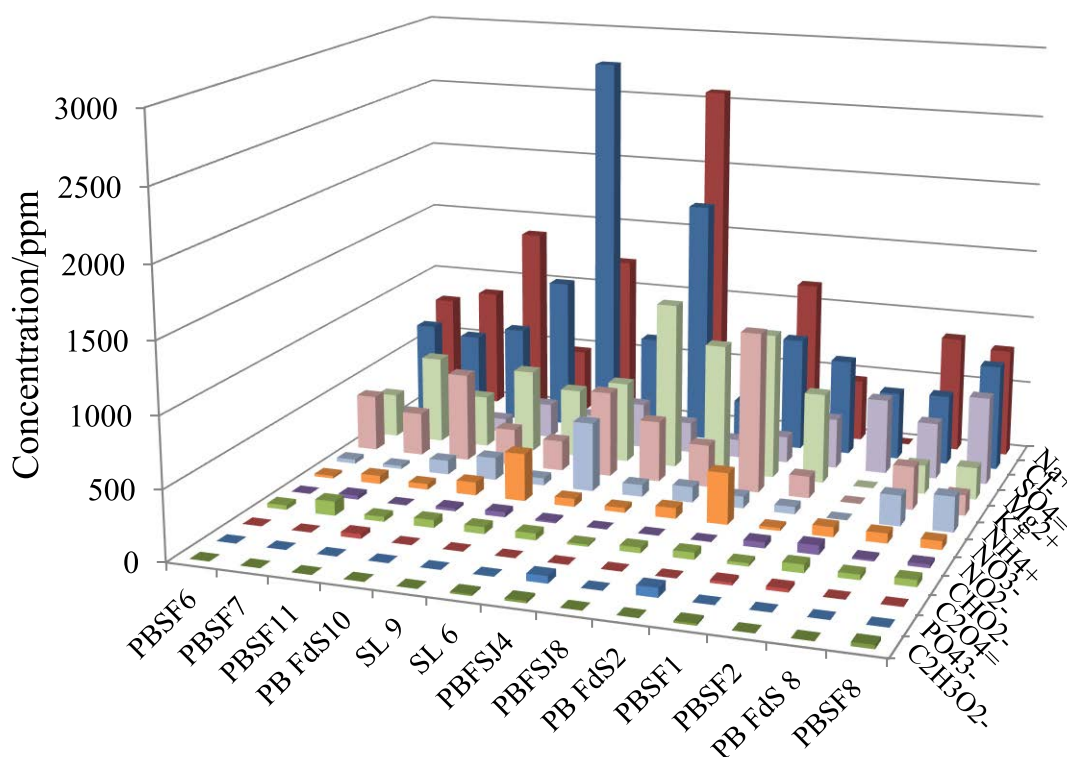


Figure 3.6. 2. Ion concentration in Portobelo and San Lorenzo samples, calcium is excluded in order to have a clearer visualization of the other ions.

Nevertheless, considering the high values of chloride anion, also magnesium, potassium and ammonium chloride can be present, also in view of the sites proximity to the sea and to the infiltration of seawater into the forts structure (Chap.1). The presence of Cl<sup>-</sup> can be also a precursor of the hydrochloric acid, so creating an aggressive ambient, especially for the carbonate stones.

Consequence of a "corrosive situation", also due to the possible formation of sulfuric and nitric acid, respectively from the sulphates and nitrates, is the dissolution and re-crystallization of calcite, observed as encrustations sampled at Fort San Fernando and Fort of Santiago and analysed by IC investigations.

Considering the anions concentration, the most abundant one is always the chloride, followed by sulphate, nitrate, nitrite and formate; PB FdS 3 also shows quite high oxalate (Tab. 3.6.5).

Table 3.6. 5. Anions concentrations (ppm) in Portobelo samples of calcite encrustations.

	<b>Br<sup>-</sup></b>	<b>C<sub>2</sub>O<sub>4</sub><sup>=</sup></b>	<b>CHO<sub>2</sub><sup>-</sup></b>	<b>NO<sub>2</sub><sup>-</sup></b>	<b>NO<sub>3</sub><sup>-</sup></b>	<b>SO<sub>4</sub><sup>=</sup></b>	<b>Cl<sup>-</sup></b>
<b>PBSF5</b>	0	0	29	23	114	234	1149
<b>PBFdS3</b>	32	217	40	16	81	135	1161

Obviously, calcium is the most abundant cation, followed by sodium, potassium, magnesium, ammonium and magnesium, listed in order of abundance (Tab. 3.6.6).

Table 3.6. 6. Cations concentrations (ppm) in Portobelo samples of calcite encrustations.

	<b>NH<sub>4</sub><sup>+</sup></b>	<b>K<sup>+</sup></b>	<b>Mg<sup>2+</sup></b>	<b>Na<sup>+</sup></b>	<b>Ca<sup>2+</sup></b>
<b>PBSF5</b>	126	228	102	258	43616
<b>PBFdS3</b>	138	277	41	268	47291

Final remarks

All samples analysed by IC investigations show calcium as the most abundant cation.

Analysis revealed also a high presence of sulphates and nitrates at Panama Viejo site, since it is within an urban area in proximity to a high traffic road, thus interested by elevated anthropic pollution.

At Portobelo and San Lorenzo, the most abundant anion is the chloride, and, considering the cations detected, it can form sodium, potassium, ammonium and magnesium chloride.

Furthermore, in presence of water, Cl<sup>-</sup> can create the hydrochloric acid, as sulphates and nitrates, which can form respectively the sulphuric and nitric acid, causing the dissolution of carbonates. These latter ones can re-crystallize inside the stone porosity, provoking internal tensions, or on the surface, forming superficial encrustations. Moreover, in both sites the presence of halite is presumable.





## 4. Chapter 4 - Extraction of Climate Parameters

### 4.1 Comparison between climate simulations and monitoring stations

The data obtained by the monitoring stations and the ones extracted from the Arpege and EC-Earth models are compared in this section. In particular, Figure 4.1.1 shows the areas of Arpege (black squares) and EC-Earth (red squares) overlapped on the Panamanian geographical silhouette. They correspond to the zones selected and utilized to perform the comparison, specifically four squared areas of 50 km per side related to Arpege (black lines), and five squared areas of 25 km per side of EC-Earth simulation (red lines).

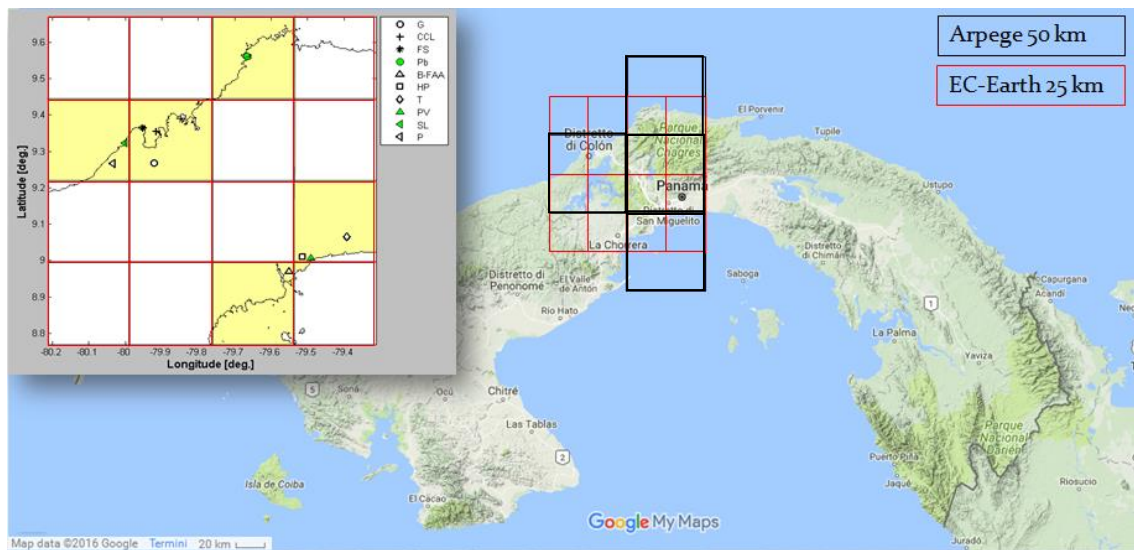


Figure 4.1. 1 Black squares belong to Arpege model; red squares belong to EC-Earth model and the 5 areas here presented are highlighted on the left with yellow filling.

The historic periods compared are generally of 30 years from 1979 to 2008, nevertheless some of the monitoring stations data present periods of less duration or with missing years or months, since the series are not complete. These anomalies are reported and specified, when present, in the following paragraphs, divided in areas related to the zones understudy.

#### 4.1.1. Panama Viejo area

Site location: Long.-79.49; Lat.9.01; central point of EC-Earth:-79.45, 9.1; central point of Arpege-FN1: -79.50; 9.24.

In this zone, the comparison has been carried out with Hato Pintado and Tocumen stations (period covered 1988-2008). The location under investigation is highlighted with red squares in Figures 4. 4.1.1.1 and 4.1.1.2, respectively for the EC-Earth and the Arpege model.



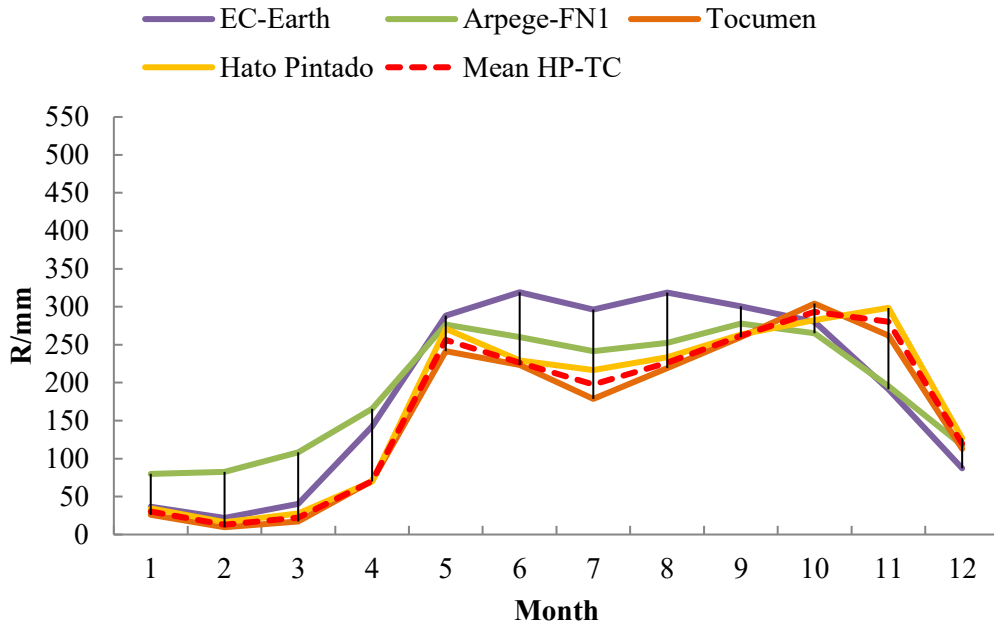


Figure 4.1.1. 3 Average of rainfall monthly amount over 20 years (1988-2008), at the area of Panama Viejo (Long.-79.49; Lat.9.01). Comparison among the historic series of the Hato Pintado and Tocumen monitoring stations and the historic simulation of the Arpege-FN1 and EC-Earth models.

Considering the coefficient of determination ( $R^2$ ) (Figs.4.1.1.4-5) of the rainfall monthly amount (mm) calculated by the model simulations versus the measured of the monitoring station, for the period 1988-2008, Arpege-FN1 results the most similar to the average obtained by Tocumen and Hato Pintado data, with a  $R^2 = 0.82$ .

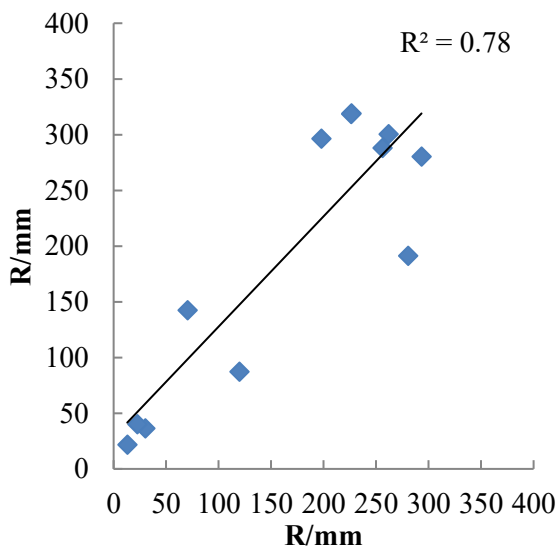


Figure 4.1.1. 4. Rainfall data of EC-Earth vs Hato Pintado.

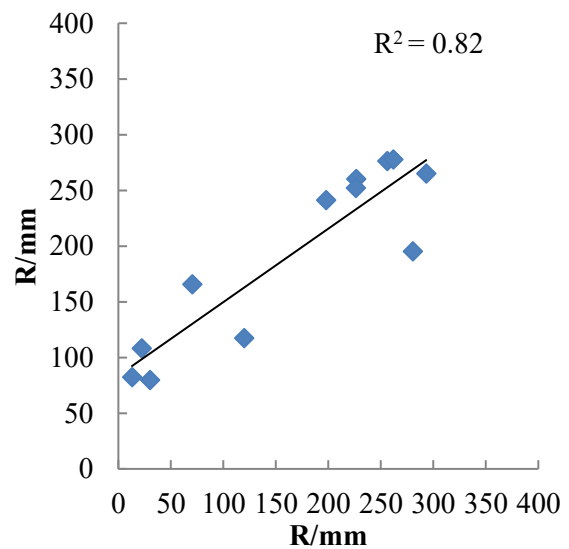


Figure 4.1.1. 5. Rainfall data of Arpege-FN1 vs Hato Pintado.

### Temperature (T)

Regarding the comparison of the T values for the period 1979-2008, of Panama Viejo area, as it is clearly visible in the Table 4.1.1.2 and in the graph below (Fig.4.1.1.6), the most suitable simulation of the seasonal trend is represented by EC-Earth, even if the values are underestimate of 2 °C on average. This is further confirmed by the  $R^2$  coefficient, which is highly better the EC-Earth one, illustrated in Figures 4.1.1.7-8.

Table 4.1.1. 2 Comparison of monthly average of temperature of Tocumen monitoring station and models data, over 30 years (1979-2008).

**T monthly average (°C)  
1979-2008**

Month	Tocumen	EC-Earth	Arpege-FN1
1	26	25	24
2	27	25	24
3	27	25	25
4	28	25	25
5	27	24	26
6	26	24	26
7	26	24	25
8	26	24	25
9	26	24	25
10	26	24	25
11	26	23	24
2	26	24	24

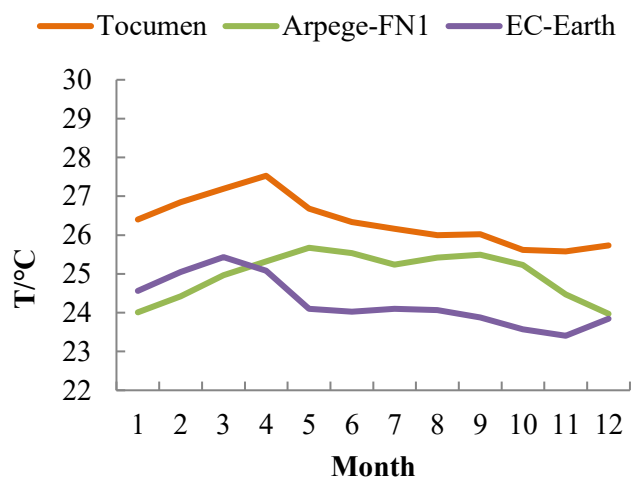


Figure 4.1.1. 6. Comparison of monthly average of temperature of Tocumen monitoring station and Arpege-FN1 and EC-Earth experiments, over 30 years (1979-2008).

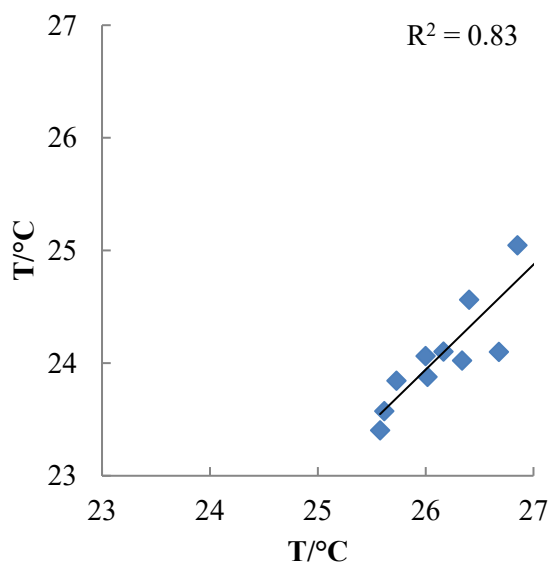


Figure 4.1.1. 7. Temperature data of EC-Earth vs Tocumen.

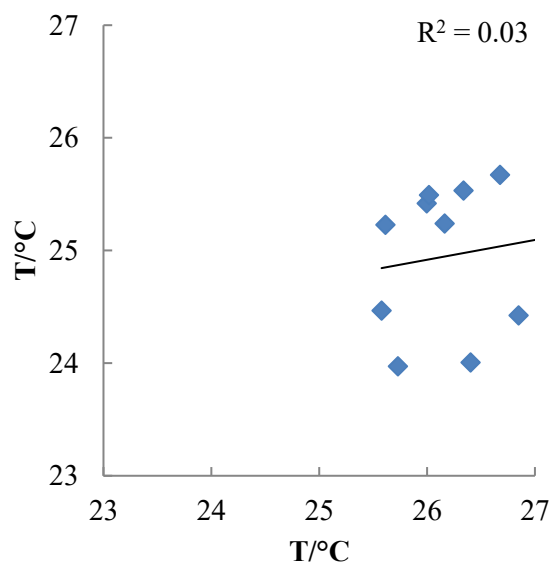


Figure 4.1.1. 8. Temperature data of Arpege-FN1 vs Tocumen.

Relative Humidity (RH)

Similar situation is present observing RH values (period 1979-2008), where EC-Earth model represents better the tendency of the measured data at the Tocumen monitoring station (Tab. 4.1.1.3 and Fig. 4.1.1.9), with a  $R^2$  of 0.96, respect to  $R^2 = 0.86$  of Arpege-FN1 versus Tocumen (Figs. 4.1.1.10-11).

Table 4.1.1. 3 Comparison of monthly average of relative humidity of Tocumen monitoring station and models data, over 30 years (1979-2008).

RH/% monthly average 1979-2008			
Month	Tocumen	EC-Earth	Arpege-FN1
1	74	81	89
2	71	77	87
3	73	76	86
4	75	83	88
5	85	91	90
6	86	93	91
7	85	92	92
8	86	93	92
9	87	93	92
10	87	93	92
11	86	92	92
12	80	87	91

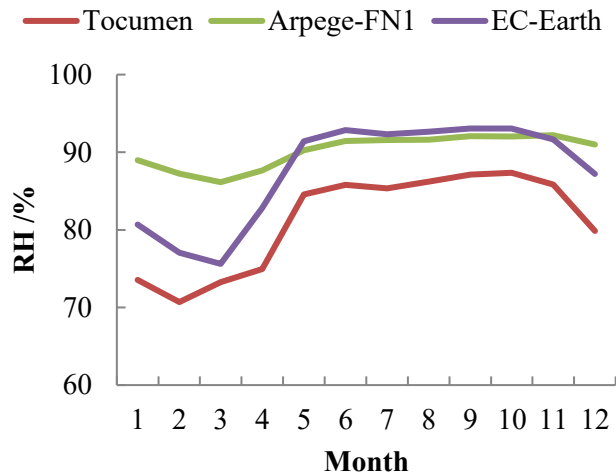


Figure 4.1.1. 9. Comparison of monthly average of relative humidity of Tocumen monitoring station and Arpege-FN1 and EC-Earth experiments, over 30 years (1979-2008).

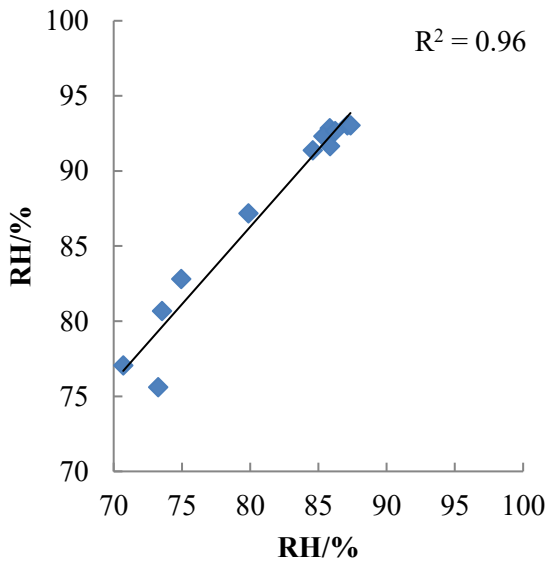


Figure 4.1.1. 10. Relative humidity data of EC-Earth vs Tocumen.

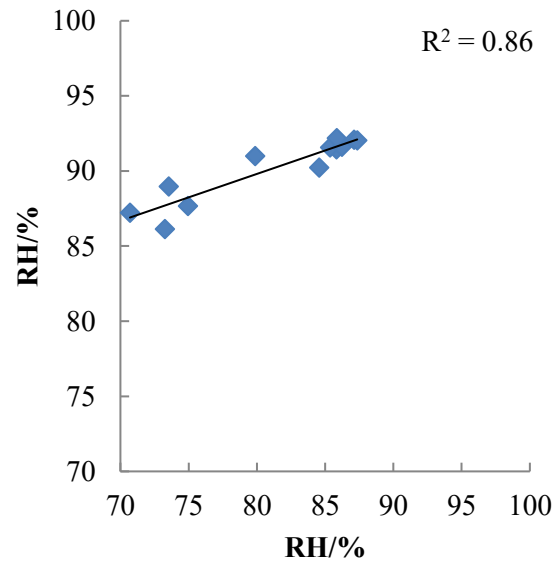


Figure 4.1.1. 11. Relative humidity data of Arpege-FN1 vs Tocumen.

#### 4.1.2. Area near Panama Viejo

Site location: Long.-79.49; Lat.9.01; EC-Earth central point: -79.6, 8.9; FN1 central point: -79.5; 8.74  
 Considering the comparison with Balboa FAA station (period 1979-2008), the location under investigation is highlighted with a red square in Figure 4.1.2.1, for the EC-Earth model, and in Figure 4.1.2.2 for the Arpege simulation.

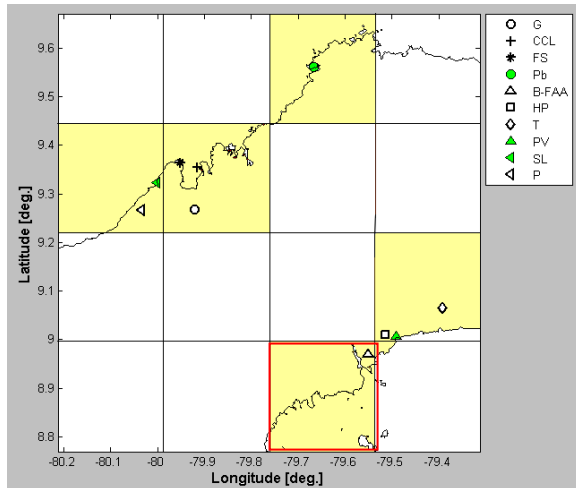


Figure 4.1.2. 1 EC-Earth selected area. In red is highlighted the zone under investigation in this paragraph.

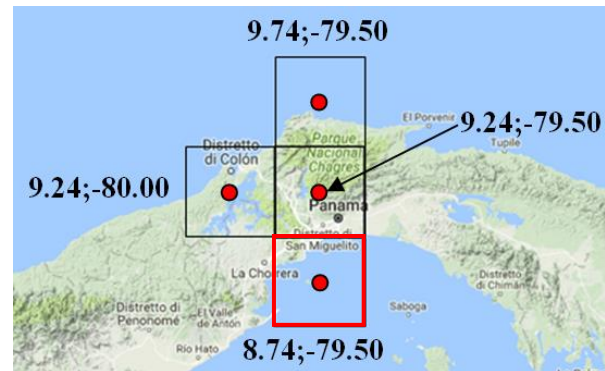


Figure 4.1.2. 2. Arpege selected area. In red is highlighted the zone under investigation in this paragraph.

#### Rainfall (R)

As noticed in the previous circumstance, observing the measured data (period 1979-2008), in this case of the Balboa FAA monitoring station, the most suitable simulation records are obtained by Arpege-FN1 (Tab. 4.1.2.1 and Fig. 4.1.2.3), with a coefficient of determination tending towards 1 (Figs. 4.1.2.4-5).

Table 4.1.2. 1. Comparison of average of rainfall monthly amount of Balboa FAA monitoring station and models data, over 30 years (1979-2008).

Month	R/mm average monthly amount 1979-2008		
	Balboa FAA	EC-Earth	Arpege-FN1
1	37	44	18
2	16	30	11
3	22	47	14
4	78	149	63
5	239	311	275
6	222	343	290
7	203	292	254
8	200	327	283
9	235	324	323
10	271	293	314
11	243	172	220
12	127	84	75

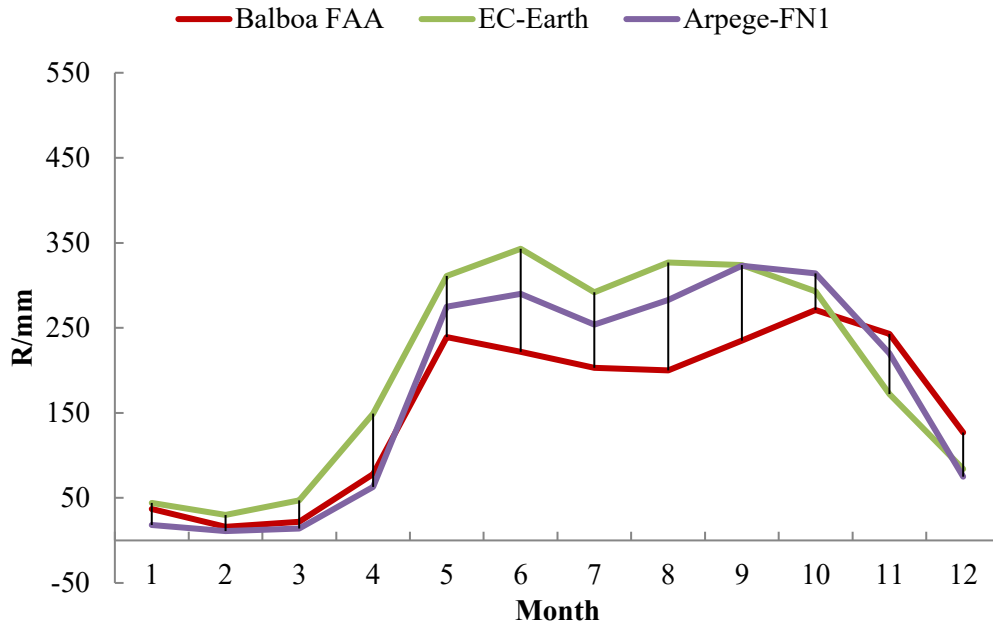


Figure 4.1.2. 3. Average of rainfall monthly amount over 30 years (1979-2008), at the area near Panama Viejo (Long.-79.50; Lat.9.01). Comparison among the historic series of the Balboa FAA monitoring station and the historic simulation of the Arpege-FN1 and EC-Earth models

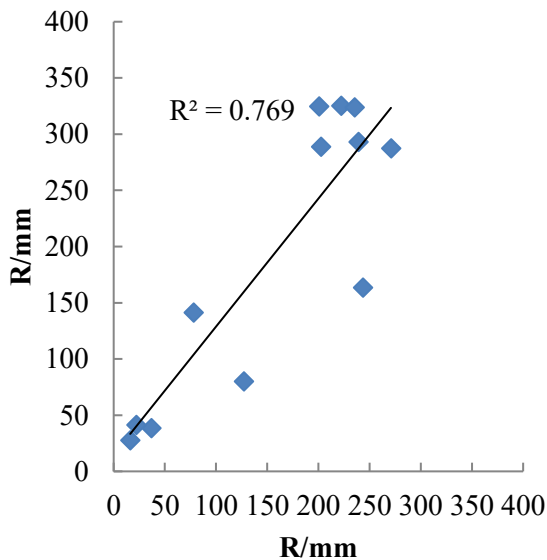


Figure 4.1.2. 4. Rainfall data of EC-Earth vs Balboa FAA.

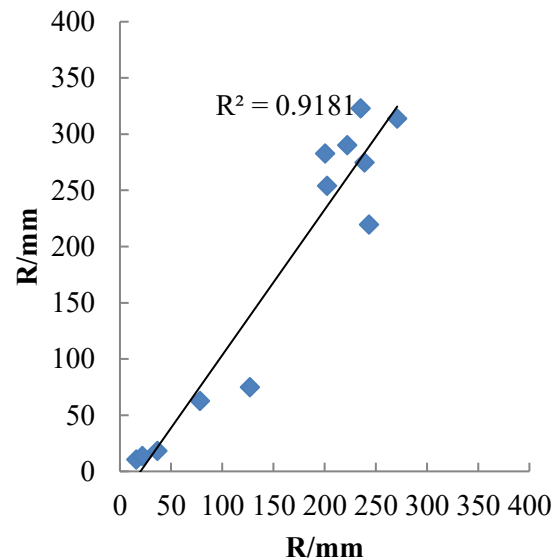


Figure 4.1.2. 5. Rainfall data of Arpege-FN1 vs Balboa FAA.

Temperature (T)

In the 30 years timespan (1979-2008), the monthly average of temperature have been calculated without the following listed periods since they were missing in the series of the Balboa FAA monitoring station:

- Entire 1983 year;
- From January to May (1 to 5 month, extremes included) of the year 1984;
- Months 9 to 12 (extremes included ) of the year 1999;
- Entire 2003 year;
- From January to March and May of the year 2005.

In order to have a more precise comparison between the measured and the calculated data, this removal has been carried out also for obtaining the average values of the models series. After this operation, it can be affirmed that the rainfall simulation of EC-Earth model follows smoothly the average seasonal trend of the measured data of the Balboa FAA monitoring station, with a  $R^2 = 0.73$ . However, it shows an underestimation nearly of  $2^{\circ}\text{C}$  (Tab. 4.1.2.2 and Figs.4.1.2.6-8).

Table 4.1.2. 2. Comparison of monthly average of temperature of Balboa FAA monitoring station and models data, over 30 years (1979-2008).

T/°C monthly average 1979-2008			
Month	Balboa FAA	EC-Earth	Arpege-FN1
1	27	25	26
2	27	26	26
3	28	26	26
4	28	26	27
5	27	25	27
6	27	25	27
7	27	25	27
8	27	25	27
9	27	25	27
10	26	24	27
11	26	24	27
12	27	25	26

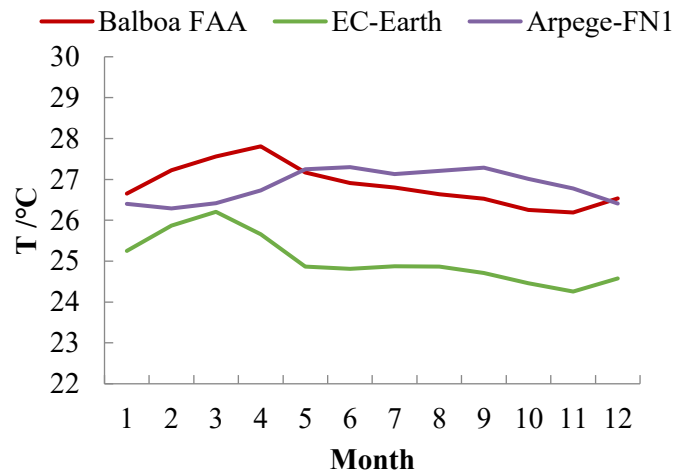


Figure 4.1.2. 6. Comparison of monthly average of temperature of Balboa FAA monitoring station and models data, over 30 years (1979-2008).

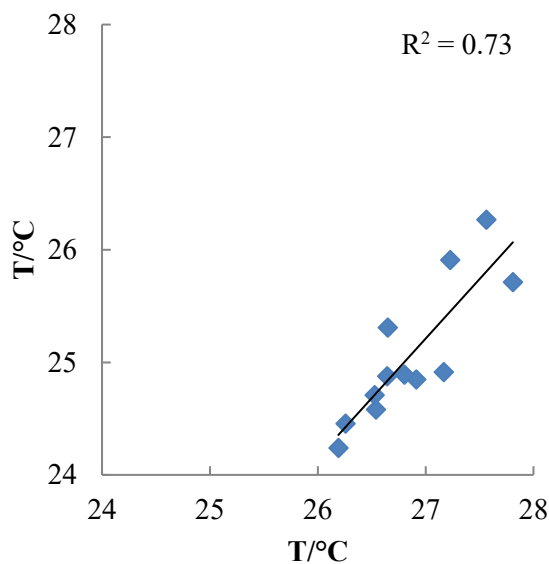


Figure 4.1.2. 7. Temperature data of EC-Earth vs Balboa FAA.

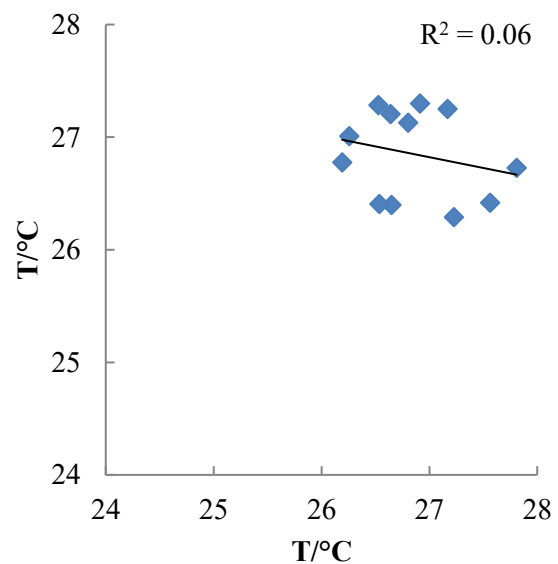


Figure 4.1.2. 8. Temperature data of Arpege-FN1 vs Balboa FAA.

### Relative Humidity (RH)

Even RH data present, over the 30 years, the same missing periods aforementioned for the T values; therefore the same procedure of removal has been adopted for and specifically they are:

This removal has been carried out also from the models series for calculating the average values and realizing the following comparisons.



Observing the trend of the monitoring station of Balboa-FAA, we can sustain that is better represented by EC-Earth model, with a  $R^2$  coefficient of 0.94 (Tab. 4.1.2.3 Figs. 4.1.2.9-11).

Table 4.1.2. 3. Comparison of monthly average of relative humidity of Balboa FAA monitoring station and models data, over 30 years (1979-2008).

RH/% monthly average 1979-2008			
Month	Balboa FAA	EC-Earth	Arpege -FN1
1	73	82	79
2	69	83	75
3	69	83	74
4	73	83	82
5	79	83	90
6	82	83	92
7	82	82	91
8	83	83	91
9	83	84	92
10	84	84	91
11	84	82	90
12	80	82	86

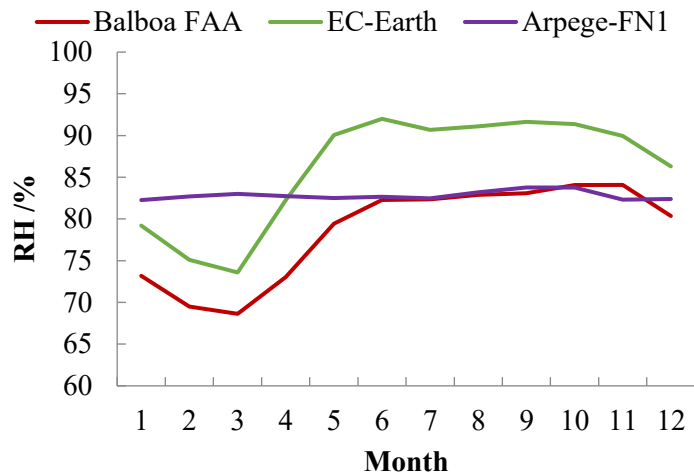


Figure 4.1.2. 9. Comparison of monthly average of relative humidity of Balboa FAA monitoring station and models data, over 30 years (1979-2008).

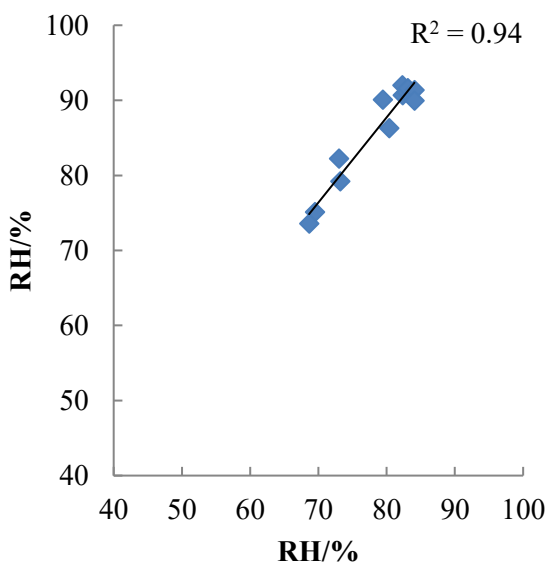


Figure 4.1.2. 10. Relative humidity data of EC-Earth vs Balboa FAA.

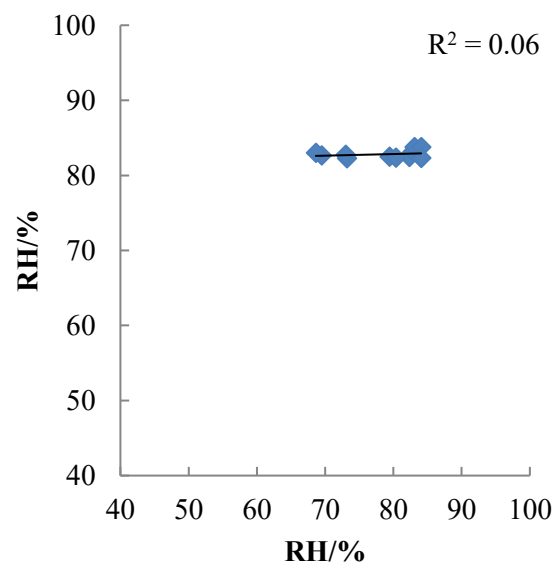


Figure 4.1.2. 11. Relative humidity data of Arpege-FN1 vs Balboa FAA.

### 4.1.3. Area near San Lorenzo

Site location: Long.-80.00, Lat.9.32, EC-Earth central point: Long.-79.85; Lat. 9.3; FN1 central point: Long.-80.00; Lat. 9.24

The comparison with Gatún (G) and Cocosolo-Cristóbal-Limonbay (CCL) monitoring stations, cover a period of 28 years 1981-2008. The area subject of this investigation is highlighted with a red square in Figure 4.1.3.1, for the EC-Earth model, and in Figure 4.1.3.2 for the Arpege model.

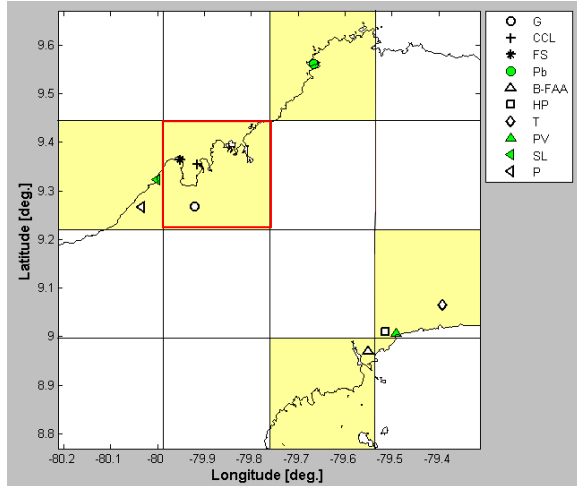


Figure 4.1.3. 1 EC-Earth selected area. In red is highlighted the zone under investigation in this paragraph.

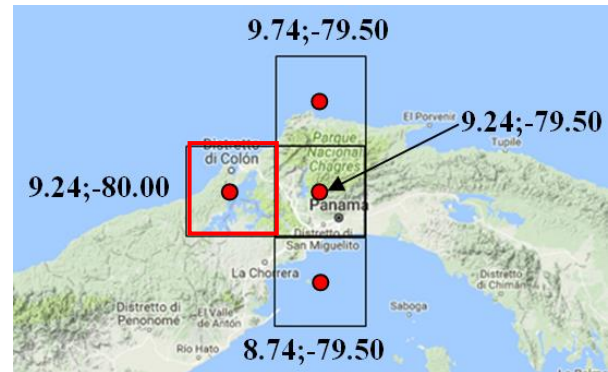


Figure 4.1.3. 2. Arpege selected area. In red is highlighted the zone under investigation in this paragraph.

### Rainfall (R)

The series of this parameter, covering from 1981 to 2008, present missing periods in the data of Cocosolo-Cristóbal-Limonbay station, corresponding to months 7-12 (extremes included) of the entire year 1996, while in 1998 the months absent are 1-7 (extremes included).

The graphical comparisons are here showed as an average between the Gatún and CCL data, and the missing periods have been removed also from the Gatún and model series for realizing the comparative tables and graphs (Tab. 4.1.3.1 and Fig.4.1.3.3).

Referring to the coefficient of determination, the more suitable model simulation is represented by Arpege-FN1, corresponding to  $R^2 = 0.71$  (Figs. 4.1.3.4-5).

Table 4.1.3. 1. Comparison of the average of rainfall monthly amount of Gatún (G) and Cocosolo-Cristóbal-Limonbay (CCL) monitoring stations, and their average, and models data, over 28 years (1981-2008).

Month	R/mm monthly amount 1981-2008			EC - Earth	Arpege-FN1
	G	CCL	Av. G - CCL		
1	100	73	86	89	19
2	36	20	28	65	10
3	50	26	38	81	14
4	148	132	140	204	61
5	294	300	297	309	284
6	243	308	275	341	298
7	294	315	304	383	232
8	314	374	344	364	300
9	286	319	302	297	320
10	341	390	365	280	327
11	420	472	446	241	233
12	274	286	280	150	77

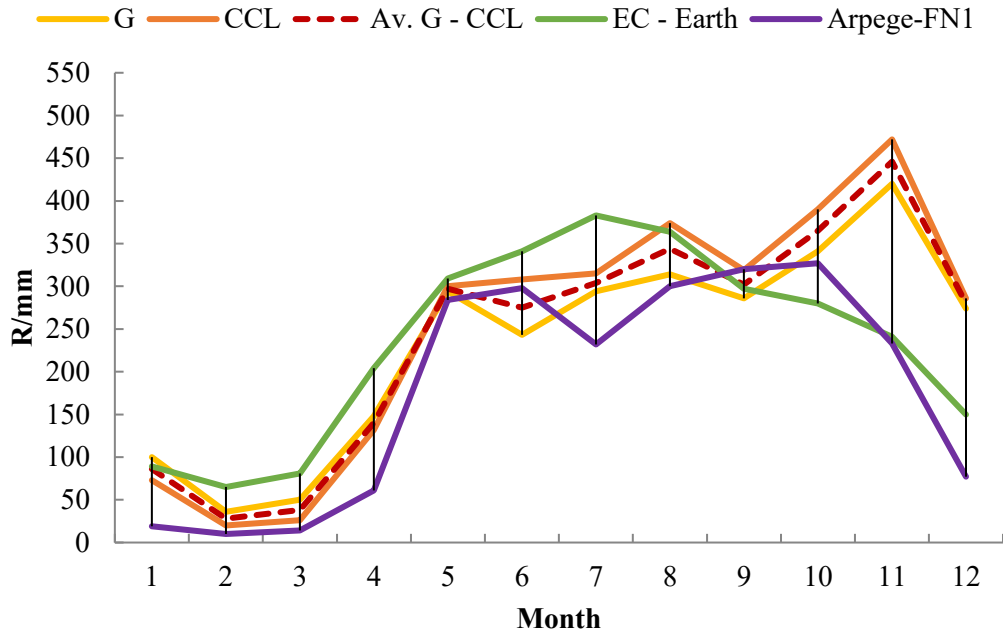


Figure 4.1.3. 3 Average of rainfall monthly amount over 28 years (1981-2008), at the area Near San Lorenzo (Long.-80.00, Lat.9.32). Comparison among the historic series of the Gatún (G) and Cocosolo-Cristóbal-Limonbay (CCL) monitoring stations and the historic simulation of the Arpege-FN1 and EC-Earth models.

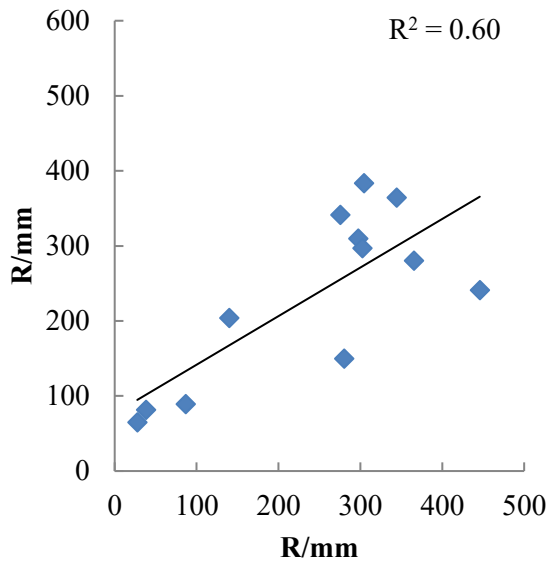


Figure 4.1.3. 4. Rainfall data of EC-Earth vs average G-CCL.

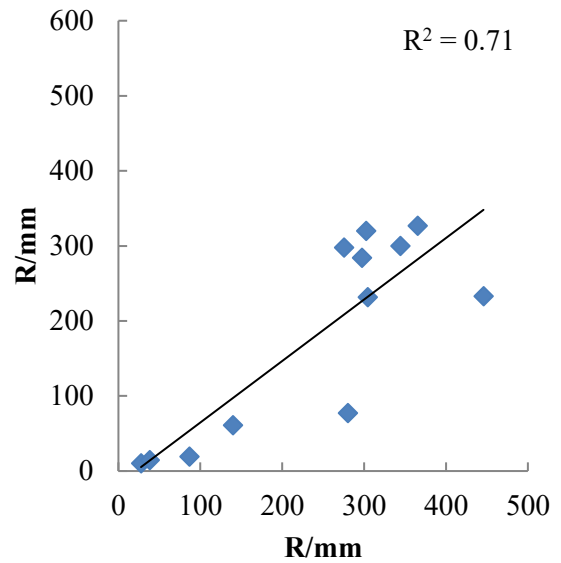


Figure 4.1.3. 5. Rainfall data of Arpege-FN1 vs average G-CCL.

If we include also the data belonging to the monitoring station of Fort Sherman the comparable years are 12, from 1997 to 2008, excluding the missing periods previously mentioned. In this case, both the models shows less comparability with the measured data, demonstrated even by similar  $R^2$  values, around 0.4 (Tab. 4.1.3.2 and Figs. 4.1.3.6-8).

Table 4.1.3. 2. Comparison of the average of rainfall monthly amount of Gatún (G), Cocosolo-Cristóbal-Limonbay (CCL) and Sherman monitoring stations, and their average, and models data, over 12 years (1997-2008).

Month	R/mm monthly amount 1997-2008				EC - Earth	Arpege-FN1
	FS	CCL	G	Av. G-CCL-FS		
1	73	72	87	77	103	86
2	38	13	28	26	66	90
3	62	34	66	54	80	92
4	175	129	138	147	220	146
5	335	278	275	296	340	213
6	246	260	219	241	337	215
7	338	304	277	306	382	217
8	374	366	317	353	368	222
9	278	274	262	271	298	253
10	301	344	318	321	269	244
11	538	503	436	493	235	174
12	346	330	325	334	167	120

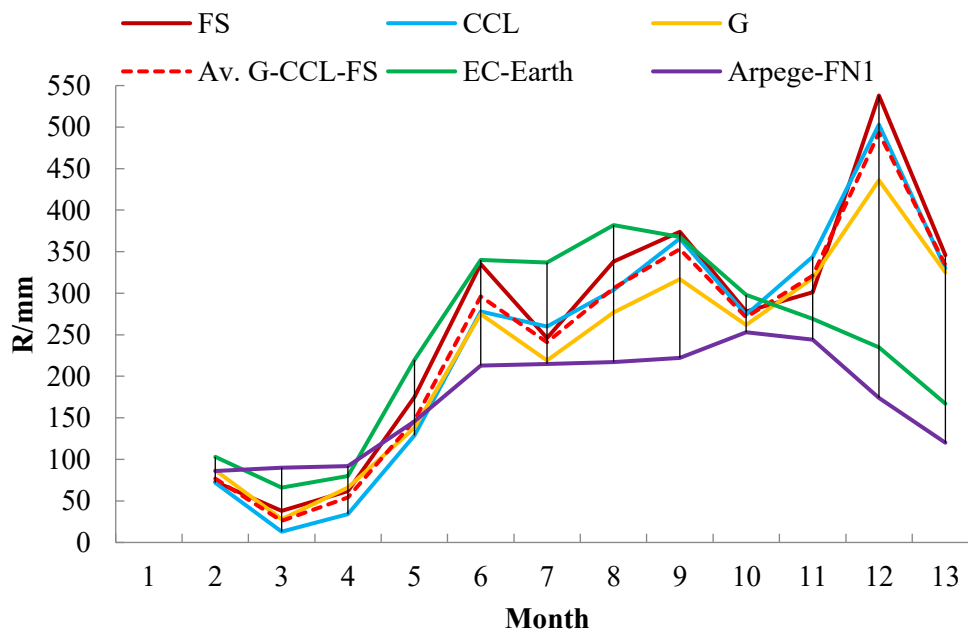


Figure 4.1.3. 6. Comparison of the average of rainfall monthly amount of Gatún (G), Cocosolo-Cristóbal-Limonbay (CCL) and Fort Sherman (FS) monitoring stations, and their average, and models data, over 12 years (1997-2008).

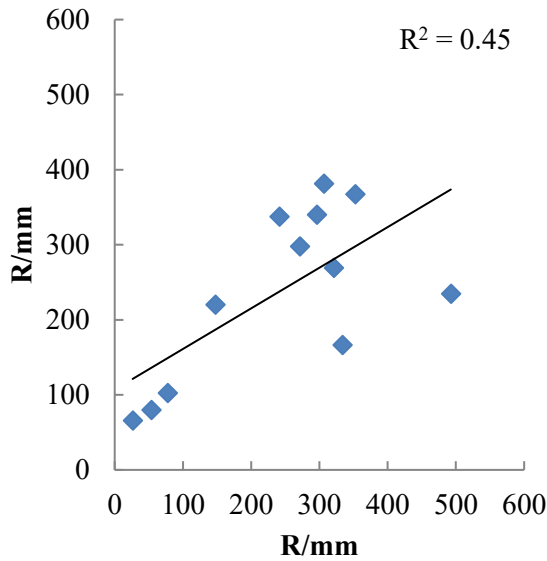


Figure 4.1.3. 7. Rainfall data of EC-Earth vs average G-CCL-FS.

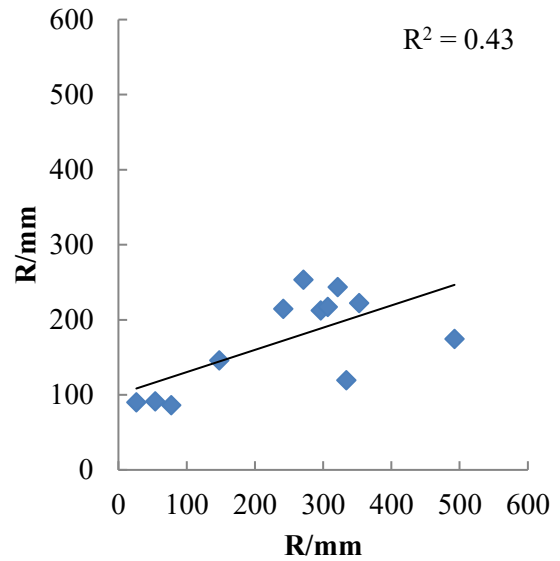


Figure 4.1.3. 8. Rainfall data of Arpege-FN1 vs average G-CCL-FS.

Temperature (T)

Gatún and Cocosolo+Cristóbal+Limonbay

The comparison has been performed within the period from 1979 to 2006. The missing times, considering the Gatún station, are the following: during the year 1999 months 9 to 12; in 2005 months 1-3 and 5; while in 2006 the second half is missing (months 6-12, extremes included). Considering CCL station, the missing periods are the years from 1996 to 1999; in 2000 months 1-5; the whole year 2003 and month 1-3 and 5 of 2005. Observing the data listed in Table 4.1.3.3 the monthly average of both the stations are the same for every month, since we can plot only the average G-CCL in the graph (Fig. 4.1.3.9)

As observed in the previous locations, the most suitable situation is showed by EC-Earth experiment, since it presents a coefficient of determination of 0.69 (Figs. 4.1.3.10-11).

Table 4.1.3. 3. Comparison of the average of monthly temperature of Gatún (G) and Cocosolo-Cristóbal-Limonbay (CCL) monitoring stations, and their average, and models data, over 28 years (1979-2006).

T/°C monthly average 1979-2006					
Month	G	CCL	Av. G-CCL	EC-Earth	Arpege- FN1
1	27	27	27	25	25
2	27	27	27	25	25
3	27	27	27	25	25
4	27	27	27	25	26
5	27	27	27	25	27
6	27	27	27	25	27
7	27	27	27	25	26
8	27	27	27	25	26
9	27	27	27	25	27
10	27	27	27	24	26
11	26	26	26	24	25
12	27	27	27	24	25

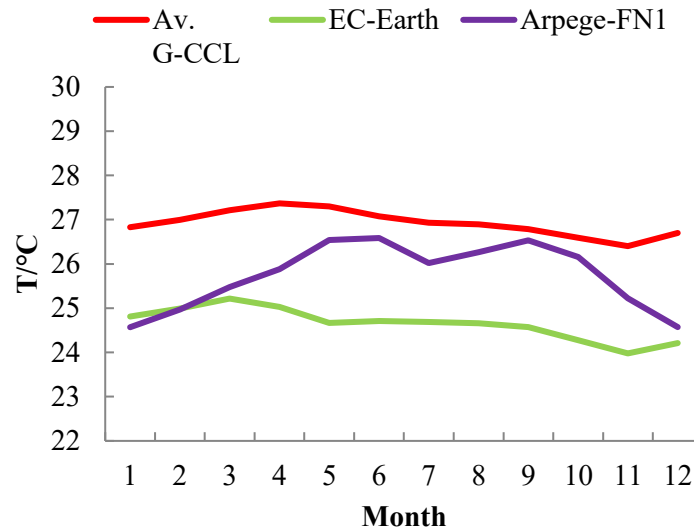


Figure 4.1.3. 9. Comparison of the average of monthly temperature of Gatún (G) and Cocosolo-Cristóbal-Limonbay (CCL) monitoring stations, and their average, and models data, over 28 years (1979-2006).

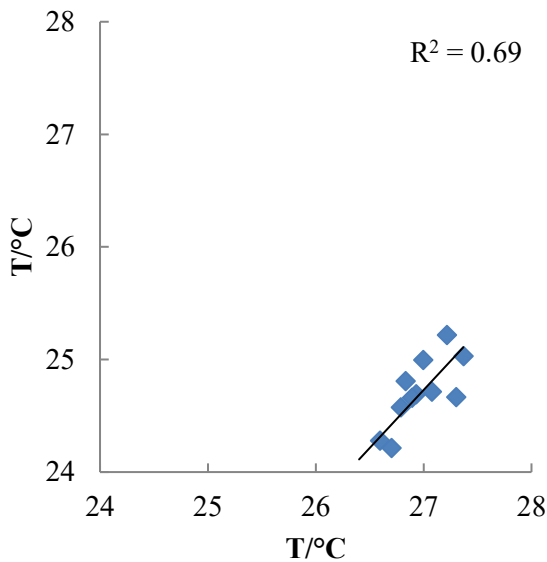


Figure 4.1.3. 10. Temperature data of EC-Earth vs average G-CCL.

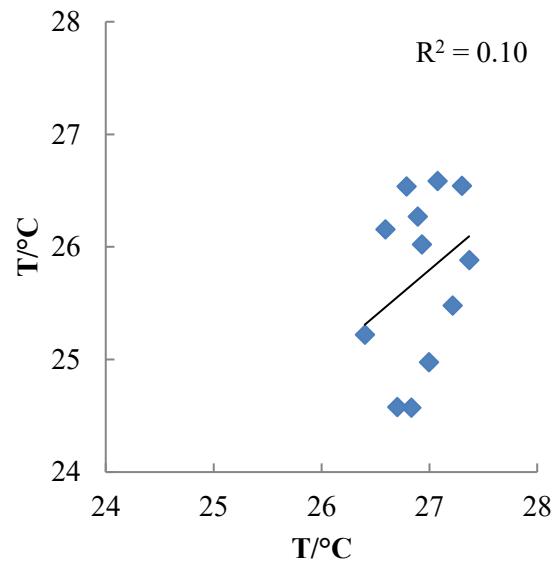


Figure 4.1.3. 11. Temperature data of Arpege-FN1 vs average G-CCL.

Gatún, Cocosolo+Cristóbal+Limonbay and Fort Sherman

Even for the temperature parameter, the third station present in this area, Fort Sherman, can be involved. It presents historic data within 1997-2008, with missing periods during the three first months of the 1997 (months 1-3, extremes included).

Making a comparison between the values obtained by averaging the three stations data and the models one (Tab. 4.1.3.4 and Fig. 4.1.3.12), EC-Earth resulted fitting better the trend of the observed data, as previously noticed (Figs. 4.1.3.13-14).

Table 4.1.3. 4. Comparison of the average of monthly temperature of Gatún (G), Cocosolo-Cristóbal-Limonbay (CCL) and Fort Sherman (FS) monitoring stations, and their average, and models data, over 12 years (1997-2008).

**T/°C monthly average  
1997-2008**

Month	FS	G	CCL	Av. G-CCL-FS	EC-Earth	Arpege-FN1
1	25	27	27	26	25	25
2	25	27	27	26	25	25
3	25	27	27	27	25	26
4	26	27	27	27	25	26
5	26	27	27	27	25	27
6	25	27	27	27	25	27
7	25	27	27	26	25	26
8	25	27	27	26	25	26
9	25	27	27	26	25	27
10	25	27	27	26	25	26
11	25	26	26	26	24	25
12	25	27	27	26	24	25

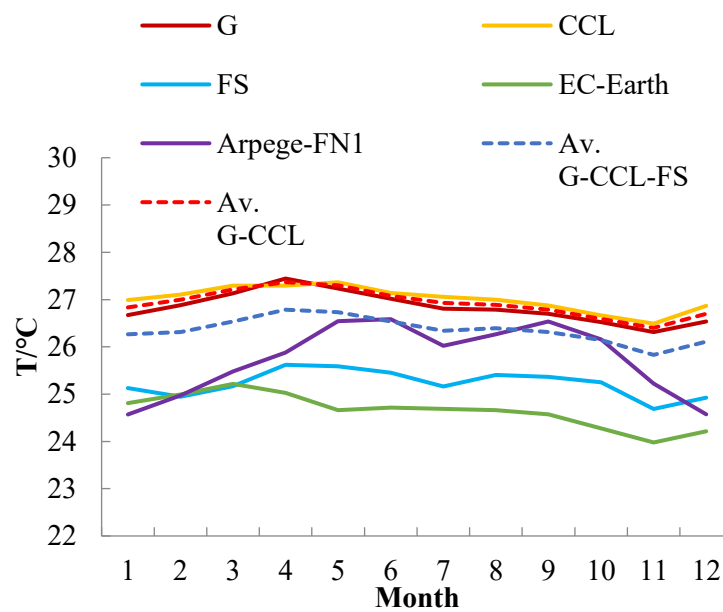


Figure 4.1.3. 12. Average of the air T (°C) monthly amount over 1997-2008 at the area near San Lorenzo.

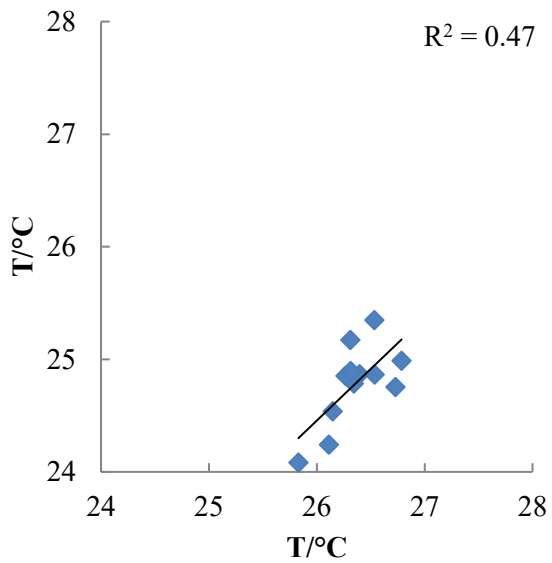


Figure 4.1.3. 13. Temperature data of EC-Earth vs Average G-CCL.

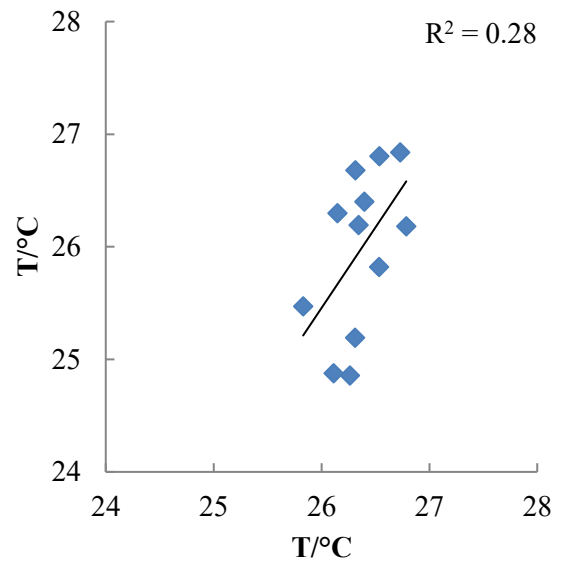


Figure 4.1.3. 14. Temperature data of Arpege-FN1 vs Average G-CCL.

Relative Humidity (RH)

Gatún and Cocosolo+Cristóbal+Limonbay

The period of comparison is the entire period of 30 years (1979-2008). Nevertheless, both stations present missing periods, specifically, for Gatún station, they are the same previously indicated for the T parameter. In addition to them, RH data of entire years 2007-2008 are absent. In the case of CCL station, during 1979, months 10-12 are missing, while in 1980, months 1-7 are not measured. Moreover, the years 1983, from 1985 to 1989 and from 1996 to 1999 are totally absent. During 2000, the months not present are 1-5, while in 2005 months 1-3 and 5 are missing.

Considering the comparison among the monitoring station data and the modelled ones, even with an overestimation of 10%, EC-Earth shows the best representation of the trend of the measured data (Tab. 4.1.3.5 and Figs. 4.1.3.15-17).

Table 4.1.3. 5. Comparison of the average of monthly relative humidity of Gatún (G) and Cocosolo-Cristóbal-Limonbay (CCL) monitoring stations, and their average, and models data, over 28 years (1979-2008).

Month	RH monthly average (%) 1979-2008				
	G	CCL	Av. G-CCL	EC-Earth	Arpege-FN1
1	76	77	76	84	89
2	73	76	74	82	87
3	73	76	73	81	86
4	75	75	75	87	87
5	79	82	79	92	88
6	81	83	81	92	89
7	81	83	82	92	90
8	82	85	83	93	90
9	83	86	84	92	90
10	83	86	84	92	90
11	83	85	83	93	91
12	80	82	81	90	90



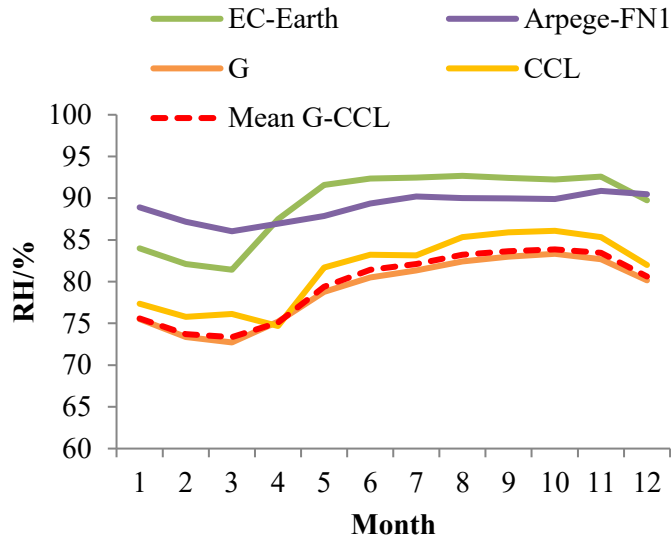


Figure 4.1.3. 15. Average of the RH monthly amount over 1979-2006 at the area near San Lorenzo.

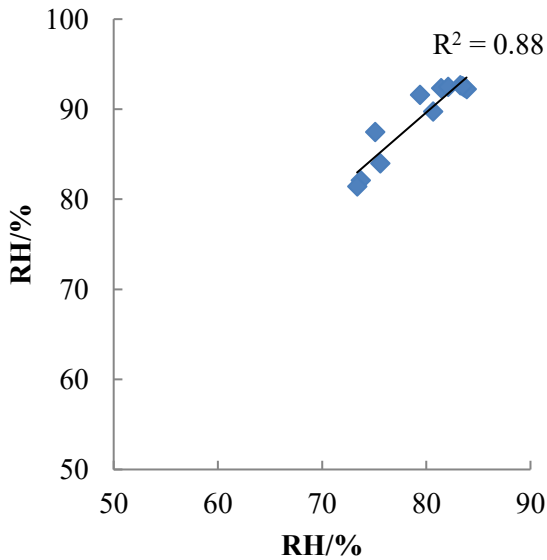


Figure 4.1.3. 16. Relative humidity data of EC-Earth vs Average G-CCL.

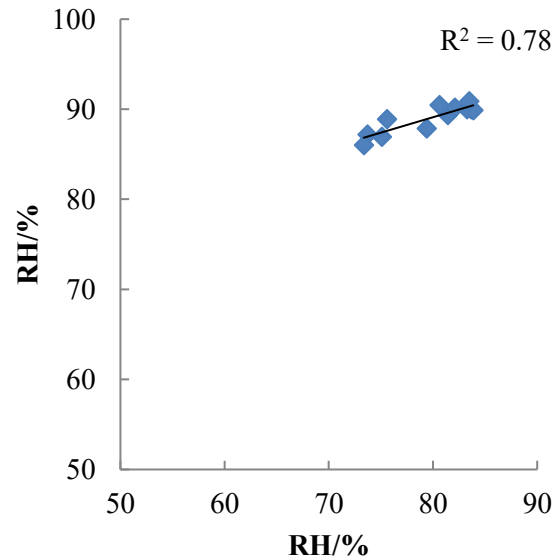


Figure 4.1.3. 17. Relative humidity data of Arpege-FN1 vs Average G-CCL.

### Gatún, Cocosolo+Cristóbal+Limonbay and Fort Sherman

As previously described, we can include also the third station, Fort Sherman, covering a shorter period of 12 years (1997-2008), with the following missing months: 10-12 in 1979, 1-7 in 1980, 1-5 in 2000, 1-3 and 5 in 2005. Comparing the values of the average obtained by the three stations with the models data, the trend of EC-Earth is the most similar, showing a  $R^2 = 0.91$  (Tab. 4.1.3.6 and Figs. 4.1.3.18-20).

Table 4.1.3. 6. Comparison of the average of monthly relative humidity of Gatún (G) and Cocosolo-Cristóbal-Limonbay (CCL) and Fort Sherman (FS) monitoring stations, and their average, and models data, over 12 years (1997-2008).

**RH monthly average (%)**  
**1997-2008**

Month	FS	Av. G-CCL	Av. G-CCL-FS	EC-Earth	Arpege-FN1
1	89	79	84	86	88
2	87	78	83	82	87
3	88	77	83	82	85
4	90	80	85	88	86
5	93	83	88	92	87
6	94	84	89	92	89
7	94	85	90	93	90
8	94	87	90	92	90
9	93	87	90	92	91
10	93	87	90	92	91
11	95	87	91	92	91
12	92	85	89	90	90

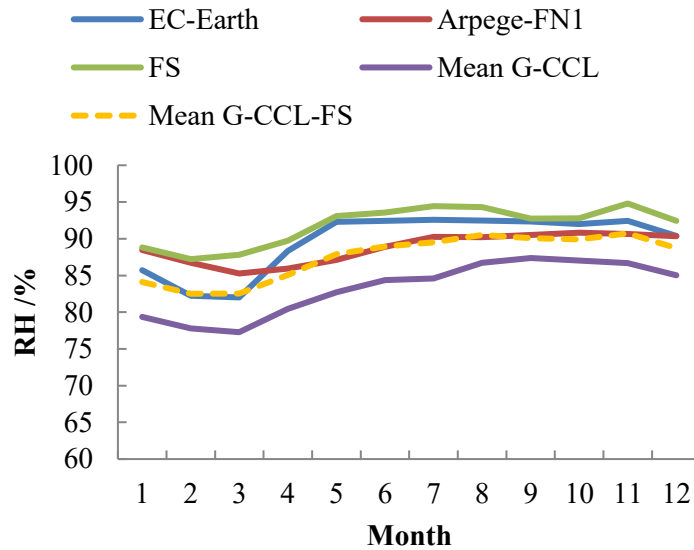


Figure 4.1.3. 18. Average of the RH monthly amount over 1997-2008 at the area near San Lorenzo.

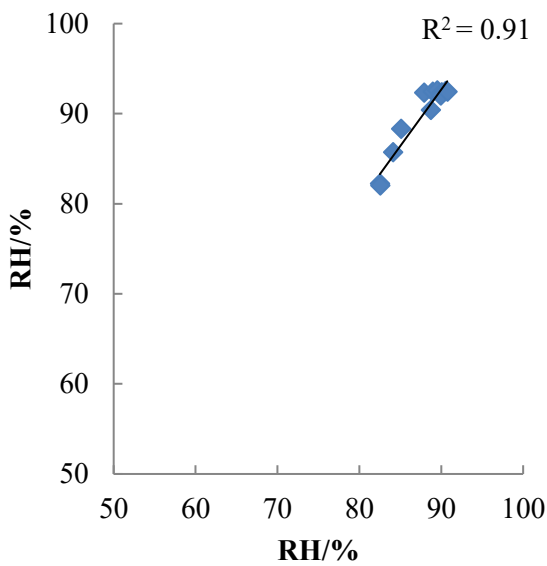


Figure 4.1.3. 19 Relative humidity data of EC-Earth vs Mean G-CCL-FS.

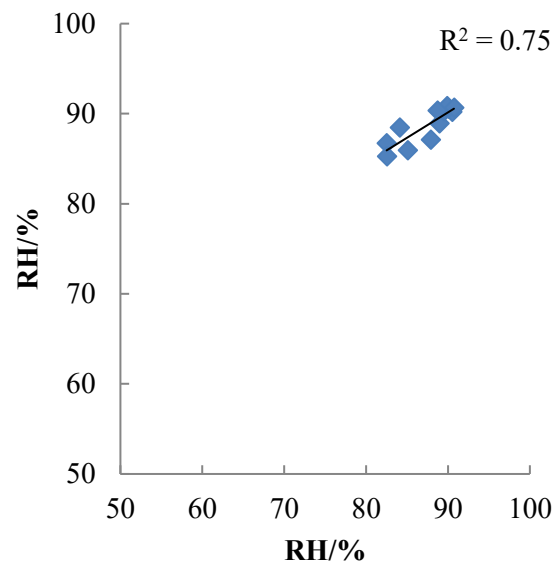


Figure 4.1.3. 20. Relative humidity data of FN1 vs Mean G-CCL-FS.

#### 4.1.4. San Lorenzo area

Site location: Long. -80.00, Lat. 9.32; EC-Earth central point: Long.-80.05; Lat. 9.3; FN1 central point: Long.-80.00; Lat. 9.24 (Figs. 4.1.4.1-2).

It has to be underlined that this monitoring station presented only rainfall data.

#### Rainfall (R)

The common period considered is from 1979 to 1998, with missing 10 and 11 months of the year 1994. Comparing the modelled data with the observed ones, it is noticeable that none model represents exactly the real trend; moreover, the simulated data underestimate the range of rainfall measured at the monitoring station (Tab.4.1.4.1 and Fig. 4.1.4.3).

Indeed, considering the  $R^2$ , the values obtained are 0.6, by EC-Earth and 0.7 by Arpege (Figs. 4.1.4.4-5).

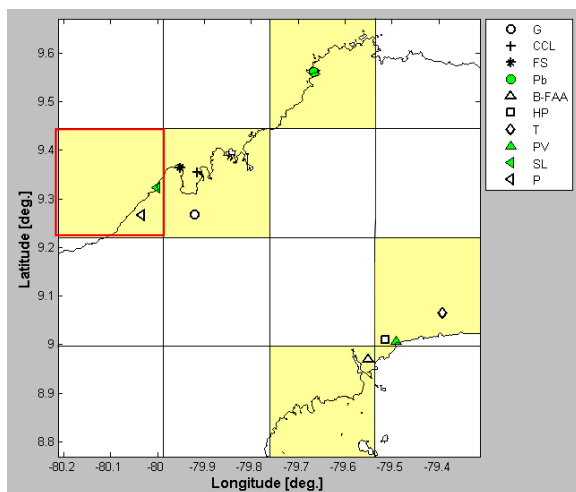


Figure 4.1.4. 1. EC-Earth selected area. In red is highlighted the zone under investigation in this paragraph.

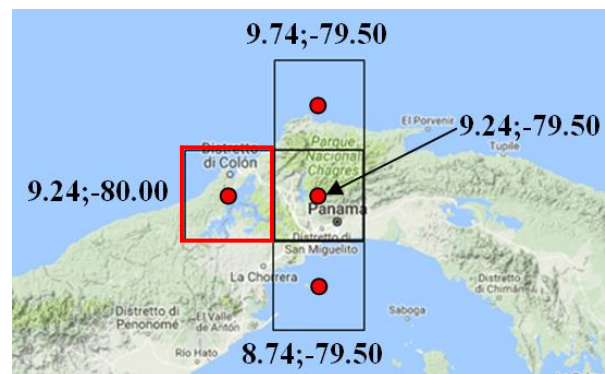


Figure 4.1.4. 2. Arpege selected area. In red is highlighted the zone under investigation in this paragraph.

Table 4.1.4. 1. Comparison of the average of monthly relative humidity of Pina (P) monitoring station and models data, over 20 years (1979-1998).

<b>R monthly amount 1979-1998 (mm)</b>			
<b>Month</b>	<b>Pina</b>	<b>EC-Earth</b>	<b>Arpege-FN1</b>
1	97	122	93
2	44	104	95
3	47	99	115
4	157	158	161
5	371	157	212
6	357	149	233
7	373	193	219
8	282	158	225
9	286	121	248
10	378	163	212
11	402	223	177
12	225	182	118

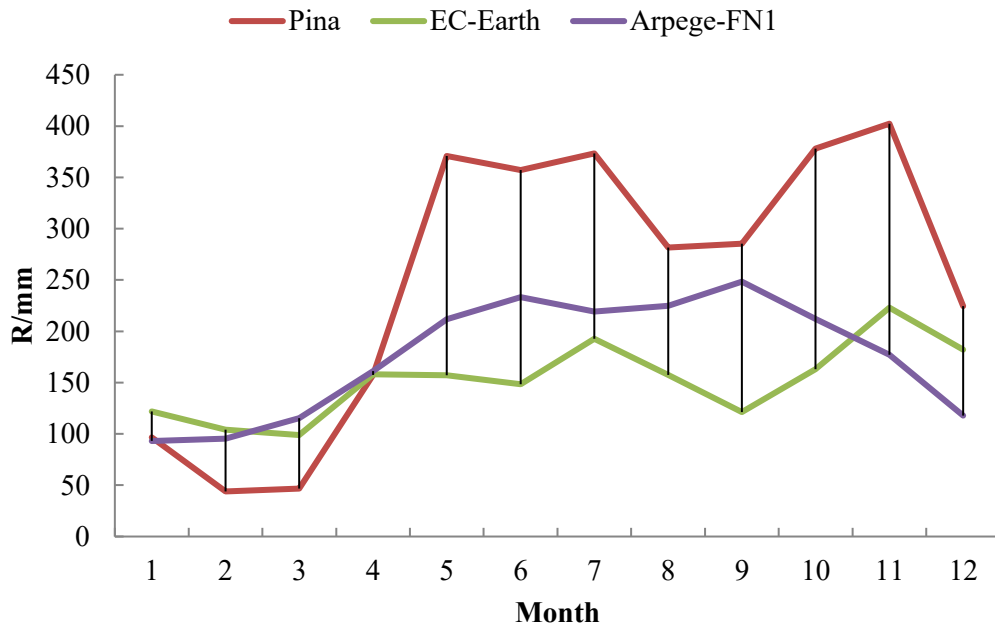


Figure 4.1.4. 3. Average of the rainfall monthly amount over 1979-1998 at the area of San Lorenzo.

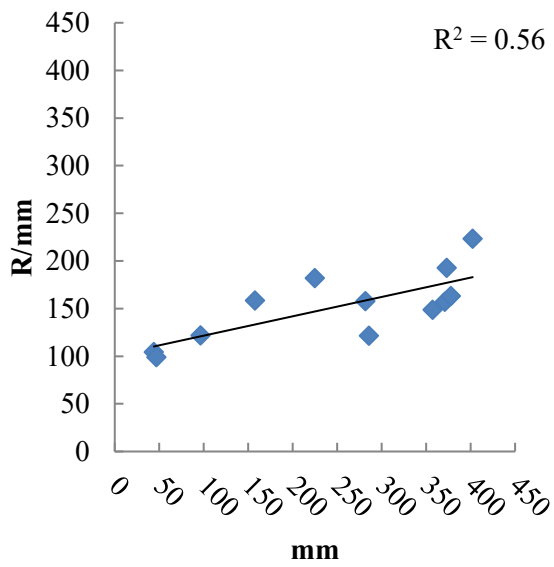


Figure 4.1.4. 4. Rainfall data of EC-Earth vs Pina.

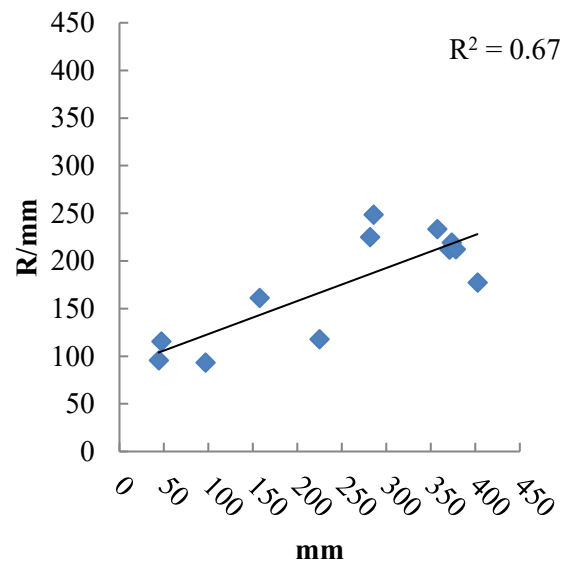


Figure 4.1.4. 5. Rainfall data of FN1 vs Pina.

#### 4.1.5. Portobelo area

Site location: Long -79.67, Lat.9.56; EC-Earth central point: Long. -79.65, Lat. 9.55; FN1 central point: Long. -79.50, Lat. 9.74 (Figs. 4.5.1.1-2).

As the previous one, this monitoring station shows only rainfall records.

#### Rainfall (R)

The comparison with Portobelo station covers 22 years (1979-2000) and it has been performed excluding the missing periods of the station (months from 3 to 9 of 1999 year). Between the two simulations, Arpege-FN1 resulted slightly better in the representation of the seasonality of rainfall measured by Portobelo monitoring station (Tab. 4.1.5.1 and Fig. 4.1.5.3), indeed, also considering the  $R^2$ , Arpege-FN1 shows a little higher value, of 0.8, respect to 0.7 obtained by EC-Earth model (Figs. 4.1.5.4-5).

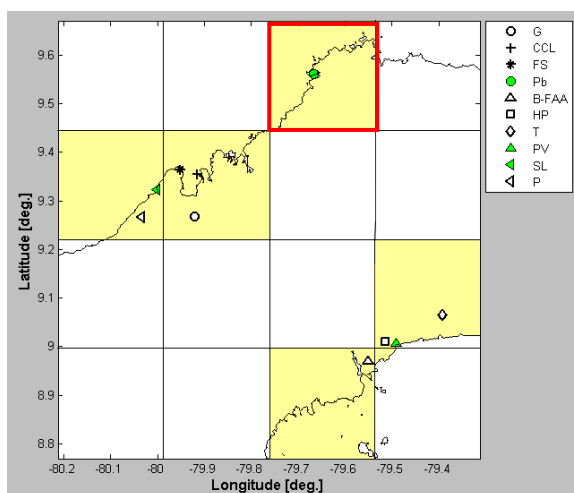


Figure 4.1.5. 1. EC-Earth selected area. In red is highlighted the zone under investigation in this paragraph.

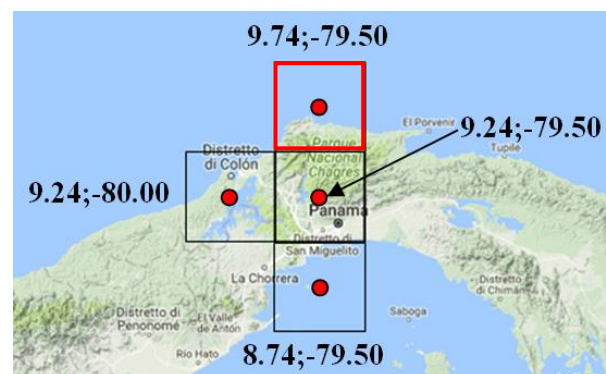


Figure 4.1.5. 2. Arpege selected area. In red is highlighted the zone under investigation in this paragraph.

Table 4.1.5. 1 Comparison of the average of monthly relative humidity of Portobelo (Pb) monitoring station and models data, over 22 years (1979-2000).

Month	<u>R monthly amount 1979-2000 (mm)</u>		
	Portobelo	EC - Earth	Arpege-FN1
1	121	112	103
2	68	88	93
3	55	94	101
4	173	202	123
5	340	344	245
6	426	404	282
7	422	411	225
8	428	435	246
9	357	404	282
10	443	342	305
11	461	256	265
12	365	170	129

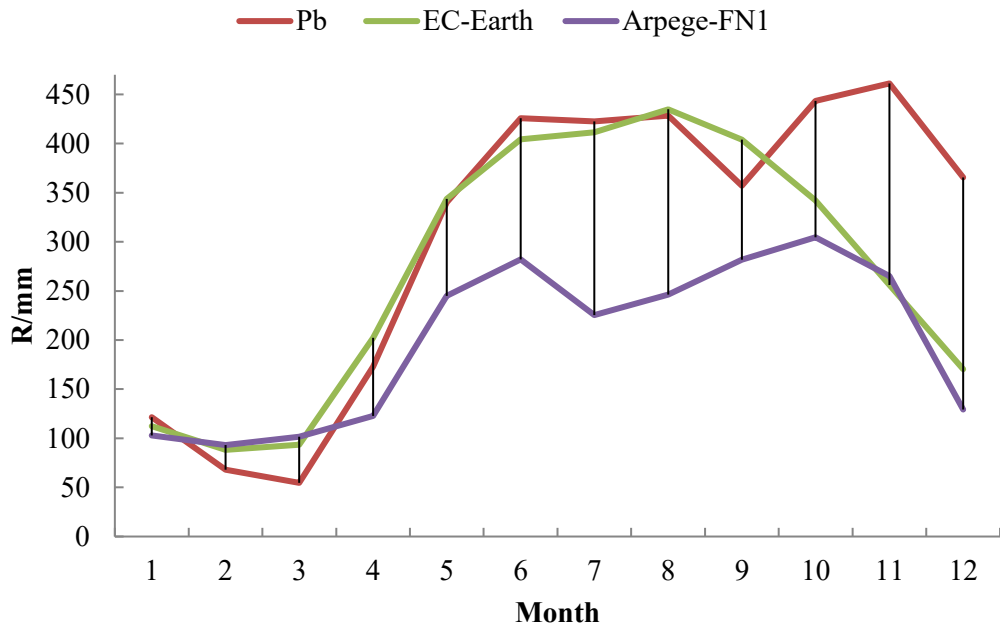


Figure 4.1.5. 3. Average of the rainfall monthly amount over 1979-2000 at the area of Portobelo.

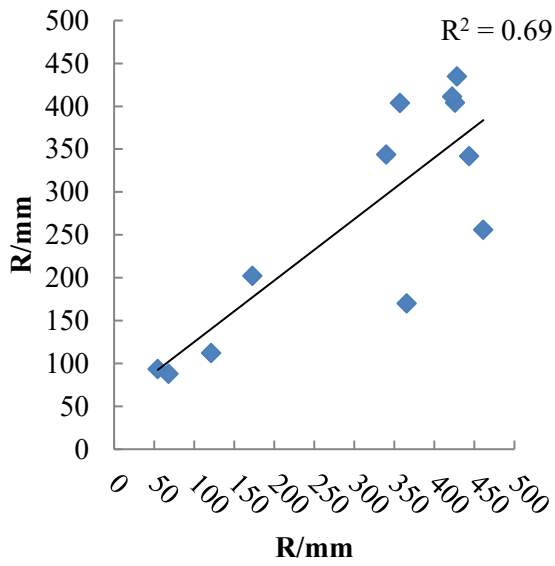


Figure 4.1.5. 4. Rainfall data of EC-Earth vs Portobelo.

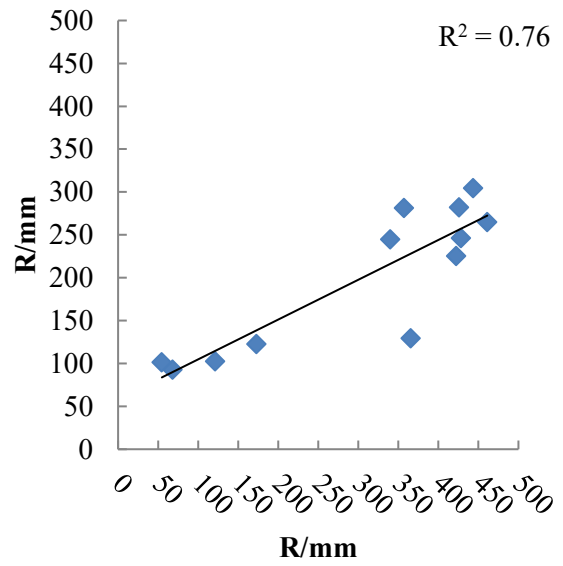


Figure 4.1.5. 5. Rainfall data of FN1 vs Portobelo.

## 4.2 Bias Correction

Observing the comparisons present in the previous paragraphs, it can be noticed that the data series of to the observed data (collected from the monitoring stations) and the calculated ones (from the models) show several differences.

In order to perform a bias correction of the simulation data, the procedures, listed below, have been described and adopted for each area of interest, thus for each point extracted from the models and specifically compared with the data of the corresponding monitoring stations.

Moreover, the correction has been utilized also for the future period, selecting the middle-future 30 years, 2039-2068, for both EC-Earth and Arpege models. Since EC-Earth future experiment represents the RCP 8.5 IPCC scenario, for comparing a similar projection, also for Arpege the same scenario typology has been selected, described by the FN2 experiment.

- **Rainfall:** in this case the bias utilized is a multiplying factor ( $f_P$ ) obtained with function (e1):

$$f_P = \frac{\overline{P_o}}{\overline{P_m}} \quad (e1)$$

Where  $\overline{P_o}$  is the daily precipitation average of the observed data during the entire historic period considered (e.g. 30 years, 1979-2008) and  $\overline{P_m}$  is the rainfall average of the model data referred to the same period.

The  $f_P$  is multiplied for each daily precipitation data of both historic and future simulation.

- **Relative Humidity:** the same procedure has been used also for the RH correction. So in this case the a multiplying factor will be  $f_{RH}$  (e2):

$$f_{RH} = \frac{\overline{RH_o}}{\overline{RH_m}} \quad (e2)$$

Where  $\overline{RH_o}$  is the daily RH average of the observed data during the entire historic period considered (e.g. 30 years, 1979-2008) and  $\overline{RH_m}$  is the RH average of the model data referred to the same period.

The  $f_{RH}$  is multiplied for each daily data of relative humidity of both historic and future simulation.

- **Temperature:** considering the temperature, the method adopted is the additive factor ( $f_T$ ). For calculating it, the annual temperature of the whole period of reference (e.g. 1979-2008) has been determined for both the measured data ( $T_o$ ) of the stations and the records of the models ( $T_m$ ). The  $f_T$  is obtained by subtracting the  $T_o$  from  $T_m$ , as represented in e3.

$$f_T = T_m - T_o \quad (e3)$$

Thus, the value of  $f_T$  is added to both the historic and future series of the models.

In the following paragraphs, the bias correction for each parameters and for each point of EC-Earth and Arpege historic and future simulation are reported.

#### 4.2.1 Panama Viejo area

Site location: Long.-79.49; Lat.9.01; EC-Earth central point:-79.45, 9.1; Arpege-FN1 central point: -79.50; 9.24.

##### Rainfall (R)

In this case the period considered was 1979-2008, considering the EC-Earth experiment, the  $\overline{P_o} = 5.50$  mm, calculated by the average of the two stations of Hato Pintado (HP) and Tocumen (T), while  $P_m = 6.23$  mm, therefore  $f_p = 0.88$  mm. While for FN1-Arpege simulation the  $P_m = 6.4$  mm, therefore  $f_p = 0.86$  mm.

The results obtained and the comparisons are showed in Table 4.2.1.1 and Figure 4.2.1.1.

Table 4.2.1. 1. Comparison of yearly amount of rainfall, over the past period 1979-2008, between the average of the monitoring stations records and the models data with or without bias ( $f_p$ ).

R yearly amount (mm)							
Past (1979-2008)							
Year	Hato Pintado	Tocumen	Av.HP-T	EC-Earth		Arpege-FN1	
				without $f_p$	with $f_p$	without $f_p$	with $f_p$
1979		2425	2425	2206	1948	2078	1797
1980		1801	1801	2304	2035	2491	2154
1981		2645	2645	2579	2278	2333	2017
1982		1505	1505	1915	1691	2272	1964
1983		1955	1955	1800	1590	2308	1996
1984		2240	2240	2349	2075	2382	2060
1985		1513	1513	2092	1848	2075	1794
1986		1757	1757	2050	1811	2574	2226
1987		1793	1793	2215	1957	2461	2128
1988	2219	2233	2226	2603	2299	2196	1899
1989	1729	1882	1806	2011	1776	2359	2040
1990	1732	1686	1709	2447	2161	2503	2164
1991	1934	1398	1666	2007	1773	2850	2464
1992	1823	1583	1703	1870	1651	2617	2262
1993	2282	2044	2163	2190	1934	2051	1773
1994	1855	1639	1747	2176	1922	1896	1640
1995	2283	2516	2399	2501	2209	2503	2165
1996	2229	1958	2093	2601	2297	2366	2046
1997	1860	1456	1658	1745	1541	2323	2008
1998	2381	2293	2337	2344	2070	2223	1922
1999	2266	2142	2204	2514	2220	2527	2185
2000	2349	1829	2089	2420	2137	2366	2046
2001	2128	1779	1954	2323	2052	2269	1961
2002	1987	1573	1780	2132	1883	2402	2077
2003	2105	2015	2060	2452	2166	2386	2063
2004	1865	1973	1919	2755	2434	1951	1687
2005	2151	2026	2089	2343	2070	2348	2030
2006	1962	2371	2166	2355	2080	2275	1967
2007	2218	1877	2048	2692	2377	1940	1677
2008	1971	2162	2067	2281	2015	2416	2089



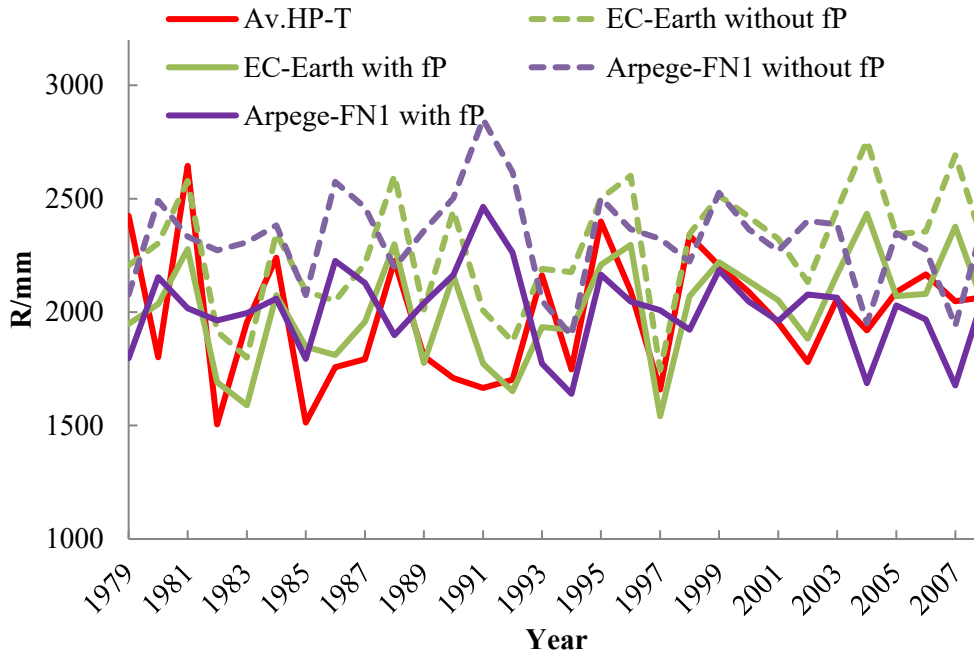


Figure 4.2.1. 1. Comparison of the yearly rainfall amount HP-T / EC-Earth / FN1-Arpege (1979-2008).

Concerning the future situation, 2039-2068 years, if we consider the data without bias correction, no changes in rainfall are foreseen for the future 30 years considering the EC-Earth scenario, while applying the multiplicative factor it can be noticed an increase of the precipitation trend (Fig. 4.2.1.2 and Tab. 4.2.1.2).

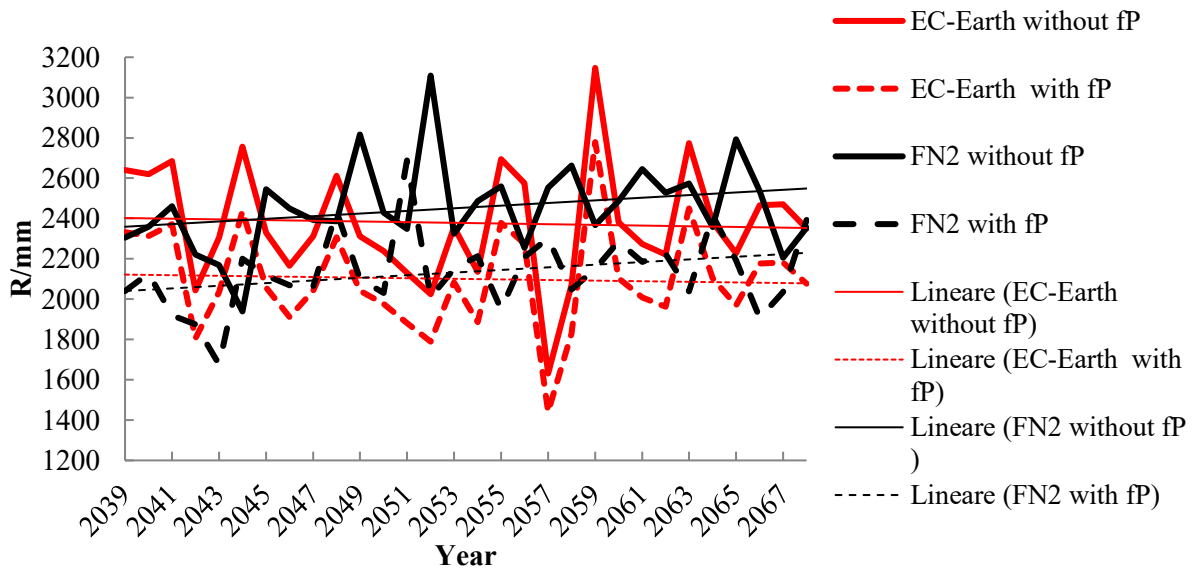


Figure 4.2.1. 2. Comparison of the yearly R amount EC-Earth – Arpege-FN 2.

Table 4.2.1. 2. Comparison of yearly amount of rainfall, over the future period 2039-2068, models data with or without bias ( $f_P$ ).  
R yearly amount/mm

Year	<i>Future (2039-2068)</i>			
	EC-Earth		Arpege-FN2	
	without $f_P$	with $f_P$	without $f_P$	with $f_P$
2039	2640	2332	2306	2040
2040	2620	2314	2359	2127
2041	2685	2372	2461	1920
2042	2044	1805	2221	1875
2043	2306	2036	2169	1676
2044	2757	2435	1939	2201
2045	2329	2057	2545	2118
2046	2165	1912	2450	2069
2047	2311	2041	2393	2063
2048	2612	2307	2387	2434
2049	2312	2042	2816	2101
2050	2239	1977	2429	2031
2051	2131	1882	2349	2688
2052	2025	1789	3109	2010
2053	2358	2083	2325	2149
2054	2135	1886	2486	2213
2055	2694	2379	2559	1949
2056	2576	2275	2254	2208
2057	1631	1441	2553	2302
2058	2070	1829	2663	2048
2059	3147	2779	2368	2150
2060	2381	2103	2487	2287
2061	2274	2009	2645	2185
2062	2222	1962	2527	2225
2063	2774	2450	2573	2038
2064	2381	2103	2357	2415
2065	2228	1968	2793	2192
2066	2465	2177	2536	1906
2067	2470	2182	2205	2036
2068	2350	2076	2354	2392

Relative Humidity (RH)

In consideration of the RH in this location, only data belonging to Tocumen presented relative humidity records with a  $\overline{RH_o} = 8.35\%$ , while EC-Earth has a  $\overline{RHm} = 87.58\%$ , obtaining a 0.93% of  $f_{RH}$ . In case of Arpege-FN1  $\overline{RHm} = 90.20\%$ , since  $f_{RH} = 0.90\%$  (Tab. 4.2.1.3 and Fig. 4.2.1.3).

Table 4.2.1. 3. Comparison of monthly average of Relative Humidity, over the past period 1979-2008, between the average of the monitoring station records and the models data with or without bias  $f_{RH}$ .

RH monthly average/%					
Past 1979-2008					
Month	Tocumen	EC-Earth		Arpege-FN1	
		without $f_{RH}$	with $f_{RH}$	without $f_{RH}$	with $f_{RH}$
1	74	81	75	89	80
2	71	77	72	87	79
3	73	76	70	86	78
4	75	83	77	88	79
5	85	91	85	90	81
6	86	93	86	91	82
7	85	92	86	92	83
8	86	93	86	92	83
9	87	93	86	92	83
10	87	93	86	92	83
11	86	92	85	92	83
12	80	87	81	91	82

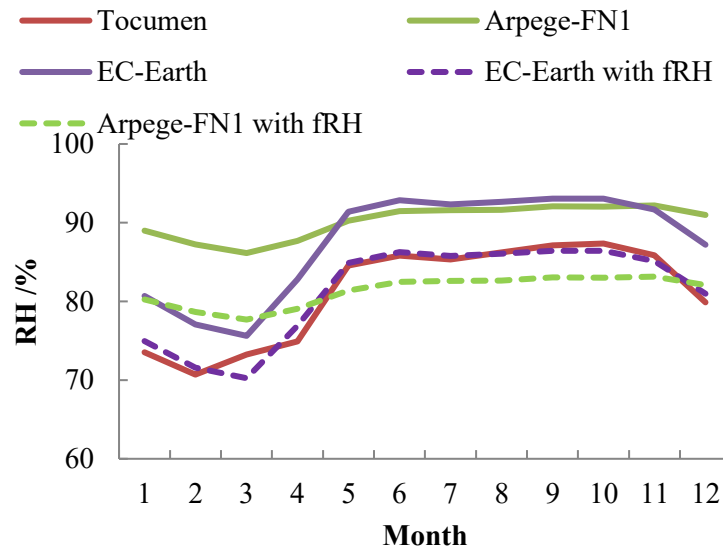


Figure 4.2.1. 3. RH monthly average over 30 years (1979-2008).

Considering the future period, EC-Earth shows a trend similar to the past period of reference, while Arpege has an overestimation of the dry season (January-April) even after the bias correction (Tab. 4.2.1.4 and Fig. 4.2.1.4).

Table 4.2.1. 4. Comparison of monthly average of Relative Humidity, over the future period 2039-2068, between the average of the models data with or without bias ( $f_{RH}$ ).

RH monthly average/%				
<i>Future 2039-2068</i>				
Month	EC-Earth		Arpege-FN2	
	without $f_{RH}$	with $f_{RH}$	without $f_{RH}$	with $f_{RH}$
1	81	75	89	80
2	76	71	87	78
3	76	71	85	76
4	82	77	87	78
5	92	85	90	81
6	93	86	92	83
7	92	86	92	83
8	93	86	92	83
9	93	86	92	83
10	93	87	92	83
11	92	86	92	83
12	88	82	91	82

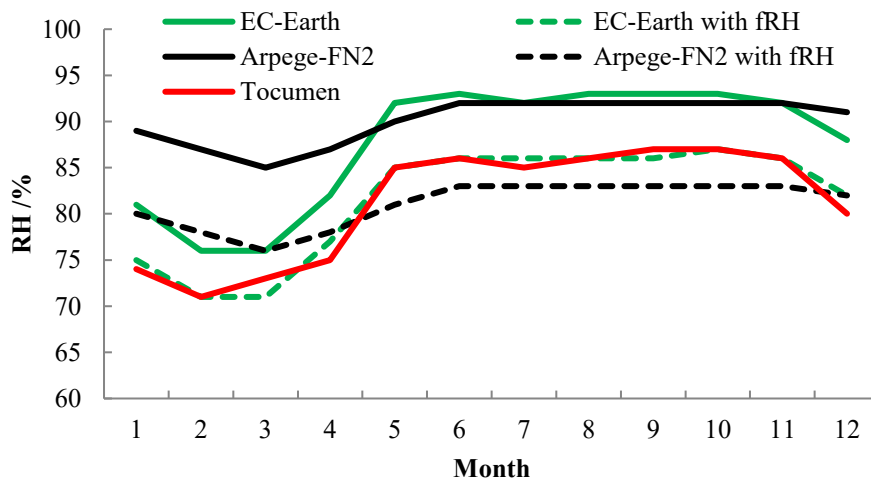


Figure 4.2.1. 4. RH monthly average over 30 years (2039-2068).

### Temperature (T)

The parameter of temperature shows in both models an underestimation of the real data, by simulation records, indeed  $f_T = 1^\circ\text{C}$  for both models. It has to be underlined that the average values have been obtained without the following years: 1983, 1987 and 1988, since they were missing at the Tocumen monitoring station (Tab. 4.2.1.5 and Fig. 4.2.1.5).

Table 4.2.1. 5. Comparison of monthly average of Temperature, over the past period 1979-2008, between the average of the monitoring station records and the models data with or without bias ( $f_{RH}$ ).

<b>T monthly average/°C</b>					
<b>Past 1979-2008</b>					
<b>Month</b>	<b>EC-Earth</b>		<b>Arpege-FN1</b>		
	<b>Tocumen</b>	<b>without <math>f_T</math></b>	<b>with <math>f_T</math></b>	<b>without <math>f_T</math></b>	
1	27	25	27	24	25
2	27	25	27	24	26
3	27	25	28	25	26
4	27	25	27	25	27
5	26	24	26	26	27
6	26	24	26	26	27
7	26	24	26	25	27
8	26	24	26	25	27
9	26	24	26	26	27
10	26	24	26	25	27
11	26	23	26	25	26
12	26	24	26	24	25

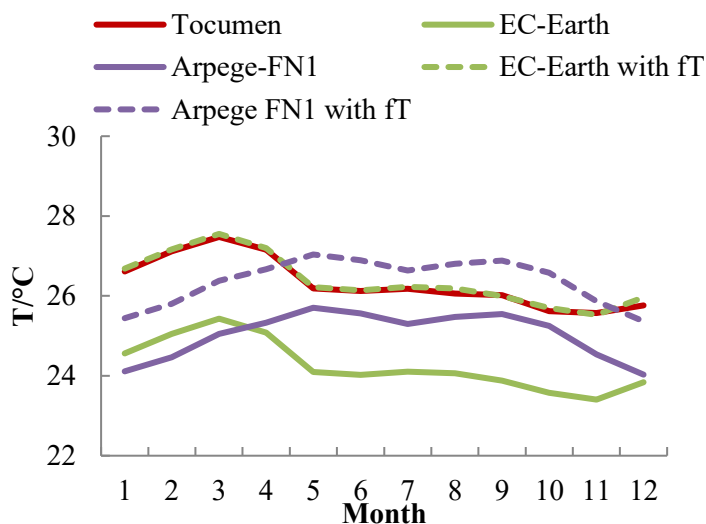


Figure 4.2.1. 5. T monthly average over 30 years (1979-2008).

Regarding the future, EC-Earth simulation shows a similar trend compared with the past situation, in particular the experiment without bias shows the same T values of the past measured data at Tocumen (Tab. 4.2.1.6 and Fig. 4.2.1.6).

Table 4.2.1. 6. Comparison of monthly average of Relative Humidity, over the future period 2039-2068, between the average of the models data with or without bias ( $f_{RH}$ ).

<b>T monthly average/°C</b>				
<b>Future 2039-2068</b>				
<b>Month</b>	<b>EC-Earth</b>		<b>Arpege-FN2</b>	
	<b>without <math>f_T</math></b>	<b>with <math>f_T</math></b>	<b>without <math>f_T</math></b>	<b>with <math>f_T</math></b>
1	26	27	26	27
2	27	28	26	27
3	27	28	27	28
4	27	28	27	28
5	26	27	27	28
6	26	27	27	28
7	26	27	27	28
8	26	27	27	28
9	26	27	27	28
10	25	26	27	28
11	25	26	26	27
12	26	27	26	27

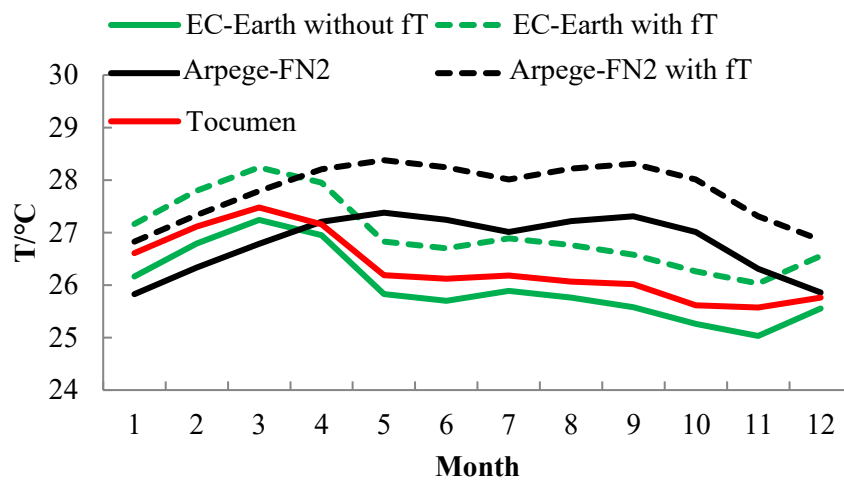


Figure 4.2.1. 6. T monthly average over 30 years (2039-2068).

#### 4.2.2. Area near Panama Viejo

Site location: Long.-79.49; Lat.9.01; EC-Earth central point: -79.6, 8.9; FN1 central point: -79.5; 8.74.

#### Rainfall (R)

In the area near Panama Viejo, the bias correction was obtained by a comparison with the Balboa FAA monitoring station. Therefore, the  $f_p$  of EC-Earth is of 0.81, while considering Arpege-FN1, it is of 0.89 (Tab. 4.2.2.1). .

Table 4.2.2. 1. Comparison of yearly amount of rainfall, over the past period 1979-2008, between the monitoring station records and the models data with or without bias ( $f_p$ ).

<b>R yearly amount (mm)</b>					
<i>Past (1979-2008)</i>					
<b>Year</b>	<b>Balboa FAA</b>	<b>EC-Earth</b>		<b>Arpege-FN1</b>	
		<b>without <math>f_T</math></b>	<b>with <math>f_T</math></b>	<b>without <math>f_T</math></b>	<b>with <math>f_T</math></b>
1979	1483	2251	1770	1600	1416
1980	1242	2192	1724	2438	2158
1981	2380	2643	2079	2274	2013
1982	1615	1908	1500	2184	1933
1983	1681	1670	1314	2057	1821
1984	1699	2164	1702	2509	2221
1985	1501	2192	1724	1414	1251
1986	1569	2008	1579	2534	2243
1987	1732	2292	1802	2236	1980
1988	2210	2808	2208	2217	1963
1989	1600	2125	1671	2195	1943
1990	1963	2457	1932	2653	2348
1991	2123	2019	1588	2986	2643
1992	2207	1835	1443	2026	1794
1993	2443	2305	1813	1663	1473
1994	2101	2211	1739	1756	1554
1995	2875	2657	2090	2311	2046
1996	2451	2725	2143	1774	1571
1997	1905	1773	1394	2156	1908
1998	1953	2460	1934	1743	1543
1999	1941	2709	2130	2450	2169
2000	1928	2350	1848	2473	2189
2001	1684	2347	1845	2141	1895
2002	1435	2157	1696	2222	1967
2003	2019	2672	2101	2278	2017
2004	1783	2949	2319	1651	1461
2005	1814	2518	1980	2062	1825
2006	2042	2480	1951	2023	1790
2007	1783	2793	2197	1350	1195
2008	1649	2405	1891	2804	2482

Considering the tendency of the past yearly rainy amount, of the bias corrected models records (Fig. 4.2.2.1), it can be noticed an increase for both the monitoring station and EC-Earth data, while Arpege-FN1 shows a slight decrease.

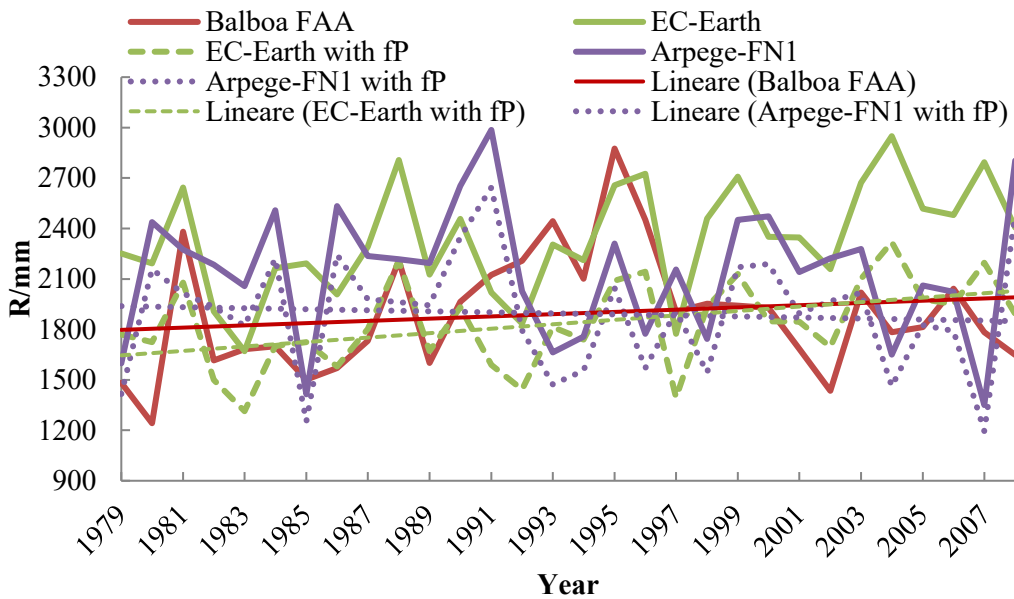


Figure 4.2.2. 1. Comparison of the yearly rainfall amount Balboa FAA/ EC-Earth / Arpege-FN1 (1979-2008).

This trend is opposite in the future 2039-2968, where the scenarios of both models, considering the situation with and without bias, show respectively a small decrease in EC-Earth simulation, and a slight increase, in Arpege-FN2 simulation (Fig. 4.2.2.2 and Tab. 4.2.2.2).

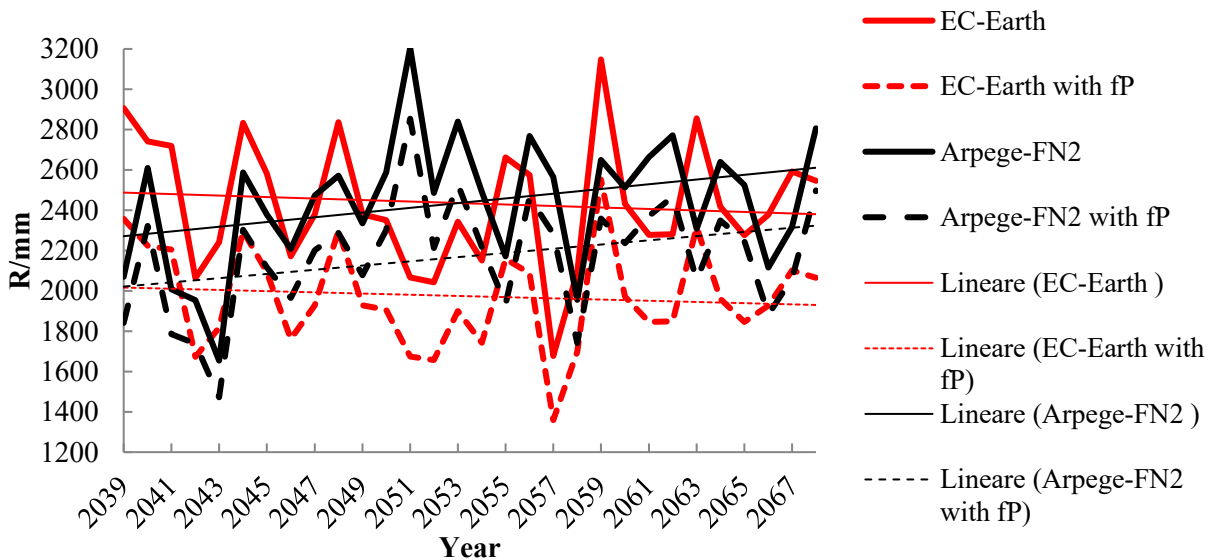


Figure 4.2.2. 2. Comparison of the yearly R amount EC-Earth –Arpege-FN2.



Table 4.2.2. 2. Comparison of yearly amount of rainfall, over the future period 2039-2068, models data with or without bias (*fP*).

<b>R yearly amount (mm)</b>				
<i>Future (2039-2068)</i>				
<b>Year</b>	<b>EC-Earth</b>		<b>Arpege-FN2</b>	
	<b>without <i>fP</i></b>	<b>with <i>fP</i></b>	<b>without <i>fP</i></b>	<b>with <i>fP</i></b>
2039	2907	2357	2069	1841
2040	2742	2223	2609	2322
2041	2719	2204	2007	1786
2042	2064	1673	1953	1738
2043	2241	1817	1654	1472
2044	2833	2297	2588	2303
2045	2583	2094	2379	2117
2046	2172	1761	2208	1965
2047	2380	1929	2473	2201
2048	2836	2299	2571	2288
2049	2379	1929	2335	2078
2050	2351	1906	2587	2302
2051	2067	1675	3206	2854
2052	2043	1656	2486	2213
2053	2342	1899	2840	2528
2054	2150	1743	2491	2217
2055	2662	2158	2172	1933
2056	2574	2087	2769	2464
2057	1677	1359	2565	2283
2058	2094	1698	1956	1741
2059	3148	2552	2650	2359
2060	2431	1971	2513	2236
2061	2277	1846	2664	2371
2062	2281	1849	2771	2466
2063	2856	2316	2308	2054
2064	2418	1960	2639	2349
2065	2276	1845	2526	2248
2066	2377	1927	2116	1883
2067	2592	2102	2317	2062
2068	2546	2065	2807	2498

Relative Humidity (RH)

The bias for this parameter has been obtained through the daily average calculated over the 1979-2008 period, removing the missing periods of Balboa FAA station even in the model series. Thus, in this case the  $f_{RH}$  of EC-Earth corresponds to 0.92, while Arpege-FN1 presents a  $f_{RH}$  of 0.95 (Tab. 4.2.2.3).

Table 4.2.2. 3. Comparison of monthly average of Relative Humidity, over the past period 1979-2008, between the average of the monitoring station records and the models data with or without bias ( $f_{RH}$ ).

Month	RH monthly average/%				
	Past 1979-2008				
	Balboa FAA	EC-Earth		Arpege-FN1	
		without $f_{RH}$	with $f_{RH}$	without $f_{RH}$	with $f_{RH}$
1	74	79	73	82	78
2	71	75	69	83	79
3	70	74	68	83	79
4	74	82	75	83	79
5	80	90	83	82	79
6	83	92	84	83	79
7	83	91	83	83	79
8	83	91	83	83	79
9	83	92	84	84	80
10	84	91	84	84	80
11	84	90	82	82	78
12	81	86	79	82	79

Observing the monthly average, for the period 1979-2008, it is evident the similarity between the measured data at the Balboa FAA station and the model EC-Earth, which well represents the seasonality in these thirty years (Fig. 4.2.2.3).

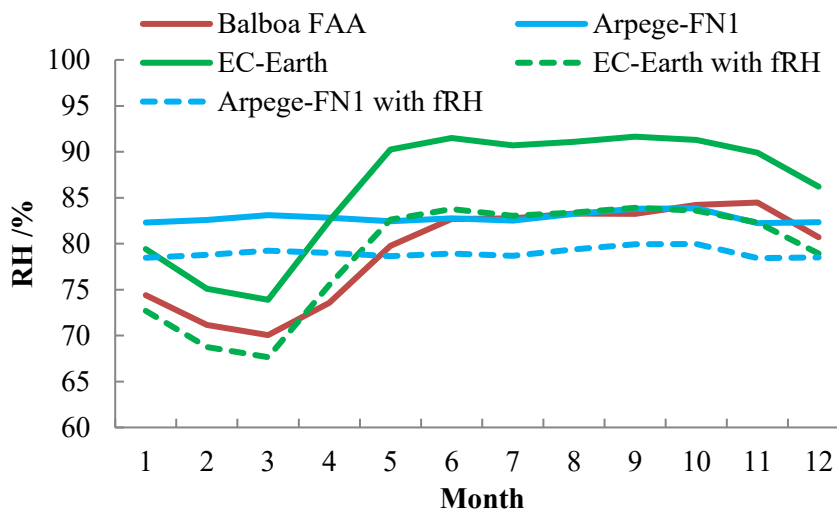


Figure 4.2.2. 3. RH monthly average over past 30 years (1979-2008).

Applying the multiplying factor also in the future situation, considering the RCP 8.5 scenario for both models, EC-Earth results again the most suitable in representing the seasonality, since its trend is the most comparable to the past situation (Tab. 4.2.2.4 and Fig. 4.2.2.4).

Table 4.2.2. 4 . Comparison of monthly average of Relative Humidity, over the future period 2039-2068, between the average of the monitoring station records and the models data with or without bias ( $f_{RH}$ ).

<b>RH monthly average/%</b>				
<b>Future 2039-2068</b>				
<b>Month</b>	<b>EC-Earth</b>		<b>Arpege-FN2</b>	
	<b>without <math>f_{RH}</math></b>	<b>with <math>f_{RH}</math></b>	<b>without <math>f_{RH}</math></b>	<b>with <math>f_{RH}</math></b>
1	79	73	82	78
2	75	69	82	78
3	74	68	82	78
4	82	75	82	78
5	90	83	83	79
6	92	84	83	79
7	91	83	83	79
8	91	83	84	80
9	92	84	84	80
10	91	84	84	80
11	90	82	83	78
12	86	79	82	78

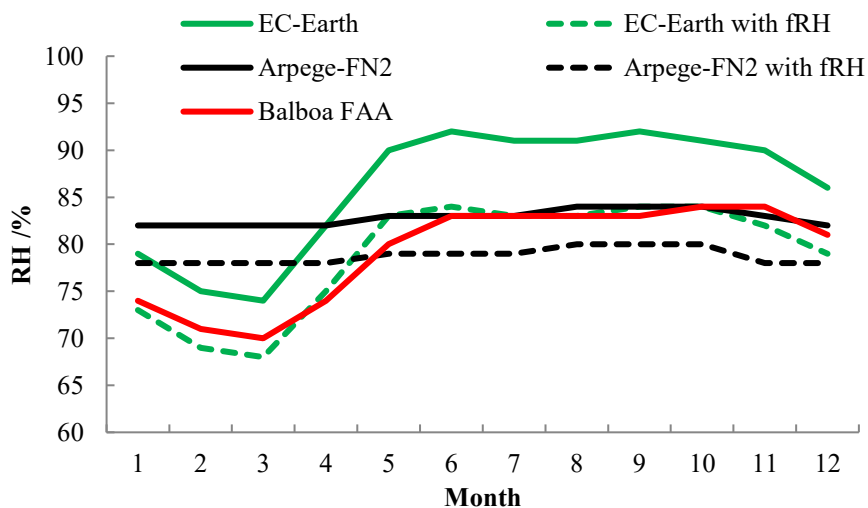


Figure 4.2.2. 4. RH monthly average over future 30 years (2039-2068).

Temperature (T)

Considering the temperature, EC-Earth model underestimates it, with a  $f_T$  1.8, while Arpege-FN1 presents a slight overestimation, with a  $f_T$  of -0.01. Even in this case the model EC-Earth describes in the better way the trend of the measured temperature (Tab. 4.2.2.5 and Fig. 4.2.2.5).

Table 4.2.2. 5. Comparison of monthly average of Temperature, over the past period 1979-2008, between the average of the monitoring station records and the models data with or without bias ( $f_T$ ).

T monthly average/°C					
Past 1979-2008					
Month	Balboa FAA	EC-Earth		Arpege-FN1	
		without $f_T$	with $f_T$	without $f_T$	with $f_T$
1	27	25	27	26	26
2	27	26	28	26	26
3	28	26	28	26	26
4	28	26	28	27	27
5	27	25	27	27	27
6	27	25	27	27	27
7	27	25	27	27	27
8	27	25	27	27	27
9	27	25	26	27	27
10	26	24	26	27	27
11	26	24	26	27	27
12	27	25	26	26	26

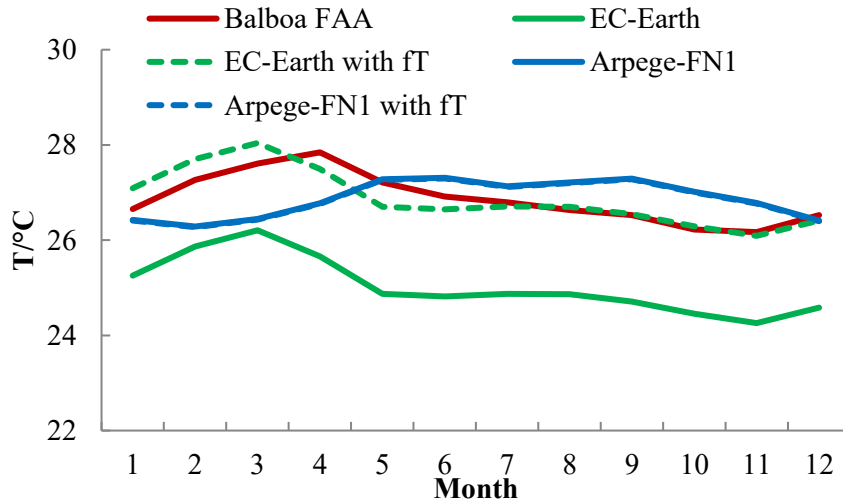


Figure 4.2.2. 5. T monthly average over past 30 years (1979-2008).

The future situation shows an average increase of 2 degrees of EC-Earth and 1 degree for Arpege-FN1 (Tab. 4.2.2.6). EC-Earth simulation represents better the difference between the dry and the rainy season (Fig. 4.2.2.6).

Table 4.2.2. 6. Comparison of monthly average of Temperature, over the future period 2039-2068, between the average of the monitoring station records and the models data with or without bias ( $f_T$ ).

T monthly average/°C				
Future 2039-2068				
Month	EC-Earth		Arpege-FN2	
	without $f_T$	with $f_T$	without $f_T$	with $f_T$
1	27	29	28	28
2	28	30	28	28
3	28	30	28	28
4	28	29	28	28
5	27	28	29	29
6	26	28	29	29
7	27	28	28	28
8	27	28	29	29
9	26	28	29	29
10	26	28	29	29
11	26	28	28	28
12	26	28	28	28

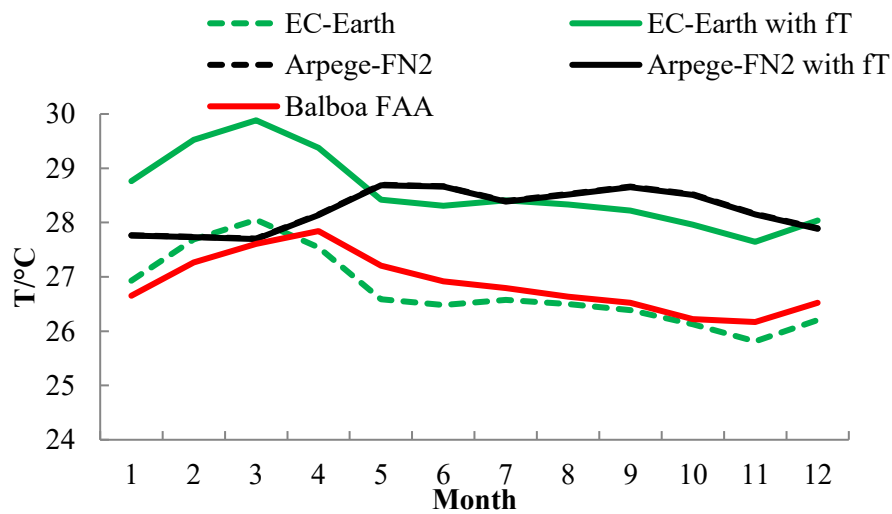


Figure 4.2.2. 6. T monthly average over future 30 years (2039-2068).

### 4.2.3. Area near San Lorenzo

Site location: Long.-80.00, Lat.9.32; EC-Earth central point: Long. -79.85, Lat. 9.30; Arpege-FN1 central point: Long.-80.00; Lat. 9.24.

#### Rainfall (R)

In this case, for obtaining the daily average over 28 years (1981-2008), the data source utilized were the monthly rainfall amount calculated by the Smithsonian Tropical Research Institute (Tab. 4.2.3.1). In order to perform the bias correction, it was utilized the average of Gatún and CCL stations, thus having a multiplicative factor respectively for EC-Earth of 1.04 and of 1.39 for Arpege.

Table 4.2.3. 1. Comparison of yearly amount of rainfall, over the past period 1981-2008, between the average of monitoring stations records and the models data with or without bias ( $f_P$ ).

<b>R yearly amount (mm)</b>					
<i>Past (1981-2008)</i>					
<b>Year</b>	<b>Av. G + CCL</b>	<b>EC-Earth</b>		<b>Arpege-FN1</b>	
		<b>without <math>f_P</math></b>	<b>with <math>f_P</math></b>	<b>without <math>f_P</math></b>	<b>with <math>f_P</math></b>
1981	4256	2872	2990	2063	2865
1982	2503	2632	2740	1962	2725
1983	2882	2422	2521	2031	2820
1984	2435	2872	2990	2143	2975
1985	2902	2594	2701	1826	2535
1986	2385	2752	2865	2174	3019
1987	3913	2808	2923	2225	3090
1988	2463	2946	3067	1993	2768
1989	2456	2755	2868	2015	2798
1990	3164	2737	2850	2086	2896
1991	2662	2762	2875	2542	3530
1992	3112	2531	2635	2572	3571
1993	3076	2782	2896	1754	2435
1994	2739	3033	3157	1708	2372
1995	3288	2583	2689	2382	3308
1996		3230	3363	2194	3047
1997	1859	2681	2791	2144	2977
1998		2806	2921	2091	2903
1999	3381	2878	2996	2230	3096
2000	3120	2835	2951	2220	3083
2001	2761	3019	3143	2101	2918
2002	2638	2731	2843	2252	3127
2003	2852	3022	3146	2199	3053
2004	3062	3132	3260	1750	2431
2005	2797	2718	2829	2114	2936
2006	2991	2895	3013	1950	2708
2007	3374	2991	3114	1766	2452
2008	2605	2666	2775	2059	2860

Through the observation of the yearly rainfall amount over the past period, the best representation of the trend of this parameter is due to Arpege-FN1 simulation corrected with bias, which shows a little decrease. On the contrary, EC-Earth with bias presents a modest increase (Fig. 4.2.3.1).

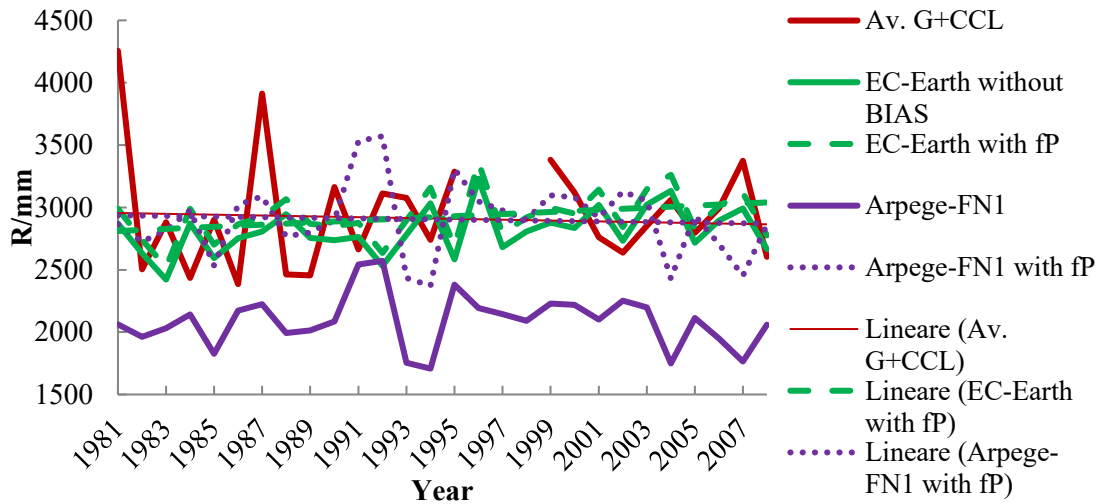


Figure 4.2.3. 1. R yearly amount over past 28 years (1981-2008).

In the future 2039-2068, the two simulations present, respectively, a slight decrease (EC-Earth scenario) and a slight increase (Arpege-FN2 experiment) (Fig. 4.2.3.2 and Tab. 4.2.3.2).

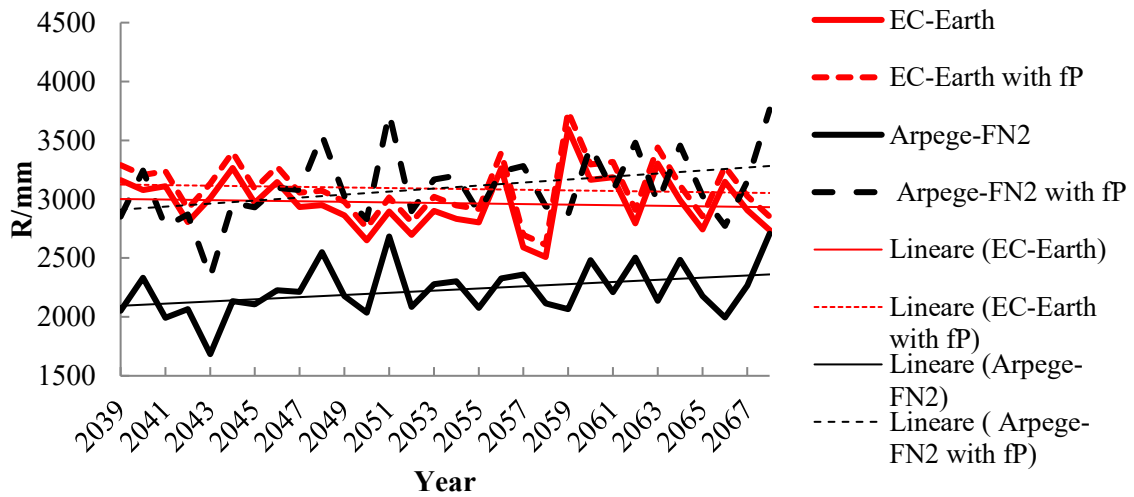


Figure 4.2.3. 2. R yearly amount over future 30 years (2039-2068).

Table 4.2.3. 2. Comparison of yearly amount of rainfall, over the future period 2039-2068, between the models data with or without bias ( $f_P$ ).

<b>R yearly amount (mm)</b>				
<b><i>Future (2039-2068)</i></b>				
<b>Year</b>	<b>EC-Earth</b>		<b>Arpege-FN2</b>	
	<b>without <math>f_P</math></b>	<b>with <math>f_P</math></b>	<b>without <math>f_P</math></b>	<b>with <math>f_P</math></b>
2039	3161	3290	2052	2852
2040	3079	3205	2333	3243
2041	3111	3238	1992	2769
2042	2806	2921	2065	2870
2043	3009	3132	1684	2341
2044	3266	3400	2135	2968
2045	2969	3090	2108	2930
2046	3146	3275	2227	3096
2047	2934	3055	2214	3077
2048	2951	3072	2551	3546
2049	2862	2979	2177	3026
2050	2650	2758	2037	2831
2051	2896	3014	2684	3731
2052	2696	2807	2084	2897
2053	2902	3021	2279	3168
2054	2832	2948	2303	3201
2055	2804	2918	2078	2888
2056	3264	3397	2328	3236
2057	2591	2697	2361	3282
2058	2509	2612	2115	2940
2059	3596	3744	2065	2870
2060	3166	3296	2482	3450
2061	3187	3317	2209	3071
2062	2794	2908	2504	3481
2063	3303	3439	2137	2971
2064	2992	3115	2485	3455
2065	2743	2856	2179	3028
2066	3148	3277	1995	2773
2067	2907	3026	2268	3153
2068	2739	2852	2707	3762



Relative Humidity (RH)

Since the Cocosolo-Cristobal-Limonbay complex station presents RH data with several lacks, the bias correction has been performed considering only Gatún station. The period considered is from 1979 to 2005, without 1983 year, 9-12 months of 1999 year and 1-3, 5 months of 2005 year. Therefore, these missing days have been removed also to the model series.

EC-Earth shows a  $f_P$  corresponding to 0.88, while in Arpege-FN1 it is equal to 0.89. Comparing the data, listed in Table 4.2.3.3. and showed in the graph (Fig.4.2.3.3) it is possible to affirm that EC-Earth model represents the seasonality of RH better.

Table 4.2.3. 3. Comparison of monthly average of Relative Humidity, over the past period 1979-2005, between the average of the monitoring station records and the models data with or without bias ( $f_{RH}$ ).

RH monthly average/%					
Past 1979-2005					
Month	Gatún	EC-Earth		Arpege-FN1	
		without $f_{RH}$	with $f_{RH}$	without $f_{RH}$	with $f_{RH}$
1	75	84	74	89	79
2	73	82	72	87	77
3	72	81	72	86	76
4	75	87	77	87	77
5	79	92	81	88	78
6	80	92	82	89	79
7	81	92	82	90	80
8	82	93	82	90	80
9	83	92	82	90	80
10	83	92	81	90	80
11	83	93	82	91	81
12	80	90	79	90	80

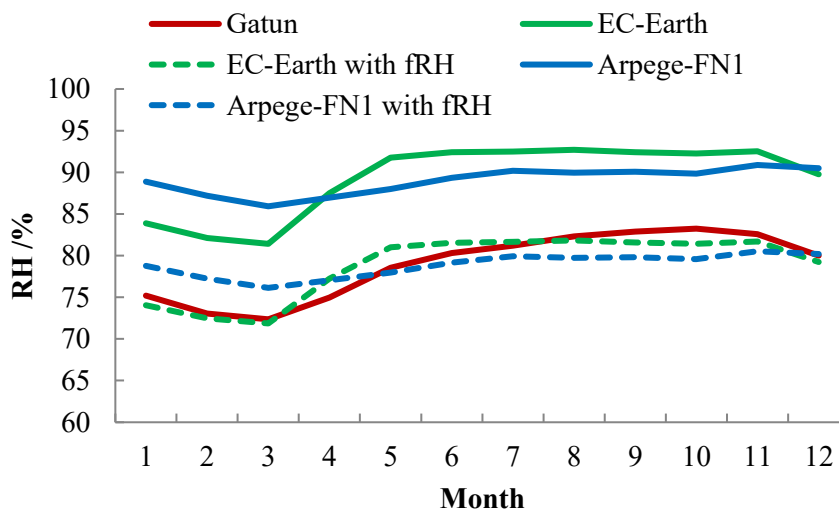


Figure 4.2.3. 3. RH monthly average over past 27 years (1979-2005).

As observed in the previous locations, the future trend of relative humidity is better represented by EC-Earth with the bias correction, as observable in Table 4.2.3.4 and Figure 4.2.3.4.

Table 4.2.3. 4. Comparison of monthly average of Relative Humidity, over the future period 2039-2068, between the average of the monitoring station records and the models data with or without bias ( $f_{RH}$ ).

<b>RH monthly average/%</b>				
<b>Future 2039-2068</b>				
<b>Month</b>	<b>EC-Earth</b>		<b>Arpege-FN2</b>	
	<b>without <math>f_{RH}</math></b>	<b>with <math>f_{RH}</math></b>	<b>without <math>f_{RH}</math></b>	<b>with <math>f_{RH}</math></b>
1	85	75	89	79
2	81	72	87	77
3	83	73	85	75
4	88	77	86	76
5	92	81	88	78
6	93	82	90	80
7	93	82	90	80
8	93	82	91	81
9	93	82	90	81
10	92	82	90	80
11	93	82	91	81
12	91	80	90	80

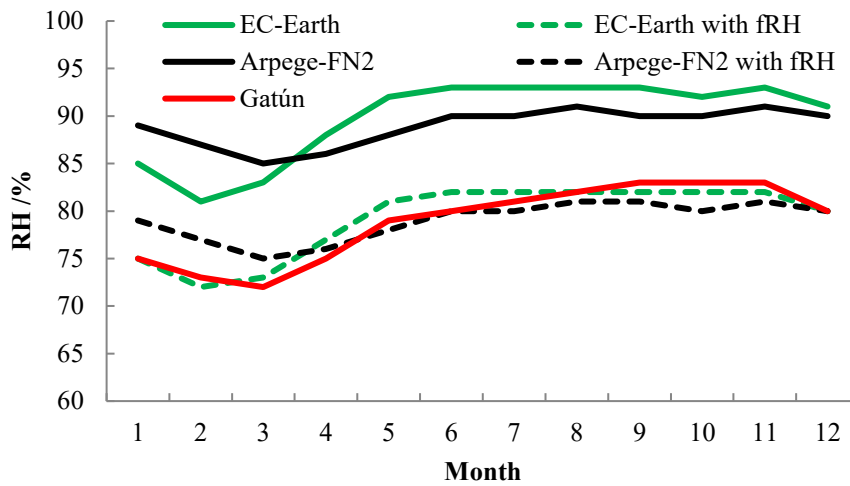


Figure 4.2.3. 4. RH monthly average over future 30 years (2039-2068).

Temperature (T)

The temperature data considered belong to the only Gatún station, as for the previous parameter. The missing period are the same of RH, so, the 1983 year, 9-12 months of 1999 year and 1-3, 5 months of 2005 year. Nevertheless, the 2006, 2007 and 2008 years are present, so the period of comparison is 30 years.

Considering the bias correction, EC-Earth shows a  $f_T$  of 2.16 °C, while in Arpege-FN1 it corresponds to 1.00°C. Through this correction it possible to appreciate the high compatibility between the seasonality of EC-Earth and the Gatún station (Tab. 4.2.3.5; Fig. 4.2.3.5).

Table 4.2.3. 5. Comparison of monthly average of Temperature, over the past period 1979-2008, between the average of the monitoring station records and the models data with or without bias ( $f_T$ ).

T monthly average/°C					
Past 1979-2008					
Month	Gatún	EC-Earth		Arpege-FN1	
		without $f_T$	with $f_T$	without $f_T$	with $f_T$
1	27	25	27	25	26
2	27	25	27	25	26
3	27	25	27	26	27
4	27	25	27	26	27
5	27	25	27	27	28
6	27	25	27	27	28
7	27	25	27	26	27
8	27	25	27	26	27
9	27	25	27	27	28
10	27	24	26	26	27
11	26	24	26	25	26
12	26	24	26	25	26

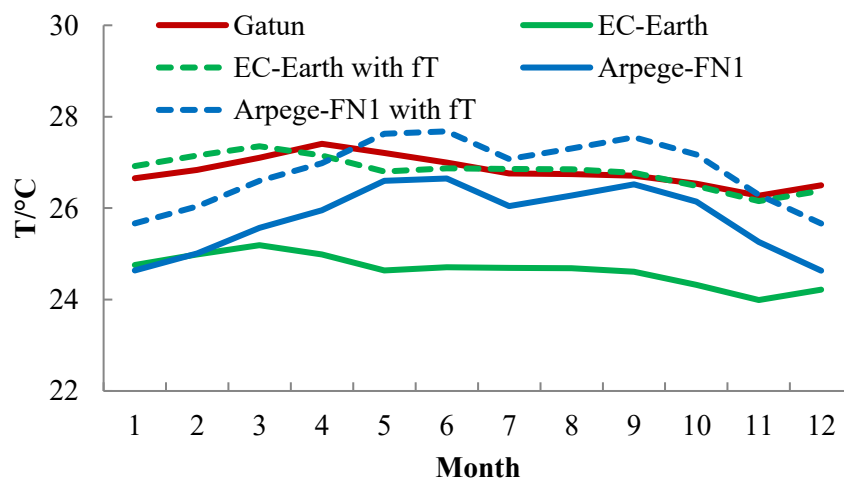


Figure 4.2.3. 5. T monthly average over past 30 years (1979-2008).

Therefore, according to the previous considerations, also for the future period EC-Earth can be considered the most probable as future trend of the temperature parameter in this area (Tab. 4.2.3.6 Fig. 4.2.3.6).

Table 4.2.3. 6. Comparison of monthly average of Temperature, over the future period 2039-2068, between the average of the monitoring station records and the models data with or without bias ( $f_T$ ).

<b>T monthly average/°C</b>				
<i>Future 2039-2068</i>				
<b>Month</b>	<b>EC-Earth</b>		<b>Arpege-FN2</b>	
	<b>without <math>f_T</math></b>	<b>with <math>f_T</math></b>	<b>without <math>f_T</math></b>	<b>with <math>f_T</math></b>
1	26	29	26	27
2	27	29	27	28
3	27	29	27	28
4	27	29	28	29
5	26	29	28	29
6	26	29	28	29
7	26	29	28	29
8	26	28	28	29
9	26	28	28	29
10	26	28	28	29
11	26	28	27	28
12	26	28	26	27

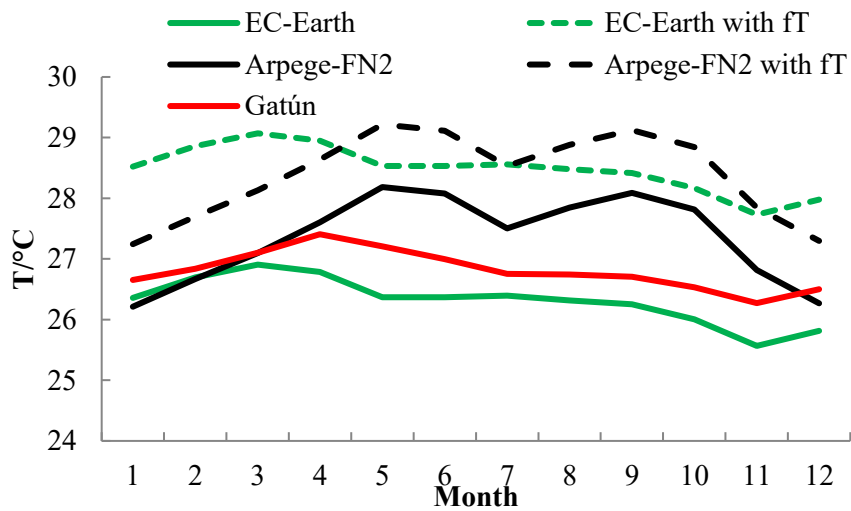


Figure 4.2.3. 6. T monthly average over future 30 years (2039-2068).

#### 4.2.4. San Lorenzo area

Site Location: Long. -80.00, Lat. 9.32; EC-Earth central point: Long.-80.05, Lat. 9.30; Arpege-FN1 central point: Long.-80.00, Lat. 9.24.

##### Rainfall (R)

In San Lorenzo area, Pina monitoring station was compared with the two models. Therefore, EC-Earth presents a  $f_P$  equal to 1.68, while Arpege-FN1 has a  $f_P$  of 1.45 (Tab. 4.2.4.1).

Table 4.2.4. 1. Comparison of yearly amount of rainfall, over the past period 1979-1998, between the monitoring station records and the models data with or without bias ( $f_P$ ). In red are highlighted the maximum values.

		<b>R yearly amount (mm)</b>			
		<i>Past (1981-1998)</i>			
<b>Year</b>	<b>Pina</b>	<b>EC-Eart</b>		<b>Arpege-FN1</b>	
		<b>without <math>f_P</math></b>	<b>with <math>f_P</math></b>	<b>without <math>f_P</math></b>	<b>with <math>f_P</math></b>
1979	2939	1417	2381	1922	2795
1980	3360	1949	3275	2284	3321
1981	4584	1702	2859	2063	3000
1982	3152	1969	3308	1962	2853
1983	3863	1741	2926	2031	2953
1984	3028	2122	3566	2143	3115
1985	4025	1635	2747	1826	2655
1986	2667	1835	3083	2174	3161
1987	2267	1926	3237	2225	3235
1988	1965	2011	3378	1993	2898
1989	2649	1838	3088	2015	2930
1990	3208	1658	2786	2086	3033
1991	2063	1935	3252	2542	3696
1992	3426	1933	3248	2572	3739
1993	2782	1736	2918	1754	2550
1994	2908	1494	2510	1407	2045
1995	3816	1687	2835	2382	3463
1996	3662	2084	3501	2194	3190
1997	1924	1981	3329	2144	3117
1998	1288	1526	2564	2091	3040

Observing the records plotted in a graph (Fig. 4.2.4.1), Pina data shows a strong decrease over the 20 years considered, while both the simulations, bias corrected, show a slight increase, comparable to an unvaried situation, for EC-Earth case. If we consider the first decade, the yearly amounts measured by the station are considerably greater than the simulated ones, while in the last years the range is better represented.

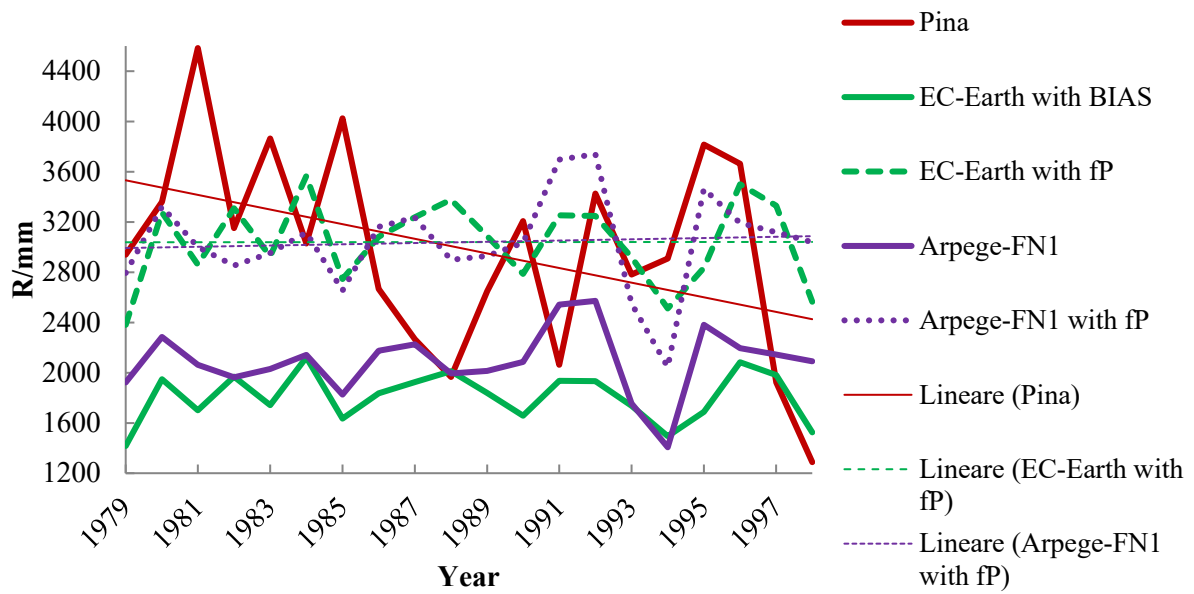


Figure 4.2.4. 1. R yearly amount (mm), over the past period 1979-1998.

This condition of invariability over time, is maintained also in the future period by the EC-Earth experiment, while Arpege-FN2 show an increase in the middle future period. (Fig. 4.2.4.2 and Tab. 4.2.4.2).

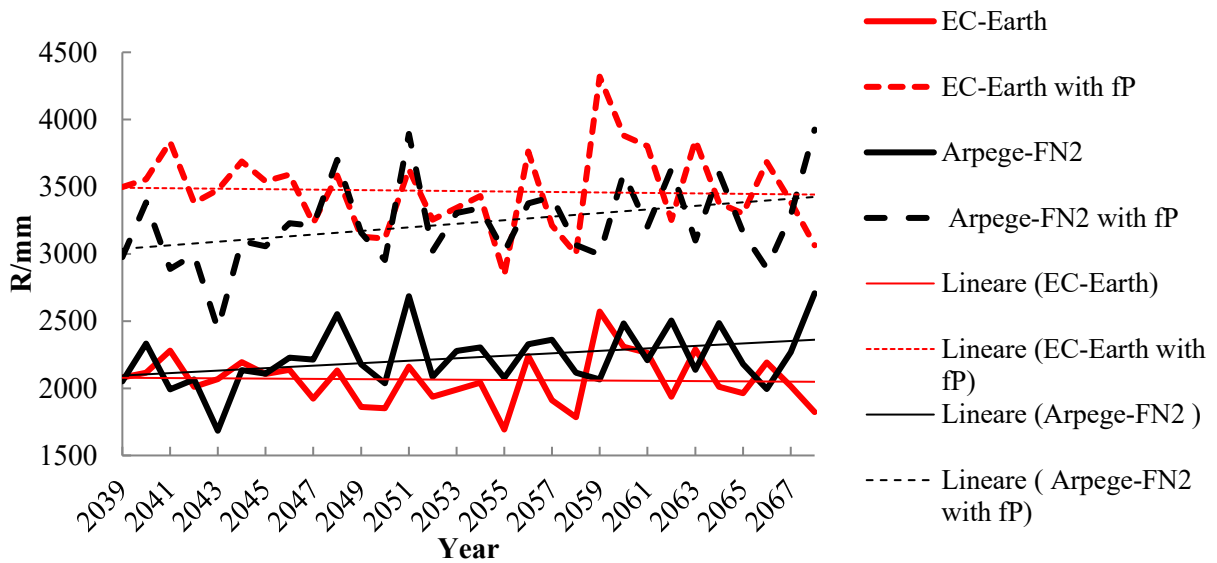


Figure 4.2.4. 2. Comparison of the yearly R amount EC-Earth - Arpege-FN2.

Table 4.2.4. 2. Comparison of yearly amount of rainfall, over the future period 2039-2068, between the two models data with or without bias (fP).

<i>Future (2039-2068)</i>				
<b>Year</b>	<b>EC-Earth</b>		<b>Arpege-FN2</b>	
	<b>without <math>f_P</math></b>	<b>with <math>f_P</math></b>	<b>without <math>f_P</math></b>	<b>without <math>f_P</math></b>
2039	2081	3497	2052	2975
2040	2115	3554	2333	3383
2041	2281	3833	1992	2888
2042	2012	3381	2065	2994
2043	2069	3477	1684	2442
2044	2195	3687	2135	3096
2045	2107	3540	2108	3057
2046	2137	3590	2227	3229
2047	1922	3229	2214	3210
2048	2133	3583	2551	3699
2049	1862	3129	2177	3157
2050	1852	3113	2037	2954
2051	2160	3630	2684	3892
2052	1936	3254	2084	3022
2053	1990	3343	2279	3305
2054	2042	3431	2303	3339
2055	1693	2844	2078	3013
2056	2239	3762	2328	3376
2057	1912	3212	2361	3423
2058	1785	3000	2115	3067
2059	2571	4319	2065	2994
2060	2309	3880	2482	3599
2061	2264	3803	2209	3203
2062	1936	3252	2504	3631
2063	2289	3846	2137	3099
2064	2010	3378	2485	3603
2065	1963	3299	2179	3160
2066	2192	3683	1995	2893
2067	2016	3387	2268	3289
2068	1824	3064	2707	3925

#### 4.2.5. Portobelo area

Site Location: Long -79.67, Lat.9.56; EC-Earth point: Long. -79.65, Lat. 9.55; Arpege-FN1 point: Long. -79.50, Lat. 9.74.

#### Rainfall (R)

The past period considered in Portobelo area is from 1979 to 2000. The bias obtained for the two models is respectively of  $f_P$  1.14, for EC-Earth, and  $f_P$  1.54, for Arpege-FN1. As evident observing Table 4.2.4.1, Portobelo monitoring station recorded consistently high values of yearly rainfall amount, reaching values greater than 5000 and 6000 mm per year.

Table 4.2.5. 1. Comparison of yearly amount of rainfall, over the past period 1979-2000, between the monitoring station records and the models data with or without bias ( $f_P$ ). In red are highlighted the maximum values.

<b>R yearly amount (mm)</b>					
<i>Past (1979-2000)</i>					
<b>Year</b>	<b>Portobelo</b>	<b>EC-Earth</b>		<b>Arpege-FN1</b>	
		<b>without <math>f_P</math></b>	<b>with <math>f_P</math></b>	<b>without <math>f_P</math></b>	<b>with <math>f_P</math></b>
1979	3156	2938	3335	2067	3180
1980	3115	3160	3587	2752	4233
1981	3747	3484	3955	2246	3455
1982	3037	2905	3298	2315	3560
1983	3524	2695	3060	2264	3483
1984	3251	3474	3944	2722	4187
1985	3857	3115	3536	1738	2673
1986	3051	3258	3699	2602	4002
1987	5644	3304	3751	2717	4179
1988	2888	3363	3818	2375	3654
1989	3917	3441	3907	2155	3315
1990	3979	3332	3782	2388	3674
1991	3807	3257	3698	3477	5349
1992	4233	2926	3322	2630	4046
1993	3925	3259	3699	1887	2902
1994	4201	3469	3938	1762	2711
1995	6279	3228	3664	2677	4118
1996	3401	3831	4350	2419	3721
1997	2645	2996	3402	2374	3652
1998	2823	3430	3894	2142	3294
1999	1015	1225	1391	907	1395
2000	2903	3402	3862	2671	4108



Plotting the records, an increase of yearly rainfall amount in the monitoring station data is clearly noticeable. This trend is better represented by EC-Earth simulation that, even if it does not show consistent peaks of rainfall during the past period, presents an increase over the 22 years (Fig. 4.2.5.1).

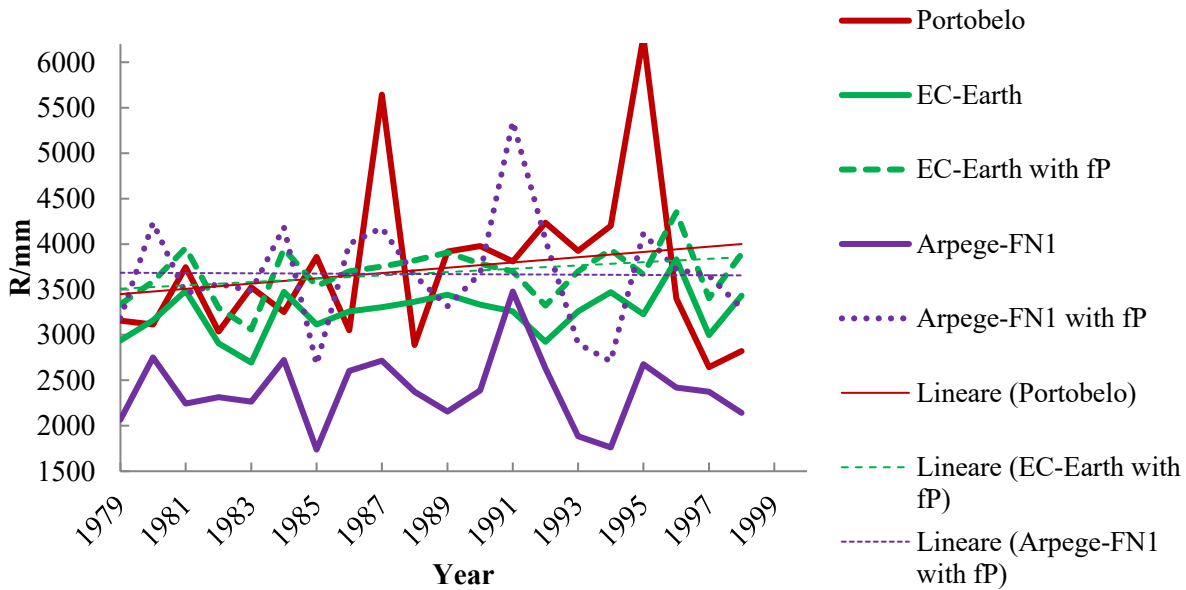


Figure 4.2.5. 1. R yearly amount (mm), over the past period 1979-2000.

Nevertheless, considering the future, EC-Earth shows a decrease over 2039-2068, while Arpege-FN2 simulation present an increasing trend over the period (Fig. 4.2.5.2 and Tab. 4.2.5.2).

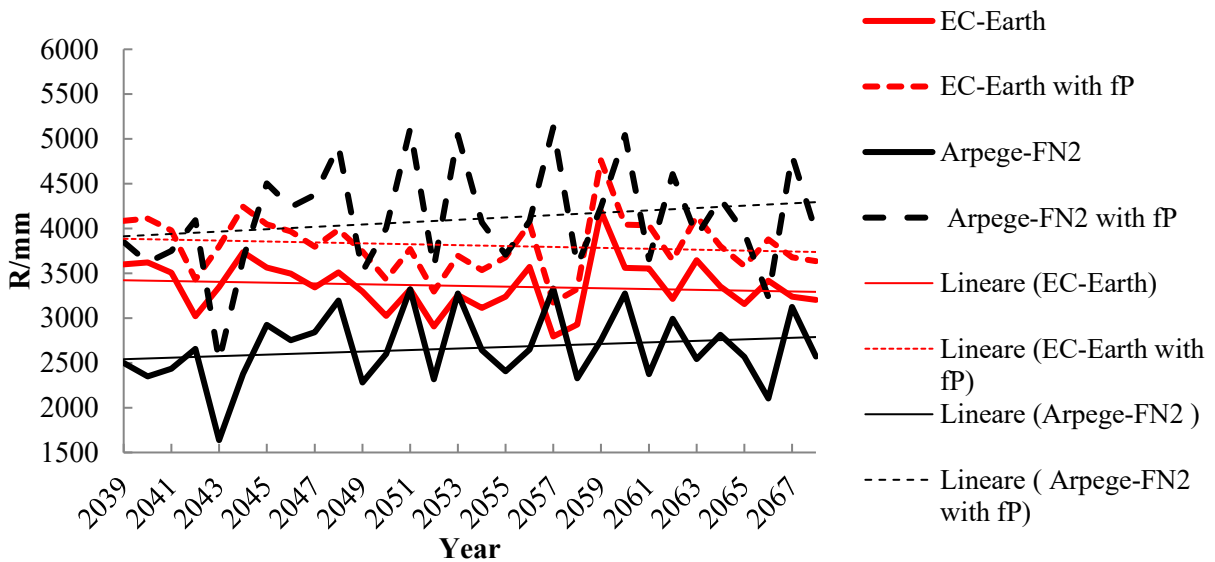


Figure 4.2.5. 2. Comparison of the yearly R amount EC-Earth - Arpege-FN2.

Table 4.2.5. 2. Comparison of yearly amount of rainfall, over the future period 2039-2068, between the two models data with or without bias (fP).

<b>R yearly amount (mm)</b>				
<i>Future (2039-2068)</i>				
<b>Year</b>	<b>EC-Earth</b>		<b>Arpege-FN2</b>	
	<b>without <math>f_P</math></b>	<b>with <math>f_P</math></b>	<b>without <math>f_P</math></b>	<b>with <math>f_P</math></b>
2039	3598	4085	2500	2500
2040	3622	4112	2351	2351
2041	3506	3980	2436	2436
2042	3022	3431	2658	2658
2043	3346	3799	1638	1638
2044	3736	4242	2378	2378
2045	3564	4045	2924	2924
2046	3495	3967	2752	2752
2047	3343	3795	2842	2842
2048	3511	3986	3195	3195
2049	3297	3743	2283	2283
2050	3024	3433	2599	2599
2051	3321	3770	3321	3321
2052	2905	3297	2316	2316
2053	3255	3695	3276	3276
2054	3115	3536	2642	2642
2055	3240	3678	2407	2407
2056	3570	4053	2650	2650
2057	2795	3173	3330	3330
2058	2928	3324	2328	2328
2059	4194	4761	2752	2752
2060	3561	4043	3276	3276
2061	3555	4036	2375	2375
2062	3213	3648	2992	2992
2063	3645	4137	2541	2541
2064	3352	3805	2813	2813
2065	3156	3582	2567	2567
2066	3417	3879	2101	2101
2067	3239	3677	3126	3126
2068	3203	3636	2571	2571